

2019

ACCOMPLISHMENTS AND OPPORTUNITIES

NIST SP 1242

NIST

National Institute of Standards and Technology
U.S. Department of Commerce



ON THE COVER

The NCNR's neutron source provides a valuable research tool for a wide variety of scientific fields from biological systems, engineering materials, to magnetic structures, and more. The cover features data from only a few of the experiments highlighted in this report.

NIST Special Publication 1242

2019 NIST Center for Neutron Research Accomplishments and Opportunities

Robert M. Dimeo, Director

Steven R. Kline, Editor

This publication is available free of charge on
the [International DOI Foundation website](#)

December 2019



*U.S. Department of Commerce
Wilbur L. Ross, Jr., Secretary*

*National Institute of Standards and Technology
Walter Copan, NIST Director and Undersecretary of
Commerce for Standards and Technology*

DISCLAIMER

Certain commercial entities, equipment, or materials may be identified in this document in order to describe an experimental procedure or concept adequately. Such identification is not intended to imply recommendation or endorsement by the National Institute of Standards and Technology, nor is it intended to imply that the entities, materials, or equipment are necessarily the best available for the purpose. Throughout the text, unless otherwise stated, q refers to the momentum transfer. Error bars in figures and uncertainties in the text represent one standard deviation unless otherwise stated.

National Institute of Standards and Technology Special
Publication 1242, 96 pages (December 2019)
CODEN: NSPUE2

This publication is available free of charge from:
<https://doi.org/10.6028/NIST.SP.1242>

Table of Contents

ii FOREWORD

01 THE NIST CENTER FOR NEUTRON RESEARCH

02 NIST CENTER FOR NEUTRON RESEARCH INSTRUMENTS

04 NCNR IMAGES 2019

HIGHLIGHTS

BIOSCIENCES

- 06 Methanol accelerates DMPC flip-flop and transfer: A SANS study on lipid dynamics, M. H. L. Nguyen, et al. (CHNRNS)
- 08 Conductivity and dynamics of biomimetic synthetic polypeptides, A. Pena-Francesch, et al. (CHNRNS)
- 10 Characterization of porous alucone membranes used for single-molecule DNA sequencing, V. Jadhav, et al.

CHEMICAL PHYSICS

- 12 Record high hydrogen storage capacity in the metal-organic framework $\text{Ni}_2(\text{m-dobdc})$ at near-ambient temperatures, M. T. Kapelewski, et al.
- 14 Short acoustic phonon lifetimes limit thermal transport in photovoltaic methylammonium lead iodide, A. Gold-Parker, et al.
- 16 Metal-organic frameworks for highly effective ethane/ethylene separation, R.-B. Lin, et al.
- 18 Probing structure-dependent reorientational behavior of SiH_3^- anions in alkali-metal silanides by quasielastic neutron scattering, M. Dimitrievska, et al. (CHNRNS)

CONDENSED MATTER

- 20 Spin triplet superconductivity in UTe_2 , S. Ran, et al.
- 22 Spin stripe order in a square planar trilayer nickelate, J. Zhang, et al. (CHNRNS)
- 24 Kondo insulator-like state in antiferromagnetically ordered YbIr_3Si_7 , M. Stavinoha, et al.
- 26 Deciphering the coupling between structural disorder and magnetic order in chiral skyrmion host materials, J. D. Bocarsly, et al.
- 28 Symmetry breaking and singular angular magnetoresistance in a magnetic nodal semimetal, T. Suzuki, et al.
- 30 Tuning topology in thin films using antiferromagnetism, Q. L. He, et al.

ENGINEERING PHYSICS

- 32 Why do automotive springs fracture? Stress induced splitting in automotive coil springs, T. Gnaupel-Herold, et al.

GEOLOGY

- 34 Solvent-pore interactions in Eagle Ford shale by ultra and small-angle neutron scattering, J. McFarlane, et al. (CHNRNS)

INSTRUMENTATION

- 36 The very Small Angle Neutron Scattering (vSANS) Instrument, J. G. Barker, et al. (CHNRNS)

SOFT MATTER

- 38 Structure-property-processing relationships of soft viscoelastic materials, J. C.-W. Lee, et al. (CHNRNS)
- 40 Segmental diffusion in attractive polymer nanocomposites: A quasi-elastic neutron scattering study, E. J. Bailey, et al. (CHNRNS)
- 42 Electrolyte concentration dependence on electrode SEI formation revealed by operando SANS, C. J. Jafta, et al. (CHNRNS)
- 44 Towards architecturally designed all-polymer based nanocomposites, E. Senses, et al. (CHNRNS)
- 46 Investigating the structures of polygalactomannans in water, M. Chawathe, et al. (nSoft)

ADVANCES IN MEASUREMENT

- 48 Probing fluid nanostructure under complex flow histories using SANS in a fluidic four-roll mill (FFORM), P. T. Corona, et al. (nSoft)
- 49 In-situ sample orientation at cryogenic temperatures, S. Gladchenko. (CHNRNS)
- 50 Optimization of biological reflectometry experiments using information theory, B.W. Treece, et al.
- 51 In-situ NAA: Measurement of delayed gamma rays from short lived nuclei using a linear neutron beam chopper with arbitrary duty cycles, H. H. Chen-Mayer, et al.
- 52 Fabrication and treatment of perfect crystals for neutron interferometry, M. Arif, et al.
- 53 *Reductus*: a web-based data reduction service for reflectometry, B. B. Maranville, et al.

54 NEUTRON SOURCE OPERATIONS

56 FACILITY DEVELOPMENTS 2019

59 SERVING THE SCIENCE AND TECHNOLOGY COMMUNITY

62 THE CENTER FOR HIGH RESOLUTION NEUTRON SCATTERING (CHNRNS)

67 2019 AWARDS

70 PUBLICATIONS: AUGUST 1, 2018 TO JULY 31, 2019

90 INSTRUMENTS AND CONTACTS

92 NIST CENTER FOR NEUTRON RESEARCH CONTACTS

Foreword

I am delighted to present to you this year's Accomplishments and Opportunities for the NIST Center for Neutron Research. 2019 was marked by numerous noteworthy accomplishments despite the government furlough spanning December 22, 2018 – January 25, 2019. The reactor operated for 212 days, fewer operating days than expected due to the government furlough, but operational reliability exceeded 98%, not counting the loss of the operational days.

There were numerous facility developments completed in 2019 that support NIST's commitment to provide world-class neutron measurement capabilities to the scientific community. Several key instrument development milestones were achieved. The new white beam reflectometer, CANDOR, had its beam shutter opened for the first time for an initial radiation survey on February 28th, detected first neutrons on June 28th, and it is currently in the commissioning phase. There were several additional, late-breaking projects that will not appear in this year's annual report. First, we began a major cryogenic helium mitigation project to reduce helium consumption with new dry cryo-magnets and a helium recovery system. Second, the Neutron Spin Echo spectrometer will have a substantial performance upgrade thanks to a University of Delaware-led initiative funded by the National Science Foundation. Third, we received funding from NIST to begin the development of a neutron interferometric microscope prototype based on far field interferometry. In addition, the entire safety relay system for the reactor was replaced in a major evolution that was successfully completed in May. This is just one of many projects integral to the continued reliability and availability



of the NCNR far into the future. Many more developments contributing to the future of the NCNR are described in the pages of this report.

As always, the science enabled by the NCNR is the reason for our existence. The highlights in this report exemplify the scientific excellence of the user community in diverse domains of research and illustrate the many ways that the community uses these state-of-the-art research tools. I am proud of these accomplishments and I hope you enjoy reading this year's report.

A handwritten signature in black ink, reading "Paul D. Smith".

The NIST Center for Neutron Research

Neutrons provide a uniquely effective probe of the structure and dynamics of materials ranging from water moving near the surface of proteins to magnetic domains in memory storage materials. The properties of neutrons (outlined below) can be exploited using a variety of measurement techniques to provide information not otherwise available. The positions of atomic nuclei in crystals, especially of those of light atoms, can be determined precisely. Atomic motion can be directly measured and monitored as a function of temperature or pressure. Neutrons are especially sensitive to hydrogen, so that hydrogen motion can be followed in H-storage materials and water flow in fuel cells can be imaged. Residual stresses such as those deep within oil pipelines or in highway trusses can be mapped. Neutron-based measurements contribute to a broad spectrum of activities including engineering, materials development, polymer dynamics, chemical technology, medicine, and physics.

The NCNR's neutron source provides the intense, conditioned beams of neutrons required for these types of measurements. In addition to the thermal neutron beams from the heavy water moderator, the NCNR has two liquid hydrogen moderators, or cold sources which supply neutrons to three-fourths of the instruments. One is a large area moderator and the other is smaller, but with high brightness. These moderators provide long wavelength guided neutron beams for industrial, government, and academic researchers.

There are currently 30 experiment stations: 12 are used for neutron physics, analytical chemistry, or imaging, and 18 are beam facilities for neutron scattering research. The subsequent pages provide a schematic description of our instruments. More complete descriptions can be found at the [neutron instruments webpage](#). The newest instrument, a quasi-white beam neutron reflectometer (CANDOR) is currently in the commissioning stage.

The Center supports important NIST measurement needs but is also operated as a major national user facility with merit-based access made available to the entire U.S. technological community. Each year, about 2000 research participants from government, industry, and academia from all areas of the country are served by the facility (see pp. 59). Beam time for research to be published in the open literature is without cost to the user, but full operating costs are recovered for proprietary research. Access is gained mainly through a web-based, peer-reviewed proposal system with user time allotted by a beamtime allocation committee twice a year. For details see the [Obtaining Instrument Time webpage](#). The National Science Foundation and NIST co-fund the Center for High Resolution Neutron Scattering (CHRNS) that currently operates five of the world's most advanced instruments (see pp. 62). Time on CHRNS instruments is made available through the proposal system. Some access to beam time for collaborative measurements with the NIST science staff can also be arranged on other instruments.

Why Neutrons?

Neutrons reveal properties not readily probed by photons or electrons. They are electrically neutral and therefore easily penetrate ordinary matter. They behave like microscopic magnets, propagate as waves, can set particles into motion, losing or gaining energy and momentum in the process, and they can be absorbed with subsequent emission of radiation to uniquely fingerprint chemical elements.

WAVELENGTHS – in practice range from ≈ 0.01 nm (thermal) to ≈ 1.5 nm (cold) ($1 \text{ nm} = 10 \text{ \AA}$), allowing the formation of observable interference patterns when scattered from structures as small as atoms to as large as biological cells.

ENERGIES – of millielectronvolts, the same magnitude as atomic motions. Exchanges of energy as small as nanoelectronvolts and as large as tenths of electronvolts can be detected between samples and neutrons, allowing motions in folding proteins, melting glasses and diffusing hydrogen to be measured.

SELECTIVITY – in scattering power varies from nucleus to nucleus somewhat randomly. Specific isotopes can stand out from other isotopes of the same kind of atom. Specific light atoms, difficult to observe with x-rays, are revealed by neutrons. Hydrogen, especially, can be distinguished from chemically equivalent deuterium, allowing a variety of powerful contrast techniques.

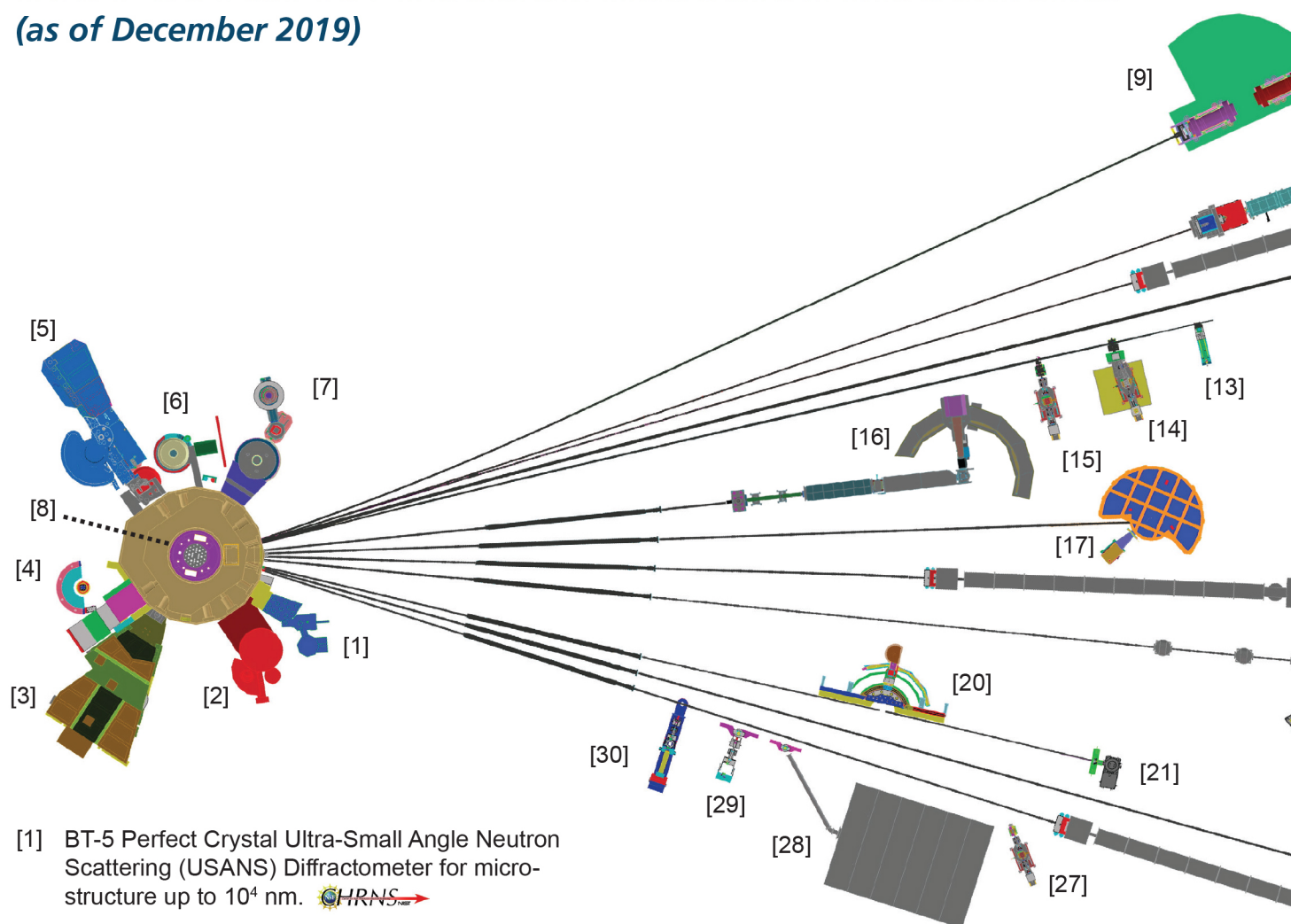
MAGNETISM – makes the neutron sensitive to the magnetic moments of both nuclei and electrons, allowing the structure and behavior of ordinary and exotic magnetic materials to be detailed precisely.


NEUTRALITY – of the uncharged neutrons allows them to penetrate deeply without destroying samples, passing through walls that condition a sample's environment, permitting measurements under extreme conditions of temperature and pressure.

CAPTURE – characteristic radiation emanating from specific nuclei capturing incident neutrons can be used to identify and quantify minute amounts of elements in samples as diverse as ancient pottery shards and lake water pollutants.

NIST Center for Neutron Research Instruments

(as of December 2019)

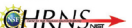


[1] BT-5 Perfect Crystal Ultra-Small Angle Neutron Scattering (USANS) Diffractometer for micro-structure up to 10^4 nm. 

[2] BT-4 Filter Analyzer Neutron Spectrometer with cooled Be/Graphite filter analyzer for chemical spectroscopy and thermal triple axis spectrometer.

[3] BT-2 Neutron Imaging Facility for imaging hydrogenous matter in large components such as water in fuel cells and lubricants in engines, in partnership with General Motors and DOE.


[4] BT-1 Powder Diffractometer with 32 detectors; incident wavelengths of 0.208 nm, 0.154 nm, and 0.120 nm, with resolution up to $\Delta d/d \approx 8 \times 10^{-4}$.


[5] BT-9 Multi Axis Crystal Spectrometer (MACS II), a cold neutron spectrometer for ultra high sensitivity access to dynamic correlations in condensed matter on length scales from 0.1 nm to 50 nm and energy scales from 2.2 meV to 20 meV. 

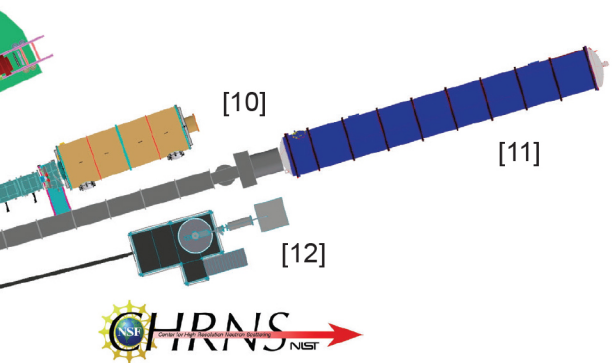
[6] BT-8 Residual Stress Diffractometer optimized for depth profiling of residual stresses in large components.

[7] BT-7 Thermal Triple Axis Spectrometer with large double focusing monochromator and interchangeable analyzer/detectors systems.

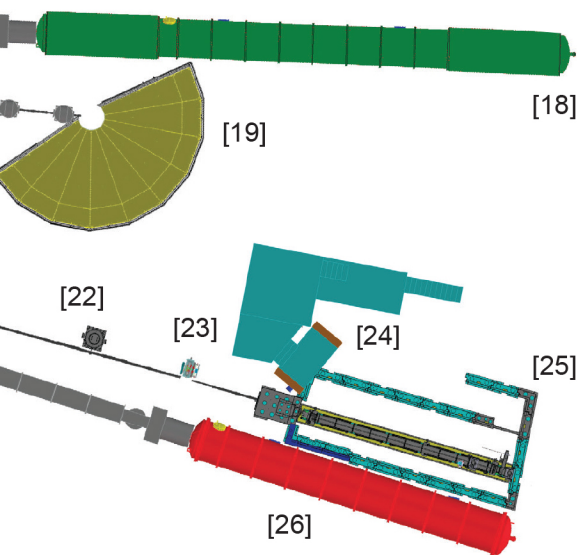
[8] VT-5 Thermal Neutron Capture Prompt Gamma-ray Activation Analysis Instrument used for quantitative elemental analysis of bulk materials including highly hydrogenous materials ($\approx 1\%$ H) such as foods, oils, and biological materials.

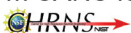
[9] NG-A Neutron Spin-Echo Spectrometer (NSE) for measuring dynamics from 5 ps to 100 ns. 



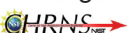
[10] NG-B 10 m SANS for macromolecular structure measurements. 



The Center for High Resolution Neutron Scattering (HRNS) is a partnership between NIST and the National Science Foundation that develops and operates neutron scattering instrumentation for use by the scientific community. The following instruments are part of the Center: 1 (USANS), 5 (MACS II), 9 (NSE), 11 (NG-B 30m SANS), 16 (CANDOR), 17 (HFBS), and 18 (vSANS).



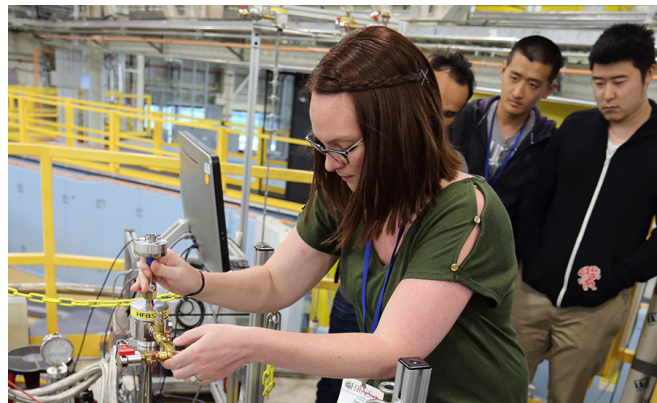
- [11] NG-B 30 m SANS for microstructure measurements. 
- [12] NG-C Neutron lifetime experiment.
- [13] NG-D Cold neutron capture Prompt Gamma Activation Analysis, for quantitative elemental analysis of bulk materials
- [14] NG-D MAGIK off-specular reflectometer for studies of thin-film samples with in-plane structure.
- [15] NG-D Polarized Beam Reflectometer (PBR) for measuring reflectivities as low as 10^{-8} to determine subsurface structure.

- [16] NG-1 CANDOR Chromatic Analysis Diffractometer or Reflectometer, capable of high throughput measurements (commissioning). 
- [17] NG-2 Backscattering Spectrometer (HFBS), high intensity inelastic scattering instrument with energy resolution $< 1 \mu\text{eV}$ for studies of motion in molecular and biological systems. 
- [18] NG-3 VSANS for single measurement investigation of lengths from 1 nm to 2 micron. 
- [19] NG-4 Disk Chopper Time-of-Flight Spectrometer for diffusive motions and low energy dynamics. Wavelengths from $\approx 0.18 \text{ nm}$ to 2.0 nm and energy resolutions from $\approx 2 \text{ meV}$ to $< 10 \mu\text{eV}$.
- [20] NG-5 Spin-Polarized Triple Axis Spectrometer (SPINS) using cold neutrons with position sensitive detector capability for high-resolution studies.
- [21] NG-5 Cold Neutron Depth Profiling for profiling of subsurface elemental composition.
- [22] NG-6 Precision measurement of the magnetic dipole moment of the neutron.
- [23] NG-6 Precision measurement of neutron flux.
- [24] NG-6 LAND detector development, neutron source calibration, and neutron cross section measurement
- [25] NG-6 Cold Neutron Imaging Facility for imaging hydrogenous matter in large components such as water in fuel cells and lubricants in engines.
- [26] NG-7 30 m SANS for microstructure measurements, in partnership with ExxonMobil and University of Minnesota's IPrime.
- [27] NG-7 PHADES Cold neutron test station.
- [28] NG-7 Neutron Interferometry and Optics Station with perfect crystal silicon interferometer. A vibration isolation system provides exceptional phase stability and fringe visibility.
- [29] NG-7 Neutron Physics Interferometry Test Bed for quantum information science.
- [30] NG-7 Horizontal Sample Reflectometer allows reflectivity measurements of free surfaces, liquid/vapor interfaces, as well as polymer coatings.

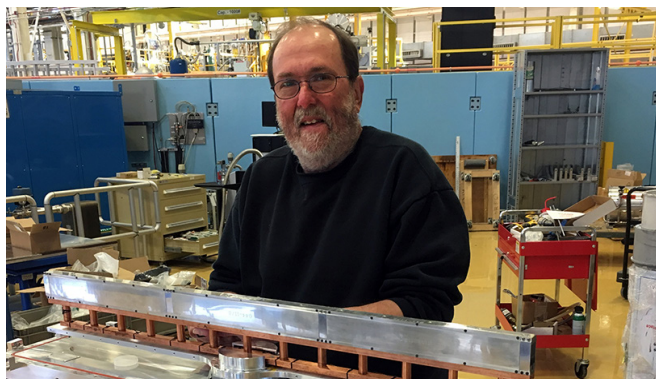
NCNR Images 2019



Crystal growth is the lesson of the day for teachers at the 2019 NIST Summer Institute for Middle School Science Teachers at NCNR. Tanya Dax of the NCNR (far right) leads the discussion.



Summer school students are learning hands-on how to perform an experiment at DCS.



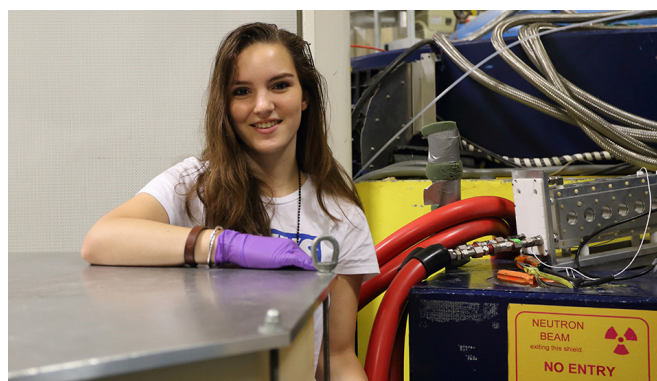
Scott Slifer of the NCNR assembling CANDOR hardware for installation.



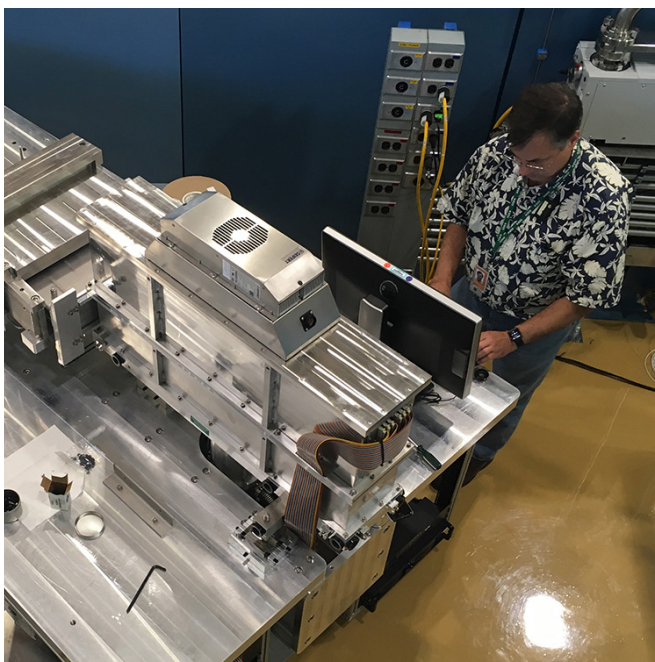
IEEE Magnetic Society Summer School students from Virginia Commonwealth University are given a tour of the NCNR, guided by Brian Kirby.



Ruidan Zhong (Princeton University) aligning samples at the X-ray Laue machine.



Melissa Henderson (University of Waterloo, Canada) at USANS measuring skyrmions in a transverse magnetic field.



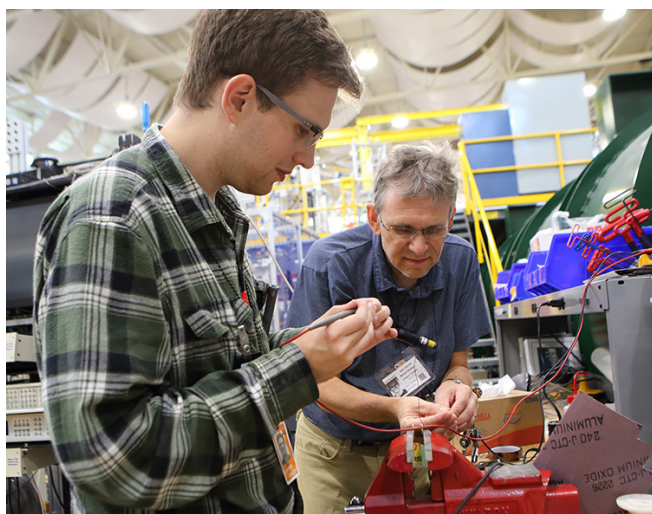
On Hawaiian shirt day, the NCNR's Nick Maliszewskyj is setting up the detector system on CANDOR, an instrument that saw its first neutrons in 2019.



A portion of the Design and Engineering of Neutron Instruments Meeting (DENIM) was a design challenge to keep the engineers thinking creatively.



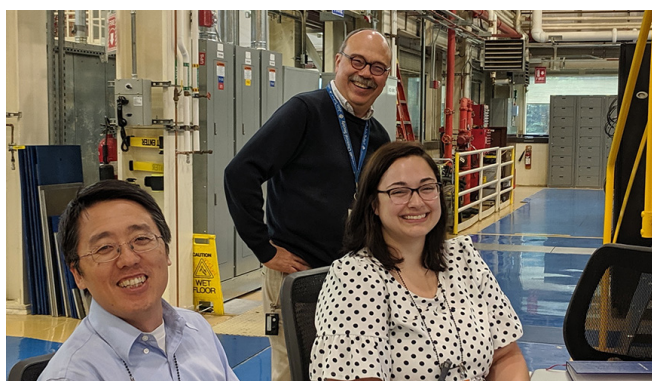
Wes Fuhrman (University of Maryland) preparing a sensitive sample for an experiment at NCNR.



Allan Leishman and Morten Eskildsen (University of Notre Dame) prepare a sample for a vortex lattice measurement at NG7 SANS.



Priyanka Ketkar and Melody Morris (University of Delaware) at MAGIK studying lithium-ion battery block copolymer electrolytes with the help of Joe Dura (NCNR).



Yun Liu, Dan Neumann (NCNR), and Caitlyn Wolf (University of Washington) are all smiles as they measure conjugated polymers at VSANS.

Methanol accelerates DMPC flip-flop and transfer: A SANS study on lipid dynamics

M. H. L. Nguyen,¹ M. DiPasquale,¹ B. W. Rieckard,¹ C. B. Stanley,² E. G. Kelley,³ and D. Marquardt¹

Lipid bilayers form the structural backbone of cellular membranes and possess marked lateral and transversal organization of lipids. This strict lipid organization has implications in vital cellular processes, including protein function and localization, vesicle fusion and budding, and apoptosis. Lipids undergo diffusive motions that can disrupt their carefully assembled organization. This study focused on lipid exchange (between bilayers) and transverse diffusion (lipid flip-flop) as the former pertains to how lipids arrive, remain, and leave cellular membranes, whereas the latter disrupts the maintained membrane asymmetry (i.e., the compositional difference between leaflets) found in cells. In essence, both dynamical actions are intrinsically linked to bilayers and their compositional stability. Here, we examined how the common organic solvent methanol impact these dynamics.

In this work, we applied very small angle neutron scattering (VSANS) to monitor lipid mixing of two distinct 1,2-dimyristoyl-sn-glycero-3-phosphocholine (DMPC) populations, one chain perdeuterated DMPC (d-DMPC) and the other fully protiated DMPC (h-DMPC), in the presence of an increasing deuterated methanol concentration. The measurements were achieved by setting the ratio of H₂O and D₂O (here 45 % D₂O) such that the water solvent neutron scattering length density was matched to uniformly mixed d-DMPC/h-DMPC vesicles. Unmixed vesicles will thus display contrast versus the water solvent, resulting in heightened scattering intensity, whereas fully mixed samples will display scattering intensities akin to the solvent background (i.e., a flat and featureless curve). Thus, as h-DMPC and d-DMPC large unilamellar vesicles begin to mix via lipid monomers transferring within and between bilayers, the measured intensity will decay and eventually reach an intensity baseline, corresponding to a single population of completely mixed vesicles (shown in Fig. 2a). Fig 1 illustrates such a strategy [1]. Further, a normalized intensity decay was calculated from the collective scattering curves of each sample and analyzed with a model for exchange/flip-flop (Fig. 2b). With this experimental setup, we quantified both DMPC flip-flop (k_f) and exchange (k_e) rates under the influence of methanol.

Increasing methanol concentrations had a profound effect on the kinetics of DMPC monomers in free-floating vesicles. Despite differences in vesicle size and investigative techniques,

our unperturbed DMPC flip-flop and transfer rates agree and contrast previous findings. For example, Gerelli *et al.* used neutron reflectometry to measure DMPC flip-flop and exchange between vesicle dispersions and adsorbed planar bilayers [2]. Their exchange half-times for fluid-phase DMPC coincide with values found here (timescale of hours), whereas flip-flop was magnitudes faster (≤ 2.5 min). As recently shown however, the incomplete surface coverage of planar bilayers results in microscopic defects, which can facilitate lipid flip-flop and thus result in flip-flop rates on the order of seconds to minutes [3]. This study, with fully sealed vesicles, bypasses such issues.

More significantly, our results reveal that methanol accelerates both fluid-phase DMPC flip-flop and transfer rates. The flip-flop rate increases exponentially, whereas the exchange rate increases linearly under the studied concentrations (Fig. 2c). Methanol has by far the weakest hydrophobic character in the short-chain alcohol group yet seems to perturb the membrane through a similar fashion as longer chained alcohols and alkyl diols. Although it has been shown that other short-chain alcohols affect inward flipping rates, to our knowledge, we provide new insights with regards to both flip-flop and transfer rates in the presence of methanol. In general, at low methanol levels, DMPC undergoes slower flip-flop than transfer, but at methanol volume fractions greater than 2 %, the situation is reversed. Interestingly, these observations suggest that methanol affects the two dynamical processes in distinct ways.

Dynamic light scattering (DLS) measurements of size and polydispersity were taken before and after incubation at multiple methanol concentrations, neither of which revealed significant changes, maintaining a vesicle diameter of 140 nm and a polydispersity index of 0.15 ± 0.02 . Significantly, these results suggest fusion events did not occur as an increase in mean particle size and a polydispersity index would have been observed. Furthermore, SANS and small angle x-ray scattering (SAXS), were applied. SANS and SAXS are complementary techniques used to probe sample structure and are known to be extremely sensitive to membrane lamellarity and lipid bilayer structure. Both SANS and SAXS yielded curves that displayed diffuse scattering (i.e., no detectable sharp Bragg peak) demonstrating that multilamellar bilayers did not evolve under the presence of d-methanol. Collectively, DLS, SAXS and SANS indicate that methanol did not

¹ University of Windsor, Windsor, Ontario ON N9B 3P4, Canada

² Oak Ridge National Laboratory, Oak Ridge, TN 37831

³ NIST Center for Neutron Research, National Institute of Standards and Technology, Gaithersburg, MD 20899

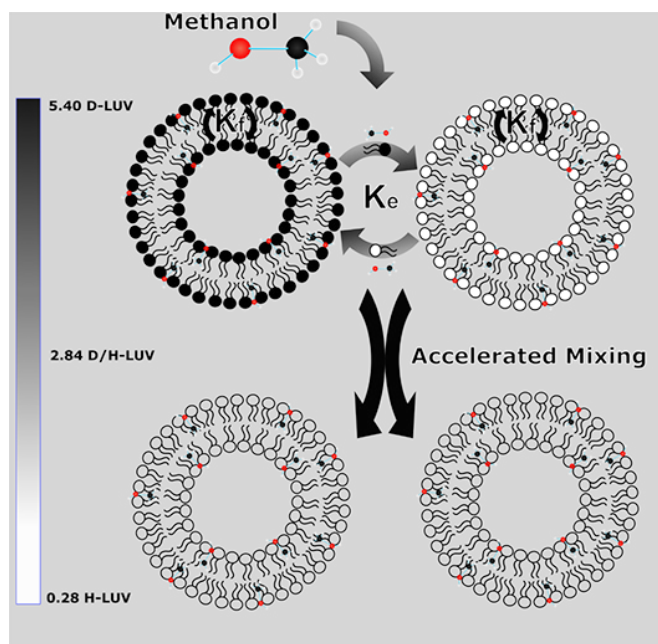


FIGURE 1: Contrast matching strategy employed. Vesicles composed solely of d-DMPC d_{54} -DMPC and h-DMPC are placed together in a H_2O/D_2O (55/45) mixture with varying amounts of methanol, contrast matched to fully mixed vesicles of d-DMPC and h-DMPC. Over time, intensity loss can be monitored as vesicles mix (via exchange and flip-flop) and near the contrast match point.

alter the vesicles' morphological structure at these concentrations. To determine if a defect-mediated mechanism is responsible, we examined pertinent bilayer properties. Previous *in silico* studies revealed that area per lipid (A_L) generally increases with increasing alcohol concentrations and this led to greater occurrences of bilayer defects [4]. Such defects can permit lipid headgroups to traverse the bilayer core and flip-flop. A joint refinement of SANS and SAXS data revealed that this was not the case; the scattering profiles of pure lipid and methanol-treated samples are near indiscernible. In terms of relevant bilayer structural parameters, the A_L and bilayer thickness were essentially unchanged. Thus, the most likely explanation must involve methanol inducing short-range and perhaps short-lived defects, which are thus difficult to discern via methods (as those used here) that measure an ensemble structural average.

Time-resolved SANS in combination with structural SANS, SAXS, and DLS measured the dynamical and structural effects of methanol on DMPC liposomes. Though structural deviations were not detected in the concentration regime studied, DMPC flip-flop and exchange were markedly enhanced. Our findings highlight an additional complication when externally adding biomolecules, whether it be protein, peptides or drugs. For example, in antimicrobial peptide (AMP) studies, though AMP attack is better simulated by external addition, these studies have the potential to incorrectly assign the cause of the enhanced lipid kinetics to the AMP. Ultimately, this work highlights the importance of understanding the interplay between the system of interest and the carrier solvent on lipid mobility whether it be model lipid systems or *in vitro* screening in cell biology.

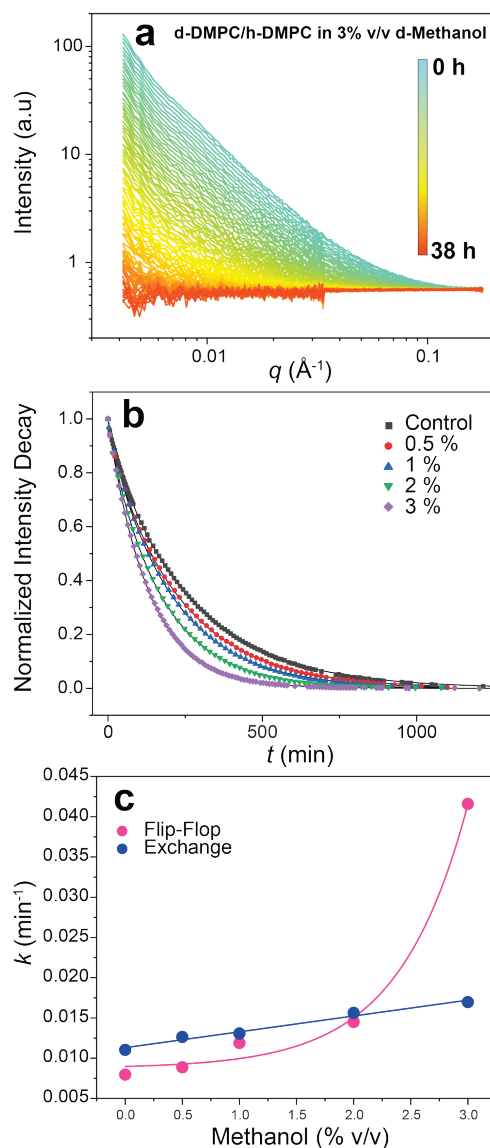


FIGURE 2: (a) SANS curves of d-DMPC and h-DMPC vesicles with 3% (v/v) d-methanol solvent. Periodic measurements were conducted at 37 °C over 38 h. (b) Normalized contrast decay curves of increasing d-methanol presence; continuous lines indicate fitted curves used to derive flip-flop and lipid exchange rate constants. Each data point represents the normalized integrated intensity of a single SANS curve like those found in (a). (c) Plot of measured flip-flop and lipid exchange rate constants as a function of d-methanol volume percent. Solid lines represent curves of best fit.

References

- [1] M. Nguyen, M. DiPasquale, B. Rikeard, C. Stanley, E. Kelley, D. Marquardt, *Biophysical Journal*, **116**(5), 755 (2019).
- [2] Y. Gerelli, L. Porcar, L. Lombardi, G. Fragneto, *Langmuir*, **29**(41), 12762 (2013).
- [3] D. Marquardt, F. A. Heberle, T. Miti, B. Eicher, E. London, J. Katsaras, G. Pabst, *Langmuir*, **33**(15), 3731 (2017).
- [4] H. V. Ly, M. L. Longo, *Biophysical Journal*, **87**(2), 1013 (2004).

Conductivity and dynamics of biomimetic synthetic polypeptides

A. Pena-Francesch,¹ H. Jung,¹ M. Tyagi,^{2,3} and M. C. Demirel¹

Squid-inspired synthetic proteins self-assemble into a hydrogen-bonding physically crosslinked network that gives rise to remarkable thermal and protonic conductivity. Understanding the chain dynamics of biomimetic structural proteins and their role in heat and proton transport will help design novel biodegradable protein-based materials with programmable properties for bioelectronics and thermal switching devices.

Proteins are heteropolymers that provide a variety of building blocks for designing novel biological materials. Proteins are diverse but often display substantial similarity in sequence and three-dimensional structure. A new family of repetitive structural proteins with remarkable properties was recently identified in the tentacles of several squid species. Using the tools of molecular biology and proteomics, we demonstrated that these squid ring teeth (SRT) proteins have segmented semi-crystalline morphology with repetitive amorphous and crystalline domains. However, a clear relationship between the protein architecture (repetition and length of crystalline/amorphous domains), the self-assembled nanostructure, and conducting properties remains elusive due to complexity of native amino acid sequences.

To investigate the genetic basis of material properties in natural and artificial SRT sequences, we have developed a new approach for the design and production of structural proteins. These synthetic proteins have identical sequences but increasing repeat unit number n ($n = 4, 7, 11$ and 25) and molecular weights (15, 25, 42 and 86) kDa. Synthetic SRT proteins have remarkable protonic conductivity in the range of (1 to 5) mS/cm, which is the highest reported to date for protein-based materials as measured by Electrochemical Impedance Spectroscopy. In addition, synthetic SRT proteins exhibit a programmable thermal conductivity from 0.3 W/mK to 1.4 W/mK.

To investigate these vibrational dynamics, we turned to elastic and quasi-elastic neutron scattering (QENS) using the High-Flux Backscattering Spectrometer (HFBS) and Disk-chopper time-of-flight spectrometer (DCS) at the NIST Center for Neutron Research. QENS can measure molecular dynamic processes such as rotations, relaxations and diffusive motions with 1 Å to 30 Å and pico- to nanosecond resolution by directly probing

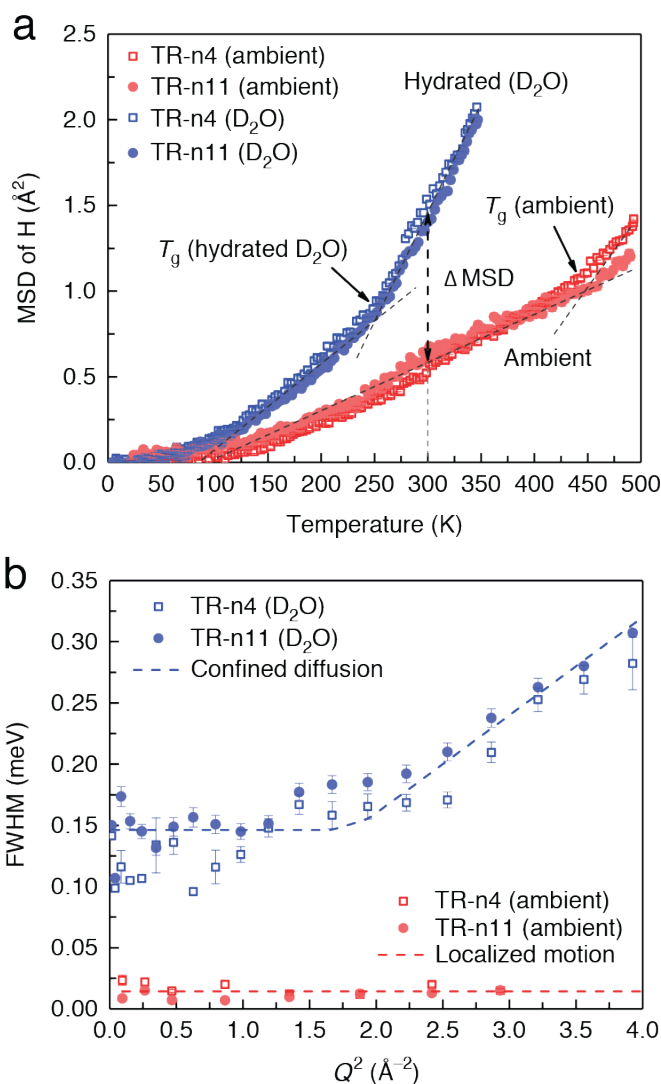


FIGURE 1: a) Measured mean square displacement, or vibrational amplitude, of hydrogen atoms in the TR films as a function of sample temperature. As seen, the dense, hydrogen-bonded network opens up and allows for increased movement following hydration. b) Full-width at half-maximum of the quasi-elastic peaks of the ambient and hydrated proteins as a function of the square of the scattering wavevector, Q^2 . Error bars represent one standard deviation.

¹ Pennsylvania State University, University Park, PA 16801

² NIST Center for Neutron Research, National Institute of Standards and Technology, Gaithersburg, MD 20899

³ University of Maryland, College Park, MD 20742

the self-diffusion of hydrogen atoms. The hydrated chain dynamics were measured using deuterated water (D_2O), as deuterium has a negligible neutron scattering cross-section and therefore it does not contribute to the signal. The mean square displacement (MSD) of hydrogen atoms in the protein (shown in Fig. 1a) was calculated from the scattering intensity in fixed window elastic scans, as a function of temperature, using the Debye–Waller factor (which is a standard Gaussian approximation method). Tandem Repeat (TR) polypeptides under ambient conditions show very localized motions at $T > 70$ K, which is common for proteins and typically originates from methyl group rotations, and exhibit a glass transition around 450 K. Therefore, neutron spectroscopy does not show significant segmental or backbone motion at room temperature (300 K). Thus, the disordered chains are constrained in a dense hydrogen-bonding network with minimal vibrational freedom. Conversely, in the hydrated state, the MSD of the hydrogen atoms increases and we observe much larger vibrational amplitudes, as well as a decrease in the glass transition temperature (250 K). In this case, the water molecules break the hydrogen bonding between the disordered chains, allowing for more delocalization of the hydrogen motion. Protein chain dynamics were further investigated by quasi-elastic measurements. Figure 1 shows the full-width at half-maximum, $\Gamma(Q)$, of the quasi-elastic peaks of ambient and D_2O -hydrated TR-n4 and TR-n11 proteins, plotted as function of Q^2 . Under ambient conditions (<1 % relative humidity during our

QENS measurements), TR proteins show a Q -independent behavior (15 μ eV) characteristic of localized motions (that is, methyl group rotations). On the other hand, D_2O -hydrated TR proteins show a Q -independent plateau at low Q values (0.15 meV), while a linear scaling with Q^2 is observed at higher Q . This two-regime Q dependence is characteristic of diffusion in a confined space and can be described by the Volino and Dianoux (VD) model for bounded diffusion in a potential of spherical symmetry, which corresponds to confined diffusive motions of the amorphous segments within the β -sheet nanocrystals.

In order to understand the transport processes at the molecular level, we have designed variants of squid-inspired proteins with variable repeat unit number (n). Our results of elastic fixed window scan data collected at HFBS shows the hydration dynamics of two variants of biomimetic SRT proteins changes upon hydration for both polypeptides. QENS analysis at HFBS and DCS are necessary to understand the protein chain dynamics. Based on these results, we concluded that the hydration plays a key role in localized motions, and faster self-diffusion of amorphous chains in SRT polypeptides, which enhances the thermal conductivity. The thermal conductivity values scales with increasing repeat unit number n (enabling precise control of the physical properties by sequence design), and are highly dependent on protein hydration (enabling fast reversible switching of thermal conductivity), with a switch ratio of 4.5 at room temperature, which is among the highest reported to date.

Characterization of porous alucone membranes used for single-molecule DNA sequencing

V. Jadhav,¹ D. P. Hoogerheide,² and M. Wanunu¹

In recent years, personalized genomics have begun to revolutionize the way we think about patient care and disease prevention. Humans are nearly identical in their DNA makeup, but genetic and epigenetic differences make all the difference in how we look, what we are sensitive to, and what diseases we are susceptible to. One person may respond well to a certain cancer-fighting drug, while another person may be allergic to that drug, or may not respond well at all to it. How do we know which drug to administer to whom in these circumstances? We don't, because we still lack a better way to assess the genetic makeup of each individual, collect enough data from many individuals with similar genotypes, and then conclude which therapy is most effective. This requires large-scale genome readout from a large population, a task that is currently prohibitively costly. Furthermore, our genomes are long (≈ 6 billion nucleotides arranged in 2 sets of 23 chromosomes) and the organization and repetitiveness of various regions is significant on the phenotypes of individuals. Therefore, it is important to read out the genome in a way that preserves the long-range order. While current sequencing technologies do well in terms of throughput and cost ($\approx \$2,000$ per genome, ≈ 1 week turnaround time), these read short fragments that lead to ambiguity in the assembly of a full genome and areas of low certainty (so-called "genome gaps," or the "dark matter of the genome"). Furthermore, existing technology cannot detect chemical changes to our DNA backbones ("epigenetic modifications"), which are critical elements for diagnosis and treatment of disease.

To address these standing challenges, single-molecule DNA sequencing has been in development for over 15 years. Pacific Biosciences was among the first batch of companies to sequence single DNA molecules by monitoring DNA replication in real-time using fluorescence. The underlying technology, known as single molecule, real-time (SMRT) sequencing, involves a ≈ 100 nm wide metallic nanowell called a zero-mode waveguide (ZMW), in which light is localized at the nanoscale to enable single-molecule sensitivity (Figure 1A). In order to perform sequencing of any DNA sample, a library of DNA molecules first needs to be prepared. Usually, the DNA sample (e.g., from saliva, blood) is amplified using an enzymatic method to produce many copies of the genome that consist of short and long fragments of identical sequence to the original, and these DNA fragments of various lengths are then wrapped at the tails by a molecule that enables

binding of the DNA replication molecule (a DNA polymerase). The issue with this library preparation method is that short molecules prefer to enter the 100 nm ZMWs over longer ones, and therefore, there is a length bias (i.e., longer molecules are not represented equally). Further, typical input requirements of DNA are in the ≈ 100 ng to 1 μ g range, which is a lot of DNA (one cell contains ≈ 100 times less DNA).

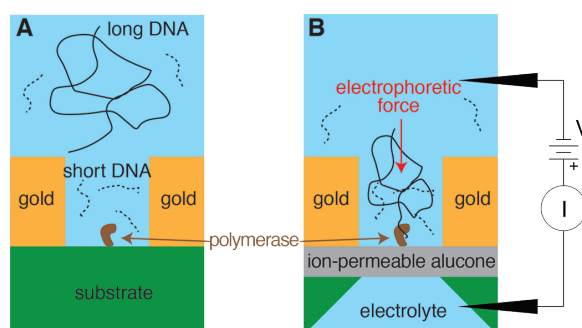


FIGURE 1: Schematic of SMRT sequencing with optical amplification using ZMWs. (A) In conventional SMRT sequencing using ZMWs, the accessibility of long DNA to polymerases is reduced by entropic exclusion from the gold ZMW nanowells. (B) In the porous ZMW design, an ion-permeable, DNA-impermeable, free-standing, porous alucone membrane is introduced at the base of ZMW. Application of an external potential across the membrane creates an electrophoretic force that drives long DNA into the ZMW and into proximity to the sequencing polymerase.

To address the length bias and input requirement issues, we have developed a platform in which the ZMWs contain a porous membrane underneath them, which allows molecules to be electrophoretically drawn into the waveguides (Figure 1B), reducing the length bias and the required concentration of DNA. We deposit a nanoporous alucone [1] membrane through molecular layer deposition (MLD). MLD is a recently developed technique which can be utilized for many of the same applications as atomic layer deposition (ALD), including functionalization of nanoparticles, porous membranes, and customization of surfaces [1]. MLD, through the sequential deposition of a metal alkyl and diol, results in a hybrid organic-inorganic film of varying thickness dependent upon deposition temperature and the number of cycles. Alucone is produced by MLD using trimethylaluminum and ethylene glycol, creating a meshwork of poly(aluminum ethylene glycol)[2] that, after

¹ Northeastern University, Boston, MA 02115

² NIST Center for Neutron Research, National Institute of Standards and Technology, Gaithersburg, MD 20899

exposure to air or water, dehydrates to produce a complicated porous network through the entirety of the deposited layers.

The substrate is then locally etched away, exposing both sides of the porous layer to an electrolyte solution required to apply the electrophoretic force (Figure 1B). Notably, the MLD layer is also optically transparent, making it more suitable for optical measurements of the ZMWs that are fabricated on top of the porous layer.

While the stepwise fabrication process of this alucone polymer is well understood and well-studied, the intentional degradation of the organic component of the membrane to produce a porous membrane network is challenging to characterize. Specifically, atomic-level understanding of membrane composition and geometry of the substrate, along with the method of small molecule attachment to the modified surface, are sought out.

The reflectivity of a thin film to cold neutrons reports on the depth profile of a thin film's scattering length density (SLD), a combination of the elemental composition and atomic density. An alucone thin film was prepared for neutron reflectivity (NR) measurements by depositing 200 Å alucone by MLD, followed by 20 Å SiO₂ deposited by ALD. The film was hydrated through immersion in an aqueous reservoir and the *in situ* reflectivity to 5 Å neutrons was measured at the NIST Center for Neutron Research's MAGIK reflectometer [3].

To characterize the scattering length density and porosity of the film, the deuteration level, or "contrast" of the water in the liquid reservoir was varied. Three contrast conditions were employed: D₂O, 2:1 D₂O:H₂O, and H₂O. The reflectivity at each condition is shown in Figure 2A. The high amplitude oscillations in the reflectivity when the alucone film is in contact with D₂O and H₂O reflect the thickness of the alucone film and the SLD difference between the immersion solvent and the alucone film. The suppression of these oscillations in the 2:1 D₂O:H₂O reflectivity suggests that the alucone SLD is nearly equal to that of 2:1 D₂O:H₂O.

Quantitative results for the alucone film properties are obtained by constructing a physically relevant model of the alucone SLD and optimizing parameters of this model to the experimental data. The model construction is done by filling space with various fixed components as a function of depth, such as the substrate, the alucone film, and the capping layer of SiO₂. Any space that remains unfilled is assumed filled with water; if a significant amount of water is present at any depth, the SLD profile at that depth will change when the contrast is varied. The results of this so-called "composition space modeling" for alucone are shown in Figure 2b (SLD profiles) and Figure 2c (model components). The alucone film is found to be 205 Å ± 4 Å thick with a porosity of 28 % ± 1 %. The size of the alucone pores is not immediately apparent but must be less than the penetration of the SiO₂ capping layer into the film, which is 24 Å ± 4 Å. The narrow pores create a strong confinement entropy that prevent even flexible single-stranded DNA molecules from penetrating alucone films used in sequencing devices.

In conclusion, neutron reflectometry has proven useful for characterizing the porosity, thickness, and composition of MLD-based porous membranes. Optimizing the porosity, stability, and uniformity of the films, as well as their chemical properties, may result in suitable films for single-molecule SMRT-sequencing technologies.

References

- [1] D. Miller, R. Foster, S. Jen, J. Bertrand, D. Seghete, Y. Byunghoon, Y. Lee, S. George, M. Dunn, *Journal of Acta Materialia*, **57**, 5083 (2009).
- [2] A. Dameron, D. Seghete, B. Burton, S. Davidson, A. Cavanagh, J. Bertrand, S. M. George, *Journal of Chemical Materials* **20**, 3315 (2007).
- [3] V. Jadhav, D. P. Hoogerheide, J. Korlach, M. Wanunu, *Nano Lett.*, **19**, 921 (2019).

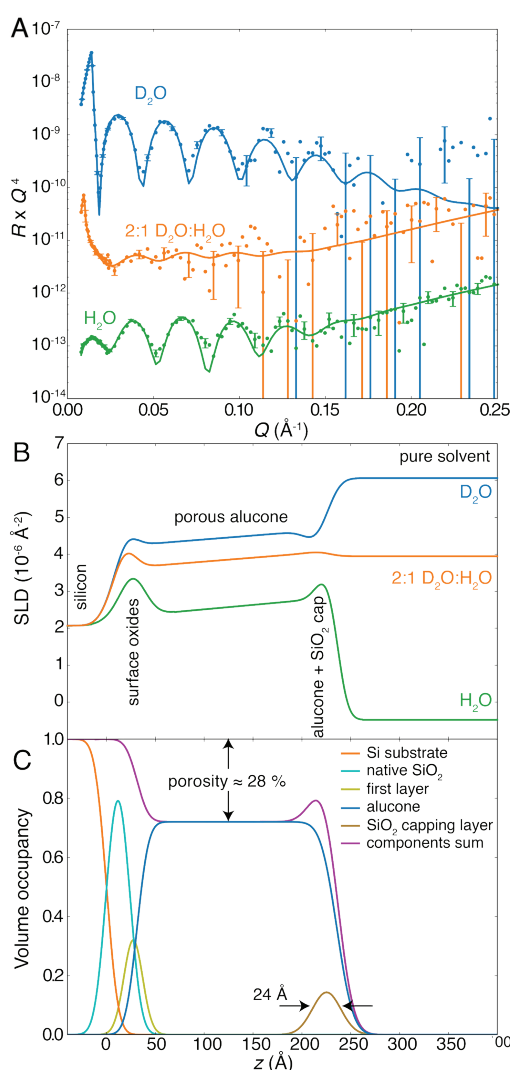


FIGURE 2: Neutron reflectivity of MLD alucone. (A) Reflectivity of an MLD alucone film at various contrasts with the solvent, achieved by immersion in water with varying levels of deuteration. (B) Scattering length density profiles of the alucone film at each contrast condition. Separation of the profiles in the alucone film region confirms penetration of water into the film. (C) Quantitation of the alucone film dimensions and porosity using a composition space model. The unfilled space in the film is assumed filled by solvent and is the porosity of the film.

Record high hydrogen storage capacity in the metal–organic framework $\text{Ni}_2(m\text{-dobdc})$ at near-ambient temperatures

M. T. Kapelewski,^{1,2} T. Runčevski,^{1,2} J. D. Tarver,^{3,4} H. Z. H. Jiang,^{1,2} K. E. Hurst,⁴ P. A. Parilla,⁵ A. Ayala,^{3,6} T. Gennett,^{4,7} S. A. FitzGerald,⁸ C. M. Brown,^{3,9} and J. R. Long^{1,2,10}

Molecular hydrogen is a commercial transportation fuel currently employed in several niche markets, and its widespread adoption is essential for a zero-emission Hydrogen Economy. While hydrogen has many attractive qualities as an energy carrier, such as high gravimetric energy density, fast refueling characteristics, and the potential for carbon-free production, a key challenge lies in its low volumetric energy density and the subsequent difficulty for on-board storage. Current systems in light-duty passenger vehicles store H_2 in pressurized carbon fiber cylinders at 700 bar in order to achieve an operating range of 300 miles, however reducing this pressure while maintaining the same capacity would allow the use of conformal fuel tanks on board and vastly simplify the pre-cooling and compression apparatus required at refueling stations. Adsorbent-based solutions have been proposed, however H_2 binding to most adsorbents is still too weak for operation at ambient temperatures, thus measurements have typically been undertaken at 77 K in order to demonstrate any significant uptake [1].

Metal–organic frameworks are a class of materials with great potential for hydrogen storage, as their tunability and crystalline structure allows for a high density of strong H_2 binding sites to be engineered into the structure. These sites are typically coordinatively-unsaturated metal sites, where a metal ion lacking a full coordination shell is embedded in the structure of the framework and is able to polarize H_2 strongly through its empty coordination site. The most promising metal–organic framework identified to date for H_2 storage is $\text{Ni}_2(m\text{-dobdc})$ ($m\text{-dobdc}^{4-} = 4,6\text{-dioxido-1,3-benzenedicarboxylate}$) because of its large H_2 binding enthalpy of -13.7 kJ/mol at numerous five-coordinate, highly charge-dense Ni^{2+} sites [2]. In order to evaluate the performance of promising hydrogen-storage materials near operating conditions, we have characterized the hydrogen storage behavior of $\text{Ni}_2(m\text{-dobdc})$, $\text{Co}_2(m\text{-dobdc})$, $\text{Ni}_2(\text{dobdc})$, $\text{Co}_2(\text{dobdc})$ and MOF-5, a benchmark hydrogen storage material, at near ambient temperatures and pressures up to 100 bar [3].

While these frameworks have primarily been examined under low pressures of H_2 at 77 K, measurements under conditions relevant to on-board storage will provide vital insight into the nature of H_2 packing under practical conditions.

The parameters of our study were informed by the DOE 2020 guidelines for on-board, light-duty vehicle storage [4]. We chose an adsorption pressure of 100 bar as a compromise between storage capacity and the need to alleviate the problems associated with high-pressure storage, while a desorption pressure of 5 bar was chosen as a standard input pressure for a fuel cell injector. High-pressure H_2 adsorption isotherms of these materials were measured between 0 bar and 100 bar at temperatures of -75 °C to 100 °C. Gratifyingly, $\text{Ni}_2(m\text{-dobdc})$ exhibits the highest adsorption capacities at all temperatures and pressures, and all isotherms in this material at 75 °C and below exhibit a H_2 capacity higher than that of pure compressed H_2 at 25 °C. Furthermore, the usable capacity of $\text{Ni}_2(m\text{-dobdc})$ is 11.0 g/L, once again outperforming other materials from this study as well as compressed H_2 gas. While these results surpass other frameworks, $\text{Ni}_2(m\text{-dobdc})$ still falls short of the DOE targets.

In order to approach the storage capacity goals set out by the DOE, however, adsorption and desorption conditions can be carefully selected to maximize the usable capacity of the material. First, cooling the system will lead to better performance of the adsorbent. Due to the high binding enthalpy of $\text{Ni}_2(m\text{-dobdc})$, significant improvements may be achieved without the need to cool to 77 K, the standard for most adsorbent materials. Under 100 bar of hydrogen, at -75 °C the usable capacity increases to 19.0 g/L, around 66% of the current DOE target, while at -173 °C the capacity of the material fulfils the current DOE target. Yet another strategy uses temperature swing desorption, a process where active cooling is used to achieve high filling levels while higher temperatures are employed during utilization for desorption. A theoretical

¹ Department of Chemistry, University of California, Berkeley, Berkeley, CA 94720

² Lawrence Berkeley National Laboratory, Berkeley, CA 94720

³ NIST Center for Neutron Research, National Institute of Standards and Technology, Gaithersburg, MD 20899

⁴ Chemistry & Nanoscience Center, National Renewable Energy Laboratory, Golden, CO 80401

⁵ Materials Science Center, National Renewable Energy Laboratory, Golden, CO 80401

⁶ University of Maryland, College Park, MD 20742

⁷ Colorado School of Mines, Golden, CO 80401

⁸ Oberlin College, Oberlin, OH 44074

⁹ University of Delaware, Newark, DE 19716

¹⁰ Department of Chemical and Biomolecular Engineering, University of California, Berkeley, Berkeley, CA 94720

swing from adsorption at $-75\text{ }^{\circ}\text{C}$ to desorption at $25\text{ }^{\circ}\text{C}$ gives a usable capacity of 23.0 g/L . This enhanced usable capacity represents 77% of the DOE system target of 30 g/L , which is the highest H_2 volumetric usable capacity achieved to date for an adsorbent operating in this temperature range. It should be emphasized that the DOE goals are system targets, and as such these numbers represent upper bounds. In order to achieve the DOE goals, it is likely that trade-offs between adsorbent performance and the additional space and weight taken up by the support systems must be optimized.

Powder neutron diffraction provides a unique ability to locate adsorbed hydrogen in the $\text{M}_2(m\text{-dobdc})$ frameworks, thereby offering insight into the binding behavior in these materials. As the $\text{Ni}_2(m\text{-dobdc})$ sample was not crystalline enough for satisfactory structure solution, measurements were performed on the isostructural $\text{Co}_2(m\text{-dobdc})$. While these do not provide a direct measure of the performance of $\text{Ni}_2(m\text{-dobdc})$, the structural characterization of $\text{Co}_2(m\text{-dobdc})$ will yield information about the nature of H_2 packing crucial in designing high-performing storage materials. Astoundingly, we were able to resolve 7 distinct adsorption sites within the sample of $\text{Co}_2(m\text{-dobdc})$ loaded with D_2 at 78 bar and 77 K (Figure 1). At the strongest adsorption site, D_2 is bound to the open Co^{2+} coordination site with a $\text{Co}\cdots\text{D}_2$ (centroid) separation of $2.25(7)\text{ \AA}$. Three other sites lie near the pore walls of the framework, and in addition to the metal-bound D_2 , have previously been observed in $\text{Co}_2(m\text{-dobdc})$ at 4 K and pressures below 1 bar [2]. Sites 5 and 6 lie at the center of the hexagonal channels of the framework, while site 7 resides $3.10(3)\text{ \AA}$ from the D_2 located at site 5 and primarily relies on $\text{D}_2\cdots\text{D}_2$ interactions for stabilization. At 77 K and 78 bar, sites 1–6 show full occupancy of D_2 , and site 7 shows approximately half occupancy. Importantly, a comparison of the adsorption isotherm data collected at 198 K and the D_2 loadings observed by powder neutron diffraction at the same temperature reveal a quantitative agreement between the two methods for measuring storage capacity, suggesting the results of *in situ* neutron diffraction experiments accurately reflect the material *in operando*.

Such detailed structural characterizations of H_2 -loaded frameworks reveal key features resulting in high H_2 capacities. First, the $\text{D}_2\cdots\text{D}_2$ distances measured for certain sites within the pores of $\text{Co}_2(m\text{-dobdc})$ are very short. For example, the distance between the D_2 molecules at sites 1 and 2 is only $2.86(3)\text{ \AA}$. This is significantly shorter than the $\text{H}_2\cdots\text{H}_2$ separation of 3.21 \AA in solid hydrogen and approaches the $\text{H}_2\cdots\text{H}_2$ distance of 2.656 \AA in solid H_2 pressurized to 54 kbar at 300 K. These comparisons to solid hydrogen powerfully illustrate the ability of materials in the $\text{M}_2(m\text{-dobdc})$ series to densify hydrogen within their pores. Significantly, the high charge density on the metals not only strongly polarizes D_2 bound at the coordinatively unsaturated Co^{2+} center, but it additionally affects D_2 bound in more weakly physisorbing secondary sites, leading to a high hydrogen packing density within the adsorbent. It is likely that $\text{Ni}_2(m\text{-dobdc})$ benefits from similar effects and packing configurations, albeit to a greater degree, leading to record-high H_2 usable capacities.

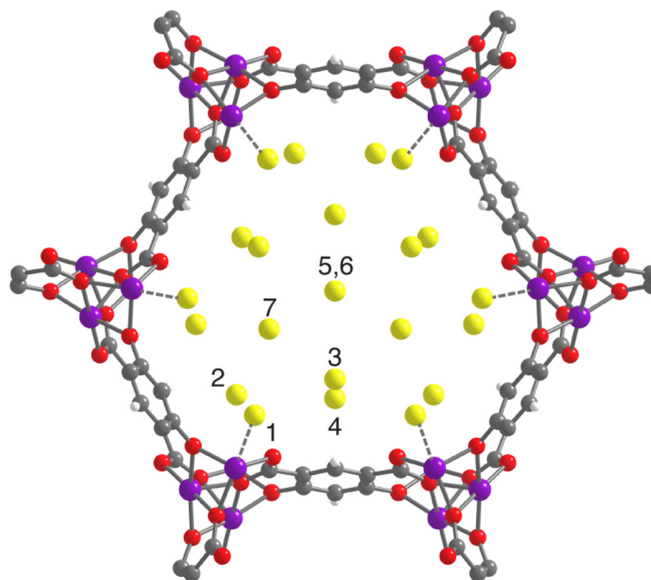


FIGURE 1: A single pore of $\text{Co}_2(m\text{-dobdc})$ showing the seven distinct D_2 binding sites as determined from neutron diffraction data. Purple, red, grey, white, and yellow spheres represent Co, O, C, H atoms and D_2 molecules, respectively.

In conclusion, we have demonstrated the ability of several promising H_2 adsorbents to achieve significant usable capacities under conditions relevant to on-board vehicle storage. The outstanding performance of $\text{Ni}_2(m\text{-dobdc})$ was shown to be extended from low temperature, low pressure conditions to high temperature, high pressure conditions more relevant to applicable systems. Neutron powder diffraction was able to determine a number of binding sites in the material that corresponded quantitatively with isotherm measurements. Furthermore, examination of the structure solution revealed closely packed D_2 comparable to intermolecular distances within solid hydrogen. This close packing suggests that the influence of the strongly polarizing primary binding sites extends through $\text{H}_2\cdots\text{H}_2$ interactions to sites further from the pore surface, resulting in record H_2 capacities.

References

- [1] L. J. Murray, M. Dincă, J. R. Long, *Chem. Soc. Rev.* **38** (5), 1294 (2009).
- [2] M. T. Kapelewski, S. J. Geier, M. R. Hudson, D. Stück, J. A. Mason, J. N. Nelson, D. J. Xiao, Z. Hulvey, E. Gilmour, S. A. FitzGerald, et al., *J. Am. Chem. Soc.* **136** (34), 12119 (2014).
- [3] M. T. Kapelewski, T. Runčevski, J. D. Tarver, H. Z. H. Jiang, K. E. Hurst, P. A. Parilla, A. Ayala, T. Gennett, S. A. FitzGerald, C. M. Brown, et al., *Chem. Mater.* **30** (22), 8179 (2018).
- [4] [DOE Technical Targets for Onboard Hydrogen Storage for Light-Duty Vehicles](#) (accessed Sep 29, 2019).

Short acoustic phonon lifetimes limit thermal transport in photovoltaic methylammonium lead iodide

A. Gold-Parker,^{1,2} P. M. Gehring,³ J. M. Skelton,⁴ I. C. Smith,¹ D. Parshall,³ J. M. Frost,⁵ H. I. Karunadasa,¹ A. Walsh,^{6,7} and M. F. Toney²

Hybrid organic–inorganic perovskites (HOIPs) are a class of materials showing remarkable photovoltaic properties that hold enormous promise for the next-generation of efficient and low-cost solar cells. Methylammonium lead iodide ($\text{CH}_3\text{NH}_3\text{PbI}_3$ or MAPi) displays the highest photovoltaic power conversion efficiency (PCE) of all the HOIPs (over 21% to date). It is composed of organic methylammonium cations confined to the interstitial spaces of an inorganic framework of corner-sharing PbI_6 octahedra. Unlike conventional inorganic semiconductors such as silicon and gallium arsenide, HOIPs exhibit significant dynamic disorder, which can be broadly classified into lattice vibrations (phonons), rotations of the organic molecule, and internal molecular vibrations. In solar cells, electrons are excited from the valence band to the conduction band by photons having energies equal to or exceeding the band gap. These photo-excited charge carriers interact with and lose energy to the lattice vibrations through electron–phonon coupling, which is one of the most important factors governing solar cell performance. Our study shows that the acoustic phonons in MAPi, the type responsible for transmitting heat in conventional semiconductors, have anomalously short lifetimes that result in an extremely low thermal conductivity [1]. This finding has direct implications on the cooling and transport of photo-excited electrons and represents a fundamental difference between HOIPs and conventional photovoltaic semiconductors.

We report a high-precision, wavevector-resolved study of the acoustic phonon lifetimes in MAPi using cold neutron inelastic spectroscopy to provide high-energy resolution and fully deuterated single crystals to reduce the incoherent scattering from hydrogen. Our measurements reveal anomalously short lifetimes on the order of picoseconds, 100 to 500 times shorter than those in GaAs or CdTe, that correspond to nanometer-sized mean free paths and thus demonstrate that acoustic phonons in MAPi are unable to dissipate heat efficiently. Lattice-dynamics calculations using *ab initio* third-order perturbation theory indicate that the short lifetimes arise from strong three-phonon interactions and a high density of low-energy

optical phonon modes related to the degrees of freedom of the organic methylammonium cation. Such short lifetimes strongly alter the electron–phonon coupling in MAPi and other HOIPs relative to that in conventional semiconductors, with direct effects on the cooling of photo-excited charge carriers and the transport and recombination of band-edge carriers. Our results on MAPi illustrate the importance of understanding the lattice dynamics of HOIPs to efforts to develop cheaper, more efficient optoelectronic devices based on these metal halide perovskites.

The data shown in Fig. 1, measured on the SPINS cold neutron triple-axis spectrometer at the NIST Center for Neutron Research, illustrate how transverse acoustic (TA) phonons in MAPi, propagating along one of the high-symmetry directions ($\Gamma \rightarrow X$) in the cubic phase, rapidly broaden in energy (indicating an increasingly shorter lifetime) as the phonon wavelength ($\lambda = 2\pi/k$) decreases. This broadening is observed along all high-symmetry directions and at all temperatures, although the degree of broadening lessens on cooling. In order to extract the phonon energies and linewidths (half-width at half-maximum or HWHM) as a function of the reduced wavevector k , all data were fit to the sum of a damped harmonic oscillator lineshape, corrected for the instrumental energy resolution; a Gaussian function centered at zero energy transfer ($E_T = 0$); and a flat background. The resulting dispersions for the TA

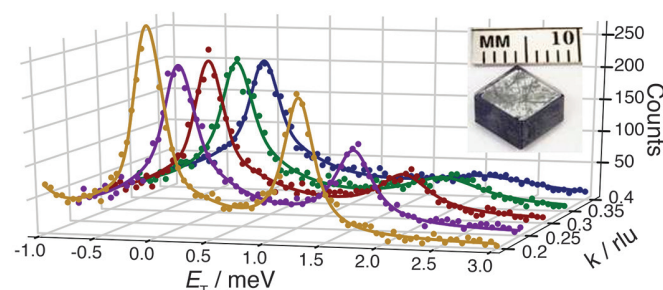


FIGURE 1: Neutron scattering measurements of TA phonons in MAPi propagating along [010] in the cubic phase at 350 K. As the reduced wave vector k increases, the TA phonon energy/wavelength increases/decreases, and the energy linewidth broadens.

¹ Stanford University, Stanford, CA 94305

² Stanford Synchrotron Radiation Lightsources, SLAC National Accelerator Laboratory, Menlo Park, CA 94025

³ NIST Center for Neutron Research, National Institute of Standards and Technology, Gaithersburg, MD 20899

⁴ University of Bath, Bath BA2 7AY, United Kingdom

⁵ King's College London, London WC2R 2LS, United Kingdom

⁶ Imperial College London, London SW7 2AZ, United Kingdom

⁷ Yonsei University, Seoul 03722, Korea

phonons propagating along $[110]$ ($\Gamma \rightarrow M$) and $[010]$ ($\Gamma \rightarrow X$) are shown in Fig. 2. *Ab initio* lattice-dynamical calculations of the phonon dispersions in the orthorhombic phase using third-order perturbation theory are given by the red dashed line and are in excellent agreement with the measurements. Data for longitudinal acoustic (LA) phonons propagating along $[100]$ were also measured in the cubic phase and show the same rapid broadening with decreasing wavelength.

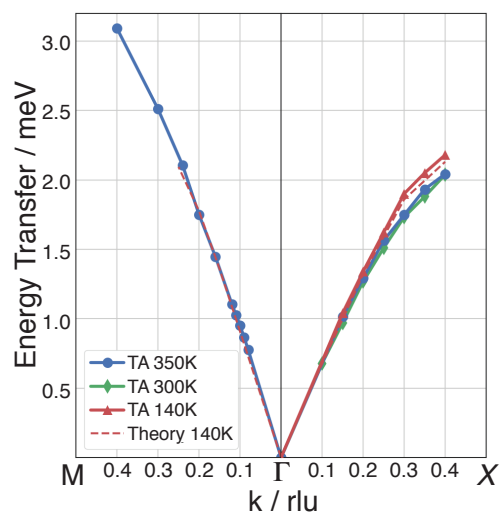


FIGURE 2: TA phonon dispersions along $M\text{-}\Gamma\text{-}X$ in the cubic (350 K), tetragonal (300 K), and orthorhombic (140 K) phases. The dashed lines show the dispersion simulated from *ab initio* lattice-dynamical calculations.

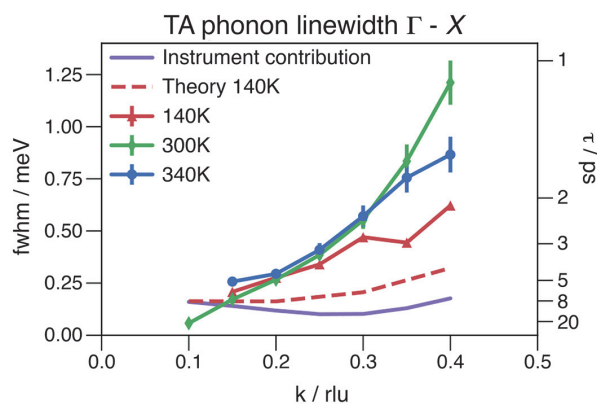


FIGURE 3: Intrinsic TA phonon linewidths along $\Gamma \rightarrow X$ in the orthorhombic (140 K), tetragonal (300 K), and cubic (350 K) phases. Error bars represent the standard error in the fitted values. Errors in the orthorhombic phase are likely larger due to complications from crystal twinning. Dashed lines show the calculated linewidths of the orthorhombic phase, while the purple lines show the instrumental contribution to the linewidths.

The phonon mean free path can be estimated as a function of wavevector by forming the product of the phonon lifetime (\hbar/HWHM) with the phonon group velocity $\partial E/\partial k$. The values so obtained are plotted in Fig. 3 for wave vectors along $[010]$ at 350 K, 300 K, and 140 K, which correspond to the cubic, tetragonal, and orthorhombic phases of MAPbI₃. *Ab initio* calculations of the phonon lifetime for the orthorhombic phase are depicted in Fig. 3 by the red dashed line. The experimental

and theoretical lifetimes exhibit the same trend with increasing wavevector k and are within a factor of two of one another. This agreement is quite good considering that the calculations assume only three-phonon interactions and do not include scattering from defects or electrons.

The lattice contribution to the total thermal conductivity, κ_{iso} , was calculated within the single-mode relaxation time approximation and is given by the product of the modal heat capacity, the phonon group velocity $\partial E/\partial k$, and the phonon mean free path, summed over all phonon branches and averaged over all wavevectors. These results, shown in Figure 4, demonstrate that the acoustic modes, which primarily lie below 3 meV, contribute little to the lattice thermal conductivity. Instead, most of the heat transport in MAPbI₃ is carried by the low-lying optical modes associated with the lead-halide framework.

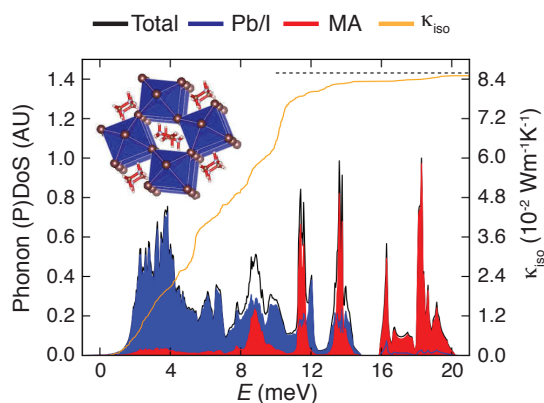


FIGURE 4: Phonon density of states from 0 meV to 20 meV (black) with projections onto the Pb-I framework (blue) and MA cation (red). The cumulative lattice thermal conductivity κ_{iso} at 300 K is overlaid in orange. The dashed line shows the total thermal conductivity summed over all modes, including the "pure" molecular modes at higher energies.

Our measurements show that the acoustic phonon lifetimes in the prototypical hybrid perovskite MAPbI₃ are 50 to 500 times shorter than those in conventional semiconductors. We have used high-energy resolution neutron scattering to measure the TA phonon dispersions as well as the critically important phonon lifetimes, which range from 1 ps to 20 ps throughout the Brillouin zone. Anharmonic lattice dynamics calculations reveal that the short lifetimes result from a high-density of low-energy optical modes, arising from the degrees of freedom of the organic cation, together with strong phonon-phonon interactions. Such short lifetimes likely affect hot carrier cooling and may also play a role in reducing the nonradiative recombination of band edge carriers.

Reference

- [1] A. Gold-Parker et al., Proc. Nat. Acad. Sci. **115** (47), 11905 (2018).

Metal–organic frameworks for highly effective ethane/ethylene separation

R.-B. Lin,¹ L. Li,^{1,2} R. Krishna,³ H. Li,^{1,4} S. Xiang,⁴ H. Wu,⁵ J. Li,² W. Zhou,⁵ and B. Chen¹

Ethylene (C_2H_4) is the largest feedstock in petrochemical industries, with a global production capacity of more than 170 million tons per year. It is usually produced by steam cracking or thermal decomposition of ethane (C_2H_6), in which a certain amount of C_2H_6 residue coexists in the product and needs to be removed to produce polymer-grade ($\geq 99.95\%$ pure) C_2H_4 as the starting chemical for many other products, particularly the widely utilized polyethylene. Owing to the very similar sizes and volatilities of ethylene and ethane, the purification of ethylene is currently accomplished by repeated distillation–compression cycling of the mixture at low temperature. This well-established separation technology is one of the most energy-intensive processes in the chemical industry. To replace the cryogenic distillation processes, exploration of new adsorptive separation technologies based on porous materials is strongly motivated by the tremendous energy savings. As customizable porous materials, metal–organic frameworks (MOFs) are highly versatile in pore engineering, affording precise tuning and functionalization of the pore structure, and thus have been intensively investigated as promising adsorbents for selective gas separation.

Most MOFs studied so far adsorb larger amounts of C_2H_4 than of C_2H_6 , mainly because of the stronger interactions of the pore surfaces with unsaturated C_2H_4 molecules. A few MOFs have demonstrated excellent C_2H_4/C_2H_6 separation performance, by selectively adsorbing ethylene [1]. However, production of polymer-grade C_2H_4 is still quite energy intensive, because C_2H_4 , as the preferentially adsorbed gas, needs to be further desorbed to get the C_2H_4 product. If instead, C_2H_6 is preferentially adsorbed, the desired C_2H_4 product can then be directly recovered, saving approximately 40% of energy. Unfortunately, very few MOFs were known to exhibit preferential binding toward C_2H_6 , and they suffer from low C_2H_6/C_2H_4 separation selectivity and productivity.

Recently, we developed two novel strategies in MOF systems for selective C_2H_6/C_2H_4 separation, and for the first time demonstrated that excellent separation selectivity and productivity can be achieved when C_2H_6 is preferentially

adsorbed. The first MOF is $[Fe_2(O_2)(dobdc)]$ (dobdc: 2,5-dioxido-1,4-benzenedicarboxylate), with iron–peroxo sites on the pore surface for the preferential binding of ethane over ethylene [2]. The second MOF is $[Cu(Qc)_2]$ (Qc = quinoline-5-carboxylate), whose pore surface mainly features aromatic rings of low polarity, enabling preferential binding of ethane over ethylene [3]. In both cases, neutron powder diffraction and theoretical calculations, performed at NCNR, played a critical role in understanding the ethane recognition mechanisms.

Our first strategy was inspired by natural metalloenzymes and synthetic compounds for alkane C–H activation in which M-peroxo, M-hydroperoxo, and M-oxo [M = Cu(II), Co(III), and Fe(III/IV)] are active catalytic intermediates. We hypothesized that similar functional sites within MOFs might have stronger binding with alkanes than alkenes and thus could be utilized for the selective separation of C_2H_6/C_2H_4 . In this regard, the MOF $Fe_2(O_2)(dobdc)$, containing iron(III)–peroxo sites on the pore surfaces [4], is of special interest. We thus investigated this MOF in great details. We found that $Fe_2(O_2)(dobdc)$ indeed exhibits preferential binding of C_2H_6 over C_2H_4 and displays the highest C_2H_6/C_2H_4 separation selectivities (≈ 4) among all examined porous materials.

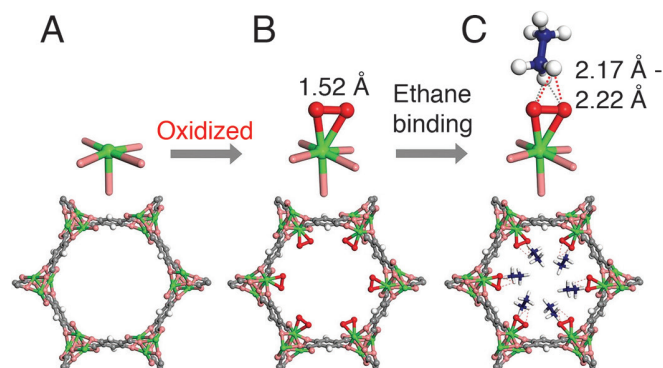


FIGURE 1: Structures of (A) $Fe_2(dobdc)$, (B) $Fe_2(O_2)(dobdc)$, and (C) $Fe_2(O_2)(dobdc)$ with adsorbed C_2D_6 , determined from neutron powder diffraction studies. Note the change from the open Fe(II) site to the Fe(III)–peroxo site for the preferential binding of ethane. Fe, green; C, dark gray; O, pink; O_2^{2-} , red; H or D, white; C in C_2D_6 , blue.

¹ University of Texas at San Antonio, One UTSA Circle, San Antonio, TX 78249

² College of Chemistry and Chemical Engineering, Taiyuan University of Technology, Taiyuan 030024, Shanxi, China

³ Van't Hoff Institute for Molecular Sciences, University of Amsterdam, Science Park 904, 1098 XH Amsterdam, Netherlands

⁴ Fujian Provincial Key Laboratory of Polymer Materials, College of Materials Science and Engineering, Fujian Normal University, Fuzhou 350007, Fujian, China

⁵ NIST Center for Neutron Research, National Institute of Standards and Technology, Gaithersburg, MD 20899

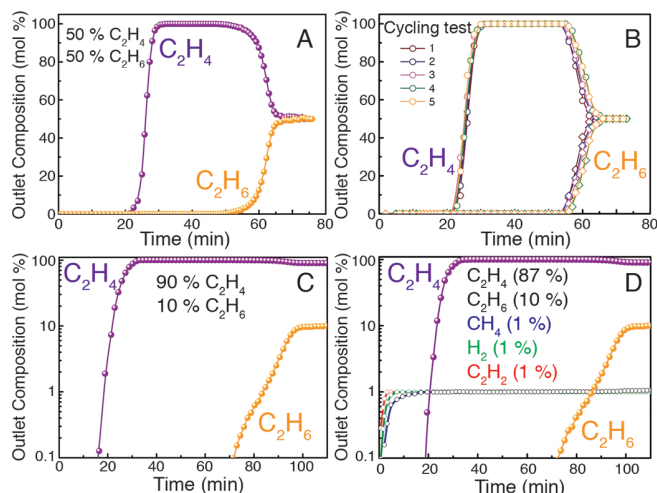


FIGURE 2: Experimental column breakthrough curves for (A) a C₂H₆/C₂H₄ (50/50) mixture, (B) a cycling test of C₂H₆/C₂H₄ (50/50) mixtures, (C) C₂H₆/C₂H₄ (10/90) mixtures, and (D) C₂H₆/C₂H₄/C₂H₂/CH₄/H₂ (10/87/1/1/1) mixtures in an absorber bed packed with Fe₂(O₂)(dobdc) at 298 K and 1.01 bar.

To structurally elucidate how C₂H₆ and C₂H₄ are adsorbed in this MOF, high-resolution neutron powder diffraction (NPD) measurements were carried out on C₂H₆-loaded and C₂H₄-loaded samples of Fe₂(O₂)(dobdc). As shown in Fig. 1, C₂D₆ molecules exhibit preferential binding with the peroxo sites through C–D···O hydrogen bonds. The D···O distance (≈ 2.17 Å to 2.22 Å) is much shorter than the sum of van der Waals radii of oxygen (1.52 Å) and hydrogen (1.20 Å) atoms, indicating a relatively strong interaction. In addition, sterically, the nonplanar C₂D₆ molecule happens to match better to the uneven pore surface in Fe₂(O₂)(dobdc) than the planar C₂D₄ molecule, resulting in stronger hydrogen bonds with the Fe-peroxo active site and stronger van der Waals interactions with the ligand surface. We further conducted first-principles calculations. The optimized C₂H₆ binding configuration on the Fe-peroxo site agrees reasonably well with the C₂D₆-loaded structure determined from the NPD data, confirming that the C₂H₆/C₂H₄ adsorption selectivity originates from the peroxo active sites in Fe₂(O₂)(dobdc).

To evaluate the separation performance of Fe₂(O₂)(dobdc) in the actual separation process, several breakthrough experiments for various mixtures were performed (see Figure 2). The results proved that Fe₂(O₂)(dobdc) can be used to purify C₂H₄ with low concentrations of C₂H₆ even in the presence of CH₄, H₂, and C₂H₂ impurities.

Our second strategy utilizes MOFs with inert pore surfaces (e.g., featuring aromatic or aliphatic moieties), where there are no specific gas adsorption sites. Here, the dispersion and induction interactions make major contributions, which are proportional to the polarizability of gas molecules. Since C₂H₆ has a slightly larger polarizability than C₂H₄, a feasible approach is to increase the efficient contact area or the quantity of interactions between C₂H₆ molecules and the host framework. Based on this idea, we identified a MOF, Cu(Qc)₂, as a promising candidate. The accessible pore surface of Cu(Qc)₂ mainly features aromatic rings of low polarity, enabling

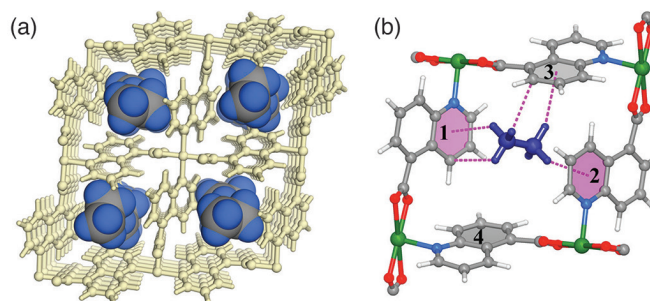


FIGURE 3: (a) Crystal structure of Cu(Qc)₂ with adsorbed C₂D₆, determined from neutron powder diffraction studies. (b) Preferential binding site for C₂D₆ molecule and the close vdW contacts within the rhombic cavity of aromatic rings (numbered as 1–4), with C–H···π interactions highlighted in pink dashed bonds. Cu, green; O, red; N, light blue; C, gray.

preferential binding of ethane over ethylene. In addition, Cu(Qc)₂ exhibits a small pore aperture size of ≈ 3.3 Å, facilitating possible multiple adsorbent–adsorbate interactions.

Our detailed experimental studies confirmed that Cu(Qc)₂ is indeed a ethane-selective adsorbent, with a very good C₂H₆/C₂H₄ selectivity (≈ 3.4). Again, NPD measurements were carried out to structurally understand the host–guest interactions. We found that C₂D₆ molecule locates in a rhombic cavity formed by aromatic rings of ligands (see Figure 3). As expected, multiple C–D···π interactions (D···π $2.34(3)$ – $3.34(3)$ Å, C–D···π $3.22(3)$ – $4.16(3)$ Å) were found between each C₂D₆ molecule and the aromatic rings within the rhombic cavity. The cavity of Cu(Qc)₂ fits well with the shape of C₂H₆ molecule, which enables the binding for C₂H₆ through multiple C–H···π interactions. To further evaluate the C₂H₆/C₂H₄ separation performance of Cu(Qc)₂ in practical adsorption process, experimental breakthrough studies were carried out and proved that high-purity C₂H₄ can be directly obtained in a single separating operation.

In summary, we have developed two novel strategies to realize preferred C₂H₆ adsorption in MOFs: 1) incorporating metal peroxo functional groups as strong C₂H₆ adsorption sites on the pore surface, and 2) coupling inert pore surface with narrow pore size to enhance the C₂H₆ binding through multiple interactions. The two MOFs, Fe₂(O₂)(dobdc) and Cu(Qc)₂, can both preferentially capture C₂H₆ from the C₂H₆/C₂H₄ mixture under ambient conditions with high separation selectivity and productivity. We are currently investigating more MOFs for this application, and fully believe that materials with even better performance will be discovered soon.

References

- [1] E. D. Bloch, W. L. Queen, R. Krishna, J. M. Zadrozny, C. M. Brown, J. R. Long, *Science* **335**, 1606 (2012).
- [2] L. Li, R.-B. Lin, R. Krishna, H. Li, S. Xiang, H. Wu, J. Li, W. Zhou, B. Chen, *Science* **362**, 443 (2018).
- [3] R.-B. Lin, H. Wu, L. Li, X.-L. Tang, Z. Li, J. Gao, H. Cui, W. Zhou, B. Chen, *J. Am. Chem. Soc.* **140**, 12940 (2018).

Probing structure-dependent reorientational behavior of SiH_3^- anions in alkali-metal silanides by quasielastic neutron scattering



M. Dimitrievska,^{1,2} J.-N. Chotard,³ R. Janot,³ A. Faraone,¹ W. S. Tang,^{1,4,5} A. V. Skripov,⁶ and T. J. Udovic¹

Alkali-metal silanides (MSiH_3 , $M = \text{K}, \text{Rb}, \text{and Cs}$) have recently gained attention as potential hydrogen-storage compounds due to their reversible dehydrogenation/ hydrogenation properties. Typically, a silanide \leftrightarrow silicide equilibrium (i.e., $\text{MSiH}_3 \leftrightarrow \text{MSi} + 1.5\text{H}_2$) exists, providing favorable hydrogen vapor pressures of 0.1 MPa near 410 K for all three alkali-metal compounds due to an enthalpy–entropy compensation effect, i.e., as the cation size increases, there are simultaneous linear increases in the enthalpy (more stable silanide) and entropy changes (more localized H atoms in the crystal structure). Hence, the dynamical nature of the H atoms in the various MSiH_3 compounds is of interest from an entropic viewpoint. All MSiH_3 compounds undergo hysteretic phase transitions upon heating and cooling between ordered monoclinic or orthorhombic β -phase structures to disordered face-centered-cubic α -phase structures (see Figure 1). In contrast to crystallographically ordered β -phase SiH_3^- anions, the α -phase anions exhibit three-dimensional orientational disorder. Previous quasielastic neutron scattering (QENS) results for all three α -phase compounds indicated decreasing SiH_3^- reorientational mobility (increasing order) with increasing cation size [1,2], which is qualitatively consistent with the observed compensation effect. Here, QENS measurements on the DCS, HFBS, and NSE spectrometers over a wide range of resolutions were used to fully characterize the alkali-metal-dependent anion reorientational dynamics in the ordered β - MSiH_3 compounds as well as the unusual nature of the rotator-phase transition between the β -phases and α -phases for CsSiH_3 [3].

The QENS data in Figure 2 show that the anion reorientational mobility in the β -phases trends dramatically higher with increasing cation size, which is opposite to what was observed in the α -phases, but makes sense from a purely steric perspective (i.e., lattice volume to accommodate the SiH_3^- anion increases with increasing cation size). Maximum jump frequencies of the β -phase anions near the β - α transitions range from around 10^9 s^{-1} for β - KSiH_3 to 10^{10} s^{-1} and higher for β - RbSiH_3 and β - CsSiH_3 . Due to the ordered nature of the β -phase lattice, the anions are effectively restricted to undergo

only uniaxial three-fold rotational jumps around the anion quasi- C_3 symmetry axis, which is consistent with the observed behaviors of the β -phase elastic incoherent structure factors (EISFs) in Figure 3.

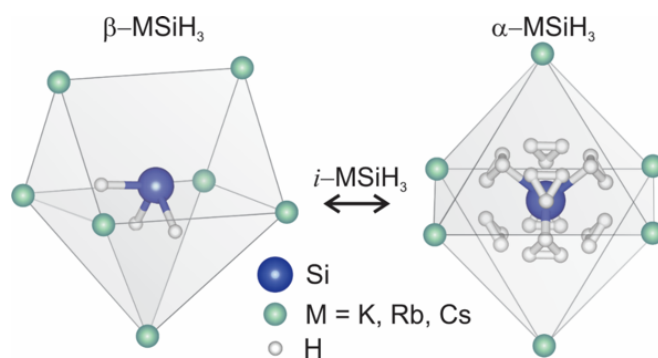


FIGURE 1: Structural differences between the ordered β - MSiH_3 and disordered α - MSiH_3 ($M = \text{K}, \text{Rb}, \text{Cs}$) phases showing the respective near-neighbor cation environments surrounding the pyramidal SiH_3^- anions. The multiple H atoms distributed radially around the Si atom represent all of the possible H positions associated with the orientationally disordered SiH_3^- anions in this structure. i - MSiH_3 denotes the possible formation of “intermediate” phases in the transition regions.

CsSiH_3 was the focus of further studies to map out the evolving anion dynamical behavior at temperatures above the β -phase region. As in α - KSiH_3 and α - RbSiH_3 , the highly mobile anions (with reorientational jump frequencies approaching and exceeding 10^{12} s^{-1} , see Figure 2) in the disordered α - CsSiH_3 are all adequately modeled by H jumps between 24 different locations distributed radially around the anion center of gravity (see Figure 3), although even higher anion reorientational disorder cannot be ruled out. QENS data for CsSiH_3 in the transition region between the α - and β -phases corroborated the appearance of dynamically distinct intermediate (i -) phases. The associated SiH_3^- anions possess orientational mobilities that are an order-of-magnitude lower than those for α -phase anions but also an

¹ NIST Center for Neutron Research, National Institute of Standards and Technology, Gaithersburg, MD 20899

² National Renewable Energy Laboratory, Golden, CO 80401

³ Laboratoire de Réactivité et Chimie des Solides, UMR 7314 CNRS, Université de Picardie Jules Verne, 80039 Amiens Cedex, France

⁴ Department of Materials Science and Engineering, University of Maryland, College Park, MD 20742

⁵ Geophysical Laboratory, Carnegie Institution of Washington, Washington, DC 20015

⁶ Institute of Metal Physics, Ural Branch of the Russian Academy of Sciences, Ekaterinburg, 620108, Russia

order-of-magnitude higher than those for β -phase anions (see Figure 2). These anions appear to undergo uniaxial small-angular-jump reorientations that are more akin to the lower-dimensional β -phase anion motions rather than to the multi-dimensional α -phase anion motions (see Figure 3). Combined QENS and neutron powder diffraction results strongly suggest that this i -phase is associated chiefly with the more short-range-ordered, nanocrystalline portions (invisible to diffraction) that appear to dominate the CsSiH_3 . Figure 2 depicts the hysteretic CsSiH_3 phase diagrams in heating and cooling regimens derived solely from the temperature-dependent QENS measurements for the various component phases.

These QENS results for CsSiH_3 bolster the previous observation for KSiH_3 and RbSiH_3 [4] that distinct nanosized intermediate phases exist and exhibit anion orientational mobilities intermediate between those for the α - and β -phases. Determining the exact structural nature of these i -phase nanodomains will require further investigation.

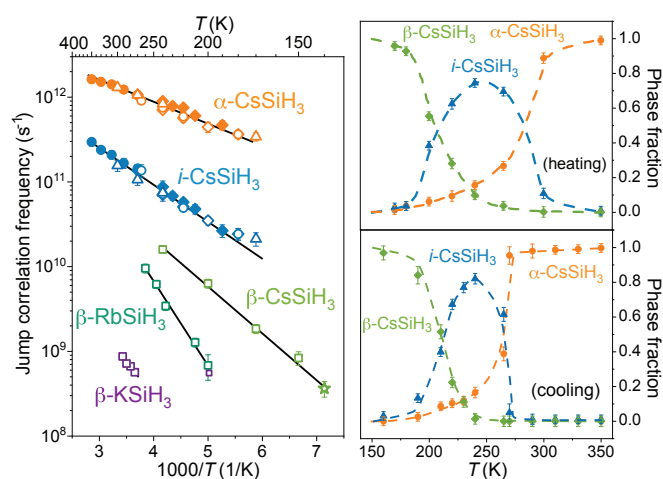


FIGURE 2: (left) Anion jump correlation frequencies τ_1^{-1} vs. $1/T$ for various MSiH_3 phases as determined from measurements on DCS (circles, diamonds, triangles, and pentagons), HFBS (squares), and NSE (stars) spectrometers. Filled and open symbols indicate measurements during cooling and heating regimens, respectively. (right) Phase diagrams for CsSiH_3 derived from anion dynamical behavior with temperature upon (a) cooling from 350 K and (b) heating from 25 K. The symbols present the calculation of the phase fractions obtained from QENS measurements.

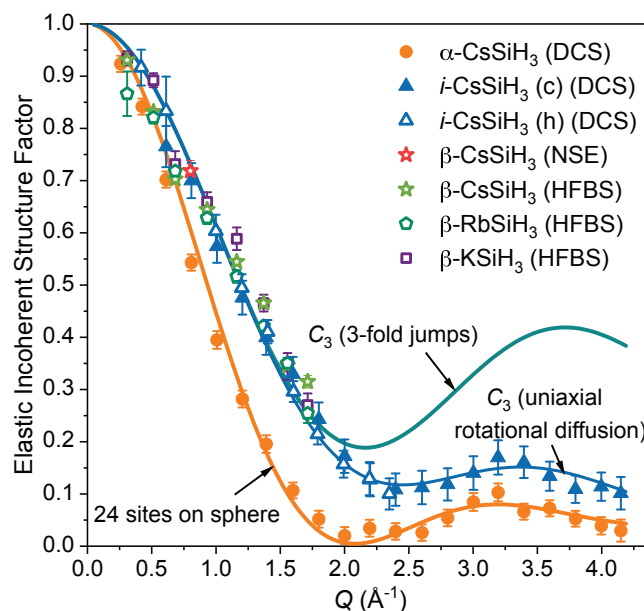


FIGURE 3: Elastic incoherent structure factor (EISF) data vs. Q (using various spectrometers) for α -CsSiH₃ (270 K), i -CsSiH₃ (cooling (c)/heating (h), 240 K), β -CsSiH₃ (green, 200 K; red, 140 K), β -RbSiH₃ (247 K), and β -KSiH₃ (292 K). EISF model curves for various reorientational mechanisms are shown for comparison.

References

- [1] C. Österberg, H. Fahlquist, U. Häussermann, C. M. Brown, T. J. Udovic, M. Karlsson, J. Phys. Chem. C **120**, 6369 (2016).
- [2] W. S. Tang, M. Dimitrievska, J.-N. Chotard, W. Zhou, R. Janot, A. V. Skripov, T. J. Udovic, J. Phys. Chem. C **120**, 21218 (2016).
- [3] M. Dimitrievska, J.-N. Chotard, R. Janot, A. Faraone, W. S. Tang, A. V. Skripov, T. J. Udovic, J. Phys. Chem. C **122**, 23985 (2018).
- [4] R. Nedumkandathil, A. Jaworski, A. Fischer, C. Österberg, Y.-C. Lin, M. Karlsson, J. Grins, A. J. Pell, M. Edén, U. Häussermann, J. Phys. Chem. C **121**, 5241 (2017).

Spin triplet superconductivity in UTe_2

S. Ran,^{1,2} C. Eckberg,² Q.-P. Ding,³ Y. Furukawa,³ T. Metz,² S. R. Saha,^{1,2} I.-L. Liu,^{1,2,4} M. Zic,² H. Kim,² J. Paglione,^{1,2} and N. P. Butch^{1,2}

Superconductivity is a form of quantum mechanical ordering in which conduction electrons in a metal, which otherwise act individually, instead pair up once cooled below a critical temperature. The pairs form a collective state having peculiar properties, such as dissipationless electrical conduction. Although superconductivity is sometimes presented as an esoteric curiosity, superconductors are a part of everyday life, most prevalently in the large magnets operating in the Magnetic Resonance Imaging (MRI) machines found in hospitals. One focus of superconductivity research today is fault-tolerant quantum computing [2].

Superconductors are often classified based on the relative orientation of the magnetic moments, or spins, of the paired electrons. The more common form of superconductivity is labeled spin singlet, in which case, the spins of the paired electrons can be thought of as pointing in opposite directions. If instead the electron spins of the pair are aligned, then the superconducting state is called spin triplet. Spin triplet superconductors are particularly enticing as a subset are topologically nontrivial, which in theory makes them suitable for development into fault-tolerant quantum computers. Unfortunately, in nature spin triplet superconductors are uncommon and require extensive testing to definitively identify, with few good candidate cases known to date.

Spin triplet superconductivity has been convincingly established in only a few materials, such as the ferromagnetic superconductors URhGe, UCoGe, and UGe₂ [1]. Adding to this short list, we recently discovered a unique new spin triplet superconductor, UTe_2 , which has the highest superconducting critical temperature, 1.6 K, as well as an anomalously large superconducting upper critical field, approximately 35 T. This very unusual superconducting state may in the future become a platform for encoding and processing quantum information using topological excitations.

This is one of the reasons that it is very exciting to identify spin triplet superconductivity in UTe_2 [3]. We synthesized single crystals of this material at the University of Maryland, College Park in the Center for Nanophysics and Advanced Materials. Because UTe_2 has been known for decades to be a relatively mundane paramagnet, the discovery of

a superconducting phase transition at 1.6 K was quite unexpected. Measurements of the specific heat (Fig. 1a) confirm that superconductivity occupies the entire volume of the sample and is not an impurity phase. Perplexingly, there is a very large residual heat capacity in the superconducting state, which is the first clue that something UTe_2 is quite unusual. Historically, the rare cases of similar specific heat signatures in other superconductors have been linked to poor sample quality. In the case of UTe_2 , we observe no variation in this residual specific heat, and its value has been reproduced by other researchers [4]. Our current understanding of this property is that roughly half of the electrons in UTe_2 do not participate in the superconducting pairing.

Low-temperature electrical resistivity measurements performed at the University of Maryland reveal the truly bizarre magnetic field dependence of superconductivity in UTe_2 . A fundamental property of all superconductors is instability in applied magnetic fields, eventually leading to the demise of the electron pairing interaction in sufficiently strong fields. The upper critical magnetic field that destroys superconductivity is material-dependent and reveals important information about the nature of the pairing interaction. A map of the superconducting upper critical field of UTe_2 (Fig. 1b) shows a strong direction-dependence, and very large values of the upper critical field, especially along the crystallographic b-axis. In fact, the upper critical field exceeds the highest magnetic field available at the University of Maryland, 20 T (Further measurements at the National High Magnetic Field Laboratory were necessary to establish a value of approximately 35 T and are the subject of a subsequent report [5]). This remarkably high upper critical field identifies UTe_2 as a spin triplet superconductor, because it far exceeds the much smaller magnetic fields required to suppress conventional spin singlet superconductivity.

Further proof of spin triplet pairing was found in Nuclear Magnetic Resonance (NMR) measurements performed at Ames Laboratory with Yuji Furukawa's group. Specifically, we identified a characteristic NMR signature of spin triplet pairing, no change in the Knight shift, in the superconducting state. Considered together, these rather bizarre physical properties point to a new and unusual flavor of superconductivity in UTe_2 .

¹ NIST Center for Neutron Research, National Institute of Standards and Technology, Gaithersburg, MD 20899

² Department of Physics, University of Maryland, College Park, MD 20742

³ Ames Laboratory, U.S. DOE and Department of Physics and Astronomy, Iowa State University, Ames, IA 50011

⁴ Department of Materials Science and Engineering, University of Maryland, College Park, MD 20742

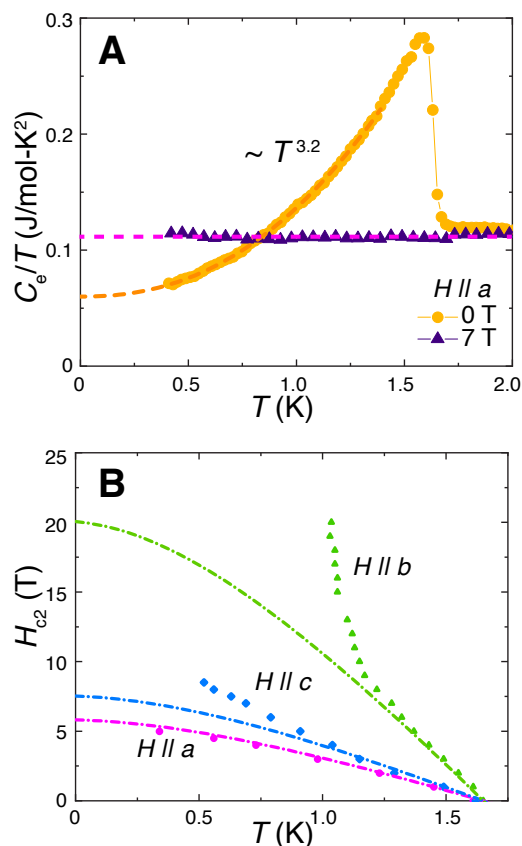


FIGURE 1: Superconducting properties of UTe₂. a) Low-temperature specific heat, emphasizing the jump associated with the superconducting transition and the large residual specific heat. b) The crystallographic-axis dependence of the upper critical field. Dashed lines represent the shape of a conventional upper critical field curve based on the Werthamer-Helfand-Hohenberg form.

What gives rise to this unusual superconductivity in the first place? In most spin triplet superconductors, the superconductivity is accompanied by ferromagnetism, and magnetic interactions appear to play a very important role in the superconducting pairing. However, bulk magnetometry and neutron measurements performed using NCNR's Disk Chopper Spectrometer (DCS) and at the MLZ in Munich [6] show no sign of ferromagnetism or any kind of magnetic order in UTe₂. Yet, it turns out that UTe₂ is not really a mundane paramagnet.

Instead, temperature-field scaling of the bulk magnetization suggests that this material is a quantum critical ferromagnet, or almost, but not quite, ferromagnetic. Under such conditions, plentiful magnetic fluctuations can lead to spin triplet superconductivity. Bolstering this idea, strong low-temperature magnetic fluctuations were detected by recent Muon Spin Resonance (μSR) measurements done in collaboration with researchers at Simon Fraser University [7].

As a picture emerges of the unusual superconducting properties of UTe₂, many questions remain open. Chief among them: what is the precise superconducting wave function, and is it topologically nontrivial? To get this answer, details of the electronic structure, superconducting gap symmetry, and time reversal symmetry, to name a few, need to be experimentally addressed, and theoretical and computational efforts are required to put everything in context. Undoubtedly, UTe₂ holds more in store for us, as we continue down the road in search of topological superconductivity.

References

- [1] D. Aoki, K. Ishida, J. Flouquet, J. Phys. Soc. Jpn. **88**, 022001 (2019).
- [2] A. Y. Kitaev, Physics-Uspekhi **44**, 131 (2001).
- [3] S. Ran, C. Eckberg, Q.-P. Ding, Y. Furukawa, T. Metz, S. R. Saha, I.-L. Liu, M. Zic, J. Paglione, N. P. Butch, arXiv:1811.11808.
- [4] D. Aoki, A. Nakamura, F. Honda, D. Li, Y. Homma, Y. Shimizu, Y. J. Sato, G. Knebel, J.-P. Brison, A. Pourret, D. Braithwaite, G. Lapertot, Q. Niu, M. Vališka, H. Harima, J. Flouquet, J. Phys. Soc. Jpn. **88**, 043702 (2019).
- [5] S. Ran, I.-L. Liu, Y. S. Eo, D. J. Campbell, P. Neves, W. T. Fuhrman, S. R. Saha, C. Eckberg, H. Kim, J. Paglione, D. Graf, J. Singleton, N. P. Butch, arXiv:1905.04343.
- [6] V. Hutanu, H. Deng, S. Ran, W. T. Fuhrman, H. Thoma, N. P. Butch, arXiv:1905.04377.
- [7] S. Sundar, S. Gheidi, K. Akintola, A. M. Cote, S. R. Dunsiger, S. Ran, N. P. Butch, S. R. Saha, J. Paglione, J. E. Sonier, arXiv:1905.06901.

Spin stripe order in a square planar trilayer nickelate

J. Zhang,^{1,2} D.M. Pajerowski,³ A.S. Botana,^{1,4} H. Zheng,¹ L. Harriger,⁵ J. Rodriguez-Rivera,^{5,6} J.P.C. Ruff,⁷ N.J. Schreiber,⁸ B. Wang,¹ Y.-S. Chen,⁹ M.R. Norman,¹ S. Rosenkranz,¹ J.F. Mitchell,¹ and D. Phelan¹

Like medieval knights chasing the *Holy Grail*, condensed matter physicists have long been allured by the glitter of high temperature superconductivity. The most famous advance in this effort was the Nobel-prize winning discovery in 1986 by Bednorz and Müller of superconductivity in layered copper oxides. The ensuing years have revealed that these materials have certain common features that seem to be part of the ‘recipe’ for copper oxide superconductivity: they are layered materials containing Cu-O planes; they consistently possess the same number of electrons in the copper 3d orbitals, which are strongly polarized with holes in the $d_{x^2-y^2}$ orbitals; and they are proximal to states where the electron spins order antiferromagnetically. Finding similar superconductivity in other transition metal oxides has thus far proven fruitless, but are copper oxides really the only ones? Nickel, which sits one column to the left of copper on the periodic table, has long been considered a tantalizing alternative for achieving superconductivity in a copper-free transition metal oxide. Recently, trilayer nickelates with the chemical formula $R_4Ni_3O_8$ (where R is a trivalent rare earth), which possess low valence nickel cations in square planar coordination, are particularly interesting candidate materials because they possess many of the same characteristics identified above as common to copper oxide superconductors [1]. Given the importance of magnetic interactions in the copper oxide superconductors, as well as in the iron pnictide superconductors, unraveling the magnetism in these trilayer nickelates is essential for understanding their behavior as well as their potential as superconductors. However, relatively few detailed investigations have been performed because single crystals have been unavailable, leading to a critical gap in our understanding of the magnetic behavior of these compounds.

Recently, single crystals of $La_4Ni_3O_8$ (La-438) have become available as a result of the advent of high-pressure floating zone technology. La-438 crystals exhibit a semiconductor-insulator transition on cooling that is concomitant with the

formation of charge stripes of higher and lower oxidation state on the nickel sites [2]. One of the major questions remaining is whether or not there is magnetic ordering in the ground-state, and if there is, how it relates to the charge ordering that is observed. Unfortunately, previous neutron powder diffraction experiments proved inconclusive. No magnetic Bragg reflections were observed from polycrystalline materials, either because the peaks were too weak to be detected by powder diffraction, or because the system did not develop long-range order. In order to resolve this quandary, single crystal neutron diffraction measurements were performed on MACS [3], which was chosen because of its large cold neutron flux, which is beneficial for investigating small single crystals with weak magnetic moments, and because of its spin-polarization capabilities.

Weak satellite reflections were observed in the two-dimensional plot of neutron intensity in the ground-state (Fig. 2A). Spin-polarized diffraction data, collected on MACS using the ^3He polarizers and analyzers, conclusively evidenced a magnetic origin to the scattering – thus proving that $La_4Ni_3O_8$ does have a magnetically-ordered ground-state (Fig. 2B, C). Using the charge-stripe state as a starting point, an antiferromagnetic spin-stripe-ordering model was developed in which ordered spins are present on Ni^{1+} sites ($S = 1/2$) and absent on Ni^{2+} sites ($S = 0$), as shown in Fig. 3. The nearest neighboring Ni^{1+} sites have antiferromagnetic interactions within the basal plane, as well as antiferromagnetic interactions out of the basal plane. The data are consistent with a quasi-two-dimensional ordering that occurs within Ni-O trilayers that are uncoupled along the c-axis.

Surprisingly, several characteristics were discovered that distinguish $La_4Ni_3O_8$ from copper oxides or single-layer nickelates. First, in these latter compounds, charge is the primary order parameter, and spin is a secondary order parameter that follows the charge. However, for $La_4Ni_3O_8$

¹ Argonne National Laboratory, Lemont, IL 60439

² Materials Science and Technology Division, Oak Ridge National Laboratory, Oak Ridge, TN 37831

³ Neutron Scattering Division, Oak Ridge National Laboratory, Oak Ridge, TN 37831

⁴ Arizona State University, Tempe, AZ 85287

⁵ NIST Center for Neutron Research, National Institute of Standards and Technology, Gaithersburg, MD 20899

⁶ University of Maryland, College Park, MD 20742

⁷ CHESS, Cornell University, Ithaca, NY 14853

⁸ Cornell University, Ithaca, NY 14853

⁹ The University of Chicago, Lemont, IL 60439

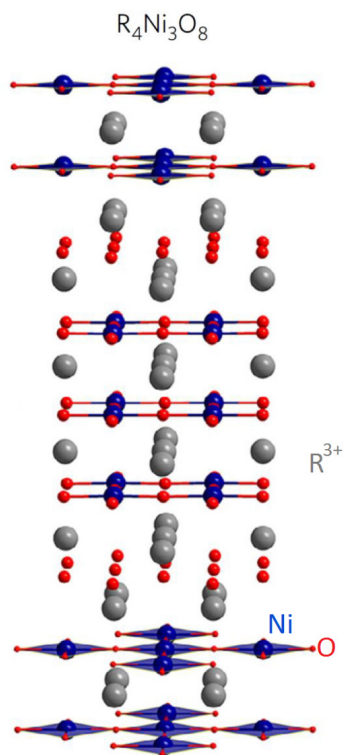


FIGURE 1: Structural motif of $R_4Ni_3O_8$ compounds ($R = La, Pr, Nd$). After [1].

the strong coupling between the charge and spin leads to a situation in which neither order parameter appears secondary to the other. Second, both the polarized data as well as density functional theory calculations indicate that the ordered spins point parallel and antiparallel to the c-axis. This contrasts with other layered oxides, where the spin prefers to orient in the basal plane.

These neutron scattering experiments have laid a foundation for our understanding of the magnetic correlations in $La_4Ni_3O_8$, which possesses an electron count that matches the over-doped regime of the superconducting cuprates. These experiments have revealed how a complex interplay of the spin, charge, and orbitals results in coupled charge and spin stripes. The next challenge in this work is to modify the electron count so that it overlaps the optimal concentration of the copper oxide superconductors and then to study how the magnetic and charge interactions respond.

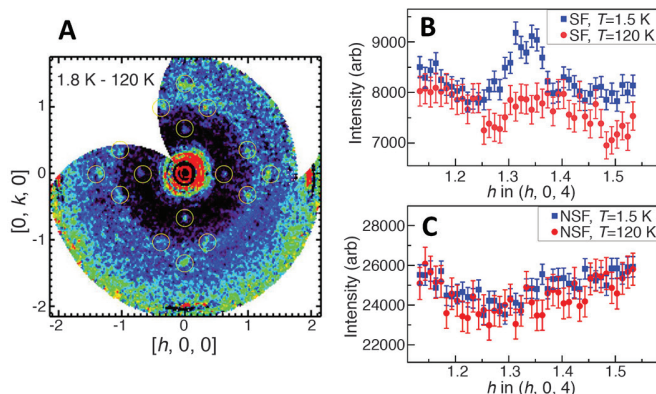


FIGURE 2: (A) Unpolarized neutron diffraction data on a specimen of $La_4Ni_3O_8$ showing weak superlattice peaks in the ground-state. (B, C) Observation of the peak in the Spin-Flip (SF) channel evidences magnetic ordering. After [3].

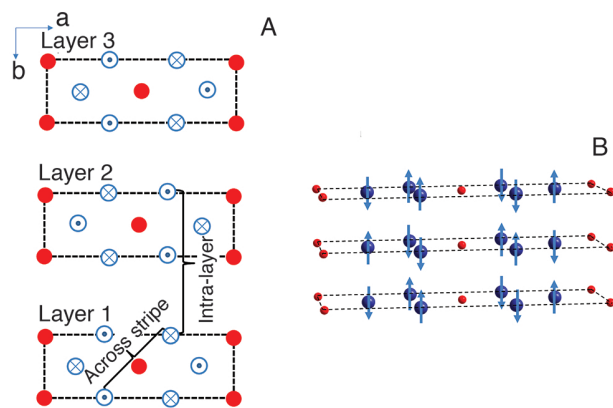


FIGURE 3: Spin-stripe pattern. Blue spheres refer to Ni^{1+} cations, and red spheres to Ni^{2+} cations. After [3].

References

- [1] J. Zhang, A. S. Botana, J. W. Freeland, D. Phelan, H. Zheng, V. Pardo, M. R. Norman, J. F. Mitchell, *Nat. Phys.* **13**, 864 (2017).
- [2] J. Zhang, Y.-S. Chen, D. Phelan, H. Zheng, M. R. Norman, J. F. Mitchell, *Proc. Natl. Acad. Sci. USA* **113**, 8945 (2016).
- [3] J. Zhang, D. M. Pajerowski, A. S. Botana, L. Harriger, J. Rodriguez-Rivera, J. P. C. Ruff, N. J. Schreiber, B. Wang, Y.-S. Chen, M. R. Norman, S. Rosenkranz, J. F. Mitchell, D. Phelan, *Phys. Rev. Lett.* **122**, 247201 (2019).

Kondo insulator-like state in antiferromagnetically ordered YbIr_3Si_7

M. Stavinoha,¹ C.-L. Huang,² A. M. Hallas,² Q. Huang,³ J. W. Lynn,³ C. Hooley,⁴ A. H. Nevidomskyy,² and E. Morosan^{1,2}

Intermetallic compounds have provided an endless source of exploration into the quantum mechanical interactions responsible for the physical properties of solids. When intermetallic compounds contain a rare earth ion in a stoichiometric ratio with metal or metalloid elements, they typically host highly localized f -electrons that often carry a magnetic moment. The local moments may order magnetically, and in special cases the magnetism is intertwined with the conduction electrons. This interplay between the magnetism, the conduction electrons, and the crystal structure allows us to determine the underlying mechanisms responsible for the magnetic, electronic, and optical properties. With a fundamental understanding of the intricate structure-function relationships present in intermetallic compounds, we can move toward a materials-by-design approach where desired properties can be intelligently crafted in a material as opposed to being discovered serendipitously.

One class of materials that falls within this description of rare earth-based intermetallic compounds are Kondo insulators [1]. In these compounds, a particularly unusual combination of physical properties has been observed due to the onset of the Kondo effect at low temperatures. The Kondo effect occurs when spins of the f -electrons couple to the spins of the conduction electrons. When this effect is spread over a lattice, the f -electron and conduction electron bands hybridize, which opens a bandgap at the Fermi level as the material cools and manifests as insulating behavior in the electrical transport. The number of confirmed Kondo insulators is relatively small, and the differences in their physical properties have rendered them particularly controversial and difficult to describe through existing theories. We recently discovered a new material, YbIr_3Si_7 , that is at the border of Kondo insulating behavior [2]. This compound exhibits a unique combination of behaviors mediated by strong electron-electron interactions. While Kondo insulating-like behavior appears as a distinctive trait in this compound, we also observe long-range antiferromagnetic order followed by the emergence of conductive surface states as the temperature is lowered. This combination of properties seems inexplicable using a simple Doniach

model in which, depending on the relative strength of the Kondo effect and the exchange interactions, the conduction electrons either mediate the magnetic order among the rare earth ions or they screen each magnetic moment. YbIr_3Si_7 exemplifies the lower limit of conduction electron density, which makes it particularly surprising that it can show both Kondo correlations and magnetic exchange interactions. In this scenario of so few conduction electrons, YbIr_3Si_7 may represent a new hierarchy of quantum mechanical interactions among Kondo screening, magnetic interactions, and the crystal electric field of the rare earth ion.

The resistivity profile of YbIr_3Si_7 is given in Fig. 1(a). At high temperatures, a broad hump emerges as Kondo correlations set in. As the temperature is decreased, a diverging insulator-like behavior dominates the electrical transport until a small peak appears at ≈ 5 K, which we will subsequently show marks an antiferromagnetic ordering transition. At even lower temperatures, the resistivity begins to level off into a plateau as conductive states form at the surface of the crystal while the bulk remains insulating. When this resistivity profile is compared to that of the nonmagnetic analog compound LuIr_3Si_7 , we see that the filled f -shell in this isostructural compound renders the crystal weakly metallic, consistent with the picture of Kondo screening in the Yb analog.

Magnetic susceptibility measurements on YbIr_3Si_7 , presented in Figure 1(b), reveal the anisotropic magnetic response of the crystal when the magnetic field H is applied along the orthogonal a and c directions. When H is applied along a , an abrupt increase in the magnetic susceptibility is noted below the magnetic ordering temperature $T_N = 4.1$ K. Conversely, when H is applied along c , the magnetic susceptibility shows a broad hump above T_N , followed by a cusp consistent with antiferromagnetic order. While these magnetic susceptibility measurements provide evidence of antiferromagnetic order, strong crystal electric field anisotropy, and short-range magnetic order above T_N when H is applied along c , neutron scattering measurements provide a detailed magnetic structure and conclusive evidence of long-range magnetic order.

¹ Department of Chemistry, Rice University, Houston, TX 77005

² Department of Physics and Astronomy, Rice University, Houston, TX 77005

³ NIST Center for Neutron Research, National Institute of Standards and Technology, Gaithersburg, Maryland 20899

⁴ Scottish Universities Physics Alliance, School of Physics and Astronomy, University of St Andrews, North Haugh, St. Andrews, Fife KY16 9SS, United Kingdom

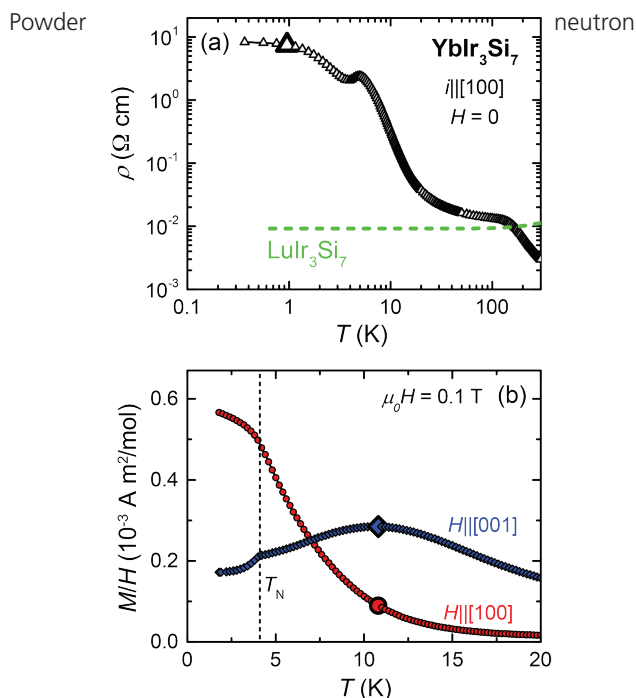


FIGURE 1: (a) Resistivity measurements show that as the temperature is lowered, the onset of Kondo correlations first appears as a broad hump followed by insulator-like divergence. This divergence is interrupted by long-range magnetic order at 4.1 K and subsequent conductive surface states that result in a plateau of the resistivity. (b) Magnetic susceptibility measurements reveal an anisotropy present among the magnetic Yb ions. When H is applied along c , a broad hump, possibly from short-range magnetic order, appears above the ordering temperature, followed by a cusp consistent with antiferromagnetic order at T_N . When H is applied along a , the magnetic susceptibility smoothly increases until it levels off at T_N .

measurements performed on cooling YbIr₃Si₇ from 25 K to 1.5 K provided conclusive evidence of the long-range antiferromagnetic order below $T_N = 4.1$ K. In Fig. 2(a), we note the formation of magnetic Bragg peaks as the temperature is lowered. The magnetic diffraction pattern obtained from subtracting data collected at 25 K from data collected at 1.5 K (Fig. 2(b)) shows excellent agreement with the Γ_1 magnetic structure for Yb³⁺ sitting at the $6b$ Wyckoff site within the $R\bar{3}c$ space group. The order parameter obtained by fitting the intensity of the (101) magnetic Bragg peak confirms that the ordering temperature is $T_N = 4.1$ K (Fig 2(c)). Lastly, the magnetic structure of YbIr₃Si₇ pictured in Fig. 2(d) shows that in the ordered state, all the Yb³⁺ moments are aligned along the c -axis with an ordered moment of $1.51(5) \mu_B/\text{Yb}^{3+}$. These Yb³⁺ moments are aligned antiparallel with their nearest neighbors, represented by the edges of the cube in Fig. 2(d), and parallel with their next nearest neighbors in the ab -plane. Understanding the relationship among the symmetry of the Yb ions, their magnetic interactions and anisotropy, and their interplay with conduction electrons in the bulk and

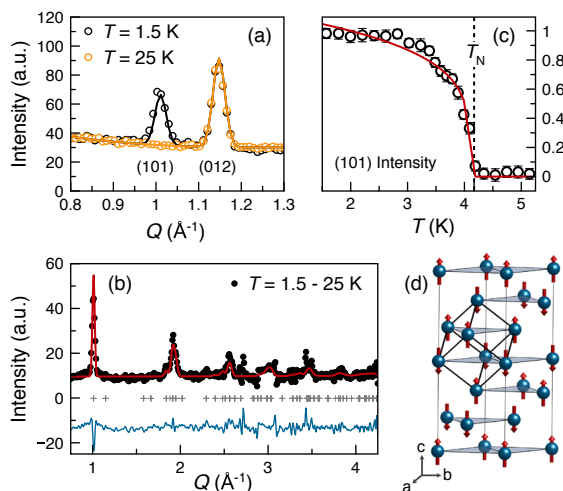


FIGURE 2: (a) Powder neutron diffraction measurements show the appearance of magnetic Bragg peaks as the temperature is lowered. (b) Rietveld refinement of the magnetic diffraction pattern, which is isolated by subtracting the 25 K data set from the 1.5 K data set, reveals excellent agreement with the Γ_1 irreducible representation. (c) The order parameter obtained by fitting the magnetic (101) Bragg peak drops to zero at the ordering temperature $T_N = 4.1$ K. (d) The magnetic structure with the Γ_1 irreducible representation shows antiferromagnetic order with the moments aligned along the c -axis. The nearest neighbors are represented by the edges of the cube, while the next nearest neighbors are given by the shaded triangles in the ab -plane.

surface of the crystals is a crucial step to unravelling the intricate physical behaviors present in this system.

In summary, we report the discovery and characterization of a unique, complex material YbIr₃Si₇. This material shows insulating-like resistivity caused by Kondo hybridization between the Yb f -electrons and the conduction electrons as the temperature is lowered, followed by the onset of antiferromagnetic order and conductive surface states. Powder neutron diffraction revealed that the antiferromagnetic transition occurs at $T_N = 4.1$ K with an ordered moment of $1.51(5) \mu_B/\text{Yb}^{3+}$. This intriguing combination of strong electron-electron interactions, crystal electric field anisotropy, and magnetic order in an environment of scarce conduction electrons provides a complex energy landscape in which to explore a variety of quantum interactions and their interplay with bulk and surface physical properties.

References

- [1] M. Dzero, J. Xia et al., Annu. Rev. Condens. Matter Phys. **7**, 249 (2016).
- [2] M. Stavinoha, C.-L. Huang, W. A. Phelan et al., Nat. Phys. (under review).

Deciphering the coupling between structural disorder and magnetic order in chiral skyrmion host materials

J. D. Bocarsly,¹ C. Heikes,² C. M. Brown,² S. D. Wilson,¹ and R. Seshadri¹

A variety of magnetic materials have recently been discovered to host magnetic “skyrmions,” nano-sized magnetic vortices that behave like stable particles and can be manipulated with electrical current or magnetic field. Skyrmions are exciting both for their novelty as interesting magnetic structures forming in seemingly mundane magnetic materials and for their potential in next generation electronic devices. In particular skyrmions are promising as bits in next-generation high-density, low-power memory architectures and for devices that manipulate electron spin instead of electron charge. The majority of materials supporting skyrmions show these exotic structures at extreme environmental conditions well below room temperature, which limits their applications. Recently the $\text{Co}_x\text{Zn}_y\text{Mn}_z$ family of compounds, with $x + y + z = 20$, has been shown to host skyrmions at temperatures up to and beyond room temperature, potentially enabling these new technologies at ambient temperatures [1]. In this system, chemical disorder has been suggested to play a role in the stabilization of a number of exotic flavors of skyrmions, including a metastable square [2] and disordered [3] skyrmion lattices. Understanding the role of disorder in this system and how it shapes the magnetic properties is necessary in order to establish control of the skyrmions. We performed a detailed neutron diffraction study of the atomic and magnetic structure of the $\text{Co}_x\text{Zn}_y\text{Mn}_z$ family of skyrmion hosts, revealing a remarkable two-part magnetic structure where ordered magnetism coexists with disordered glassy magnetism [4]. Our results suggest that this combination of order and disorder enables the formation of new the skyrmion phases.

$\text{Co}_x\text{Zn}_y\text{Mn}_z$ compounds crystallize in the β -manganese structure type, as shown in Figure 1. This structure type is chiral, allowing for the existence of long-range chiral magnetic interactions. These interactions can lead to the formation of chiral magnetic spin textures, such as magnetic helices with wavelength around 100 nm, or lattices of vortex skyrmions. The β -manganese structure consists of two crystallographic sites on which the atoms sit: a small eightfold site (8c) which forms a distorted diamondoid network, and a larger twelvefold site (12d) which forms a geometrically frustrated hyperkagome lattice.

Determining how the Co, Mn, and Zn atoms are distributed among the 8c and 12d sites is necessary in order to understand the magnetic properties. To determine this, we used

complimentary neutron powder diffraction and synchrotron x-ray powder diffraction. The combined x-ray and neutron scattering approach is critical for this system. Due to the similar x-ray scattering cross sections of Co and Mn, these atoms are nearly indistinguishable by x-ray diffraction alone. On the other hand, these elements have very different neutron scattering cross sections, and therefore neutron diffraction gives complementary structural information to x-ray diffraction, allowing the structure to be determined with high confidence.

Our co-refinement analysis of the x-ray and neutron data shows that the Mn and Zn atoms are randomly distributed over the larger 12d site, while the Co atoms prefer to occupy the smaller 8c site. This result was compared to density functional theory calculations, which explain the observed site preferences on the basis of the energies of different atomic configurations. These calculations indicate that the preference for Mn atoms to site on the 12d site is driven by its ability to hold a large local moment of about 3 μB when it sits on this site. The Co atoms on the 8c

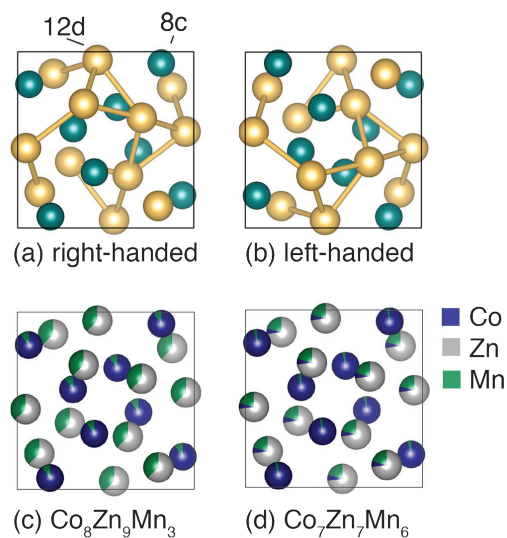


FIGURE 1: (a) and (b) show the β -manganese structure, which is chiral and can be either right-handed or left-handed. The two different atomic sites are labelled, and the yellow bonds show how the 12d atoms form a frustrated hyperkagome lattice. (c) and (d) show the atomic structure of $\text{Co}_8\text{Zn}_9\text{Mn}_3$ and $\text{Co}_7\text{Zn}_7\text{Mn}_6$, as determined by combined neutron and synchrotron diffraction. Each site hosts multiple elements, which are randomly distributed across the sample. This fractional occupation is indicated by the partial coloring of the atoms.

¹ University of California, Santa Barbara, Santa Barbara, CA 93117

² NIST Center for Neutron Research, National Institute of Standards and Technology, Gaithersburg, MD 20899

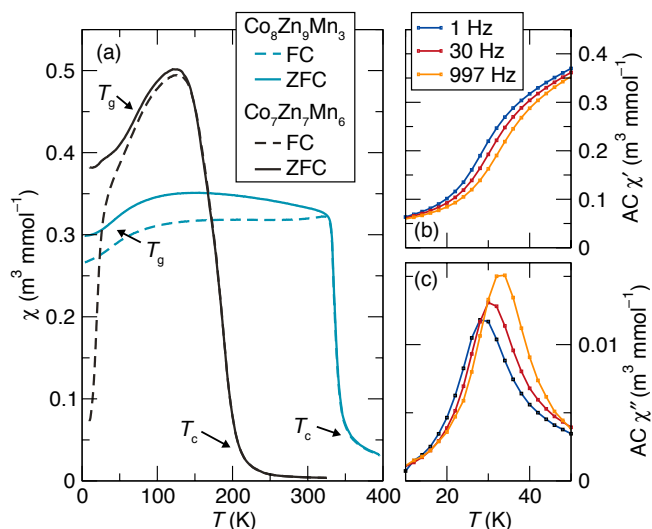


FIGURE 2: Magnetic properties of samples of $\text{Co}_8\text{Zn}_9\text{Mn}_3$ and $\text{Co}_7\text{Zn}_7\text{Mn}_6$. (a) Magnetic susceptibility vs. temperature shows two magnetic transitions for each sample: at higher temperature (T_g), the onset of magnetic moment, and at lower temperature a reduction in the moment (T_c). (b) and (c) shows the real and imaginary components of the AC magnetic susceptibility around T_g for the $\text{Co}_7\text{Zn}_7\text{Mn}_6$ sample measured at three different frequencies. The frequency-dependence of the AC magnetic susceptibility shows that the transition at T_g behaves like a spin cluster glass transition.

site, on the other hand, host a magnetic moment of about $1 \mu\text{B}$ while the Zn atoms are nonmagnetic.

With this knowledge in hand, we considered the bulk magnetic measurements shown in Figure 2. Upon cooling, both samples show an onset of a magnetic moment ($T_c = 340 \text{ K}$ for $\text{Co}_8\text{Zn}_9\text{Mn}_3$ and $T_c = 210 \text{ K}$ for $\text{Co}_7\text{Zn}_7\text{Mn}_6$), and then a second transition around 50 K . The frequency dependence of the AC magnetic susceptibility in the low temperature regime is consistent with a reentrant cluster spin glass transition. Neutron powder diffraction allows us to concurrently determine the magnetic structure and the nuclear structure of these samples, allowing us to probe the local magnetic ordering that gives rise to this interesting time- and temperature-dependent magnetic behavior. By refining a model of the magnetic contribution to neutron diffraction patterns taken at different temperatures, we see that the 8c site, which is mainly Co, is found to hold a magnetic moment of about $1 \mu\text{B}$ per Co atom at all temperatures below T_c , as expected from the density functional theory calculations. By contrast, the 12d site, which is mainly Mn and Zn, never shows the moment of $3 \mu\text{B}$ per Mn atom that is expected from the fully ordered density functional theory calculations. Rather, a moment of $1 \mu\text{B}$ /Mn atom is observed in the high temperature magnetically ordered regime (taken at 100 K), and this moment is effectively reduced to zero in the cluster spin glass regime (taken at 14 K).

Our neutron scattering measurements on this family of $\text{Co}_x\text{Zn}_y\text{Mn}_z$ compounds paint a clear picture elucidating the coupling between chemical disorder in the β -manganese crystal structure and magnetic ordering. The 8c site, which is mostly occupied by Co atoms, shows conventional ordered magnetism

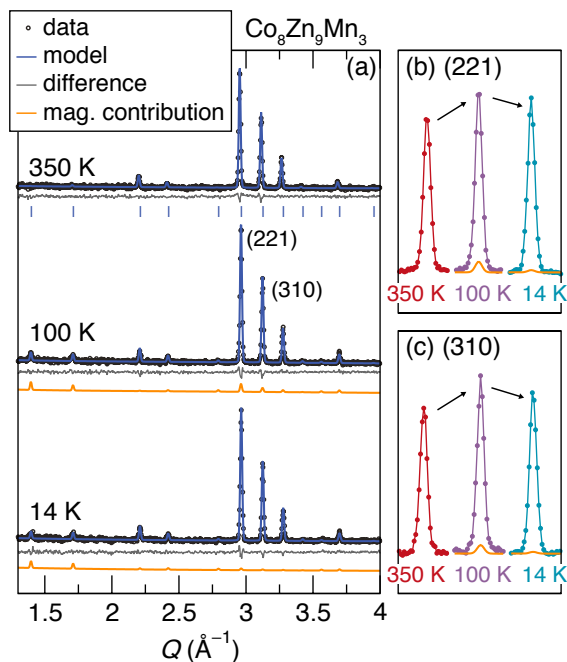


FIGURE 3: (a) Neutron diffraction patterns for a $\text{Co}_8\text{Zn}_9\text{Mn}_3$ sample at 350 K , 100 K , and 14 K . In each case, the overall fit, which includes both a nuclear and magnetic structure model, is shown in blue. The magnetic contribution to the 100 K and 14 K fits is shown in orange. As shown in (b) and (c), the magnetic contribution is smaller at 14 K than at 100 K . This is due to the freezing of Mn moments into a cluster glass with no net moment around 50 K .

across a broad temperature range. The Mn atoms on the 12d site, on the other hand, have large magnetic moments which dynamically fluctuate even while the Co moments are aligned. These Mn moments have only a partial tendency to align in the direction of the Co atoms, and therefore show a reduced overall moment by neutron diffraction. At low temperature, the Mn moment fluctuations slow and eventually freeze into a statically disordered spin glass with no net moment. This two-sublattice magnetic structure allows for the formation of ordered phases—including helical and skyrmion lattice phases—where the details of the ordering are strongly influenced by disordered magnetic interactions. These new results offer a possible route for using control of chemical and structural disorder in this system to engineer magnetic ordering by design.

References

- [1] Y. Tokunaga, X.Z. Yu, J.S. White, H.M. Rønnow, D. Morikawa, Y. Taguchi, Y. Tokura, *Nat. Commun.* **6**, 7638 (2015).
- [2] K. Karube, J.S. White, N. Reynolds, J.L. Gavilano, H. Oike, A. Kikkawa, F. Kagawa, Y. Tokunaga, H.M. Rønnow, Y. Tokura, Y. Taguchi, *Nature Mater.* **15**, 1237 (2016).
- [3] K. Karube, J.S. White, D. Morikawa, C.D. Dewhurst, R. Cubitt, A. Kikkawa, X. Yu, Y. Tokunaga, T. Arima, H.M. Rønnow, Y. Tokura, Y. Taguchi, *Sci. Adv.* **4**, 7043 (2018).
- [4] J.D. Bocarsly, C. Heikes, C.M. Brown, S.D. Wilson, R. Seshadri, *Phys. Rev. Mater.* **3**, 014402 (2019).

Symmetry breaking and singular angular magnetoresistance in a magnetic nodal semimetal

T. Suzuki,¹ L. Savary,^{1,2,3} J.-P. Liu,^{2,4} J. W. Lynn,⁵ L. Balents,² and J. G. Checkelsky¹

The interplay between conduction electrons and localized magnetic moments gives rise to a wide variety of electrical phenomena in magnetic conductors. A fundamental and technologically important effect is the change in electrical resistance of a material in a rotating magnetic field (called angular magnetoresistance); this effect has enabled a variety of magnetic sensing technologies and typically exhibits a smooth, sinusoidal variation with field rotation [1]. We have recently found that the magnetic material CeAlGe and its Si-doped alloy, rather than exhibiting this conventional behavior, display an unprecedentedly sharp increase in resistance when a magnetic field is carefully aligned within less than 1 degree of its tetragonal axes [2]. This highly confined signal (called singular angular magnetoresistance, SAMR) is observed in the intermediate magnetic field region of the magnetically ordered phase, indicating the presence of a distinct magnetic state that couples to the symmetry breaking caused by the magnetic field. We have performed a neutron powder diffraction study to determine the magnetic ordering pattern and elucidate the role of the accompanying symmetry breaking in this new magnetotransport response.

CeAlGe crystallizes in a nonsymmorphic structure (called the LaPtSi-type structure shown in Figure 1a), where the magnetic Ce ions form two interpenetrating body centered tetragonal sublattices labelled Ce (A) and Ce (B). The moments order at $T_N = 5.4$ K, below which temperature the magnetization easy axis lies in the ab plane. In this magnetically ordered phase, the rotation of an applied magnetic field produces a singular angular response, while above T_N a smooth angular dependence is observed (see Fig. 1(b)).

Neutron powder diffraction measurements in zero magnetic field were carried out using the triple-axis spectrometer BT-7 to probe the magnetic ordering pattern. Figure 2a shows the diffraction profiles above (at $T = 10$ K) and below T_N ($T = 1.8$ K), from which we determined the magnetic diffraction profile (Fig. 2(b)). There is no sign of splitting/broadening of the nuclear peaks below T_N , indicating that the magnetic transition is not accompanied by a structural distortion. The magnetic diffraction profile exhibits enhanced intensities at the nuclear Bragg peak

positions as well as additional peaks at the (002), (006) and (110) positions. The former originates from the ferromagnetically-ordered component of the Ce moments, while the latter arise from the antiferromagnetically-ordered components, which implies a ferrimagnetic-type of ordering. Analysis of the magnetic diffraction peaks based on extinction rules [3] suggests the ordering patterns shown in Figs. 2(c) and 2(d). In both cases, the moments on the same sublattice align ferromagnetically. The pattern in Fig. 2(c) is a noncollinear structure, while the pattern in Fig. 2(d) is a collinear one where the moments on the A and B sublattices have different magnitude and point in the opposite direction along the in-plane crystallographic axis. Our mean-field calculation suggests that the ground state in zero magnetic field is the structure in Fig. 2(c), and the one in Fig. 2(d) is stabilized in a magnetic field applied along the [100] direction [2].

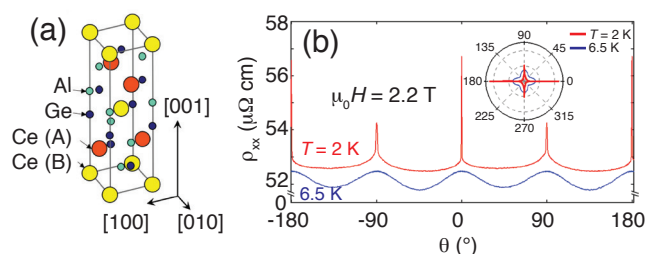


FIGURE 1: (a) Crystal structure of CeAlGe. (b) Resistivity change with magnetic field rotation in the ab plane in the paramagnetic ($T = 6.5$ K) and magnetically ordered phase ($T = 2$ K) for Si-doped CeAlGe ($\text{CeAlGe}_{0.72}\text{Si}_{0.28}$). The electric current flows along the [010] direction corresponding to $\theta = 90^\circ$. The inset is the corresponding polar plot.

Application of a larger magnetic field along the [100] direction causes a transition to the ferromagnetically-ordered state via an intermediate noncollinear structure as shown in Figs. 2(e)-2(g). The canted moment of the intermediate phase breaks the magnetic symmetry of the collinear structure; the collinear structures in small (Fig. 2(e)) and large field (Fig. 2(g)) have the combined symmetry operation of a mirror along the ac plane and time-reversal, while the noncollinear intermediate phase in Fig. 2(f) does not. This combined symmetry is also related to

¹ Massachusetts Institute of Technology, MA 02139

² University of California, Santa Barbara, Santa Barbara, CA 93106

³ Université de Lyon, École Normale Supérieure de Lyon, Université Lyon I, CNRS, Laboratoire de physique, 46, allée d'Italie, 69007 Lyon, France

⁴ Department of Physics, The Hong Kong University of Science and Technology, Kowloon, Hong Kong

⁵ NIST Center for Neutron Research, National Institute of Standards and Technology, Gaithersburg, MD 20899

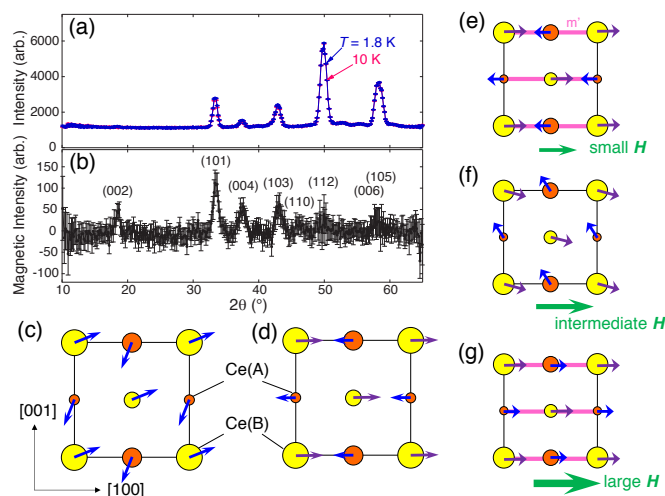


FIGURE 2: (a) Neutron powder diffraction profile of CeAlGe above ($T = 10$ K) and below (1.8 K) the magnetic transition temperature $T_N = 5.4$ K. (b) Magnetic diffraction intensity calculated by taking the difference of the profile between $T = 10$ K and $T = 1.8$ K. (c) and (d) Magnetic structures deduced for the ordered phase at zero field. Symmetrically inequivalent moments are depicted by arrows with different color. (e)-(g) Evolution of the magnetic structure with magnetic field along the [100] direction. Pink lines are the combined symmetry operation of the mirror reflection along the (010) plane with time reversal m' , which is spontaneously broken in the intermediate noncollinear phase shown in panel (f).

the in-plane magnetic field. When the field is aligned along the [100] direction, the combined symmetry is not broken by the field, and thus the intermediate phase ordering pattern shown in Fig. 2(f) is degenerate with its combined-symmetry partner.

This results in the multiple domain state with high electrical resistance at the domain boundary. The degeneracy is lifted by the in-plane field rotation, thus explaining the observed singular angular magnetoresistance behavior [2].

This neutron diffraction study has unveiled the crystallographic and magnetic symmetries in the magnetically ordered phase responsible for SAMR and revealed its microscopic origin. In particular, a theoretical model has been constructed based on the obtained symmetry that suggests that singular angular magnetoresistance may be widely observed in nodal magnetic materials [2]. This exemplifies the importance of symmetry in understanding the unprecedented magnetotransport and designing functional materials, where neutron diffraction can provide essential insight. Such materials offer a potentially new paradigm for ultrasensitive magnetic sensing using symmetry breaking.

References

- [1] T. R. McGuire, R. I. Potter, IEEE Trans. Mag. **11**, 1018 (1975).
- [2] T. Suzuki, L. Savary, J.-P. Liu, J. W. Lynn, L. Balents, J. G. Checkelsky, Science 10.1126/science.aat0348 (2019).
- [3] S. V. Gallego, E. S. Tasci, G. de la Flor, J. M. Perez-Mato, M. I. Aroyo, J. Appl. Cryst. **45**, 1236 (2012).

Tuning topology in thin films using antiferromagnetism

Q. L. He,^{1,2} G. Yin,¹ L. Yu,¹ A. J. Grutter,⁴ L. Pan,¹ C.-Z. Chen,⁵ X. Che,¹ G. Yu,¹ B. Zhang,⁶ Q. Shao,¹ A. L. Stern,⁷ B. Casas,⁷ J. Xia,⁷ X. Han,⁶ B. J. Kirby,⁶ R. K. Lake,⁸ K. T. Law,⁵ and K. L. Wang^{1,3}

Materials systems with nontrivial topology have emerged over the past decade as ideal candidates upon which next-generation magnetic and electronic devices, such as quantum computers, are based. These materials exhibit properties termed “topological invariants” that may be thought of as constant, secured qualities that are unusually stable and protected from external interference or perturbation. One of the best and most exciting examples of this behavior is the class of materials known as “topological insulators” [1]. Topological insulators are electrically insulating within the bulk of the material but host a narrow electrically conductive channel at the surface. This conductive surface state is essential and protected by the unique topology of the quantum states occupied by electrons within a topological insulator. The unique nature of this electronic surface structure allows for the observation of surprising quantum mechanical behavior, such as the quantum anomalous Hall effect (QAHE) [2]. It is thought that the realization of the quantum anomalous Hall state has opened the door to create exotic quasiparticles that may be ideal building blocks for fault-tolerant quantum computing [3].

Up to this point, the existence of the QAHE has generally relied on introducing ferromagnetic order into normally nonmagnetic topological insulators. This has generally been accomplished through chemical doping, where small amounts of magnetic elements are introduced into the crystal structure of the topological insulator. This approach has been most successful in Cr-doped $(\text{Bi,Sb})_2\text{Te}_3$, where the resulting magnetic topological insulator (MTI) does indeed display the QAHE. Unfortunately, this method is limited to extremely low temperatures (< 30 K), as the larger dopant concentrations required to strengthen the magnetic interactions rapidly begin to alter the desired topological properties of the MTI. It is therefore critical to identify and implement alternative methods that can stabilize magnetism at higher temperatures while preserving and allowing control of the topological properties of the resultant MTI.

In the quest for such alternative mechanisms, one based on the magnetic proximity effect, in which a magnetically ordered

material grown next to a nonmagnetic material transfers some magnetic properties to its neighbor, has emerged as a leading candidate. In almost all cases, a thin film of some ferromagnetic material with a large net magnetization has been used to induce a net magnetization in a neighboring nonmagnetic film. Ferromagnetic layers, however, are extremely difficult to study with common laboratory magnetometry techniques because the large signal from the ferromagnet overwhelms the contribution from the MTI. Instead, we have used thin films of an antiferromagnetic material composed of alternating atomic planes of ferromagnetically-ordered (in-plane) chromium antimonide (CrSb) to mimic the proximity effect of a ferromagnet [4]. Because the magnetization of each atomic layer in CrSb is oriented anti-parallel to that of the layers above and below it, the thin film has no net magnetization. However, by growing *atomically sharp* thin film interfaces, as shown in the scanning transmission electron microscope image in Figure 1, it is possible to create a system in which thin films of the topological insulator $(\text{Bi,Sb})_2\text{Te}_3$ are adjacent to and interact with only a single layer of the antiferromagnet, which will consequently appear ferromagnetic to the topological insulator. We may thus attempt to create an MTI using an antiferromagnet, avoiding the disadvantages of a ferromagnet-based proximity effect.

As shown in Figure 2(a), Hall effect measurements of a $\text{CrSb} / (\text{Bi,Sb})_2\text{Te}_3$ superlattice show a clear hysteresis up to 90 K, indicating a net ferromagnetic moment exists within the thin film structure. On the other hand, longitudinal magnetoresistance measurements of the superlattices surprisingly do not exhibit the butterfly shape expected for a ferromagnetic system. Instead, large positive (negative) spikes are observed in the longitudinal resistance at fields corresponding to the switching of the magnetization from positive to negative (negative to positive), as shown in Figure 2(b). Here we note that the switching events appear to occur as a series of distinct steps in the Hall measurements, so that each spike in the longitudinal magnetoresistance may be associated with a small step in the Hall resistance. These resistance spikes appear only when the topological insulator layer is sandwiched

¹ University of California, Los Angeles, CA 90095

² International Center for Quantum Materials, Peking University, Beijing 100871, China

³ University of California, Los Angeles, CA 90095

⁴ NIST Center for Neutron Research, National Institute of Standards and Technology, Gaithersburg, MD 20899

⁵ Department of Physics, Hong Kong University of Science and Technology, Clear Water Bay, Hong Kong, China

⁶ Beijing Key Lab of Microstructure and Property of Advanced Materials, Beijing University of Technology, 100124, Beijing, China

⁷ University of California, Irvine, CA 92697

⁸ University of California, Riverside, Riverside, CA 92521

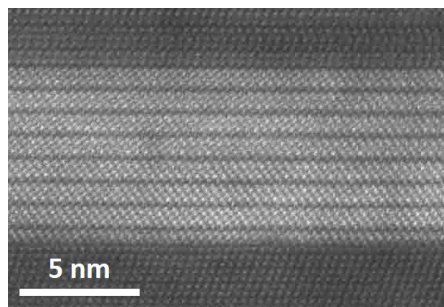


FIGURE 1: Scanning transmission electron microscope image of a CrSb / (Bi,Sb)₂Te₃ heterostructure showing the atomically sharp interfaces between the antiferromagnetic (dark) and topological insulator (light) materials.

between CrSb layers, as in trilayer structures or superlattices. When a bilayer film is deposited, the classical butterfly shape does in fact appear in the longitudinal magnetoresistance.

Theoretical calculations based on magnetotransport measurements suggest that the unusual behavior may be attributed to topological transitions induced by the relative alignment of proximity-induced magnetic layers at the top and bottom interfaces. That is, if there is indeed an interfacial magnetic moment induced in the (Bi,Sb)₂Te₃ layer at the interface with antiferromagnetic CrSb, then the topologically induced conductive channels at the top and bottom surfaces of the (Bi,Sb)₂Te₃ layer may be stabilized or destroyed by adjusting the magnetization direction of the top and bottom interfaces to be parallel or antiparallel to each other. Configurations with a conductive top and insulating bottom (or vice-versa), a conductive top and bottom, or an insulating top and bottom, should all be accessible.

Since this interpretation assumes that the observed magnetic properties are due to an antiferromagnetic proximity effect tightly localized at the interface, it is critical to understand the magnetic and structural depth profile of the system. We therefore performed the polarized neutron reflectometry measurements shown in Figure 3(a) using the PBR instrument. The magnetic contribution to the scattering can be seen more clearly in the plot of the spin-asymmetry in Figure 3(b), where the spin asymmetry is defined as the difference between the two spin-polarized reflectivities normalized by their sum. Although the induced magnetization (and corresponding scattering length densities) is extremely small, careful fitting and statistical analysis of the reflectivity allowed for the extraction of the nuclear and magnetic scattering length density profiles shown in the inset of Figure 3(a). The best fit depth profile confirms the interpretation of the magnetoresistance measurements, with sharp spikes of magnetization appearing at the interfaces between the topological insulator (Bi,Sb)₂Te₃ and the antiferromagnet CrSb. Alternative interpretations, such as a net magnetization spread uniformly throughout the CrSb or the entire superlattice structure, can be explicitly ruled out, as the theoretical scattering curves generated by such depth profiles are inconsistent with the reflectometry data.

These results not only show that it is possible to induce a net magnetization in topological insulators such as (Bi,Sb)₂Te₃ using

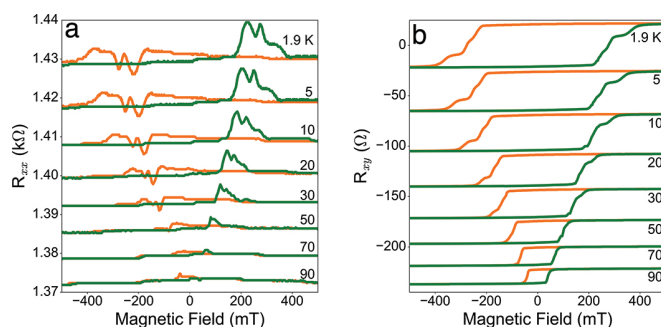


FIGURE 2: (a) Temperature-dependent Hall effect measurements showing ferromagnetic hysteresis in a superlattice of CrSb / (Bi,Sb)₂Te₃. (b) Temperature-dependent longitudinal magnetoresistance of the same sample exhibiting resistance spikes corresponding to switching of the magnetization direction.

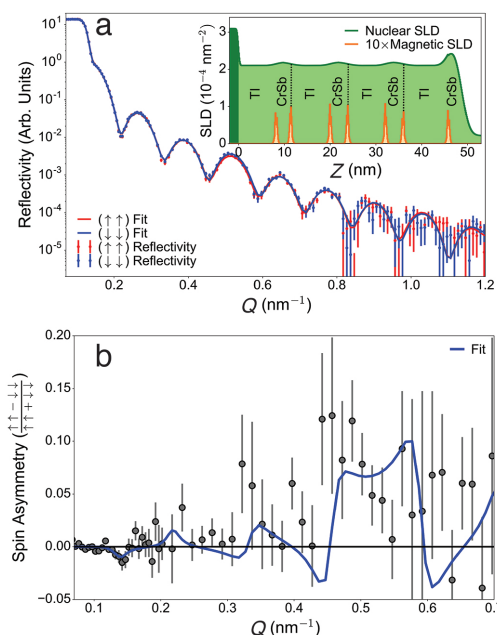


FIGURE 3: (a) Fitted polarized neutron reflectometry curve from a 4-repeat superlattice of (Bi,Sb)₂Te₃ and CrSb with the (inset) best-fit magnetic and structural depth profile. (b) Fitted spin asymmetry corresponding to the measurements and shown in panel a.

atomically sharp interfaces with an antiferromagnet, but also that the topology of the resultant system may itself be tuned through a small magnetic field. Excitingly, these effects are seen to persist up to temperatures exceeding 90 K, over 3 times the typical limit for dopant-induced magnetism. Our results therefore have significant implications for the high-temperature observation and control of quantum effects in topological systems.

References

- [1] J. E. Moore, *Nature* **464**, 194 (2010).
- [2] C.-Z. Chang et al., *Science* **340**, 167 (2013); Kou et al., *Physical Review Letters*, **113** (13): 137201/1-5. (2014); Kou et al., *Nature Communications*, **6** (8474): 1-8 (2015).
- [3] Q. L. He et al., *Science* **357**, 294 (2017).
- [4] Q. L. He et al., *Physical Review Letters* **121**, 096802 (2018).

Why do automotive springs fracture? Stress induced splitting in automotive coil springs

T. Gnaupel-Herold,¹ and Y. Prawoto²

The function of automotive coil suspension springs is readily accessible: it is to provide elastic shock absorption. Millions of automotive coil suspension springs are produced each year, and many more are in daily use in cars and trucks all over the world. In-service fracture is very rare which is a testament to quality control and to the level of understanding in the engineering science of the materials and processes involved. However, the continuing industry-wide push to reduce vehicle weight and cost extends to all components including coil springs, thus prompting a new look at spring manufacturing where splitting fracture during certain stages of production is more common, resulting in higher cost. Splitting fracture is strongly correlated with residual stresses, which are the subject of this work.

The need to use less material for weight reduction means that higher strength steels are required which comes with the tendency of more frequent fractures during production. Other considerations concerning manufacturability involve a parameter called the spring index. The spring index, defined as the ratio between spring diameter and spring wire diameter is a common descriptor for the strength of the spring, the stress induced on the spring and the difficulty in producing the spring. Instead of a conventional process in which the wire is wound around a cylindrical core the wire is fed/pushed and subsequently bent continuously between a forming roll and an adjustable pitch bar, thus allowing the production of springs with different spring indices in the same machine. Since the bending is performed at room temperature the stresses on the equipment are very large, as are the residual stresses in the coil.

The spring index range 6 to 12 is where the goal of weight reduction meets engineering limits: both wire diameter and the spring diameter are reduced to keep the spring index in the desired range. The steel grades required have ultimate tensile strengths up to 1.8 GPa which, together with the cold work imparted by the cold coiling processes, leads to very high levels of residual stress. The stress magnitudes are such that in the time between coiling and stress relief heat treatment spontaneous fractures occur in which springs split along the wire axis (Figure 1).

A striking feature of the fracture shown in Figure 1 is the uniformity of the split as it follows the winding of the coil.



FIGURE 1: Spontaneous splitting fracture of a coil. The label 'EDM' indicates the cut orientation of the cross sections shown in the inset. The diameter of the cross sections is 15 mm, the diameter of the coil is ≈ 130 mm.

The crack is extraordinarily long and uniform with respect to its location in the local coordinate system, thus allowing a visualization of its location from surface displacements after performing a cut using electro-discharge machining (EDM). A wire EDM cut is nearly ideally line shaped and it relieves stresses perpendicular to the cutting plane. The stress relief causes small surface deflections that can be measured accurately with a displacement probe. A crack that occurs after cutting represents a stress relief itself, thus causing additional surface deflection. Figure 2 shows a comparison of the post-cut deflections in a cracked and an intact cut surface.

The effect of the crack in Figure 2 a) is primarily a steep rise of the outer crack face. Subtler effects are revealed by comparison

¹ NIST Center for Neutron Research, National Institute of Standards and Technology, Gaithersburg, MD 20899

² NHK International, Novi, MI 48377

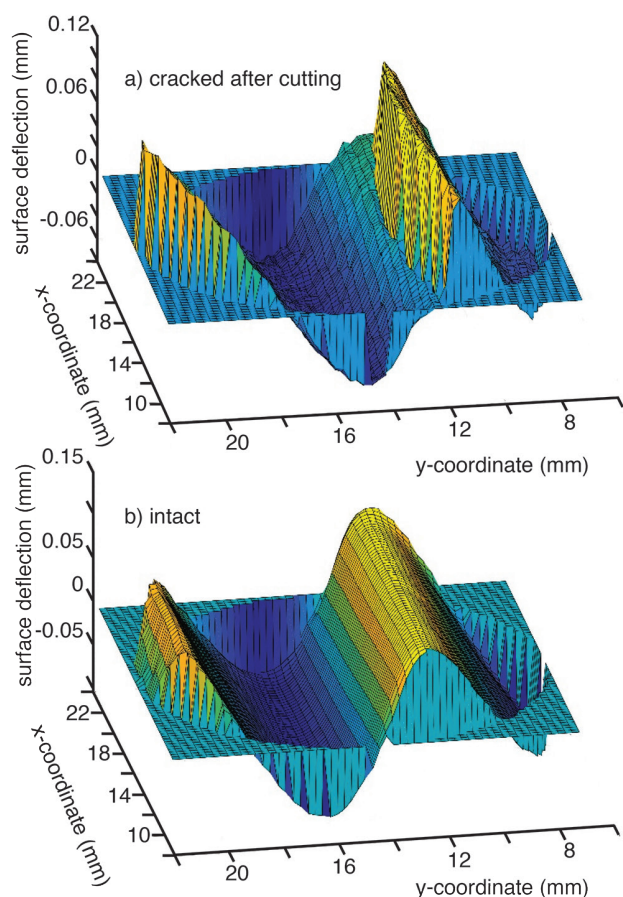


FIGURE 2: Post-cut deflection profile from stress relief in the tangential direction (see Figure 1 for coordinate directions and cut orientation).

with Figure 2 b): there is a drop in deflection in the inner crack edge and peak deflections overall are lower due to a partial reset/ lowering of the residual stresses after cracking. The sign of the deflections in in Figure 2 b) is opposite to the of the stresses causing the deflections; tensile stresses cause a contraction – i.e. a negative deflection - of the material as the line of the cut advances, and compressive stresses have the opposite effect. A recently published fracture mechanics approach [1] examined the role of residual stresses in springs with respect to crack propagation. The relationship between residual stresses and crack initiation remained unexplained, but it was found that two crack opening modes are operational: in Mode I crack opening is driven by stresses normal to the average crack plane; in Mode II the propagation is promoted by shear stresses in the crack plane. Translated in the coordinate system of the spring (Figure 1) a tensile radial stress component would drive Mode I crack opening while Mode II is driven by any positive or negative tangential-radial shear component. Neutron stress measurements show that actual stress magnitudes vary (Figure 3) but both radial and shear peak stresses do not exceed

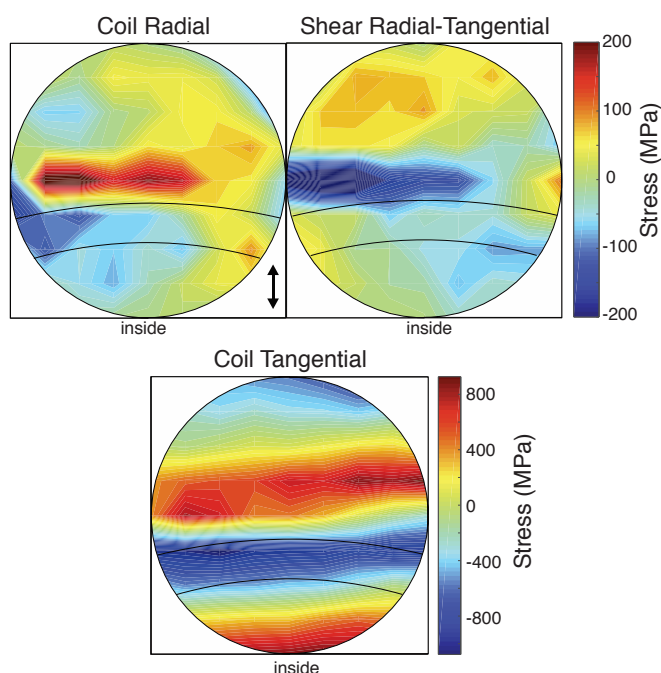


FIGURE 3: Cross-sectional distribution of selected stresses components. The direction of the shear component shown in the middle is perpendicular to the cross-section plane. The crack region is indicated by bands in the lower semicircle.

100 MPa in the crack prone region. Neutron results represent a lower limit estimate due to unavoidable spatial averaging within the neutron gauge volume (1.5 mm cube) which explains why peak stresses predicted by Finite Element simulations in [1] are significantly higher. It is tempting to correlate cracking with the very large compressive stresses in the tangential direction (Figure 3, right). However, in this case both sides of the crack are subjected to the same stress magnitude *parallel* to the crack direction, thus providing no contribution to crack opening.

The presence of stresses that promote opening and propagation of cracks occurring between production steps was confirmed in this work, with predictions showing stresses that are both highly localized and much higher in magnitude compared to neutron diffraction results. Further validation of the simulations is the subject of ongoing research. First results indicate that spatial resolutions of ≤ 0.5 mm are necessary to capture peak stresses adequately, requiring significantly longer counting. However, the results of the measurements shown in Figure 3 also show that complete areal mapping of stresses can be avoided and be replaced by high resolution scans along the line from the inside to the outside of the spring.

Reference

- [1] Y. Prawoto, S. Manville, T. Sakai, et al. J Fail. Anal. and Preven. **19**, 738 (2019).

Solvent-pore interactions in Eagle Ford shale by ultra and small-angle neutron scattering

J. McFarlane,¹ L. M. Anovitz,¹ V. H. DiStefano,^{1,2} A. G. Stack,¹ E. Perfect,³ D. F. R. Mildner,⁴ M. Bleuel,⁴ S. J. Chipera,⁵ K. C. Littrell,¹ M. C. Cheshire,¹ and K. E. Manz²

The interaction of fluids with porous materials is of interest for many applications including extraction of hydrocarbons from shales. In the field, shale fracturing can be done with pressurized water, hydrocarbons, or gases, depending on the depth and mineralogy of the formation. Although the technology is mature, the process is not well understood, leading to inefficiencies in fluid usage during fracturing and decreases in hydrocarbon production over time. In this study, we examined the effect of organic solvents and acidic aqueous solutions on rock porosity using small and ultra-small angle neutron scattering (U)SANS. The extracted material was analyzed by gas chromatography-mass spectrometry (GC-MS) to determine if there is a correlation between the type of organic extracted, shale maturity, and how the extraction process affected porosity.

Chesapeake Energy Corporation provided six cores taken from the Eagle Ford Shale formation as shown in Figure 1 [1]. Five slices from each, cut perpendicularly to bedding to minimize variation, were soaked for ≈ 2 weeks in one of five solvents: toluene, cyclohexane, methanol, dichloromethane, or 0.01 mol/L HCl (pH = 2). Total ion chromatograms from GC-MS were used to quantify and compare the amount of organic matter extracted from each sample. Chromatograms of specific ion masses were used to identify classes of chemical compounds: linear alkanes by the mass/charge $m/z = 57$ for $C_4H_9^+$ and aromatic compounds by $m/z = 77$ for $C_6H_5^+$. Most of the hydrocarbons extracted were n-alkanes, (nC_{11} to nC_{31}), although significant amounts of branched alkanes and aromatics were observed. The molecular weight distribution of the extracted hydrocarbons changed with the solvent. Methanol mostly dissolved light alkanes and extracted the smallest overall amount of hydrocarbon because it has the lowest compatibility with the organic matter. The other organic solvents—dichloromethane, toluene, and cyclohexane—all extracted similar amounts of organic matter, although toluene and cyclohexane extracted more aromatics and dichloromethane extracted more branched alkanes. The only aqueous solvent tested, HCl, surprisingly extracted the longest alkane chains, possibly because physical dissolution of carbonate minerals liberated heavier organics. Lighter

hydrocarbons were not extracted with HCl, suggesting the acid could not penetrate the hydrophobic bitumen and kerogen. Overall, the amount of extracted material correlated with the amount of total organic carbon present.

The porosity of the shale samples in the 1 nm to 20 μm range was analyzed by (U)SANS. Porosity was determined assuming a two-phase system and that scattering primarily occurs at the pore/mineral interface [2]. Because neutron scattering length density (SLD) of organic matter declines with decreasing carbon-to-hydrogen ratios, empty pores and pores filled with alkanes contribute similarly to scattering [3]. More complex organic matter has increasingly larger SLDs, behaving more like the rock matrix. Hence, the apparent porosity determined by (U)SANS includes pores filled with alkanes and aromatics. It is clear from Figure 2 that most of the change in porosity, as well as the reduction in asymmetry, occurs at low maturities – in this case between about 0.56 and 0.77 – although the reduction in asymmetry is much less in clay-rich than in carbonate-rich samples. At higher maturities there is little observable trend in porosity with maturity [4].

The mineral composition of the shale plays an important role in the total porosity. We found a positive correlation between the total porosity and the percentage of clay, pyrite, and total organic carbon. The distribution of pore sizes was bimodal in all samples in the range examined, which is typical for shale. The number distribution of smaller diameter pores (maximum 3 nm to 7 nm) corresponds to the percentage of clays, in agreement with the literature [5]. There were far fewer larger pores but, volumetrically, they contribute a large fraction of the total porosity.

Significant changes were observed in the cumulative porosities of the shale samples after solvent contact. Total cumulative porosity decreased with extraction across all solvents for clay-rich samples (Figure 3), with the greatest decrease attributed to dichloromethane. Organic extraction in carbonate-rich samples increased total porosity in some samples and decreased it in others. A positive correlation between the amount of organic matter extracted and the initial sample porosity may indicate that initial pore accessibility can affect hydrocarbon extraction.

¹ Oak Ridge National Laboratory, Oak Ridge, TN 37830

² Breddesen Center, University of Tennessee, Knoxville, TN 37996

³ Department of Earth and Planetary Science, University of Tennessee, Knoxville, TN 37996

⁴ NIST Center for Neutron Research, National Institute of Standards and Technology, Gaithersburg, MD 20899

⁵ Chesapeake Energy, Oklahoma City, OK 73154

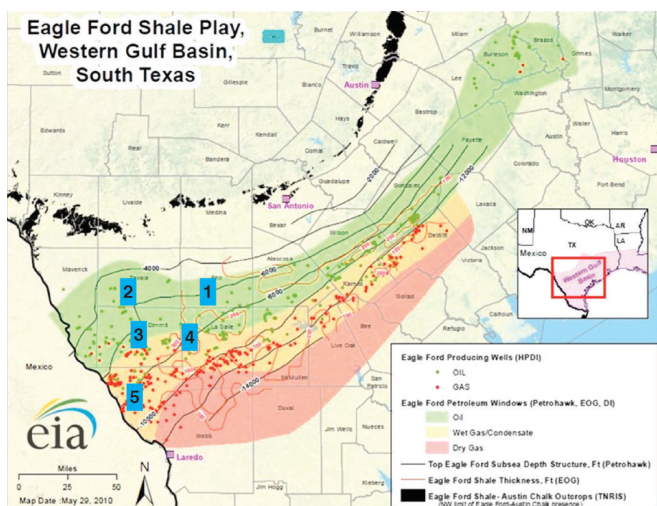


FIGURE 1: Collection sites for sample cores. ([Maps of oil and gas exploration, resources, and production from the US Energy Information Administration, 9-30-2011.](#))

Solvent-pore interactions (solvent-clay or solvent-kerogen) were considered to see if they could explain the significant changes, primarily decreases, in porosity after extraction. The pore structure may be affected by a number of chemical and physical solvent/matrix interactions, including reactions between the clay mineral interfaces, trapped hydrocarbons, and solvents [6]. Smectite layers in clay minerals can expand by exchange of interlayer cations due to intercalation of water or other fluids [7]. Acids like HCl can provide a hydrogen ion for that exchange. To a lesser extent, organic solvents have also been demonstrated to expand clay layers [6]. However, by this mechanism HCl should have caused the greatest decrease in porosity from water intercalation and cation exchange and this was not observed, so a different mechanism caused the pore volume decrease.

Kerogen swelling may also have caused some of the pore volume changes. Kerogen is a complex polymeric material based on a lattice of polyaromatic hydrocarbons. It can swell extensively when immersed in organic solvents. Hence, the measured change in porosity from the solvent contact was compared to its solubility parameter. The largest effect was observed at 20 MPa^{0.5}, which is close to a previously reported solubility parameter of kerogen (19.43 MPa^{0.5}) [8]. This suggests that kerogen swelling was the likely cause of the porosity decrease. The decrease in porosity in the samples contacted with HCl was not adequately explained by either clay-layer expansion or kerogen swelling, but kerogen swelling may have been offset by carbonate dissolution.

This study had the goal of investigating changes in porosity as a consequence of the extraction of organic matter from shale minerals using organic and acidic solvents. (U)SANS measurements showed that mineralogy, rather than maturity, controlled the measured total porosity in these Eagle Ford shales. Porosity distributions and total porosity in extracted shale samples were compared to samples from the same formations that had not been contacted with fluids. There was

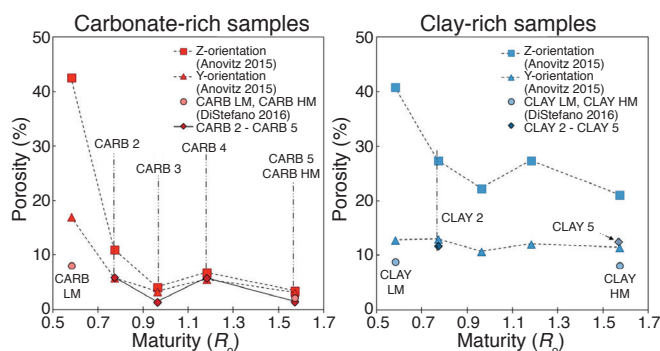


FIGURE 2: Porosity as a function of maturity, determined for carbonate- and clay-rich samples, with Y-orientation parallel to bedding, and Z-orientation perpendicular to bedding.

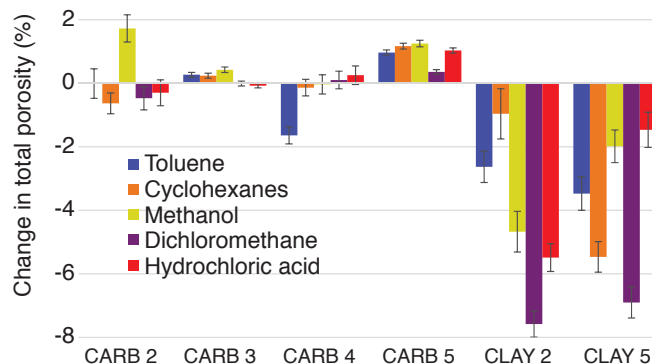


FIGURE 3: Effect of extraction of hydrocarbons on total porosity.

a positive correlation between initial porosity and the extraction of alkanes and aromatics, likely arising from the number and type of pores in the shale samples. A decrease in porosity with extraction is thought to have primarily arisen from kerogen swelling upon exposure to organic solvent(s). The extraction of hydrocarbons with exposure to HCl probably arose from the dissolution of carbonate minerals in the acid. These results contribute to our understanding of the fluid-rock interactions affecting the efficiency of oil and gas extraction.

References

- [1] V. H. DiStefano, et al., *Fuel* **238**, 298 (2018).
- [2] A. P. Radliński, *Rev. Mineral. Geochem., Neutron Scattering in Earth Sciences*, 363–397, (2006).
- [3] A. Radlinski, A. Hinde, *Neutron News*, **13**(2), (2002).
- [4] L. M. Anovitz, et al., *Interpretation*, **5**(3), SU59-SU70 (2015).
- [5] U. Kuila, et al., *Fuel*, **135**, 359 (2014).
- [6] M. Kowalska, H. Guler, D. L. Cocke, *Sci. Total Environ.* **141**, 223 (1994).
- [7] S. Aldridge, A. J. Downs, *The group 13 metals aluminum, gallium, indium and thallium: Chemical patterns and peculiarities*. John Wiley & Sons, (2011).
- [8] L. Ballice, *Fuel*, **82**(11), 1317 (2003).

The very small-angle neutron scattering (VSANS) instrument

J. G. Barker,¹ J. J. Moyer,¹ D. Adler,¹ L. Wroten,¹ C. Wrenn,¹ D. Pierce,¹ G. Jensen,^{1,2} C. Gagnon,^{1,3} S. R. Kline,¹ J. Chabot,¹ T. Thai,¹ A. Malone,¹ B. Dickerson,¹ N. Maliszewskyj,¹ C. Parikh,^{1,2} N. Shmunis,^{1,2} S. Pheiffer,¹ D. Ogg,¹ D. W. Ogg,¹ M. Rinehart,¹ S. Mullendore,¹ D. Johnson,¹ and C. J. Glinka^{1,2}

The new 48-m VSANS (Very Small Angle Neutron Scattering) instrument is now a fully subscribed member of the CHRNS instrument suite. New design features of the instrument expand the capabilities of our two 30 m SANS instruments. The minimum momentum transfer q is reduced by a factor of up to five by utilizing a higher resolution (1 mm) detector. Meanwhile, new optics increase beam intensity by a factor of 100-fold to 4,000-fold over standard pinhole collimation when using these collimation conditions. Expanding from one to nine 2D detectors placed on three carriages instead of one greatly expands the range of scattering angles from a single measurement. Typical experiments now measure a larger range of scattering angles. The ratio of the maximum to minimum angles is now 130, a factor of seven larger than that obtained on 30 m SANS instruments.

VSANS also has the ability to adjust the wavelength resolution to better match the needs of the experiment. For typical SANS instruments a neutron velocity selector (NVS) is used to choose the range of wavelengths. For VSANS the full-width-half-maximum (fwhm) of the NVS spectrum is 12.5 % of the mean wavelength. As an option to provide higher resolution, two reflections from highly oriented pyrolytic graphite (HOPG) crystals reduce the fwhm to 1 %. Alternatively, the wavelength resolution can be relaxed to increase the beam intensity through the use of filters to limit the white beam produced by the cold source to a range of 4 Å to 8 Å. A polycrystalline Be filter removes wavelengths shorter than 4 Å, and an "X" shaped supermirror insert removes wavelengths longer than 8 Å. This filtered white beam has four times the intensity produced using the NVS of the same mean wavelength of 5.3 Å, as shown in Figure 1.

The front and middle carriages use four 2D detectors composed of arrays of 8 mm diameter linear position-sensitive tube detectors. Each tube can measure count rates similar to that allowed on the entire 2D detector on the 30 m SANS. Thus, VSANS count rates now can be 100 times higher. The positions of the detector arrays are adjustable such that a center square opening allows the smaller scattering angles to pass downstream to the next carriage. Typically, the front carriage is placed at a distance one fifth of the middle carriage, thus increasing the maximum scattering angle by a factor of five. The four panels

generally cover 100 cm x 100 cm area, which is 50 % wider than the 65 cm x 65 cm detector used on the 30 m SANS instruments. This expanded angular range allows measurements of samples that are changing with time without having to measure with more than one set of detector distances.

By simultaneously increasing the sample-to-detector distance, sample aperture and beam stop sizes, the beam intensity can be increased by up to a factor of six over current practice on the 30 m SANS instruments. To take advantage of this possibility, a new version of our demountable liquid cells has been implemented with an increased sample size but with the same outer profile as the cells currently used in our existing temperature control blocks. Then, increasing the beam stop size from 50 mm to 100 mm, the sample aperture size from 13 mm to 22 mm diameter, and doubling the detector distance, the beam current for the same q_{\min} can be tripled. The larger beam stop size also doubles the contribution of gravity to the q -resolution, but the insertion of prisms eliminates the effect of gravity.

The rear carriage uses a $^6\text{LiF-ZnS(Ag)}$ scintillation screen to convert the neutron to a burst of light that is then intensified and its position detected via three charge coupled detectors (CCD). The position of the neutron is detected to an accuracy of 0.9 mm fwhm using the rear detector. This rear carriage has three small beam stops: 12 mm diameter for converging beam collimation, and 6 mm and 12 mm wide by 300 mm tall rectangular beam stops used with narrow slit collimation.

The converging beam refractive lens optics used on VSANS achieves a minimum q of $2.6 \times 10^{-4} \text{ Å}^{-1}$, a factor of three smaller than can be realized using lenses on the 30 m SANS instruments, thus enabling measuring objects three times larger. The new optics has nearly equal pathlengths of 24 m before and after the sample using a 6.7 Å wavelength beam that is blocked by a 12 mm diameter beam stop. Using standard pinhole collimation, the source and sample aperture diameters would be 6 mm and 3 mm, respectively. By using refractive lenses to focus the beam, the sample aperture is enlarged to 10.4 mm, increasing the beam intensity by a factor of $(10.4/3.0)^2 = 12$. By inserting a series of intermediate masks, twelve separate beams are defined. Inserting refractive prisms after the lenses corrects the parabolic trajectory of the neutron beam,

¹ NIST Center for Neutron Research, National Institute of Standards and Technology, Gaithersburg, MD 20899

² University of Delaware, Newark, DE 19716

³ University of Maryland, College Park, MD 20742

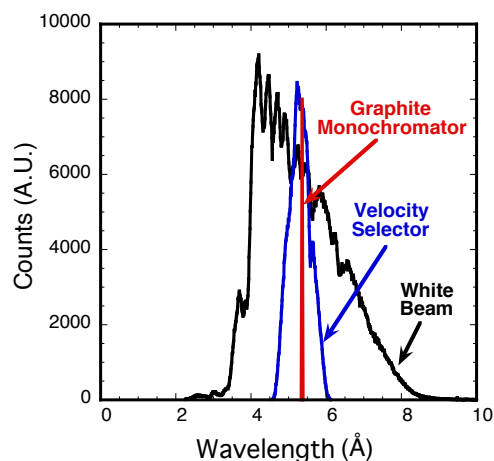


FIGURE 1: Time of flight (TOF) spectrum for the three wavelength resolution options. The blue curve is obtained using a NVS with rotation speed chosen to produce a mean wavelength of 5.3 Å. The black curve is the spectrum from the filtered white beam. The red curve is a calculated spectrum for the HOPG monochromator. The beam intensity is proportional to the area under the curve.

allowing all 12 beams to converge to the same spot on the detector. To minimize attenuation of the beam from phonon scattering, the prisms are cooled to 155 K. The observed gain in beam intensity using 12 beams versus pinhole collimation is 120 after correcting for lens and prism attenuation. A new larger demountable liquid cell and temperature-controlled sample blocks are now being designed to take full advantage of this option.

Narrow slit collimation is obtained using two motorized XY slits where the width and height of a rectangular aperture is adjustable over the full width and height of the incoming neutron guide which has a width of 60 mm and a height of 150 mm. These two slits can be adjusted to produce a narrow beam at the rear detector with a width smaller than the smallest 6 mm wide beam stop. Using 6 Å wavelength, a source aperture that is 2.5 mm wide by 150 mm tall and sample aperture that is 1.25 mm wide by 75 mm tall, the measured beam intensity is 31,000 s⁻¹. An additional factor of four increase in beam intensity is achieved by using the filtered white beam wavelength option. The measured parasitic background outside the beam stop was 91 s⁻¹. Test scattering measurements have been made to $q_{\min} = 1.5 \times 10^{-4} \text{ Å}^{-1}$. Commonly available quartz capillaries of 2 mm diameter can be used for liquid cell holders.

Polarized beam experiments are also possible at VSANS. In fact, several improvements have been made to the beam polarization compared to the NG7 30 m SANS instrument providing flipping ratios of up to 300. Mathematical simulations of beam depolarization caused by instrument magnetization profile led to redesigning of the permanent magnet and soft steel structures surrounding the double V shaped polarizing super mirror insert before the source aperture and the RF coil located upstream of the sample. The redesign minimized nonuniformity of magnetic field lines in the beam area which was causing beam depolarization in the simulations. The beam

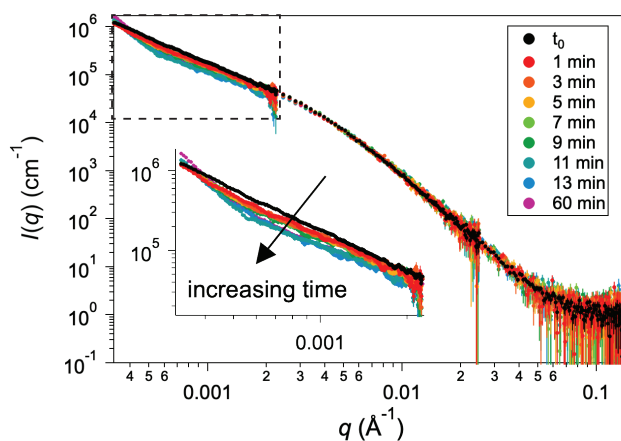


FIGURE 2: Transient structural evolution measured for a sheared sample of Vulcan XC-72 carbon black suspended in propylene carbonate.

polarization at the sample position is now measured to be 99.3 % with a measured flipping efficiency of the RF flipper approaching 100 % within our measurement capability of ± 0.0003 . The large 2 m long sample area allows room for a ³He spin filter downstream of the sample. Several experiments have been performed at VSANS, measuring all four polarization scattering cross-sections.

As an example of the capabilities of VSANS, the structural evolution of a sheared carbon black sample was measured using four converging beams and the high-resolution detector on VSANS [1]. The structure of carbon black suspensions play a pivotal role in the design and processing of electrode formulations used in electrochemical energy storage applications. Unfortunately, this structural evolution occurs at length scales too large for typical SANS experiments and time scales too short for USANS experiments. However, VSANS, with its lower attainable q -range and high neutron flux, provides a unique measurement of these structural changes under shear. VSANS data (Figure 2) shows the transient densification of carbon black agglomerates that occurs at low shear rates, as evidenced by a decrease in intensity at low q . This densification is related to a time-dependent decrease in both the viscosity and electrical conductivity of the suspension. Therefore, the combination of this time-dependent VSANS data and steady-state USANS data provides useful information for understanding the microstructural origin of the transient properties of carbon black suspensions.

Nearly all of the experiments in the last year utilized at least one of the new capabilities provided by the new instrument. Further developments in the next year will concentrate on constructing and modifying sample environment equipment to permit routine user experiments that take full advantage of the higher beam intensity collimation options available on VSANS.

Reference

- [1] J. B. Hipp, J. J. Richards, N. J. Wagner, *in preparation*, (2019).

Structure-property-processing relationships of soft viscoelastic materials

J. C.-W Lee,¹ K. M. Weigandt,² E. G. Kelley,² and S. A. Rogers¹

To design the next generation of ‘smart’ soft materials, researchers must first understand how rapidly-changing flow conditions affect model materials. Soft viscoelastic materials, such as synthetic and biological polymers, tend to generate complex material responses. The link between macroscopic flow and molecular-level microstructural rearrangements has long been sought but has remained elusive. We show, by experimentally combining new rheological techniques with time-resolved rheo-small-angle neutron scattering (rheo-SANS), such links can now be made, forming nonlinear structure-property-processing relations, by considering the evolution of the recoverable component of the strain [1].

Oscillatory shearing has been widely used to study a wide array of soft materials. In particular, rapidly-changing flow conditions that are often encountered in processing and manufacturing soft materials can be accurately simulated by large amplitude oscillatory shear (LAOS) because of the independent control of length and time scales it affords. As such, LAOS has been commonly employed as a model transient flow protocol capable of eliciting nonlinear responses. In spite of the wide adoption of LAOS, the underlying physics and resulting structural rearrangements have remained difficult to interpret [2]. In a recent study, we show that the recoverable strain, a rheological metric first proposed by Weissenberg [3] and Reiner [4], is a key to understanding oscillatory shear rheology, in not only complex macroscopic responses such as shear and normal stresses, but also in how the microstructure reacts to dynamic flows.

We investigate two distinct polymeric materials, including an industrial entangled worm-like micelle (WLM) solution and a fibrin network. The LAOS responses from WLMs across a wide range of amplitudes at a normalized frequency (Deborah number) of 0.25 are presented in Fig. 1. Traditionally, the stress response is plotted against the shear strain (Fig. 1(a)) or shear rate (Fig. 1(c)), forming the so-called elastic and viscous Lissajous curves. The distorted ellipses and the secondary loops are typical features of LAOS in these presentations. These presentations, however, view the responses from the perspective that the reference state remains fixed at zero strain, and ignores the fact that the reference state (or “ground state” originally referred by Weissenberg [3]) can be shifted by external flow conditions.

Strain can be experimentally decomposed into recoverable and unrecoverable components by unloading stresses. Recoverable strain is elastic, while viscous properties are dictated by the rate at which strain is acquired unrecoverably. The natural presentation to display elastic and viscous responses is therefore stress versus recoverable strain (Fig. 1(b)) and stress versus unrecoverable strain rate (Fig. 1(d)). Significant differences are observed from the traditional Lissajous curves. The curves collapse into a straight line at small strains and rates, where the slopes naturally correspond to the plateau modulus (Fig. 1(b)) and zero-shear viscosity (Fig. 1(d)) of the WLMs, which are traditionally thought not determinable from a single LAOS test. Further, the instant when the total strain is maximal (star in Fig. 1(a)), which is traditionally considered to be the most-strained state, actually corresponds to the point of zero recoverable strain, indicating there is little-to-no deformation from a microscopic perspective. This finding explains the origin of observations made in numerous studies of colloidal and polymeric materials, where researchers have noted the existence of linear elasticity close to total strain extrema (See [1] for references). In short, in these new experiments and their associated proposed presentations, LAOS naturally presents a sequence of physical processes: linear viscoelasticity (LVE) is observed when the recoverable strain is small, softening and thinning with larger recoverable strains and higher unrecoverable strain rates, followed by a recoil process that returns the material to the original state. The same sequence occurs twice per oscillation, as the materials respond to shearing in a symmetric manner.

While the macroscopic physics is more clearly discerned by recovery-based rheology, we complete the structure-property relationship using time-resolved SANS to monitor the microstructural evolution. Shown in Fig. 2(a) is the stress versus recoverable strain with a color scale reflecting the degree of alignment observed in the 2D SANS patterns in Fig. 2(b). Given that a natural state of the entangled micellar system is isotropic, aligning the micellar segments is entropically unfavorable, leading to a macroscopic elastic response. The alignment factors in the velocity-gradient (1-2) and velocity-vorticity (1-3) planes are presented as functions of recoverable strain in Fig. 2(c) and Fig. 2(d), where a linear proportionality with a constant prefactor is manifested. A clear physical picture therefore emerges. When

¹ University of Illinois at Urbana-Champaign, IL 61801

² NIST Center for Neutron Research, National Institute of Standards and Technology, Gaithersburg, MD 20899

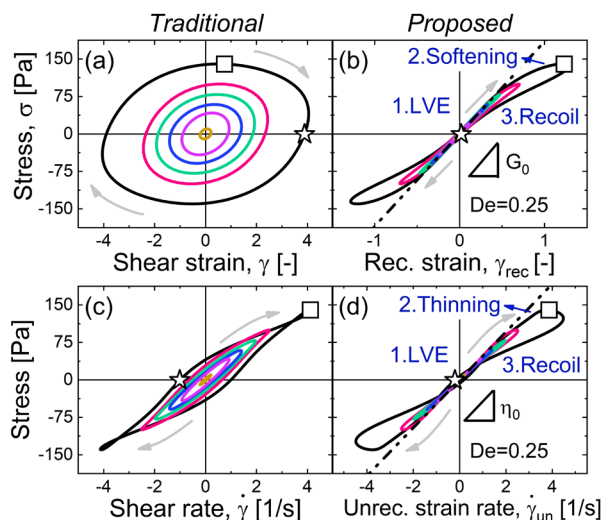


FIGURE 1: LAOS results presented in the traditional (σ - γ , σ - $\dot{\gamma}$) and proposed (σ - γ_{rec} , σ - $\dot{\gamma}_{\text{un}}$) frames from WLMs. The lines in the proposed elastic and viscous views have slopes equal to the plateau modulus $G_0 = 180$ Pa and the zero-shear viscosity $\eta_0 = 48$ Pa·s. The stars and squares correspond to zero and maximum recoverable strain at the largest amplitude, respectively.

the recoverable strain is small, linear viscoelastic responses are seen, even under LAOS, and we observe an isotropic scattering pattern that is identical to equilibrium conditions with no alignment. As the magnitude of the recoverable strain increases, so too does the alignment factor. Even when the modulus begins to drop at large recoverable strains (points ii and iv in Fig. 2(a)), the alignment is still linearly dependent on the magnitude of the recoverable strain.

In summary, we have provided key insights into the understanding of dynamic flows and how molecular-level structure reacts during changing flows. We have shown that, by monitoring the evolution of the recoverable component of strain, the material physics under dynamic flows can be identified as a sequence of processes. Combining with experimental evidence from neutron scattering, we have established structure-property-processing relationships, providing new design criteria for soft materials. Armed with such new understandings, researchers now have a clearer path for developing advanced materials for a variety of biomedical, industrial and environmental applications.

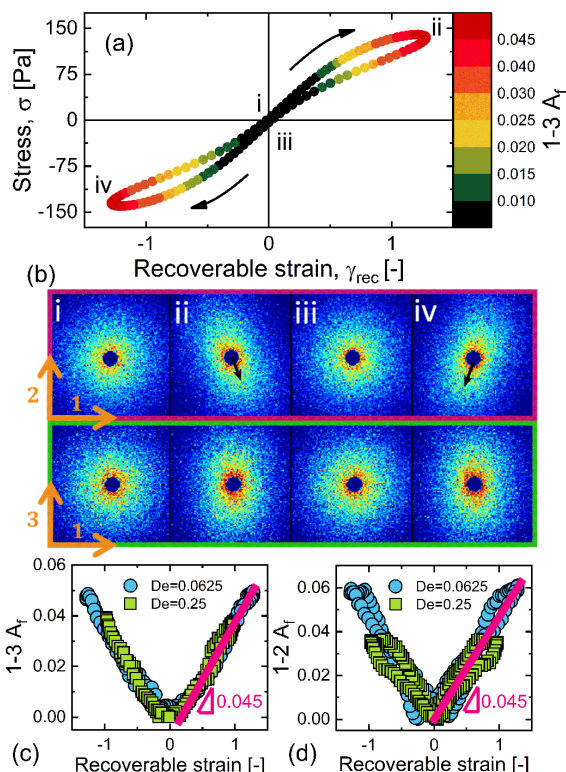


FIGURE 2: Correlation between macroscopic rheology and microscopic structure. (a) Proposed elastic Lissajous figure (σ - γ_{rec}) coupled with 1-3 alignment factor A_t denoted by the color scale. (b) 2D SANS patterns at zero (i and iii) and maximum (ii and iv) recoverable strain in both velocity-gradient and velocity-vorticity planes. Alignment factors in the 1-3 (c) and 1-2 (d) planes are plotted as functions of the recoverable strain, showing the same proportionality constant of 0.045.

References

- [1] J. C.-W. Lee, K. M. Weigandt, E. G. Kelley, S. A. Rogers, *Phys. Rev. Lett.* **122**, 248003 (2019).
- [2] S. Rogers, *Phys. Today* **71**, 34 (2018).
- [3] K. Weissenberg, *Nature* **159**, 310 (1947).
- [4] M. Reiner, in *Encycl. Phys. VI* (Springer-Verlag Berlin Heidelberg, 1958), pp. 435–549.

Segmental diffusion in attractive polymer nanocomposites: A quasi-elastic neutron scattering study

E. J. Bailey,¹ P. J. Griffin,¹ M. Tyagi,^{2,3} and K. I. Winey¹

The addition of nanoparticles (NPs) to a polymer matrix, forming a polymer nanocomposite (PNC), can significantly enhance the thermal, mechanical, and functional properties of the host matrix. As a result, PNCs are appealing materials for a variety of fields, industries, and applications [1]. The dynamics of polymer segments are particularly important because they significantly influence or dictate the processability, applications, glass transition temperature (T_g), and various macroscopic properties (such as creep, toughness, and transport) of the PNC. Despite decades of research on various PNC systems, additional fundamental studies are needed to explore the complex parameter space and understand the underlying physics of interfacial and confined polymer dynamics. In this work, we use quasi-elastic neutron scattering (QENS) and temperature modulated differential scanning calorimetry to present a systematic and detailed study of segmental dynamics in highly attractive polymer nanocomposites comprised of poly(2-vinyl pyridine) (P2VP) and colloidal silica (SiO_2) NPs as a function of temperature, NP concentration, and P2VP molecular weight.

There are several methods that can be used to analyze segmental dynamics including nuclear magnetic resonance (NMR), dynamic mechanical analysis (DMA), broadband dielectric spectroscopy (BDS), temperature-modulated differential scanning calorimetry (TMDSC), neutron spin echo (NSE), and quasi-elastic neutron scattering (QENS) [2]. The approximate timescales associated with many of these measurement techniques, as they pertain to segmental dynamics, are schematically represented in Figure 1 with measurements of neat P2VP and a global fit to Vogel-Fulcher-Tammann (VFT) temperature dependence. QENS, the focus of this paper, has the advantage of spanning short time scales (≈ 1 ns), providing simultaneous temporal and spatial information to capture the timescales and geometries of measured segmental motions, and measuring the fraction of relaxing segments through the elastic incoherent structure factor.

First, by monitoring the elastic scattering intensity in a fixed window scan (FWS) as a function of temperature, the mean-squared displacement ($\langle x^2 \rangle$) of P2VP segments was found to decrease for all $T > T_g$ as a function of NP concentration (Figure 2a). Similar results were observed by analysis of the QENS spectra for $T \gg T_g$. Specifically, we observe the full-width at

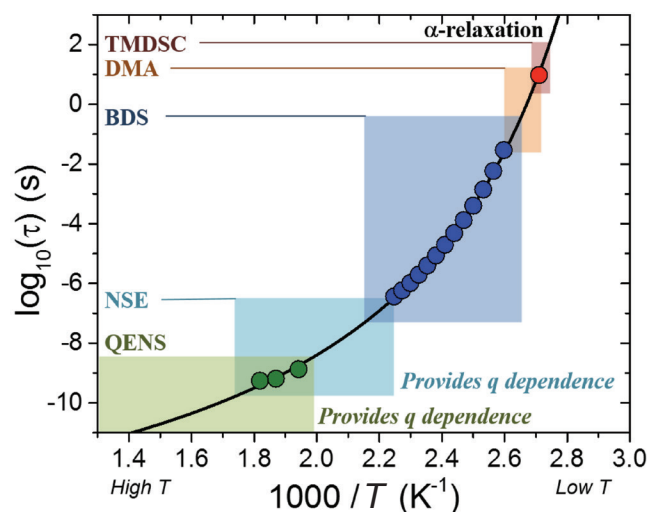


FIGURE 1: Primary segmental relaxation times (α -process) of bulk P2VP measured via TMDSC (red circle), BDS (blue circle), and QENS (green circle). Approximate time scales for five techniques, and their corresponding temperatures, are depicted by shaded regions along the relaxation curve.

half max (FWHM) of quasi-elastic broadening increases linearly as a function of q^2 for all NP concentrations, which is indicative of translational diffusive motion over these length and time scales (≈ 1 nm and ≈ 1 ns). The extracted diffusion coefficient of the alpha process (D_α) obtained from this simple model ($\text{FWHM} \sim D_\alpha q^2$) is plotted as a function of inverse temperature in Figure 2b, and the relaxation time for neat P2VP aligns with extrapolations from BDS and TMDSC measurements (Figure 1). However, as attractive SiO_2 NPs are added to the polymer matrix, D_α is slower than bulk by as much 80% at NP concentrations of ≈ 50 vol%, and despite the slowed timescale, the temperature dependence remains largely unchanged (Figure 2b). A similar q -dependence of FWHM with a simultaneous slowing of mobility indicates that segmental dynamics in PNCs are perturbed much more temporally than spatially, i.e. the segmental relaxation process is slowed but segments relax in a similar manner. Interestingly, all polymer segments in the 50 vol% PNC are in close proximity to a NP surface because the interparticle distance is ≈ 2.5 nm. Thus, our measurement of segmental relaxations shows that interfacial segments are dynamically active, albeit slowed, at these high temperatures.

¹ University of Pennsylvania, Philadelphia, PA 19104

² NIST Center for Neutron Research, National Institute of Standards and Technology, Gaithersburg, MD 20899

³ University of Maryland, College Park, MD 20742

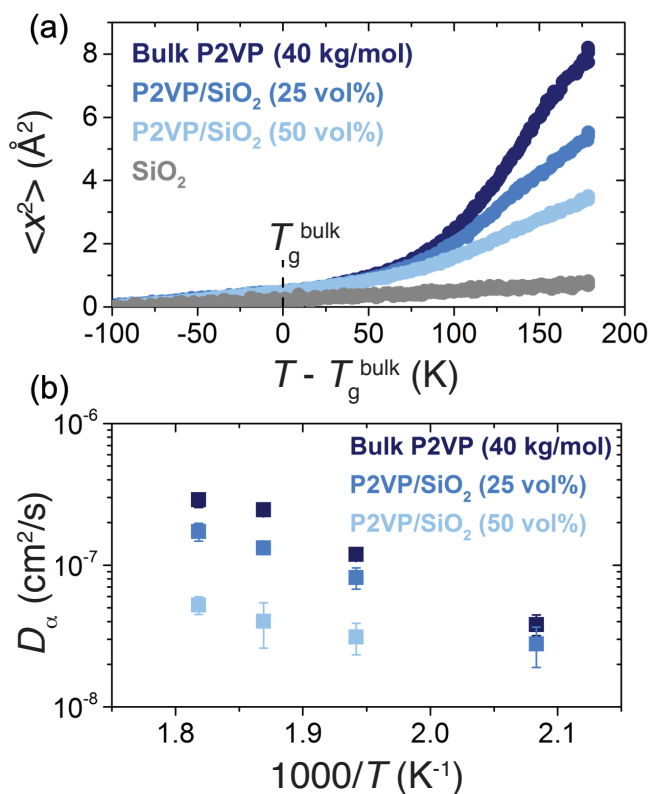


FIGURE 2: (a) Average segmental mean-squared displacement ($\langle x^2 \rangle$) obtained from FWS of bulk 40 kg/mol P2VP and P2VP/SiO₂ PNCs with concentrations of 25 vol% and 50 vol%. (b) Extracted segmental diffusion coefficient (D_α) as a function of inverse temperature for neat polymer and PNCs.

We next probe the effect of P2VP molecular weight on segmental dynamics in PNCs by studying P2VP/SiO₂ (25 vol% SiO₂) with unentangled to well entangled P2VP (10 kg/mol, 40 kg/mol, 190 kg/mol). All bulk and PNC materials exhibit classic characteristics of translational segmental diffusion ($\text{FWHM} \sim D_\alpha q^2$) that differ only in the associated timescale. In Figure 3, the extracted diffusion coefficient of the PNC is normalized to that of bulk to highlight the impact of molecular weight on segmental diffusion in PNCs. For all P2VP molecular weight, D_α in the PNC is reduced relative to neat P2VP by a factor of ≈ 2 , although a slight trend can be observed where NPs are more impactful in lower molecular weight P2VP. In contrast, a strong molecular weight dependence on segmental dynamics has been observed in P2VP/SiO₂ PNCs using BDS and TMDSC [3]. However, not only do these techniques probe and sample segmental dynamics differently, QENS measurements are at much higher temperatures which may indicate that the interfacial structure and dynamics have a strong temperature dependence or may indicate an existence of an equilibrium structure that other techniques do not access [2].

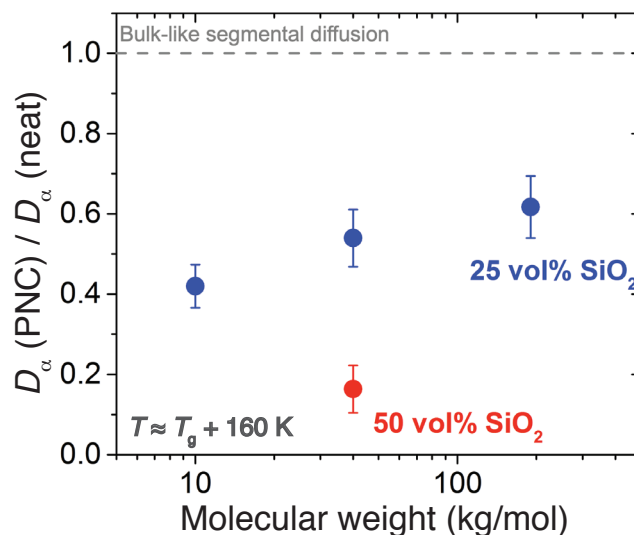


FIGURE 3: Diffusion coefficient of P2VP segments (D_α) in PNC normalized to D_α in neat P2VP as a function of polymer molecular weight for 25 vol% SiO₂ (blue) and 50 vol% SiO₂ (red).

In summary, we systematically study P2VP/SiO₂ PNCs using QENS as a function of NP concentration, temperature, and P2VP molecular weight and compare to measurements from other techniques (e.g. TMDSC and BDS). We show that motions of P2VP segments on ≈ 1 nm length scales and ≈ 1 ns time scales are well described by classic translational diffusion, even at NP concentrations of ≈ 50 vol% where the average interparticle spacing is ≈ 2.5 nm. The average segmental diffusion coefficient decreases with increasing NP concentration by up to a factor of ≈ 5 and is nearly independent of temperature over the studied temperature range. In contrast to the well-documented molecular weight dependence of segmental diffusion in the deeply supercooled regime, our measurements of the same dynamic process at higher temperatures show slowed segmental dynamics that are largely independent of matrix molecular weight [3]. Finally, by comparing TMDSC, BDS, and QENS, our results suggest that temperature has a significant impact on the NP-induced perturbation to segmental dynamics in PNCs and highlight the unique and complementary insights that can be provided by QENS.

References

- [1] S. K. Kumar et al., *Macromolecules* **50**, 714 (2017).
- [2] C. G. Robertson, C. M. Roland, *Rubber Chem. Technol.* **81**(3), 506 (2008).
- [3] S. Cheng et al., *Phys. Rev. Lett.* **116**(3) 1 (2016).

Electrolyte concentration dependence on electrode SEI formation revealed by *operando* SANS

C. J. Jafta,¹ X.-G. Sun,¹ G. M. Veith,¹ G. V. Jensen,² S. M. Mahurin,¹ M. P. Paranthaman,¹ S. Dai,¹ and C. A. Bridges¹

In recent years it has been shown that concentrated electrolytes can form a much more stable, conducting solid electrolyte interphase (SEI) as compared to traditional, more dilute electrolyte concentrations. The solid-electrolyte interface in electrochemical energy storage systems is critical for controlling both performance and safety. With this in mind, research related to the development of new electrolytes remains a key area of focus for battery researchers. It is a challenge to understand not only the differences in chemistry of the SEI with electrolyte formulation, but also the mechanism of SEI formation during cycling, and how this connects with the processes of cation intercalation and corresponding electrode microstructural changes. To address this challenge, the dynamic evolution of microstructure and surface chemistry for an ordered mesoporous carbon (OMC) electrode was probed during cycling using *operando* measurements on the NGB 30 small-angle neutron scattering (SANS) beamline [1]. Many different electrolytes have been developed, all with tradeoffs in viscosity, electrochemical stability and conductivity. The choice of salt and solvent for the electrolyte is similarly important, and the standard LiPF_6 salt and ethylene carbonate (EC) based solvent used in most commercial batteries is a compromise amongst other commercially available Li salts each with too many potential disadvantages, such as toxicity, an unstable or uneven passivation layer (SEI), or high corrosion of the current collector. Replacing LiPF_6 with $\text{LiN}(\text{SO}_2\text{CF}_3)_2$ (LiTFSI) can improve thermal and chemical stability of the electrolyte, but unfortunately result in corrosion of the cathode current collector (made of Al) at high voltages. In addition, replacing the standard EC-based solvent with propylene carbonate (PC) results in an electrolyte with better ionic conduction at room temperature, but the PC suffers from an inability to form a stable SEI and thus produces exfoliation of graphite in battery anodes. However, it has been shown that by increasing the salt concentration in electrolytes, Al corrosion and exfoliation of graphite is suppressed. It is reported that the salt in concentrated electrolytes are sacrificially reduced to form more stable passivation layers high in LiF content. These LiF based SEIs are superior in adhesion to the electrode surface, and thinner and denser with superior mechanical properties. Given the importance of the inorganic salt layer, a key question is therefore to understand how the concentration of LiTFSI, along with the increase in electrolyte viscosity, influences the formation of inorganic salt

products (i.e., LiF, LiOH) versus carbonaceous products in the SEI during the critical initial discharge cycle.

Given the sensitivity of neutron scattering to light elements (e.g., H, Li, C, F), SANS is a powerful technique to probe the formation of the SEI layer during battery discharging. In order to study the SEI evolution *operando*, a suitable neutron scattering battery cell has been designed, as shown in Figure 1, that provides minimal contribution to the scattering data, along with minimal absorption. Separate cells for dilute and concentrated LiTFSI/PC electrolytes on mesoporous hard carbon were simultaneously cycled on the beamline. The resulting data (Figure 2), demonstrate that *operando* SANS, in combination with ex-situ X-ray photoelectron spectroscopy (XPS), provides unprecedented detail on the concentration dependent filling of mesopores and micropores with Li-rich and carbonaceous products, co-intercalation of solvated Li^+ , and corresponding electrode microstructure expansion.

There are several key findings from this work derived from the SANS and supporting XPS data. SANS intensity changes indicate a displacement in the pore surface electrochemical processes to lower voltages, which is a physical effect related to pore filling – the filling of pores is shifted to lower voltages with the higher viscosity concentrated electrolyte, which can be influenced by the viscosity of the electrolyte and wetting of the surface. Moreover, the pore filling influences the expansion of the carbon framework,

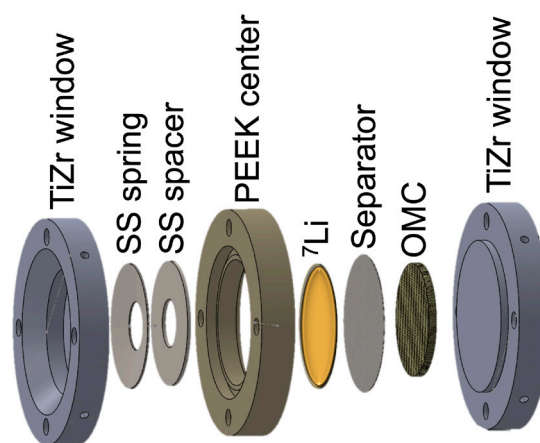


FIGURE 1: Schematic view of the *operando* SANS cell.

¹ Oak Ridge National Laboratory, Oak Ridge, TN 37831

² NIST Center for Neutron Research, National Institute of Standards and Technology, Gaithersburg, MD 20899

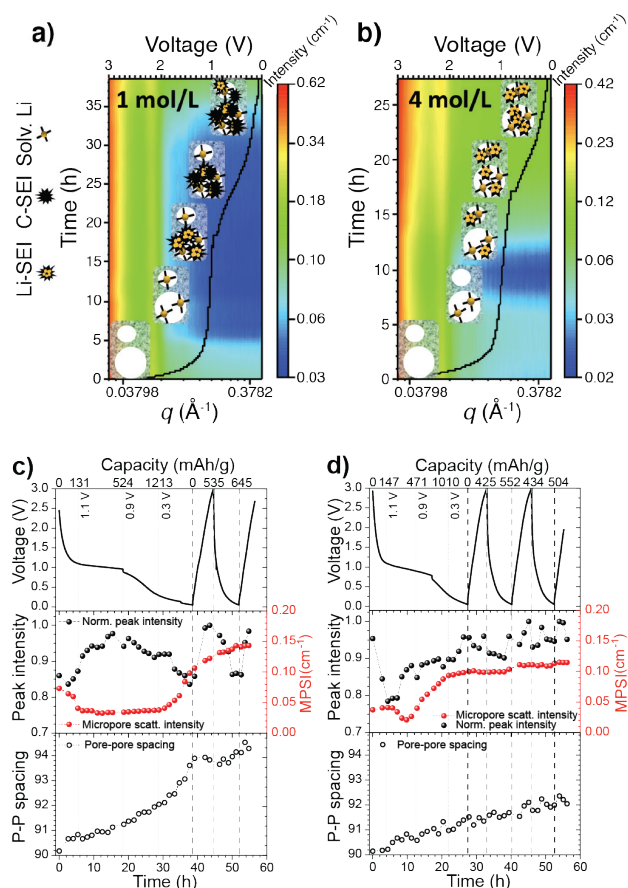


FIGURE 2: Scattering intensity is shown as a function of the scattering vector q , first discharge time and voltage for (a) the 1 mol/L and (b) 4 mol/L LiTFSI/PC (propylene carbonate) electrolyte systems. The development of carbonaceous and fluoride-rich reduction products in the SEI differs based on concentration as can be clearly seen from the extracted data for (c) the 1 mol/L and (d) 4 mol/L electrolyte systems.

with electrolyte concentration dependent results. The expansion occurs just below the open circuit voltage in the 1 mol/L cell and below 1.1 V in the 4 mol/L cell. The size of the solvation shell around Li^+ is found to influence the framework expansion during the first discharge, with the larger PC coordinated Li^+ in 1 mol/L electrolyte producing an overall 3.5 \AA ($\approx 4 \%$) increase in the

pore–pore separation as compared to the 1.4 \AA ($\approx 1.5 \%$) increase for the Li(PC)-TFSI aggregates. The overall change in framework volume during the discharge can be explained by the combination of pore filling and co-intercalation into graphitic layers, which are reflected in SANS intensity changes during *operando* cycling. Furthermore, the intensity changes can be correlated with the electrochemical discharge profile to provide more information on the mechanism of SEI formation (Figure 2(c, d)). Both the low and high concentration electrolytes show electrochemical double layer (EDL) formation by adsorption of solvated PC to the electrode surface. In the 1 mol/L electrolyte system it is known that the inner Helmholtz layer is dominated by free PC molecules and that of the 4 mol/L by salt anions. Despite the prevalence of PC in the inner Helmholtz layer of the 1 mol/L electrolyte system, the TFSI $^-$ anions present at the anode surface begin to reduce at a higher potential and at a faster rate as compared to the PC, due to the higher reduction potential of the TFSI $^-$ anions. We find that Li-rich salts (e.g., LiF, LiOH) form at higher voltages for the 1 mol/L electrolyte, but that in the sloping discharge region of 1.1 V to 0.9 V the salts begin to dominate the mesopore scattering for the 4 mol/L electrolyte, while carbonaceous products such as C–O and C–F containing compounds begin to dominate for the 1 mol/L electrolyte. By the end of the first discharge the 4 mol/L electrolyte has a passivation layer richer in low SLD Li-rich reduction products than the 1 mol/L electrolyte. Finally, with the subsequent charges and discharges PC or solvated PC is desorbed (charge) and adsorbed (discharge), which is shown to have significant reversibility in the mesopores but not in the micropores. As we have shown, *operando* SANS studies can provide knowledge about the dynamic cell chemistry that is microstructure specific in new candidate electrolyte systems for high-energy density batteries, which cannot be seen from other probes such as electrochemical cycling or XPS studies. This approach has the capability to impact a wide range of electrochemical systems, taking advantage of the unique contrast provided by neutron scattering.

References

- [1] C. J. Jafta, X.-G. Sun, G. M. Veith, G. V. Jensen, S. M. Mahurin, M. P. Paranthaman, S. Dai and C. A. Bridges, *Energy Environ. Sci.*, **12**, 1866 (2019).

Towards architecturally designed all-polymer based nanocomposites

E. Senses,¹ M. Tyagi,^{2,3} and A. Faraone²

Over the last few decades, advances in nanoparticle synthesis with precisely controlled size and shape have transformed the way we use polymers today. Dispersing these inorganic rigid nanoparticles in soft polymeric matrices resulted in new hybrid materials- *polymer nanocomposites*- with superior properties compared to those of the neat polymers [1]. Likewise, polymer chemists can now synthesize macromolecules with precise length and shape; stars, combs, bottlebrushes, rings, hyper-branched polymers have emerged with exciting new properties that cannot be provided by their linear chain analogs. In particular, the star-shaped polymers in which many linear chains share a common center are interesting as the monomer density changes along the radial direction. Therefore, these polymers can exhibit both soft/penetrable and hard/impenetrable sphere character depending on the length and number of the star arms (see schematic in Figure 1a).

In our work [2], we dispersed high- T_g (≈ 373 K) star-shaped polystyrene (PS) at 20 % by mass in low- T_g (≈ 250 K) linear long poly (vinyl methyl ether) (PVME) matrices to obtain a new kind of nanocomposite in which the interpenetration between the nanofillers and the matrix, and therefore, the bulk rheological properties, can be systematically varied via filler architecture. As the filler structure transitions from flexible linear chains to hard spheres, the resulting nanocomposites reside between the traditional linear polymer blends and conventional polymer nanocomposites- a region that has not been explored before. Our aim was to investigate these nanocomposites using static (SANS) and quasielastic neutron scattering (backscattering and spin-echo) measurements over a wide range of time and length scales in the glassy and melt states of the composites, and relate their bulk flow behavior to the microscopic relaxation mechanisms.

We used deuterated PS (d -PS) of various arm number and molecular weights to determine their conformation and dispersion in hydrogenated 20 kg/mol PVME (h -PVME) matrix by using small-angle neutron scattering (SANS). The coherent intensity results from the contrast between d - and h -chains, therefore, the stars are visible to neutrons. Figure 1b shows a peak appearing at intermediate wave-vectors, Q , in the SANS pattern of the 18-arms star shaped d -PS filler in h -PVME due

to intra-chain correlation, confirming their compact particle-like nature. A linear d -PS chains of the same total molar mass retains its flexible Gaussian coil structure in the miscible h -PVME matrix.

Particularly important for polymers are the localized fast dynamics on sub-monomer level, the segmental dynamics at the monomer level and the entangled/collective dynamics at larger scales. To obtain an overview on the chain motions over a time scale of ≈ 1 ns using the High-Flux Backscattering Spectrometer (HFBS), we first measured the temperature dependence of the elastic scattering intensity (within the 0.8 μ eV resolution of the instrument). The incoherent intensity is dominated by the h -PVME matrix. The PS fillers are essentially frozen in the time-scale of the neutron experiments, the mobile component is the matrix. Figure 2a compares the normalized elastic intensities, $I_e(Q,T)/I_e(Q,T=15\text{ K})$. Adding linear PS has a minority effect on sub- T_g dynamics of PVME, whereas the segmental dynamics is significantly slowed down above T_g due to increased monomeric friction due to the presence of frozen PS segments, as known from previous linear blend studies [3,4]. What we found different and interesting is that the 18-arms star PS significantly accelerated the localized dynamics of PVME below T_g , possibly due to additional free volume provided to the PVME chains by the free ends of the stars. This brings up exciting new opportunities for tuning glassy dynamics, which is important for high-strength applications.

The segmental dynamics of PVME in presence of PS fillers with different architectures were measured by quasi-elastic neutron scattering (QENS) measurements on HFBS. The quasi-elastic broadening at low- Q is related to thermally driven Rouse motion of the chain segments, which is determined by the local monomeric friction. We found that PS chains slow down the Rouse relaxation of PVME; however, unlike the localized sub- T_g dynamics, the monomeric friction imposed by star-PS chains is the same as their linear counterparts, suggesting that the monomeric friction coefficient is mainly determined by chemistry rather than the shape of the macromolecules.

At larger scales and longer times, the chains feel the presence of other chains in the melt, and their motion is constrained by

¹ Department of Chemical and Biological Engineering, Koç University, Istanbul, 34450 Turkey

² NIST Center for Neutron Research, National Institute of Standards and Technology Gaithersburg, MD 20899

³ University of Maryland, College Park, MD 20742

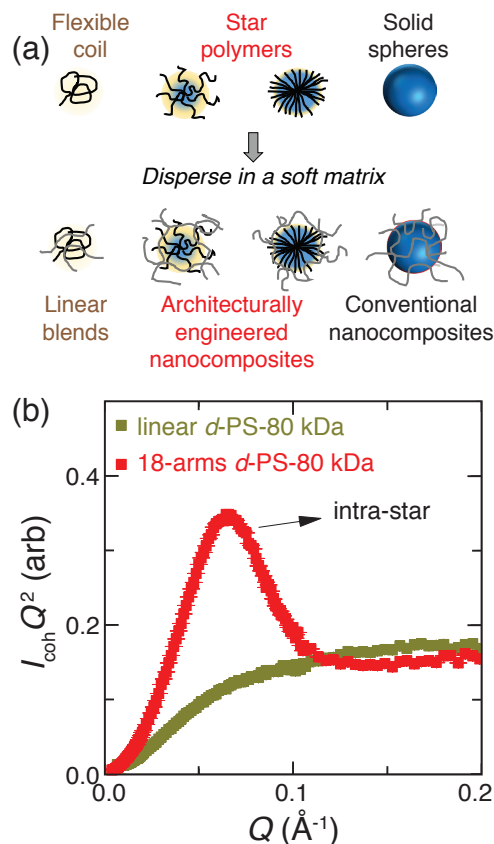


FIGURE 1: (a) Schematic representation of different type of fillers. The glassy star polymers structurally reside in between two hard sphere and flexible coils; dispersing them in soft matrices results in new hybrids between conventional linear blends and nanocomposites. (b) Kratky plot for 80 kDa linear and 18-arms *d*-PS fillers dispersed in *h*-PVME matrix, showing the compact nanoparticle like structure of the high-functionality stars.

entanglements (reptation motion). Such confined dynamics of chains is important for bulk rheological behavior of polymers as the rubbery plateau modulus is inversely proportional to the square of the distance between the entanglements, *i.e.* the reptation tube diameter. Using a mixture of *d* and *h* PVME chains, we highlighted the single *h*-PVME chains in the sea of deuterated background. NSE results suggest that star shaped particles do not much alter the apparent tube size of PVME whereas blending with linear chains reduces the tube diameter by $\approx 40\%$. This reflects directly on the rheological behavior of the samples. Linear PS chains results in a monotonic and moderate increase of viscosity relative to the neat PVME, as expected from conventional polymer blends. The 13-nm diameter silica nanoparticles, representing the conventional nanocomposites, monotonically reinforce the system orders of magnitude compared to the neat matrix, again as expected. The compact star PS remarkably decreased viscosity at moderate concentrations as they are impenetrable and small, while at higher concentrations percolation of the glassy PS stars causes reinforcement as high as the level that silica can achieve. This dual effect, softening and stiffening, of star macromolecules is novel and brings along a new design parameter- the filler architecture- for all-polymer based nanocomposites.

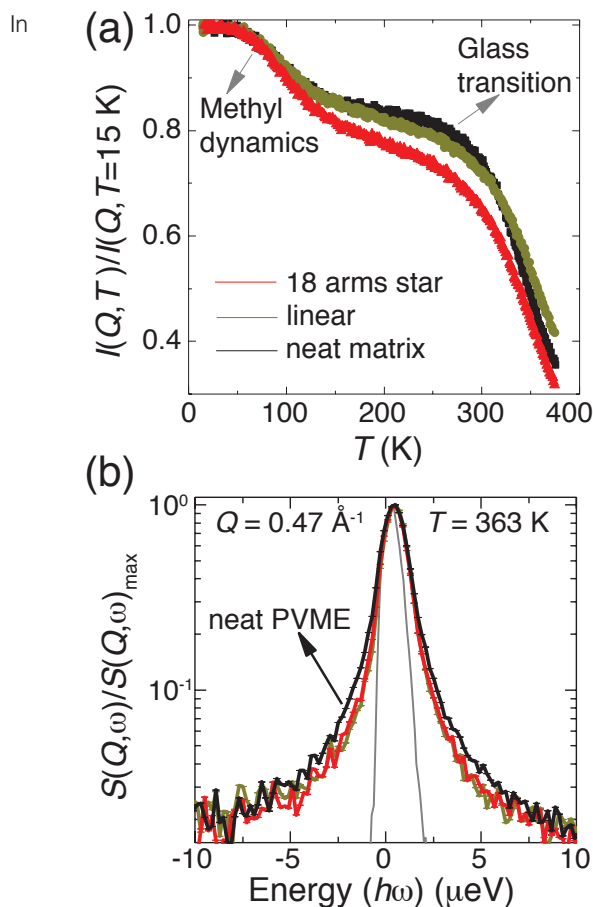


FIGURE 2: (a) Normalized scattered elastic intensities of PVME in neat forms and in composites with 20 % linear (80 kg/mol) and 18-arms (88 kg/mol) deuterated PS. (b) Normalized dynamic structure factors of the same samples at 363 K and at $Q = 4.7\text{ nm}^{-1}$. The gray line is the resolution.

conclusion, high-resolution neutron spectroscopy on isotopically labeled components in the resulting 'architecturally engineered' all-polymer nanocomposites allowed us to directly observe the chain conformation and motions at the nanoscale. The unprecedented bulk rheological behavior was therefore related to very complex microscopic mechanisms at a broad range of time-scale (from sub-nanoseconds to hundred nanoseconds), and length-scales (from monomer size to entanglement mesh sizes).

References

- [1] R. Krishnamoorti, R. A. Vaia, Polymer nanocomposites: synthesis, characterization, and modeling (American Chemical Society Washington, DC, 2002), Vol. 804.
- [2] E. Senses, M. Tyagi, M. Pasco, A. Faraone, ACS Nano **12**, 10807 (2018).
- [3] I. Cendoya, A. Alegria, J. Alberdi, J. Colmenero, H. Grimm, D. Richter, B. Frick, Macromolecules **32**, 4065 (1999).
- [4] A. Arbe, J. A. Pomposo, I. Asenjo-Sanz, D. Bhowmik, O. Ivanova, J. Kohlbrecher, J. Colmenero, Macromolecules, **49**(6), 2354 (2016).

Investigating the structures of polygalactomannans in water

M. Chawathe,¹ M. Webb,² R. Jones,³ and D. Bendejacq¹

Guar gum is a natural polysaccharide extracted from guar beans (*Cyamopsis tetragonoloba*). It belongs to the class of galactomannan and, as such, is comprised of (1-4)-β-D-mannopyranose backbone randomly attached by (1-6) linkages with pendent α-D-galactopyranose units galactose moieties (Figure 1), with a mannose to galactose ratio around 1.6 to 1. In its native high-molecular weight form, guar gum has unique thickening and suspending properties in water. Its worldwide availability (volume-wise) and sustainable sourcing have contributed to making it an additive that is often used to control rheological properties in diverse aqueous environments - from the oil & gas extraction industry, where it helps suspend sand during fracking, to the food industry, where it is used as a thickening agent for dairy products. Over the last 30 to 50 years, chemists have continued to modify this raw material in controlled ways (i.e. depolymerizing it, grafting hydrophobic or cationic moieties, etc), which has helped further expand the use of guar-based products to even more applications, from rheological to surface modification ones.

Guar gum and its unique interactions with water, remain at the center of these myriad applications. The structure of guar gum in water has been extensively studied in the dilute state, where 2-body interactions dominate. But the details of its structure in semi-dilute to concentrated states is lacking, owing to the fact that guar gum quickly form strong gels as soon as formulated at more than a few tenths of weight percent. This makes sample preparation long, cumbersome and somewhat uncertain, as far as equilibration time is concerned. Yet, even though guar gum will often be formulated in the dilute to semi-dilute states to make use of its rheological attributes, it is often in the concentrated state that guar will eventually end up. For example, after spraying and drying on surfaces, a formulation containing guar ends up as thin films in equilibrium with the natural humidity present in the surrounding atmosphere. Closing the gap between dilute and concentrated states is the overarching goal of the study that we have started over two years ago.

First, we report on the use that we have been making of nSoft and the access that it provides to small-angle neutron scattering (SANS). This technique is ideal for the study of dilute to semi-dilute solutions in D₂O of different guar gums depolymerized

down to weight-average molecular weights M_w s ranging from 32 kg/mol, 57 kg/mol and 118 kg/mol, as provided by Solvay USA Inc. These materials have been purified by dialysis and centrifuged to recover only fully soluble fractions. In Figure 2, we show a typical set of concentration-normalized scattered intensities obtained on solutions of the $M_w = 32$ kg/mol guar at mass fractions of (0.1 to 5) % in D₂O. Normalization by the concentration fails to result in the superposition of scattered intensities, suggesting a concentration-dependence – and, to some extent, a molecular-weight dependence - in the structure formed by guar gum in water.

Many empirical, phenomenological and theoretical models have been proposed over the years to describe SANS data obtained on dilute, semi-dilute and concentrated polymer solutions. To gauge the state in which SANS experiments were carried out - and determine which theoretical models to apply to extract meaningful information, we used capillary viscometry to determine the guar's crossover concentration c^* . The latter is defined as the concentration above which swollen polymer coils start overlapping, as their total hydrodynamic volume effectively exceeds the solution volume. In practice, hydrophilic polymers also exhibit non-Newtonian behavior above this critical concentration.

With c^* values ranging from $c^* = 3.0$, to 1.9 and 1.0 (% mass fraction), for $M_w = 32$ kg/mol, 57 kg/mol and 118 kg/mol, respectively, the concentrations range we have explored during our SANS experiments in fact covers states from dilute ($c < c^*$) to semi-dilute ($c > c^*$). In practice, simple models (such as the flexible cylinder, the polydisperse Gaussian coil or the Guinier-Porod function) which all account for only one characteristic length in the structure formed in solution, fail to capture the data collected experimentally, regardless of the concentration. More complex models, such as a double-Lorentzian, a Porod-Lorentzian or a Gauss-Lorentz gel model [1-4], which all take into account two different length scales in the structure formed in water, do a better job at capturing the shape of the scattered intensity in the semi-dilute state above c^* . The generalized double Lorentz model, for instance:

$$I(Q) = I_{network}(Q) + I_{blobs}(Q) \\ = A_{network} / (1 + Q^m \xi^m) + A_{blobs} / (1 + Q^p \xi^p)$$

¹ Solvay USA, Inc. 350 Georges Patterson Blvd, Bristol, PA 19007

² University of Chicago, 5640 S Ellis Ave, Chicago, IL 60637

³ Materials Science and Engineering Division, National Institute of Standards and Technology, Gaithersburg, MD 20899

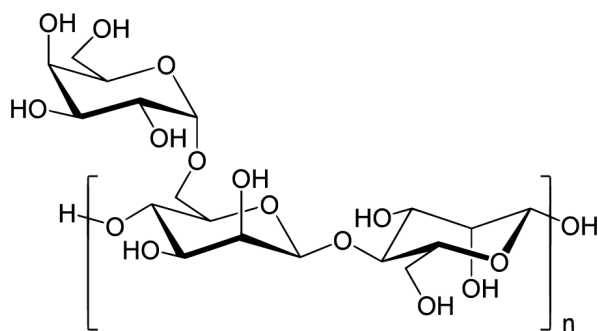


FIGURE 1: Chemical structure of guar gum, comprised of side-chain galactose motifs and a mannose backbone.

captures well the seemingly bimodal shapes of the scattering intensity obtained at $c/c^* = 1.67$ (cf. Figure 2), the two terms in this model accounting for structures (heterogeneities, local phase separations, density fluctuations, mesh size, blob size...) of different characteristic length scales Ξ and ξ . Least-square fitting of the experimental data for the sample with 32 kg/mol at a mass fraction of 5 %, yields the following results. With $\Xi = 270$ Å and $m = 2.88$, the first contribution is interpreted as arising from a large-scale network of heterogeneities of dimensionality close to three, a feature often reported in imperfect hydrogels or ill-formed swollen polymer networks. With $\xi = 9$ Å and $p = 1.96$, on the other hand, the second contribution is consistent with a Lorentzian contribution $1/(1+Q^2 \xi^2)$ that usually arises from solvated polymer chains comprised of blobs of size ξ , the length scale beyond which positional correlation is lost between polymer segments, as described by the blob theory [5, 6]. As complex as it is, the model fails at capturing the data obtained in the dilute state and there is for now no universal model that can fit all data regardless of concentration.

We note that, in the dilute state, each polymer chain contributes individually to the scattering intensity, independently of all the others. The blob size is constant, and the total blob contribution is expected to be proportional to concentration. In the semi-dilute state, on the other hand, blob theory predicts that, as chain interpenetration increases, the blob size ξ must decrease with concentration following the scaling law $\xi \propto c^{-3/4}$. In the semi-dilute state, the blob contribution to the scattering intensity, i.e. $c^2 \xi^3/(1+Q^2 \xi^2)$, eventually reads: $I(Q) \propto c^{5/4}/(1+Q^2 \xi^2)$. We surmise that the measured scattering intensities do not superpose once normalized by the concentration, precisely because the prefactors scale differently with concentration on either side of c^* .

While for low molecular weight polymers, isolating the scattering of chains free of interactions is not an issue (because their c^* is rather high), doing the same for high molecular weights is not always possible, as the total scattering intensity at low concentrations is often insufficient to collect high quality data in a reasonable amount of time. This problem is exacerbated for guar as the OH-decorated galactomannose motif can almost fully exchange hydrogen with deuterium coming from D_2O . This significantly decreases the neutron

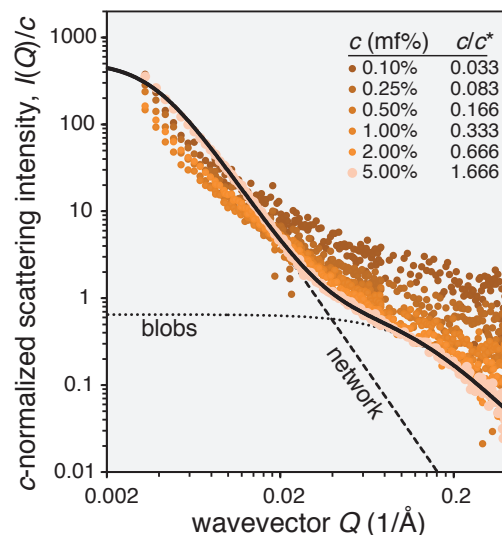


FIGURE 2: Concentration-normalized SANS data from solutions of a $M_w = 32$ kg/mol guar. The dark continuous line is a fit of the data at mass fraction of 5 % to a generalized double-Lorentzian model (see text), while the dotted lines are the two individual contributions from blobs and network.

scattering length density (NSLD) of guar, hence the contrast with D_2O and in *fine*, the scattering intensity of very dilute guar solutions. We will soon report on this feature, having fully demonstrated and quantified the exchange using a spectroscopic technique, PM-IRRAS, made available to us through a collaboration with NIST's Functional Polymers Group, arranged through the nSoft consortium.

This experimental work is now being combined with a novel hybrid coarse-grained modeling approach, parameterizing simulations onto experimental results, with the objective to create a modelling tool able to quantifiably simulate guar in water, *albeit valid in this dilute to semi-dilute concentration range*. Additional experiments using neutron reflectivity in controlled humidity (both H_2O and D_2O) have been taking place, to explore the semi-dilute to concentrated state, as thin guar films can absorb from 50 % to 200 % water, as the relative humidity is varied from 50 % to 95 %, so as to ascertain the universality of the parameterization performed on the SANS data obtained in the dilute state.

References

- [1] M. Shibayama, T. Tanaka, C. C. Han, J. Chem. Phys. **97**, 6829 (1992).
- [2] F. Horkay, A. Hecht, M. Zrínyi, E. Geissler, Polym. Gels Netw. **4**, 451 (1996).
- [3] M. Shibayama, Polym. J. **43**, 18 (2011).
- [4] M. Shibayama, H. Kurokawa, S. Nomura, M. Muthukumar, R. S. Stein, S. Roy, Polymer **33**, 2883 (1992).
- [5] P.-G. de Gennes, Scaling Concepts in Polymer Physics, Cornell University Press.
- [6] A. N. Falcao, J. Skov Pedersen, K. Mortensen, Macromolecules **26**, 5350 (1993).

Probing fluid nanostructure under complex flow histories using SANS in a fluidic four-roll mill (FFoRM)

P. T. Corona,¹ N. Ruocco,^{1,2} K. M. Weigandt,³ L. G. Leal,¹ and M. E. Helgeson¹

Flow processing of soft materials introduces complex deformation histories that lead to nonlinear changes in fluid structure that are trapped out of equilibrium. These structural changes influence not only the properties of the final product, but also affect the fluid's rheology and processability during flow. Small angle neutron scattering (SANS) provides an attractive technique to measure nanostructural changes in such fluids, but requires sample environments that can simulate diverse flow histories. Recently, Corona *et al.* presented a fluidic four-roll mill (FFoRM) sample environment that is available to the general SANS user community [1]. The device, inspired by a previously developed microfluidic version [2], enables SANS measurements of complex fluids under arbitrary programmable 2D flow histories within a single sample environment.

The FFoRM sample environment consists of two outer plates that confine the flow and enable temperature control, and an inner plate that defines the 2D FFoRM geometry (Figure 1a) consisting of eight channels feeding into a circular central region. In four of these channels, fluid is driven with syringe pumps at variable volumetric flow rates (Q_1 and Q_2) while the remaining four channels are held at constant pressure. In general, the total flow rate into the device ($Q_1 + Q_2$) controls the rate of strain, E , while the ratio of the flow rates (Q_1/Q_2) controls the flow type, Λ [2].

Since the rheology of complex fluids can impact the flows that develop, flow characterization using particle tracking velocimetry measurements of the velocity gradients (Figure 1b and c) is crucial for determining the precise flow history of fluid elements and interpreting the resulting SANS patterns (Figure 1d). To date, the operational limits of the FFoRM sample environment accommodate shear thinning, yield stress, and viscoelastic/elastic fluid responses.

The FFoRM-SANS method was validated with measurements on a model suspension of rigid rod-like nanoparticles, whose orientational order under flow can be predicted from various analytical theories. The fluid consists of a dispersion of cellulose nanocrystals (CNCs) dispersed in water at semi-dilute concentrations where the particle orientations are random at equilibrium due to thermal fluctuations but can be oriented by a steady flow when the strain rate is sufficient to overcome the randomizing effect of Brownian rotation. We define a

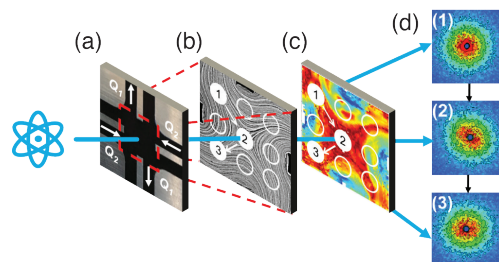


FIGURE 1: Schematic outline of FFoRM-SANS workflow. (a) The FFoRM geometry is optimized to generate spatially uniform flows. Flow field visualization enables operational mapping of (b) streamlines and (c) flow type/deformation rate field the fluid experiences. (d) SANS probes structural changes in the material under arbitrary large-strain deformation histories near the stagnation point at the center of the device. The neutron beam can be focused at different locations in the geometry, signified by the white circles labeled 1, 2, and 3, to probe the transient evolution of the microstructure.

rotational Péclet number ($Pe_r = ED_r$), which is a dimensionless strain rate that describes the degree to which a flow field orients the CNCs. We find that the orientation of CNCs is described by Pe_r for all conditions tested in this work and regardless of the imposed flow type, matching predictions from theory and validating the FFoRM-SANS methodology [1].

The studies presented by Corona *et al.* demonstrate that FFoRM-SANS is a powerful technique for rapidly probing complex fluid microstructure under tunable flow histories within a single sample environment. The transient evolution of fluid microstructure can be mapped by spatially varying the location of the neutron beam to track the evolution of structure of a material element as it moves along the flow. It is anticipated that the capabilities of FFoRM-SANS will be useful in probing the rheology and flow-induced structuring of an expanding class of complex fluids, in flows that can be programmed to simulate a wide variety of processing conditions.

References

- [1] P. T. Corona, N. Ruocco, K. M. Weigandt, L. G. Leal, M. E. Helgeson, *Sci. Rep.* **8**, 15559 (2018).
- [2] J. S. Lee, R. Dylla-Spears, N. P. Teclamarium, S. J. Muller, *Appl. Phys. Lett.* **90**, 2005 (2007).

¹ University of California Santa Barbara, Santa Barbara, CA 93106

² ExxonMobil Chemical Company, Baytown Technology and Engineering Complex, Baytown, TX 77520

³ NIST Center for Neutron Research, National Institute of Standards and Technology, Gaithersburg, MD 20899

In-situ sample orientation at cryogenic temperatures

S. Gladchenko¹

The nature of magnetism changes both with temperature and applied magnetic field. Typically, for elastic and inelastic scattering on single crystals the magnetic field should be precisely aligned along either the spin direction, or one of the crystallographic axes of the crystal. Unfortunately, with our standard vertical field magnets the sample environment equipment does not allow the scientist to control the crystal alignment. Rather, the crystal would be aligned separately and then inserted in the magnet. Subsequent alignment of the scattering plane requires tilting the entire assembly and does not allow any realignment of the sample with respect to the magnetic field direction. To address this issue, we have developed a system that allows realigning the sample inside the cryostat, changing its orientation relative to the magnetic field during a neutron experiment without disrupting the experiment temperature and magnetic field conditions.

Design of such a system is a challenging problem due to the limitations for devices operated at ultra-low temperatures. The alignment device must be located inside the small space under vacuum conditions, it should produce minimal heat load to avoid interference with stable operation of the refrigerator, and it should demonstrate minimal expansion or contraction over a wide range of temperatures. Additionally, the device must not generate an electromagnetic field and must be made from non-magnetic materials. Previous designs have had both positives and negatives. Some designs used a worm-gear mechanism to mechanically connect an external room temperature motor to the sample space [1]. Another design used a piezoelectric actuator located at ultralow temperatures to achieve sample rotation [2]. However, these actuator systems were not designed for neutron measurements. Our current design for sample rotation allows 360° rotation around the axis in the horizontal plane with resolution 0.1°. The device can be used at temperatures below 1 K, magnetic fields up to 31 T, under high vacuum, and within a neutron beam. Figure 1 is a photo of the actual device.

Dimensions of this device are 98 mm high and 55 mm wide which allows it to fit inside the ³He cryostat inserts operated within our facility. The dimensions are mostly defined by the size of the piezo electric rotator ANR240 (closed loop) by Attocube. The choice of this rotator was motivated by the amount of dynamic torque supplied (2 N·cm) to allow repositioning and maintaining sample position in a high magnetic field. An aluminum sample holder is attached to the bottom gear located at the neutron beam position. The piezo electric rotator and gears are supported by a

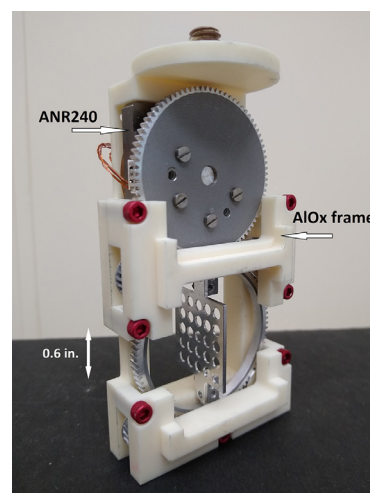


FIGURE 1: Low-temperature goniometer.

ceramic (AlO_x) frame. Figure 1 shows how the device has been designed to minimize the amount of material surrounding the sample position. The 0.6 in wide horizontal opening creates a large viewing window for undisturbed 360° sample observation. We use aluminum or copper braids to connect the sample holder and cold plate to improve thermal contact down to the ³He insert base temperature ($T = 0.3$ K).

This sample alignment device has been successfully used in exploring the metamagnetic transition in the intrinsic antiferromagnetic topological insulator MnBi₂Te₄. Tilting the sample at high field and low temperature allowed researchers to access otherwise inaccessible reflections sensitive to changes in the magnetic ordering while maintaining a large component of the magnetic field along the c-axis. This alignment device is a powerful tool for researchers, allowing them to more easily search for novel relationships between scattering geometry and applied magnetic field direction.

References

- [1] E.C. Palm, T.P. Murphy, Review of Scientific Instruments **70**(1), 237 (1999).
- [2] L.A. Yeoh, A. Srinivasan, T.P. Martin, O. Klocan, A.P. Micolich, A.R. Hamilton, Review of Scientific Instruments **81**, 113905 (2010).

¹ NIST Center for Neutron Research, National Institute of Standards and Technology, Gaithersburg, MD 20899

Optimization of biological reflectometry experiments using information theory

B.W. Treece,¹ P.A. Kienzle,² D.P. Hoogerheide,² C.F. Majkrzak,² M. Lösche,^{1,3,2} and F. Heinrich^{1,2}

Neutron reflectometry from lipid membranes and associated small molecules, peptides, and proteins is unique in structural biology as it allows for measurements under biologically relevant, fully solvent-immersed conditions. It is routinely applied to difficult structural targets such as transient membrane binders, disordered proteins, and protein complexes [1]. Experimental resources at large-scale scattering facilities are scarce and there is significant pressure to use the experimental time most efficiently. We have developed a theoretical framework to find optimal conditions that maximize the information that is obtained from a neutron reflectometry experiment [2].

The framework is broadly applicable to any type of measurement with model-based data analysis and utilizes information theory and Bayesian statistics. The information gain from an experiment is defined as the difference in entropy between the prior and the posterior model parameter probability density functions (PDFs) computed within the framework. The entropy of a PDF is a measure of parameter confidence while taking into account correlations that constrain parameter values and, therefore, also contain information. The posterior PDF is obtained from a model fit of simulated data using a Monte Carlo Markov Chain global optimizer for neutron reflectivity data developed at the NCNR [3]. Simulated data allows us to systematically vary experimental and instrumental parameters of interest while searching for maximum information gain.

Among the large number of experimental and instrumental variables that warrant a systematic investigation with this framework, we decided to first have an in-depth look at contrast variation in biological neutron reflectometry. For this problem, we had to first extend this framework to include marginalization towards parameters of interest while integrating over nuisance parameters, which allows focusing the optimization on a subset of model parameters. We then identified optimal contrast conditions between a lipid bilayer membrane, membrane-associated protein, and the surrounding aqueous solvent for a series of reflectivity measurements with solvent contrast variation [4]. We plan to further extend this framework by implementing model selection to be able to dynamically adjust the complexity of a model while optimizing the information gain from the

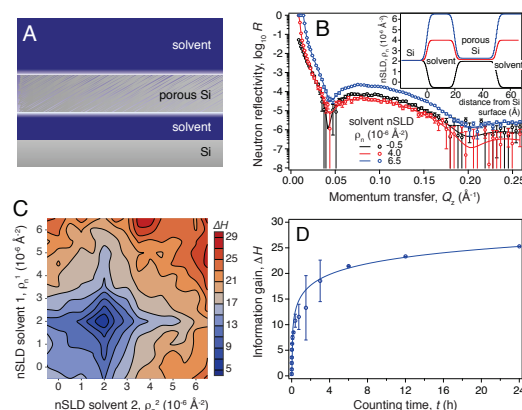


FIGURE 1: (A) Thin film test structure consisting of a porous silicon layer surrounded by aqueous solvent on a silicon support. (B) Simulated reflectivity and best fit for three exemplary values of the solvent nSLD. Inset: Best fit nSLD profiles. (C) Information gain ΔH (in bit) from two subsequently measured reflectivities under variation of the solvent nSLDs (contrasts). Most information is gained for a combination of a D_2O -solvent ($\rho_n \approx 6.5 \times 10^{-6} \text{ \AA}^{-3}$) and any other solvent, except those close to matching the nSLD of silicon ($\rho_n \approx 2.0 \times 10^{-6} \text{ \AA}^{-3}$). (D) Information gain from a single measurement with D_2O as a function of counting time, simulated for a typical configuration of the NIST MAGIK reflectometer. The optimal counting time is ≈ 6 h, beyond which further information gain requires increasingly long counting times.

measurement. Such an algorithm could find application in real-time data analysis at the scattering instrument while the data is being collected, increasing the efficiency of the data collection process and allowing for early intervention in case of a faulty measurement. In situ data analysis is particularly important for new scattering instrumentations, such as the new CHRNS-supported CANDOR reflectometer at NIST, which produce a large amount of data in a short time.

References

- [1] F. Heinrich, M. Lösche, BBA-Biomem. **1838** (9), 2341 (2014).
- [2] B. W. Treece et al., J. Appl. Cryst. **52**, 47 (2019).
- [3] B. Kirby et al., Curr. Opinion Coll. & Interface Sci. **17** (1), 44 (2012).
- [4] F. Heinrich et al., (in preparation).

¹ Department of Physics, Carnegie Mellon University, Pittsburgh, PA 15213

² NIST Center for Neutron Research, National Institute of Standards and Technology, Gaithersburg, MD 20899

³ Department of Biomedical Engineering, Carnegie Mellon University, Pittsburgh, PA 15213

In-situ NAA: Measurement of delayed gamma rays from short lived nuclei using a linear neutron beam chopper with arbitrary duty cycles

H. H. Chen-Mayer,¹ R. L. Paul,¹ D. J. Turkoglu,² and M. Dermience³

Fluorine, due to its interesting chemistry, is playing increasingly important roles in pharmaceutical, environmental, and industrial applications [1]. An F mass fraction at 100 mg/kg levels is difficult to determine non-destructively; several methods have been developed to address this measurement challenge [2]. Traditional neutron activation analysis (NAA), which involves irradiating samples in a reactor core with transport out for delayed counting, especially in conjunction with pseudo-cyclic methods of up to 10s of cycles of repeat shuttling in and out of the reactor core, can achieve good detection limit for biological materials [3]. However, INAA relies on a fast transfer system because of the short fluorine half-life. In addition, it may be subject to interferences from fast neutron activations in the reactor core. In a normal PGAA measurement, both prompt and delayed gamma rays are detected simultaneously, F in PE disks with mass fraction at 100 ppm levels cannot be measured in our standard setting, due to a combination of two issues. First, the partial gamma cross sections for the strongest F line (0.0096 barns) is much smaller than that for H (0.33 barns) and thus the sensitivity for F (count rate per unit mass) is quite low. Second, the F peak at 1633 keV lies in the region of the Compton continuum from the H peak at 2223 keV so the high prompt gamma background overwhelms the weak peak from ^{20}F decay. To overcome these issues, we use an arbitrary duty cycle neutron beam chopper [4] at an existing cold neutron beam prompt gamma activation analysis (PGAA) instrument (Fig. 1(a)) to do the measurement in-situ, effectively performing thousands of irradiation and decay counting cycles without transferring the sample.

We report the first such application for the measurement of F in polyethylene (PE). The objective was to determine F concentrations from 100 mg/kg to 1000 mg/kg in a PE matrix, which was shown to be unachievable with normal PGAA and therefore precipitated the use of the chopper to extend our measurement capability. A single disk was measured for concentrations at 1000 ppm, 500 ppm, and 300 ppm and a 3-disk stack was measured for 100 ppm. The measurement was complicated by the strong scatter and attenuation of the PE matrix, for which a simple empirical correction was made based on the measured attenuation from the disks. A standard consisting of KF on filter paper was measured using the same

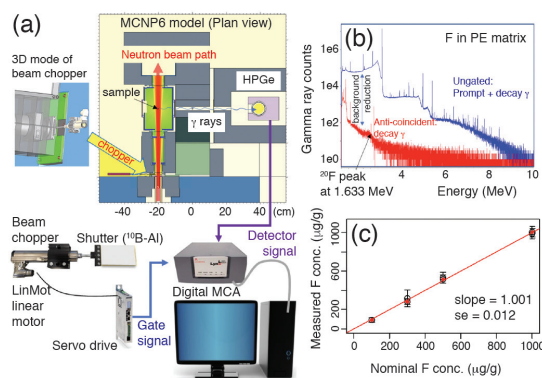


FIGURE 1: a) In-situ NAA achieved by a neutron beam chopper in anti-coincidence in the standard PGAA setting. (b) Gamma spectra of F in polyethylene, acquired with the chopper cycle set to 11 s on/off to match the half-life of ^{20}F , for nearly 2000 chopper cycles. (c) F concentration (ug F/g sample) determined for the 4 concentrations vs the nominal value. The black open symbols are from the 1-disk measurements, and the solid red circles are from the 3-disk measurements. The red line is from a weighted linear least squares fit. The overall ratio (represented by the slope) between the measured and the nominal values is unity within uncertainty.

protocol to obtain the sensitivity of F in the chopped beam. The results are summarized in Fig. 1c, where both the 1-disk and 3-disk data are plotted together against the nominal F concentrations.

Future work includes establishing the measurement and analysis procedures and performing method validation and error assessment using SRMs with certified or reference values. We anticipate that this technique will lead to lower detection limits of F and other short-lived isotopes.

References

- [1] G. Sandford, Phil. Trans. R. Soc. Lond. A **358**, 455 (2000).
- [2] V. Havránek, J. Kučera, Z. Řanda, V. Voseček, J Radioanal Nucl Chem **259**, 325 (2004).
- [3] S. Parry, R. Benzing, K. Bolstad, E. J. Steinnes, Radioanal Nucl Chem. **244**, 67 (2000).
- [4] D. Turkoglu, R. Zeisler, H. Chen-Mayer, Nucl. Instru. Meth. (to be published).

¹ Materials Measurement Laboratory, National Institute of Standards and Technology, Gaithersburg, MD 20899

² NIST Center for Neutron Research, National Institute of Standards and Technology, Gaithersburg, MD 20899

³ ExxonMobil Chemical Europe Inc., Machelen, Belgium

Fabrication and treatment of perfect crystals for neutron interferometry

M. Arif,¹ D. G. Cory,^{2,3,4,5} T. Gnaeupel-Herold,¹ R. Haun,⁶ B. Heacock,^{7,8} M. G. Huber,¹ M. E. Jamer,¹ J. Nsofini,^{2,3} D. A. Pushin,^{2,3} D. Sarenac,^{2,3} I. Taminiau,⁹ and A. R. Young^{7,8}

Neutron interferometers (NIs) are made from perfect-crystal silicon which has been machined so that there are crystal blades protruding from a rigid common base (Fig. 1) [1]. Each blade of the NI must be aligned to within 6×10^{-7} degrees with thicknesses uniform at the micron level. If either of these stringent requirements are not met, the neutron paths will not fully interfere and the NI's sensitivity will be lost. These requirements are achieved by cutting NIs from a single ingot using a rotating diamond saw. The cutting leaves microcracking and other stresses that can extend hundreds of microns into the blade's surface. To eliminate these stresses, the interferometer is etched in a hydrofluoric acid mixture [2]. However, if too much material is etched away, the fringe contrast (ideally 100 %) worsens due to thickness variations caused by uneven etch rates. Notably, NIs constructed under similar conditions can show wildly different contrasts and machining accuracy was previously thought to be a major source of this variation. However, modern machining processes eliminate this as a possibility. In our work we have demonstrated that the lack of reproducibility in NI construction is likely due to the thickness variations of the interferometer blades from uneven etch rates as well as fluctuating or greater than 6×10^{-7} degrees lattice plane misalignments between the blades. We have shown that Bragg plane misalignment can be reduced by annealing the interferometer after fabrication.

When searching for contrast, an interferometer is translated vertically and horizontally, making a "contrast map" (see Fig 2.). The contrast after annealing was excellent, improving from 23 %, as per Ref [3], to 90 %. The spatial range exhibiting high contrast is larger for the annealed interferometer and implies that the annealed interferometer may be especially useful for phase imaging, where the incoming beam is 1.0 cm^2 . It is possible that annealing treatments to the NI fabrication process will require less etching and prevent thickness variation in the crystal blades. This enables both new interferometer designs and statistically improved performance.

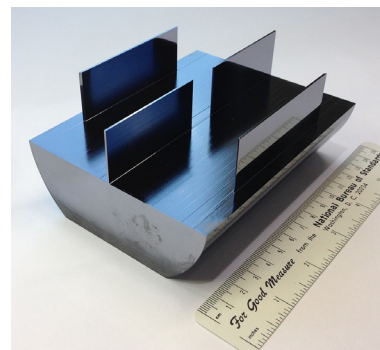


FIGURE 1: A perfect-crystal silicon interferometer.

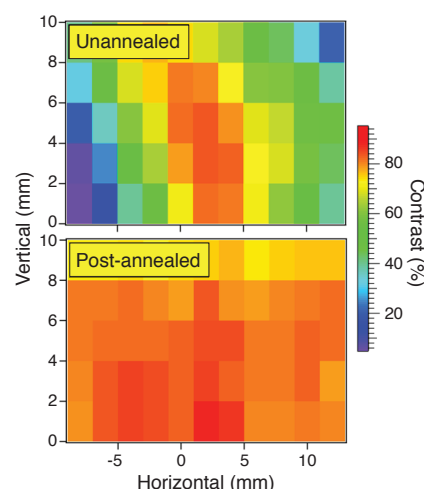


FIGURE 2: Contrast maps of a high contrast NI (top) compared to the annealed NI shown in Fig.1 (bottom).

References

- [1] B. Heacock et al., Rev. Sci. Instr., **89**, 023502 (2018).
- [2] M. Zawisky et al., Nucl. Instr. Meth. A **612**, 338 (2010).
- [3] C. J. Wood et al., Phys. Rev. A **90**, 032315 (2014).

¹ National Institute of Standards and Technology, Gaithersburg, MD 20899
² Institute for Quantum Computing, Waterloo, Ontario N2L3G1, Canada
³ University of Waterloo, Waterloo, Ontario N2L3G1, Canada
⁴ Perimeter Institute for Theoretical Physics, Waterloo, Ontario N2L2Y5, Canada
⁵ Canadian Institute for Advanced Research, Toronto, Ontario M5G 1Z8, Canada
⁶ Tulane University, New Orleans, LA 70118
⁷ North Carolina State University, Raleigh, NC 27695
⁸ Triangle Universities Nuclear Laboratory, Durham, North Carolina 27708
⁹ Quantum Valley Investments, Waterloo, Ontario N2L 0A9, Canada

Reductus: a web-based data reduction service for reflectometry

B. B. Maranville,¹ W. D. Ratcliff,¹ and P. A. Kienzle¹

As part of the core function of NCNR-based neutron instruments, we provide software to transform raw measurements taken here into meaningful, interpretable data with physical units (data reduction.) This has largely been accomplished through the distribution of single-purpose programs for visiting scientists to install on their own available computers, to allow them to reduce data when they are away from the NCNR at their home institutions after the experiment, or in their hotel rooms at 3 am during an experiment. Recently for the NCNR's neutron reflectometers, we have begun offering data reduction in a different way: at the [web-based data reduction service, reductus](#) [1]. Reflectivity data can be reduced in real time from any computer with a web browser and an internet connection.

The technique of neutron reflectometry provides nm-depth resolved information about the structure and optionally vector magnetization of planar samples, and is applied to biological membranes, polymers and polymer blends, magnetic thin-film structures, etc. The raw data is typically measured as neutron counts per unit time as a function of incident (and reflected) angle of a ribbon-like beam (well-collimated in the scattering plane, but with a broad angular divergence along the axis perpendicular to the scattering plane). In order to make physical sense of this data, a few data processing steps typically need to be made. The momentum transfer Q (and resolution, dQ) can be calculated from the angles, wavelength and collimation with associated uncertainties. A "background" signal is subtracted, that arises from incoherent or inelastic scattering in the sample, small-angle scattering from sample-environment, cosmic rays, etc. The background-subtracted signal is divided by the incident intensity.

At the bottom of Fig 1. is a flowchart-type display of the data reduction steps that are to be taken, through which the user interacts with the application. Data files (from the NCNR public data repository) are identified in the rectangles to the left of the flowchart, which are separated by measurement type (incident intensity, background or specular scattering) and where the "wires" leading to the right represent the loaded data flowing into reduction steps downstream, for example the module representing background subtraction has two inputs to the left but only one output to the right for the subtracted data.

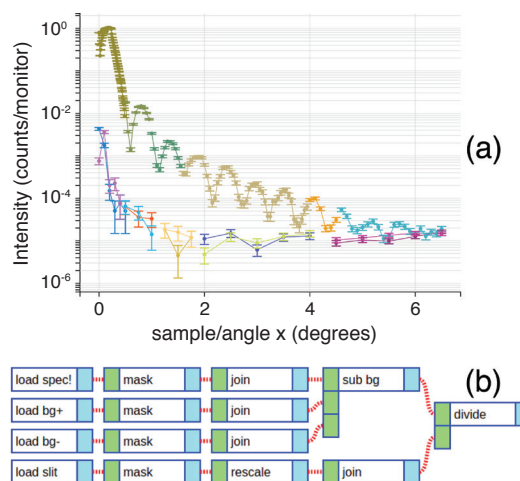


FIGURE 1: An example dataset being reduced using reductus.

Users can select data from any input or output within the diagram to inspect or export (download) to their computer. Selecting the module rectangle brings up the editable list (far right panel) of parameter values for the reduction function it represents. All exported data contains a header with a complete text representation of the reduction workflow embedded in it, so that users can reload exported data files into the *reductus* interface, and it fully recreates the data flow diagram, and repeats all of the calculations.

The calculations are carried out by a server written in Python, which receives a text representation of the data flow diagram and constructs the function calls needed to calculate the indicated outputs from a list of functions created for our data reduction. The source code for both the Python server and the Javascript client can be found at [the repository for reductus](#). The diagrams themselves are editable, and users can rewire the modules, add new calculation modules, delete modules, etc., all from the web interface. This flexible but limited high-level visual programming interface has proven to work for a wide variety of experimental setups, and feedback has been positive from the user community.

Reference

- [1] B. B. Maranville, W. D. Ratcliff, P. A. Kienzle, J. Appl. Cryst. **51**, 1500 (2018).

¹ NIST Center for Neutron Research, National Institute of Standards and Technology, Gaithersburg, MD 20899

Neutron Source Operations

Reliability and availability of the reactor

The reactor operated for 212 days during FY 2019, achieving a reliability of greater than 98%. Operational days lost to the government furlough that ended January 25, 2019 are not included in these numbers.

Replacement of reactor safety system relay box

What we call the “reactor safety system” is the logic center of the reactor. Its logic allows the operator to start, control, and shut down the reactor. The logic also provides for automatic actions, maintaining limits and interlocks required by our license for safe operation of the reactor. The old logic system consisted of (physically) tightly packed mercury wetted relays and wires. This system was largely unchanged since the original inception of the reactor. General degradation of the system itself as well as the obsolescence of mercury wetted relays required a full redesign and rebuild of the safety system.

From our experience with maintaining the tightly packed mercury wetted relay cabinet, it was decided to relocate the safety system into a large rack that allowed for the addition of several features to make the system as easily maintainable as possible. The rack has been moved away from the reactor console in its entirety. The chosen relays have quick-connect terminations that allow for regular testing and replacement if needed. Each relay point was wired out to a 1-to-4 terminal block where the logic and console interface connect to the relay. By removing the logic from the relay terminals, we can now replace the relays with any suitable alternative in the future. A detailed installation plan was developed that allowed installation and testing during a normal length reactor shutdown. This was quite an accomplishment as the new system comprises 82 modern safety relays wired into the reactor console with 3200 terminations and 4000 ft of wire. Multiple verification and validation tests at different points in the project were specified in the installation plan. This evolution will serve the NCNR well as ever more complex restoration jobs will be required to be executed as the reactor ages.

Design for a new reactor matures

The majority of scientific research at the NCNR utilizes cold neutrons that emanate from the large liquid hydrogen cold source. A liquid deuterium cold source that offers a gain of approximately 50 % in brightness of long wavelength neutrons ($> 4 \text{ \AA}$) will replace Unit 2 in 2023. Following this

upgrade, there will be limited opportunity to further expand neutron production to meet the nation’s increasing demand for neutrons. Furthermore, the current reactor has been operated since 1967 and has required significant outages for aging reactor maintenance. In this context, Reactor Operations and Engineering has been investigating designs for a replacement neutron source at NIST both to mitigate the risk of a significant period without a neutron source and to substantially upgrade the source to enhance scientific capabilities.

The brightness of a cold neutron source depends on the local neutron flux. Many reactors around the world have demonstrated a formula to achieve very high neutron flux: make the reactor core as compact as possible and have a large reflector (typically a tank of heavy water) where the neutron flux peaks. Over the past few years, we have explored various reactor designs, including the Split Core



FIGURE 1: The installation crew next to the new relay rack. Note the yellow connection wires.

concept with horizontally split compact cores. While this Split Core concept demonstrated the substantial gains that would increase cold source brightness, it was found to pose reactivity control challenges. Thus, recent efforts have focused on making a single compact core because it can provide a simpler solution that achieves excellent neutronic and fuel-efficiency performance.

The latest concept features a 20 MW light-water-cooled compact core surrounded by a large heavy water reflector in a tank – all within an open light-water pool that allows access for refueling and maintenance. The core contains just nine plate-type fuel assemblies, making its power density substantially higher than that of the NBSR with 30 plate-type fuel assemblies. The hafnium shim blades, which will need

less-frequent replacement than the cadmium shim arms of the NBSR, provide reactivity control as well as the safety shutdown system.

Most importantly, the heavy water reflector has an unperturbed neutron flux that is more than a factor of 2 greater than that of the NBSR and has ample space for multiple cold neutron sources, thermal beam tubes and other irradiation facilities. The reactor concept appears to be feasible and shows merit for selection as the design concept that could eventually succeed the NBSR as the neutron source as the NCNR. While engineering the design of a safe and cost-effective reactor core continues, we are now focusing on optimization of cold sources and neutron optics that would best serve the future needs of neutron science.

Facility Developments 2019

CANDOR

CANDOR is an advanced neutron instrument based on an innovative design employing an “energy dispersive” detector, which permits use of a polychromatic incident beam. This detector analyzes the scattered beam using a linear series of 54 crystals, each oriented to diffract neutrons of one particular wavelength into a corresponding detector while neutrons of other wavelengths pass through to other crystals located downstream. In this manner, the wavelength and scattering vector Q is known for each neutron detected. The detection elements consist of thin plates (1.5 mm) of $^6\text{LiF/ZnS(Ag)}$ scintillation material with embedded wavelength-shifting fibers. This design allows for a compact arrangement of multiple detector arrays. The energy analyzing HOPG crystals are cooled below $\approx 8\text{ K}$ to reduce the background in the detectors arising from thermal diffuse scattering. After extensive off-line cryogenic testing, this detector was installed, and first neutrons were recorded on CANDOR in June.

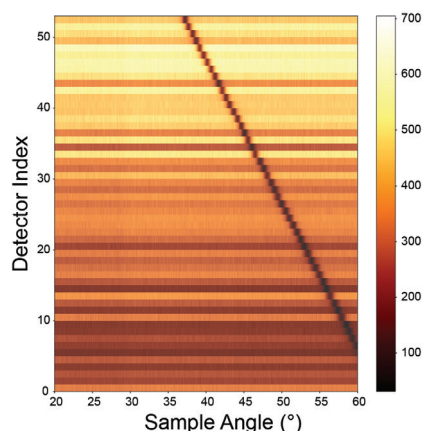


FIGURE 1: Data from a single channel of the CANDOR energy dispersive detector. Each channel has 54 individual detector modules each with its own graphite crystal. For this scan the detector was placed in the main beam and a pyrolytic graphite sample was placed at the sample position. The graphite sample was rotated, creating the line of black dots that occur when the angle of the graphite sample equals that of each of the 54 individual detector modules.

The scintillators, wavelength shifting fibers, silicon multipliers, and all support electronics are maintained in a dry gas filled (but non-cryogenic) light box above the cryostat. The data acquisition electronics based on field programmable gate arrays configured for pulse shape discrimination are being

developed in-house because the contract for procuring these electronics was cancelled due to issues with the vendor. Prototype boards have been constructed and are undergoing testing. Until that development is complete (winter 2020), we are using a stopgap solution of a previously developed discrete component discriminator. Figure 1 shows data from one channel of the CANDOR detector aligned on the main beam as a graphite crystal at the sample is rotated. The series of black squares appear at the angles at which the angle of the graphite sample matches that of a particular graphite crystal in the detector system.

Commissioning of CANDOR is continuing, and we expect the first specular reflectometry test measurements in early 2020.

MAGIK

The neutron reflectometer MAGIK was originally designed to measure the reflectivity of samples supported on a vertical planar substrate. However, liquid-gas or liquid-liquid interfaces require that the reflecting interface(s) be horizontal. The height of the NG-D guide is approximately 20 cm at the location of the MAGIK reflectometer. Fortunately, this large vertical dimension allows a horizontal ribbon beam to be defined (by an appropriate set of slits) such that a horizontal sample surface can be illuminated. This is accomplished with a pair of horizontal apertures, separated by approximately one meter, and a single pyrolytic monochromator blade. These three components, located upstream of the sample position, are translated vertically

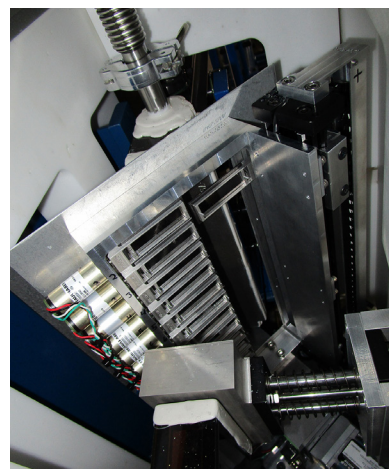


FIGURE 2: The scanning monochromator recently installed on MAGIK.

in proper unison to keep the position of the beam on the sample fixed. The vertically scanning monochromator blade (which is located adjacent to the focusing array of monochromator blades for the original vertical sample geometry (see Fig. 2)) can be translated in or out remotely. This new scanning option on MAGIK has been successfully used by researchers from the University of Delaware in rheological studies of liquid interfaces using neutron reflectometry as a probe of interfacial structure.

BT8

Neutron diffraction measurements of residual stress and preferred orientation benefit tremendously if more than one diffraction peak can be mapped into a small angular window without excessive peak overlap. This has been achieved using a new multiwavelength monochromator recently deployed on the engineering diffractometer located at BT-8 (Fig. 3). The concept exploits a sweet spot represented by the high reflectivity and low absorption of horizontally bent stacks of thin silicon wafer blades with three different orientations ([400], [311], [422]) and a common zone axis $[01\bar{1}]$. For symmetric diffraction, the device delivers three wavelengths but combinations of two wavelengths are also possible through rotation about the common zone axis. The new monochromator is intended for use with the cubic and hexagonal materials which are typically used in industrial and structural engineering applications.

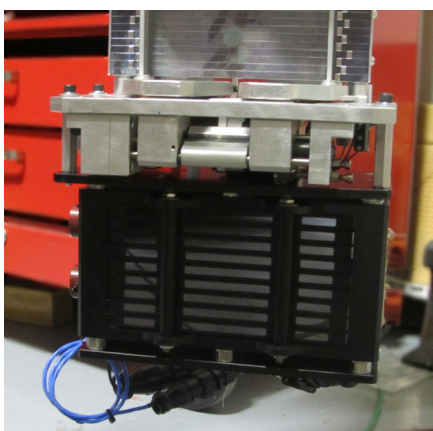


FIGURE 3: Closeup view of the new multi-wavelength monochromator before installation at BT-8.

For texture measurements from steel (Fig. 4) the new triple-wavelength monochromator delivers the same information in half the time through simultaneous collection of (200), (200), and (211) peaks grouped within a detection window $\Delta 2\theta = 9^\circ$. Collection of stress data is 50% faster through the appearance of the new 'super peak' (211) + (200) at 75° . This is a new effect arising from the equal ratios of monochromator lattice spacings and sample lattice spacings. The data rate enhancement is expected to be even larger for fcc-materials where the entire triple-wavelength intensity appears in a single sample peak.

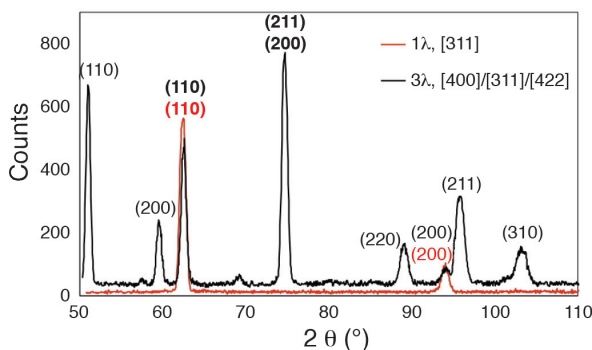


FIGURE 4: Comparison of diffraction patterns of a steel sample using the existing single wavelength (Si[311]) and the new triple-wavelength monochromator containing Si[311], Si[400] and Si[422].

Planning for the installation of a new D₂ cold neutron source

To enhance its cold neutron capabilities, NIST will replace the current large liquid H₂ cold neutron source with a liquid D₂ source that will nearly double the data acquisition rate for instruments in the NIST guide hall. The installation of the new cold source will require an extended outage of the reactor lasting 9 to 12 months. While this is a rather long outage, upgrades such as this are necessary to maintain the long-term health of the nation's scientific infrastructure. It is also essential that every effort be made to limit the duration of the outage. To this end, a comprehensive work breakdown structure was developed during the past year to determine the scope of the project. A detailed project schedule is currently being developed. The effort thus far has been focused on "Activities Necessary to Achieve Confinement"; through the procurement of guides or on setting priorities on components which will need to be designed, drafted, fabricated and installed.

A mock-up assembly representing the reactor tubes that house neutron guides (CTE, CTC, and CTW), along with the bio-shield and features attached to the bio-shield face has been created. A final design is expected by early 2020. In lieu of replacing CTW in-pile and casing, a mock-up has been modeled. It will be used to practice extraction and reinstallation of CTW.

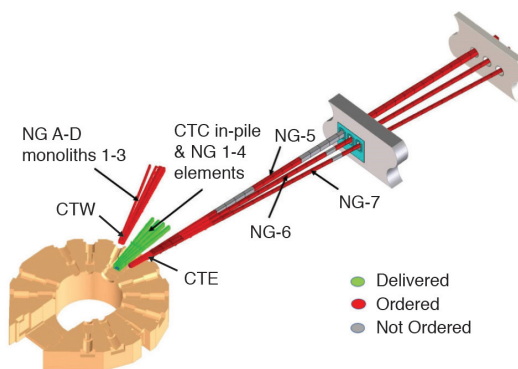


FIGURE 5: Schematic diagram of the guides that will be installed during the installation of the new D₂ cold source. Most, though not all, have been ordered.

Since neutron guides NG-5, NG-6, and NG-7 were installed nearly 30 years ago we will use the shutdown to replace the existing guides with modern ones. In addition, some other guides will also be replaced to enhance safety and structural integrity. Most of these guides have been ordered and are expected to be delivered at the end of calendar year 2020 (Fig. 5). The CTC in-pile guide monolith has been delivered. The first elements of neutron guide 1 through 4, made from aluminum, have also been delivered. The remainder of the guides needed to achieve confinement are expected to be ordered in the second quarter of FY 2020. This is pending design progress of some components such as NG-5, NG-6, and NG-7 main shutters, as well as NG 5-7 common casing. Design of these components will commence at the start of 2020.

DCS

The Disk Chopper time of flight Spectrometer has relied on a data acquisition system designed in-house to generate 20-bit timestamps relative to a synchronizing “T0” pulse. Although the equipment has been largely reliable over its lifetime it has demonstrated a number of limitations. This year that legacy system was replaced by a collection of timestamping units based on the Reuter Stokes Processing Platform system on chip (SOC). Each of the 20 modules has 48 TTL inputs and generates 96-bit event words containing the assignable pixel ID of the event input and a 64-bit precision time protocol (IEEE 1588) absolute timestamp. The equipment has been in service since May of this year.

Polarized ^3He Spin Filters

The spin filter program has two primary aims, (i) provide polarized ^3He spin filters for neutron scattering experiments on the NG-7 SANS and vSANS instruments, the Multi-Axis Crystal Spectrometer (MACS), and the BT-7 thermal TAS, and (ii) enhance polarized neutron measurement capabilities throughout the facility. During the past year, the NCNR's spin filter program served 44 user experiments, for a total of 170 days of beam time, 185 bar-liters of polarized ^3He gas, and 182 polarized ^3He cells.

During 2019, the team deployed a platform to support the ^3He spin analyzer system on vSANS. The nuclear magnetic resonance ^3He spin analyzer and flipper system is now seamlessly integrated into the vSANS data acquisition systems for polarized beam experiments. The team also developed a new ^3He cell for SANS polarization analysis (Fig. 6) that has more than doubled the relaxation time of the ^3He polarization. This has allowed polarized beam experiments on both the SANS and vSANS instruments to operate for up to three days without swapping the cells and has yielded a significant improvement in neutron polarization.

For BT-7, the team developed a polarized beam measurement capability with the 7 T superconducting magnet. The ^3He polarizer developed last year yielded an improvement in the relaxation time of the ^3He polarization at fields of 2 T to 3 T by an order of magnitude, making polarized beam experiments at high fields on BT-7 feasible. Figure 7 shows a routine polarized beam setup at low sample fields with the improved polarizer.

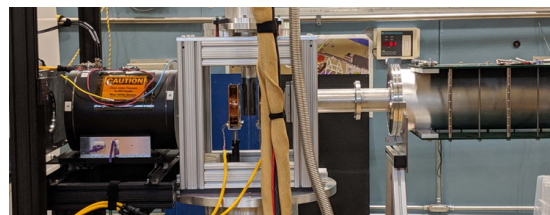


FIGURE 6: One of the polarized beam configurations implemented on vSANS for studies of a skyrmion system at low fields. Shown in the picture is the dedicated magnetic guide field around a vacuum tube upstream of the sample and the newly developed ^3He spin analyzer that has more than doubled the relaxation time.

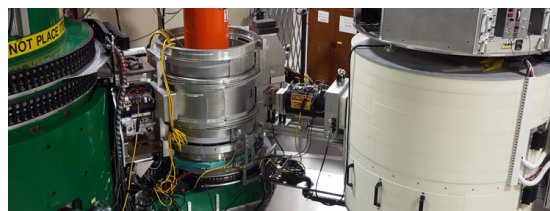


FIGURE 7: Polarized setup at low sample fields with the recently improved polarizer on BT-7. The polarizer fits into the tight space between the monochromator drum and sample enclosure. This set-up has significantly improved the relaxation time for polarized beam experiments at 2 T to 3 T.

The team, in collaboration with the University of Maryland, has also continued work on a spherical neutron polarimetry device for studies of complex magnetic structures.

Data Acquisition Software

The New Instrument Control Environment (NICE) has continued to spread to more instruments at the NCNR. This year, NICE was deployed on USANS and is also operating CANDOR, which is in the commissioning phase. Triple axis instrument control is under development. During 2019, initial BT-7-NICE requirements were gathered and prioritized, developing a schedule for development and deployment to BT-7. Planning also included time to develop general features for all triple axis instruments in the facility. A preliminary version of NICE has now been installed and tested on BT-7 during an instrument shutdown to avoid impacting scheduled experiments.

Additional features have been developed to improve the operation of NICE, both behind the scenes and for the user experience. A new, “one-click”, deployment system for the NICE client has been developed. This automatically keeps the client software and even the Java Virtual Machine, used to run it, up to date seamlessly. This has greatly increased the number of users remotely using the client to monitor their experiments. The new NICE “queueing” system is also being deployed, providing a highly accurate estimate of how long a series of commands will take to execute, giving real-time updates of time remaining. It also allows easy browsing of command histories. A real-time display of reactor and cold-source status has also been added. Looking towards future development, the NICE team transitioned to a new IDE and development environment and has started work toward upgrading from the current Long-Term Stable (LTS)

Serving the Science and Technology Community

The mission of the NIST Center for Neutron Research is to assure the availability of neutron measurement capabilities to meet the needs of U.S. researchers from industry, academia and other U.S. government agencies. To carry out this mission, the NCNR uses several different mechanisms to work with participants from outside NIST, including a competitive proposal process, instrument partnerships, and collaborative research with NIST.

Proposal System

Time on NCNR instruments is made available through a competitive, peer-review proposal process. The NCNR issues calls for proposals approximately twice a year. Proposals are reviewed at several different levels. First, expert external referees evaluate each proposal on merit and provide us with written comments and ratings. This is a very thorough process where several different referees review each proposal. Second, the proposals are evaluated on technical feasibility and safety by NCNR staff. Third, we convene our Beam Time Allocation Committee (BTAC) to assess the reviews and to allocate the available instrument time. Using the results of the external peer review and their own judgment, the BTAC makes recommendations to the NCNR Director on the amount of beam time to allocate to each approved experiment. Approved experiments are scheduled by NCNR staff members in consultation with the experimenters.

The current BTAC members are:

- Pinar Akcora (Stevens Institute of Technology)
- Andrew Allen (NIST Ceramics Division)
- Jeffrey Allen (Michigan Technological University)
- Collin Broholm (The Johns Hopkins University)
- Leslie Butler (Louisiana State University)
- Mark Dadmun (University of Tennessee)
- Thomas Epps (University of Delaware)
- Kushol Gupta (University of Pennsylvania)
- John Heron (University of Michigan)
- Hubert King (ExxonMobil)
- Valery Kiryukhin (Rutgers University)
- Ramanan Krishnamoorti (University of Houston)
- Jennifer Lee (National Institutes of Health)
- Kai Liu (Georgetown University)
- Martin Mourigal (Georgia Institute of Technology)
- James Neilson (Colorado State University)
- Lilo Pozzo (University of Washington)
- Stephen Wilson (University of California Santa Barbara)

Partnerships

The NCNR may form partnerships with other institutions to fund the development and operation of selected instruments. Partnerships are negotiated for a fixed period and may be renewed if there is mutual interest and a continued need. These partnerships have proven to be an important and effective way to expand the research community's access to NCNR capabilities.

Collaboration with NIST

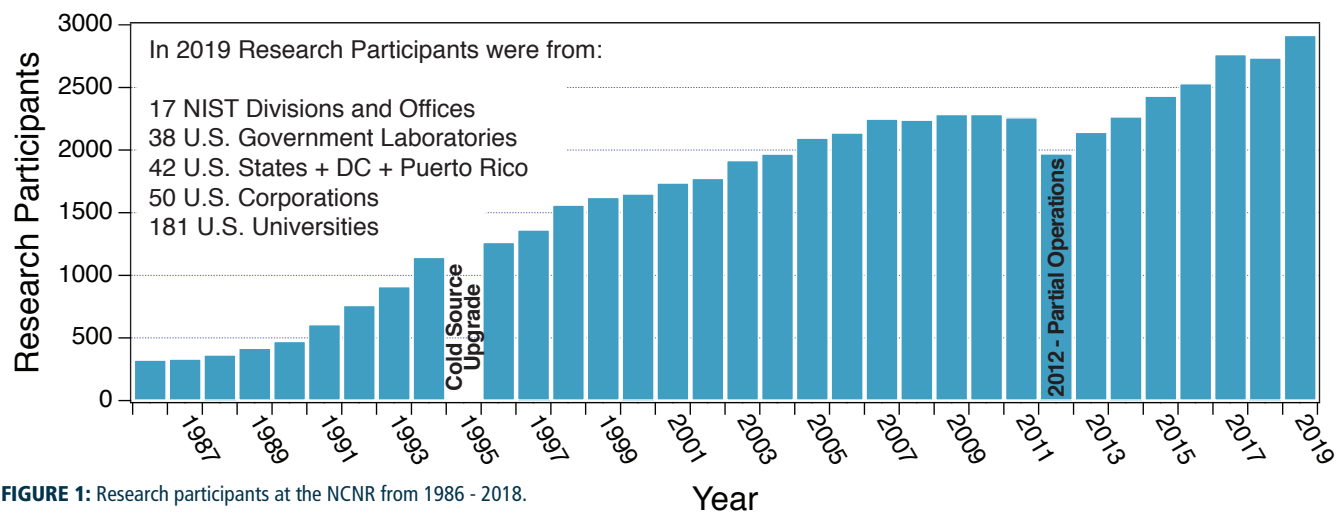
Some time on all instruments is available to support the NIST mission. This time is used to work on NIST research needs, instrument development, and promoting the widespread use of neutron measurements in important research areas, particularly by new users. As a result of these objectives, a significant fraction of the time available to NIST staff is used collaboratively by external users, who often take the lead in the research. Access through such collaborations is managed through written beam time requests. In contrast to proposals, beam time requests are reviewed and approved internally by NIST staff. We encourage users interested in exploring collaborative research opportunities to contact an appropriate NIST staff member.

Research Participation and Productivity

The NCNR continued its strong record of serving the U.S. research community this year. Over the 2019 reporting year, the NCNR served 2769 researchers. (Research participants include users who come to the NCNR to use the facility as well as active collaborators, including co-proposers of approved experiments, and co-authors of publications resulting from work performed at the NCNR.) As the number of participants has grown, the number of publications per year has also increased.

2019 NCNR Proposal Program

In response to the last two calls for proposals (calls 38 and 39) for instrument time, we received 774 proposals, of which 441 were approved and received beam time. The following table shows the statistics for several instrument classes. The oversubscription, i.e., the ratio of days requested on all proposals to the days available, was 2.3 on average. Proposal demand has grown since the NCNR first began accepting proposals in 1991 and has more than doubled in the past decade.



Instrument class	Proposals	Days requested	Days allocated
SANS	281	1033	557
Reflectometers	109	724	360
Spectrometers	339	2260	899
Diffraction	21	73	56
Imaging	24	155	72
Total	774	4245	1944

Users Group

The NCNR Users Group Executive Committee (EC) provides an independent forum for all facility users to raise issues to NCNR management, working through its executive officers to carry out this function. All members of the EC are elected by NCNR users. The current members of the EC are Carlos Lopez-Barron, Chair (ExxonMobil), Brian Habersberger (The Dow Chemical Company), Michael Hore (Case Western University), Dmitry Reznik (University of Colorado), Samantha Rhinehart (Student/Postdoc Member, University of Tennessee), Stephen Wilson (University of California Santa Barbara), and Claire White (Princeton University).

The EC regularly solicits user feedback via a variety of means. The User Group held a meeting at the American Conference on Neutron Scattering (ACNS) in June 2018 in College Park, MD and plans to have another meeting at the upcoming ACNS in 2020. The EC also administers a brief email survey that is sent to users approximately one week after the completion of their experiment. Issues identified by the EC are regularly discussed with the NCNR and CHRNS management teams with a focus on resolving those requiring immediate action. The EC also conducted a comprehensive user survey in the fall of 2015. There were more than 450 responses the majority of whom are CHRNS users. Overall the results, which are posted on the [NCNR User Group website](#), showed improvement relative to those from 2011 in 5 of the 6 general categories. Working

closely with the EC, the NCNR and CHRNS management teams developed a comprehensive response/action plan designed to make the user experience more productive and enjoyable (Refer to [NCNR's response to the User Group survey](#)).

Panel of Assessment

The major organizational units of NIST are evaluated for quality and effectiveness by the National Research Council (NRC), the principal operating agency of both the National Academy of Sciences and the National Academy of Engineering. A panel appointed by the NRC convened at the NCNR on July 10 - 12, 2018. The panel members included Tom C. Lubensky (University of Pennsylvania, chair), Simon Billinge (Columbia University), Susan Coppersmith (University of Wisconsin, Madison), Aaron Eberle (ExxonMobil Chemical Company), Paul Fleury (Yale University), Dale Klein (University of Texas), Tonya Kuhl (University of California, Davis), Peter Moore (Yale University) and Thomas Russell (University of Massachusetts, Amherst). Their findings are summarized in a report entitled ["An Assessment of the National Institute of Standards and Technology Center for Neutron Research: Fiscal Year 2018"](#).

The Center for High Resolution Neutron Scattering (CHRNS)

CHRNS is a national user facility that is jointly funded by the National Science Foundation and the NCNR. Its primary goal is to maximize access to state-of-the-art neutron scattering instrumentation for the academic research community. It operates five neutron scattering instruments at the NCNR, enabling users from around the nation to observe dynamical phenomena involving energies from ≈ 30 neV to ≈ 10 meV, and to obtain structural information on length scales from ≈ 1 nm to ≈ 10 μ m. A more detailed account of CHRNS activities may be found on pp 62 of this report.

Partnerships for Specific Instruments

NG-7 SANS Consortium

A consortium that includes NIST, the ExxonMobil Research and Engineering Company, and the Industrial Partnership for Research in Interfacial and Materials Engineering (IPRIME) led by the University of Minnesota, operates, maintains, and conducts research at the 30m SANS instrument located on NG7.

Consortium members conduct independent research programs primarily in the area of large-scale structure in soft matter. For example, ExxonMobil has used this instrument to deepen their understanding of the underlying nature of ExxonMobil's products and processes, especially in the fields of polymers, complex fluids, and petroleum mixtures.

The nSoft Consortium

The nSoft consortium was founded in 2012 to enable industrial access to neutron scattering and soft materials science at NIST. Since its founding the consortium has grown from six to thirteen member companies with representation from the specialty chemical, consumer product, pharmaceutical, automotive, and petrochemical industries. The 10 m SANS is the flagship instrument of the consortium, enabling measurement development and rapid access for industrial members. The consortium is not limited to SANS measurements, however, with members making measurements across the NCNR including reflectometry, imaging, depth profiling and dynamics. The consortium goes beyond access to neutron instrumentation by enabling collaboration between NIST staff and nSoft members toward the development of advanced measurement capabilities that enable cutting edge research and industrially relevant materials measurements. Further, through a model of expertise transfer we aim to ensure that the industrial sector can access these state-of-the-art measurement technologies and incorporate them into their own analytical research programs. Contact: Ron Jones, nSoft Director, rljones@nist.gov, 301-975-4624.

NIST / General Motors – Neutron Imaging

An ongoing partnership and collaboration between General Motors and NIST, which also includes Honda Motors through GM's partnership with Honda, continues to yield exciting results using neutron imaging. Neutron imaging has been employed to visualize the operation of fuel cells for automotive vehicle applications. Neutron imaging is an ideal method for visualizing hydrogen, the fuel of electric vehicle engines. These

unique, fundamental measurements provide valuable material characterizations that will help improve the performance, increase the reliability, and reduce the time to market introduction of the next generation electric car engines. 25% of the time on the BT-2 Neutron Imaging Facility is made available to the general scientific community through peer-reviewed proposals.

Interagency Collaborations

The Smithsonian Institution's Nuclear Laboratory for Archaeological Research is part of the Anthropology Department at the National Museum of Natural History. It has had a longstanding and productive partnership with the NCNR, during which time it has chemically analyzed over 43,100 archaeological artifacts by Instrumental Neutron Activation Analysis (INAA), drawing extensively on the collections of the Smithsonian, as well as on those of many other institutions in this country and abroad. Such chemical analyses provide a means of linking these diverse collections together in order to study continuity and change involved in the production of ceramic and other artifacts.

DENIM

The 8th annual international Design and Engineering of Neutron Instruments Meeting (DENIM) was held in North Bethesda, MD from 17th-19th September 2019. Over 125 people attended DENIM from more than 15 countries comprised of other neutron scattering institutes, universities and the corporations that support the community. DENIM is held under the patronage of the International Society of Neutron Instrument Engineers (ISNIE) and is the world's largest conference on the engineering of neutron instruments. This year DENIM was organized jointly by the NCNR and the University of Maryland.

The conference included two days of talks and posters presented by attendees of DENIM. The overall theme for the conference was "Lessons Learned" and presenters shared openly about what has worked, and more importantly, what hasn't worked in key areas of neutron instrument engineering such as shielding, motion control, vacuum, project management, neutron guide alignment, choppers and more. Another hot topic this year was how 3D printing is successfully being used by members of the community. The final day of the conference included a tour of the NCNR and other NIST labs. Attendees were extremely impressed by the labs at NIST. On Sept. 20th, the NCNR hosted the 2nd annual ISNIE summer school with a focus on neutron guides.

The Center for High Resolution Neutron Scattering (CHRNS)

The Center for High Resolution Neutron Scattering is a national user facility that is jointly funded by the National Science Foundation through its Division of Materials Research (grant number DMR-1508249) and by NIST. The CHRNS agreement was renewed for five years beginning on September 1, 2015. The primary purpose of this partnership is to maximize access for the scientific community to transformative neutron scattering instrumentation. The core mission of CHRNS is fourfold: (i) to develop and operate neutron scattering instrumentation, with broad application in materials research, for use by the general scientific community; (ii) to promote the effective use of the CHRNS instruments by having an identifiable staff whose primary function is to assist users; (iii) to conduct research that advances the capabilities and utilization of CHRNS facilities; and (iv) to contribute to the development of human resources through educational and outreach efforts. The scientific community provides essential input for new directions for CHRNS through a variety of mechanisms including post-experiment feedback and user surveys, administered by the NCNR User Group Executive Committee (EC) in the fall of 2015. The EC also led a discussion for neutron users at the recent American Conference on Neutron Scattering (ACNS) held on June 24-28, 2018 in College Park, MD. A 2 ½ minute video, *Getting Great Data with CHRNS*, highlights and summarizes CHRNS' focus on advancing neutron scattering measurement capabilities and its prominent role in expanding, educating, and diversifying the community of researchers who use neutron methods. View the video on the [NCNR website](#).

Scattering Instruments

The portfolio of instruments supported by CHRNS continues to evolve to ensure that the scientific capabilities exceed or are comparable to the best worldwide. Combined, CHRNS instruments can provide structural information on a length scale of ≈ 1 nm to ≈ 10 μ m, and dynamical information on energy scales from ≈ 30 neV to ≈ 10 meV. During FY2019 CHRNS continued to support operation of the High Flux Backscattering Spectrometer (HFBS), the Neutron Spin-Echo (NSE) spectrometer, and the Multi-Angle Crystal Spectrometer (MACS), which boasts the world's highest monochromatic cold-neutron flux and is now the premier instrument in the world for investigations of quantum magnetism. A new event mode was added to the existing time-stamped histogram data collection capability on MACS. In this new mode, all individual neutron events are recorded, and the data can later be rebinned into traditional

histogram data for analysis and visualization using the program *Mslice*. This new mode combined with the new sweeping instrument theta-angle operation greatly improves data acquisition efficiency. The data reduction and visualization has been continuously updated with new options and tools to allow users more ways to visualize the data, such as the new MACS histogram data. On NSE ongoing efforts to tune the machine at long wavelengths this past year have resulted in higher quality data. The instrumental resolution function was also improved by reducing the magnetic field inhomogeneity of the instrument.

Since its inception, CHRNS has provided the user community with outstanding SANS capabilities. During this past year, the innovative very-small-angle neutron scattering (vSANS) instrument was added to the CHRNS user program to meet the emerging needs of the scientific community. The versatile vSANS has a variety of front-end optics choices and three separate, adjustable detectors that provide an extended Q range from 0.002 nm⁻¹ to 7 nm⁻¹. The 45 m instrument provides unprecedented opportunities for structural studies of materials from the nanoscale into the mesoscale for complex systems with hierarchical structures. Following the first successful scientific use of the instrument in the spring of 2018, the first experiment awarded beamtime through the CHRNS proposal system was conducted in June 2018.



FIGURE 1: CHRNS user Adrian Rennie runs vSANS in consultation with Dan Neumann and Paul Butler.

Another significant addition to the CHRNA facility is the Chromatic Analysis Neutron Diffractometer or Reflectometer (CANDOR). This instrument is currently being commissioned. The novelty of CANDOR lies in its use of a state-of-the-art “energy-dispersive” detector, which permits a polychromatic beam to impinge on the sample. The energy-dispersive detector analyzes the scattered beam using a linear series of 54 crystals, each set to diffract neutrons of a particular wavelength to a corresponding detector while allowing neutrons of other wavelengths to pass through to other crystals down the line. In this manner, the wavelength and scattering vector Q will be known for each neutron detected. Data reduction is provided by our *Reductus* web-based software which allows users to access and reduce their data anywhere they have a web connection. User access is expected in 2020. When fully operational, CANDOR will be the only instrument of this type in the world with data rates provided by the multiplex detector that exceed those available elsewhere in the world by perhaps an order of magnitude or more.

Research

The wide ranges of instrument capabilities available in CHRNA support a very diverse scientific program, allowing researchers in materials science, chemistry, biology, geosciences, and condensed matter physics to investigate materials such as polymers, metals, ceramics, magnetic materials, colloids, fluids and gels, rocks, and biological molecules. The research community can obtain access to the state-of-the-art CHRNA instrumentation using the NCNR’s proposal system. Proposals to use the CHRNA instruments are critically reviewed on the basis of scientific merit and/or technological importance. In the previous Call for Proposals (call 39), 266 proposals requested CHRNA instruments, and 139 of these proposals received beam time. Of the 1360 days requested for the CHRNA instruments, 562 were awarded. Roughly half of the users of neutron scattering techniques at the NCNR use CHRNA-funded instruments, and more than 1/4 of NCNR publications (see the “Publications” section on p. 70), over the current one-year period, are based on research performed using these instruments. This report contains several highlights of CHRNA publications. See the labeled highlights in the table of contents.

Scientific Support Services

CHRNA provides scientific support in three critical areas: sample environment, chemical laboratories and the production and delivery of polarized neutron beams. The accomplishments in each of these areas during FY2019 are summarized below.

CHRNA offers six well-equipped and well-supplied user laboratories, including a Guide Hall Laboratory which provides a safe environment for CHRNA users to handle activated samples. The laboratory staff continues to ensure that the required equipment and/or supplies are available for users when they arrive for their experiments.

The CHRNA Sample Environment team provides users with the equipment and training needed to make neutron

measurements under external conditions of temperature, pressure, magnetic field, humidity, and fluid flow. From mK dilution refrigeration systems to a 1600 °C furnace, the equipment spans a large temperature range. Beyond precise temperature control, CHRNA users have access to a variety of flow systems, rheometers, gas-loading systems, two superconducting magnets with fields of up to 11 Tesla, and other complex equipment to control parameters such as pressure, humidity, and electric fields. During FY2019 the team set up and operated a diverse range of complex sample environment equipment for more than 137 experiments on CHRNA instruments. This total includes approximately 30 experiments involving rheometers and shear cells, 20 experiments that required access to mK temperatures, 11 of which simultaneously required magnetic fields up to 11.5 T. The valves of the 10 T superconducting magnet were replaced with electromagnetic valves to make the system more efficient. A new sample holder was developed to work with thin films. The new holder consists of a borated aluminum plate which shields background due to the sample stage components, a borated aluminum clamp for holding the sample substrate, and a boron nitride outer shell that goes to just the edge of the sample, which shields any background from the screws used for sample mounting. This has reduced the background by as much as an order of magnitude. CHRNA also enables polarized neutron scattering experiments on MACS and SANS instruments by providing ^3He spin analyzer cells with specialized geometries. During FY2019, the ^3He Spin Filter team served two MACS and ten SANS user experiments. It is notable that CHRNA runs the only SANS program in the U.S. that routinely operates with full polarization analysis. With the double-V supermirror, RF flipper and guide fields installed on vSANS, ^3He cell lifetimes of > 300 hours have been achieved with polarization efficiencies exceeding 99 %. MACS provides the most intense monochromatic polarized cold neutron beam with the largest scattering angle coverage for polarization analysis. The recent focus for MACS has been on optimizing the infrastructure for routine, high-flux, wide-angle polarization analysis over a broad energy range. To that end, the dedicated ^3He Spin Filter instrumentation rack has been upgraded. Spin filter lifetimes have been improved to enable usage for up to four experiment days without changing filters.



FIGURE 2: CANDOR reflectometer in August 2019. Commissioning is in progress.



FIGURE 3: Participants and instructors in the 2019 CHRS Summer School “Methods and Applications of Neutron Spectroscopy”

Upon commissioning, CANDOR will feature spin-polarized incident beams using a double-V supermirror polarizer (efficiency of > 95 %), along with an RF spin flipper (efficiency of 99.5 %) and will be spin-analyzed by a ^3He spin filter. The ^3He spin filter apparatus for CANDOR has been tested offline and is ready for polarized beam experiments. The setup includes a magnetically shielded solenoid to maintain the ^3He polarization and a radio-frequency flipper to flip a large cross-sectional incident beam with an efficiency exceeding 99.9 %.

Education and Outreach

CHRS sponsors a variety of educational programs and activities tailored to specific age groups and professions. The twenty-fifth annual summer school, held on July 22 – July 26, 2019 was entitled “Methods and Applications Neutron Spectroscopy.” Thirty-four graduate and postdoctoral students from 29 universities participated in the school. Guest lecturers included Prof. Kemp Plumb from Brown University and Dr. James Rhyne (emeritus) from the Department of Energy. Dr. Rob Dimeo, the NCR Director, encouraged the students to pursue careers in neutron scattering during his talk following the summer school banquet. CHRS co-sponsored several other workshops throughout the year including the third Fundamentals of Quantum Materials Winter school at the University of Maryland (January 14-19, 2019).

CHRS pursues many avenues for engaging researchers from institutions that serve diverse groups. To that end, a partnership between CHRS and the Interdisciplinary Materials Research and Education Laboratory (IMREL) at Fayetteville State University (FSU) was established in August 2018 through the NSF PREM (Partnerships for Research and Education in Materials) program (Agreement No. DMR-

1827731). The [webpage of the Partnerships for Research and Education in Materials](#) supports cutting-edge materials research as the context for producing diverse, motivated, and skilled minority and female students as future professional leaders in materials-related fields. This new partnership is organized around a common theme of structure-processing-property correlations of nanomaterials to support student training in the context of research using neutron scattering. During the summer of 2019 CHRS staff members hosted two PREM interns (Candyce Collins and Washat Roxanne Ware) and are looking forward in the coming year to giving seminars and lectures at FSU.

CHRS staff scientists also participated in teaching courses and giving lectures at nearby universities. In the fall of 2018, Susan Kreuger (CHRS Instrument Scientist) gave two lectures on small-angle scattering fundamentals and biology applications for a graduate level course taught by David Fushman at the University of Maryland. The course, entitled “Methods for Structure Determination in Solution,” also included SANS lab practicals.

As part of its expanding education and outreach effort, CHRS allows university-based research groups with BTAC-approved experimental proposals to request travel support for an additional graduate student to participate in the experiment. This support is intended to enable new graduate students, for example, to acquire first-hand experience with a technique that they may later use in their own research. Announcements of this program are sent to all of the university groups whose experimental proposals receive beam time from the BTAC. Recipients of the announcement are encouraged to consider graduate students from under-represented groups for this opportunity. The program is also



FIGURE 4: The 2019 SURF students

advertised on the [NCNR's website](#).

As in previous years, CHRNS participated in NIST's Summer Undergraduate Research Fellowship (SURF) program. In 2019 CHRNS hosted 15 SURF students, including two previous SHIP students. The students performed research on topics ranging from self-assembled amphiphilic diblock copolymers and oral insulin delivery via microencapsulation to the depth dependence of skyrmions in thin films and the thermal-hydraulics feasibility for an ultra-compact nuclear reactor. They presented their work at the NIST SURF colloquium in August 2019 in sessions moderated by program officers from the National Science Foundation. The colloquium featured a plenary talk by Emily Blick from the University of Maryland on SANS characterization of vesicle stability for liposomal nanomedicines. It is notable that SURF student, Mark Zic from the University of Maryland, recently received a scholarship from the Barry Goldwater Foundation, in part, for his CHRNS SURF research on a newly discovered spin-triplet superconductor.

CHRNS initiated a Research Experiences for Teachers (RET) program in 2010. For the summer of 2019, the program hosted two teachers from Montgomery County, MD. Scott Hanna from Winston Churchill High School returned for a second year to study the diffusion of quantum liquids in bulk and confinement using DCS under the guidance of Tim Prisk and Richard Azuah. Brennan Boothby from The Nora School investigated pluronic micelles in polymer nanocomposites using SANS with mentors Liz Kelley and Antonio Faraone. Both Mr. Hanna and Mr. Boothby highlighted their research in oral presentations in August.

Elementary, Middle, and High School Activities

The Summer High School Intern Program (SHIP) is a very successful, competitive NIST-wide program for students who are interested in performing scientific research during the summer. CHRNS hosted eight interns from local high schools. The students investigated magnetic dead layers in rhombohedral perovskites, created an enhanced web interface for the NCNR data repository, improved phase segmentation techniques for analysis of neutron tomography images, developed reinforcement learning algorithms for efficiently obtaining crystallographic measurements, and optimized a neutron spin flipper using active learning algorithms. The results of the students' summer investigations were highlighted in a NIST-wide poster session, as well as in a well-attended symposium at the NCNR. Cathy Yung from Richard

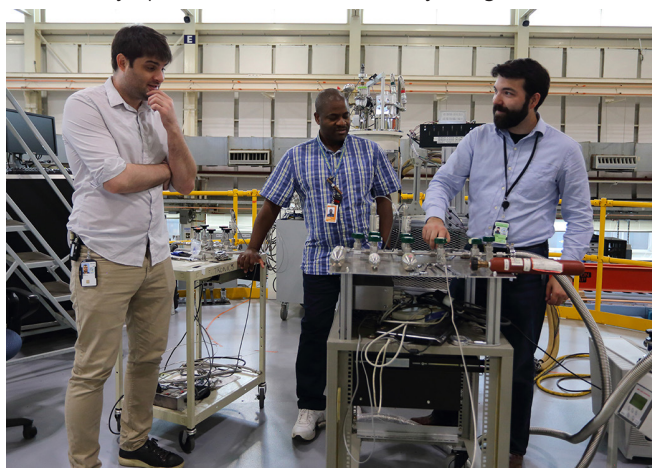


FIGURE 5: Scott Hanna (right) from Winston Churchill High School works on a pressure rig on DCS with the assistance of mentors Tim Prisk (right) and Richard Azuah (center).



FIGURE 6: The 2019 SHIP interns

the year. CHRS staff give presentations and facility tours to students as part of the NIST activities for the annual “Take Your Daughters and Sons to Work Day.” At local schools CHRS staff members also give science-based talks or lead hands-on demonstrations at local schools, participate in STEM events, and even volunteer as robotics coaches.

2019 Awards



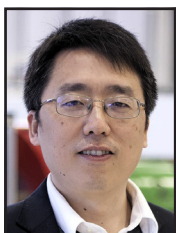
Craig Brown of the NCNR was named a **NIST Fellow**. The NIST Fellows are an elite group of 40 scientists and engineers recognized as NIST's most accomplished and influential researchers. Craig's expertise in gas storage and separation, his leadership and vision in energy materials, his thoughtful mentoring and support for young scientists, and his international recognition throughout the world in materials science contributed to NIST bestowing this honorific. In addition, Craig has also been elected as a **Fellow of the American Crystallographic Association (ACA)**. The ACA Fellows program recognizes a high level of excellence in scientific research, teaching, and professional duties, but also service, leadership, and personal engagement in the ACA and the broader world of crystallography and science.



The NCNR's **Dan Flynn, Paul Liposky, Tony Norbedo, and Rick Sprow** (L-R) were selected to receive the 2018 **Department of Commerce Bronze Medal** for their leadership of major reactor upgrade projects during the outage last year.



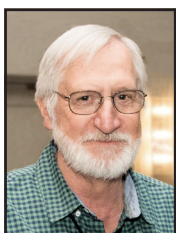
The NCNR's **William Ratcliff** has been elected a **Fellow of the American Physical Society**. William was cited "*for seminal neutron scattering studies of the magnetic order and spin dynamics in multiferroic materials.*"



Yun Liu of the NCNR was recognized by the journal "Current Opinion in Colloid & Interface Science" as one of the "**Outstanding Young Researchers in Colloid and Interface Science**" for his work on the phase behavior, structures, and dynamics of colloidal systems.



Congratulations to **Ryan Murphy** who received the **Most Outstanding Poster** award at the NIST Chapter of Sigma Xi 26th annual Postdoctoral Poster Presentation. Ryan's poster was entitled, "Capillary Rheo-SANS: Measuring the nanostructure and rheology of complex fluids at high shear rates"



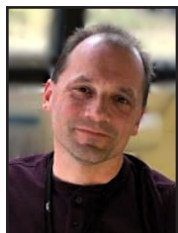
The NCNR's **Bob Williams** and **Mike Middleton** received the 2018 **Department of Commerce Silver Medal**. They were recognized "for commissioning a liquid deuterium refrigerator essential to ending HEU use in the NIST reactor while preserving or enhancing facility performance."



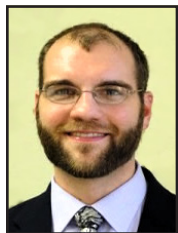
Ryan Need received an **Outstanding Poster** award in the category of Engineering and Physics at the NIST Chapter of Sigma Xi 26th annual Postdoctoral Poster Presentation. Ryan's presentation was entitled "Exchange bias and closure domains in a ferromagnetic multilayer with orthogonal anisotropies".



Yimin Mao of the NCNR was awarded the **Oxford Cryosystems Low Temperature Poster Prize** for his poster titled: "Furan-2,5-dicarboxylic acid, a promising platform molecule: polymer, monomer, and MOFs". The award was presented at the American Crystallographic Association meeting in Covington, Kentucky in July 2019.



Lawrence Wroten of the NCNR submitted the winning logo entry for the International Society for Neutron Instrument Engineers.



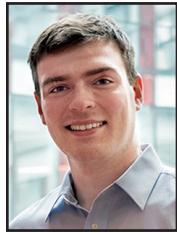
David Hoogerheide of the NCNR received the 2019 **Alumni Achievement Award** from Western Michigan University's physics department



Julia Mundy, assistant professor of physics at Harvard University was awarded the 2019 **IUPAP Young Scientist Prize** in the field of magnetism "For pathbreaking research on electric field control of magnetism using epitaxially designed multiferroics." In addition, Julia was the recipient of the 2019 **George E. Valley Jr. Prize** from the American Physical Society in recognition of "pico-engineering and synthesis of the first room-temperature magnetoelectric multiferroic material." Prof. Mundy has been a user of the NCNR neutron scattering facilities for the past several years.



Lilo Pozzo, Weyerhaeuser Associate Professor of Chemical Engineering and a member of the faculty of the Clean Energy Institute at the University of Washington, was recognized with the 2018 **Clean Energy Education and Empowerment (C3E) Award** from the Department of Energy. Lilo, a long-time user of the NCNR and a former NCNR post-doc, was recognized for her achievements and leadership in clean energy education.



Mark Zic, an undergraduate student at the University of Maryland has been awarded a scholarship by the **Barry Goldwater Scholarship** and Excellence in Education Foundation, which encourages outstanding students to pursue advanced study and research careers in the sciences, engineering and mathematics. Mark was a SURF student at the NCNR and a research intern with the NCNR's Nick Butch during the school year.



Temilouwa Okusolubo of the University of Maryland Baltimore County won a 2nd place award at the Undergraduate Research Symposium in the Chemical and Biological Sciences for her poster entitled "Correlating Gramicidin Ion-Channel Formation to Artificial Membrane Dynamics". Temilouwa was a SURF student at the NCNR.



Ian Hunt-Isaak has been awarded a **National Defense Science and Engineering Graduate (NDSEG) Fellowship**. NDSEG Fellowships are awarded to applicants who will pursue a doctoral degree in one of fifteen supported disciplines. Ian was a CHRNS user and a SURF student as an undergraduate. Ian is currently attending graduate school at the Harvard School of Engineering and Applied Sciences and is pursuing a PhD in applied physics.



Montgomery Blair High School Magnet Program hosted the 27th Annual Magnet Research Convention where several of the awardees were SHIP students mentored by NCNR staff. **Ryan Cho** was awarded the **Thomas Edison Award for Excellence in STEM**, mentored by William Ratcliff of the NCNR. **Telon Yan** was awarded the **Thomas Edison Award for Excellence in STEM**, also was mentored by William Ratcliff. **Isabella DeClue** was recognized with the **Washington Academy of Sciences Award** and the **Dr. Vaccaro Scholarship Award** in the Physical Sciences Category, mentored by Jacob LaManna of PML.



Mike Hore, an Assistant Professor of Macromolecular Science and Engineering at Case Western University, and a former NCNR post-doc was recognized as an **"Emerging Investigator"** by the "Journal of Materials Chemistry B".



Efrain Rodriguez, Associate Professor of Chemistry and Biochemistry at the University of Maryland and a former NCNR post-doc, is the recipient of the 2019 **Margaret Etter Early Career Award**. This award is given by the American Crystallographic Association "to recognize outstanding achievement and exceptional potential in crystallographic research demonstrated by a scientist at an early stage of their independent career." His research areas include iron-based superconductors, magnetic materials, transition metal oxides, crystallography, and make use of neutron scattering at the NCNR.



Stanford University graduate student **Rebecca Smaha** won the 2019 **Margaret C. Etter Student Lecturer Award** from the Neutron Special Interest Group of the American Crystallographic Association for her work on "Interconnected Signatures of Quantum Spin Liquid Physics Across the Barlowite Family of Quantum Magnets". The award was presented at the ACA meeting in Covington, Kentucky. Rebecca is a frequent user of the NCNR.

Publications: August 1, 2018 to July 31, 2019

- Adams, C.P., Callaghan-Patrachar, N., Peyronel, F., Barker, J., Pink, D.A., Marangoni, A.G., "Small and Ultra-Small Angle Neutron Scattering Studies of Commercial Milk," *Food Struct.* **21**, 100120 (2019). [CHNRNS]
- Ade-Browne, C., Dawn, A., Mirzamani, M., Qian, S., Kumari, H., "Differential Behavior of Sodium Laurylsulfate Micelles in the Presence of Nonionic Polymers," *J. Colloid Interf. Sci.* **544**, 276 (2019).
- Ali, S., Bleuel, M., Prabhu, V.M., "Lower Critical Solution Temperature in Polyelectrolyte Complex Coacervates," *ACS Macro Lett.* **8**(3), 289 (2019). [CHNRNS]
- Allen, A.J., Wong-Ng, W., Cockayne, E., Culp, J.T., Matranga, C., "Structural Basis of CO₂ Adsorption in a Flexible Metal-Organic Framework Material," *Nanomaterials* **9**(3), 354 (2019).
- Al-Rashid, M.M., Bhattacharya, D., Grutter, A., Kirby, B., Atulasimha, J., "Polarized Neutron Reflectometry Study of Depth Dependent Magnetization Variation in Co Thin Film due to Strain Transfer from PMN-PT Substrate," *J. Appl. Phys.* **124**(11), 113903 (2018).
- Anovitz, L.M., Zhang, X., Soltis, J., Nakouzi, E., Krzysko, A.J., Chun, J., Schenter, G.K., Graham, T.R., Rosso, K.M., De Yoreo, J.J., Stack, A.G., Bleuel, M., Gagnon, C., Mildner, D.F.R., Ilavsky, J., Kuzmenko, I., "Effects of Ionic Strength, Salt, and pH on Aggregation of Boehmite Nanocrystals: Tumbler Small-Angle Neutron and X-ray Scattering and Imaging Analysis," *Langmuir* **34**(51), 15839 (2018). [CHNRNS]
- Asgari, M., Semino, R., Schouwink, P., Kochetygov, I., Trukhina, O., Tarver, J.D., Bulut, S., Yang, S., Brown, C.M., Ceriotti, M., Queen, W.L., "An *In-Situ* Neutron Diffraction and DFT Study of Hydrogen Adsorption in a Sodalite-Type Metal-Organic Framework, Cu-BTTr," *Eur. J. Inorg. Chem.* **2019**(8), 1147 (2019).
- Ashenfelter, J., Balantekin, A.B., Baldenegro, C., Band, H.R., Bass, C.D., Bergeron, D.E., Berish, D., Bignell, L.J., Bowden, N.S., Bricco, J., Brodsky, J.P., Bryan, C.D., Bykadorova Telles, A., Cherwinka, J.J., Classen, T., Commeford, K., Conant, A.J., Cox, A.A., Davee, D., Dean, D., Deichert, G., Diwan, M.V., Dolinski, M.J., Erickson, A., Febbraro, M., Foust, B.T., Gaison, J.K., Galindo-Uribarri, A., Gilbert, C.E., Gilje, K.E., Glenn, A., Goddard, B.W., Hackett, B.T., Han, K., Hans, S., Hansell, A.B., Heeger, K.M., Heffron, B., Insler, J., Jaffe, D.E., Ji, X., Jones, D.C., Koehler, K., Kyzlyova, O., Lane, C.E., Langford, T.J., LaRosa, J., Littlejohn, B.R., Lopez, F., Lu, X., Martinez Caicedo, D.A., Matta, J.T., McKeown, R.D., Mendenhall, M.P., Miller, H.J., Minock, J.M., Mueller, P.E., Mumm, H.P., Napolitano, J., Neilson, R., Nikkel, J.A., Norcini, D., Nour, S., Pushin, D.A., Qian, X., Romero-Romero, E., Rosero, R., Sarenac, D., Seilhan, B.S., Sharma, R., Surukuchi, P.T., Trinh, C., Tyra, M.A., Varner, R.L., Viren, B., Wagner, J.M., Wang, W., White, B., White, C., Wilhelmi, J., Wise, T., Yao, H., Yeh, M., Yen, Y.-R., Zhang, A., Zhang, C., Zhang, X., Zhao, M., "First Search for Short-Baseline Neutrino Oscillations at HFIR with PROSPECT," *Phys. Rev. Lett.* **121**(25), 251802 (2018).
- Ashenfelter, J., Balantekin, A.B., Baldenegro, C., Band, H.R., Bass, C.D., Bergeron, D.E., Berish, D., Bignell, L.J., Bowden, N.S., Boyle, J., Bricco, J., Brodsky, J.P., Bryan, C.D., Bykadorova Telles, A., Cherwinka, J.J., Classen, T., Commeford, K., Conant, A.J., Cox, A.A., Davee, D., Dean, D., Deichert, G., Diwan, M.V., Dolinski, M.J., Erickson, A., Febbraro, M., Foust, B.T., Gaison, J.K., Galindo-Uribarri, A., Gilbert, C.E., Gilje, K.E., Glenn, A., Goddard, B.W., Hackett, B.T., Han, K., Hans, S., Hansell, A.B., Heeger, K.M., Heffron, B., Insler, J., Jaffe, D.E., Ji, X., Jones, D.C., Koehler, K., Kyzlyova, O., Lane, C.E., Langford, T.J., LaRosa, J., Littlejohn, B.R., Lopez, F., Lu, X., Martinez Caicedo, D.A., Matta, J.T., McKeown, R.D., Mendenhall, M.P., Miller, H.J., Minock, J.M., Mueller, P.E., Mumm, H.P., Napolitano, J., Neilson, R., Nikkel, J.A., Norcini, D., Nour, S., Pushin, D.A., Qian, X., Romero-Romero, E., Rosero, R., Sarenac, D., Seilhan, B.S., Sharma, R., Surukuchi, P.T., Trinh, C., Tyra, M.A., Varner, R.L., Viren, B., Wagner, J.M., Wang, W., White, B., White, C., Wilhelmi, J., Wise, T., Yao, H., Yeh, M., Yen, Y.-R., Zhang, A., Zhang, C., Zhang, X., Zhao, M., "The PROSPECT Reactor Antineutrino Experiment," *Nucl. Instrum. Meth. A* **922**, 287 (2019).

- Ashenfelter, J., Balantekin, A.B., Band, H.R., Bass, C.D., Bergeron, D.E., Berish, D., Bowden, N.S., Brodsky, J.P., Bryan, C.D., Cherwinka, J.J., Classen, T., Conant, A.J., Cox, A.A., Davee, D., Dean, D., Deichert, G., Diwan, M.V., Dolinski, M.J., Erickson, A., Febbraro, M., Foust, B.T., Gaison, J.K., Galindo-Uribarri, A., Gilbert, C.E., Gilje, K.E., Hackett, B.T., Hans, S., Hansell, A.B., Heeger, K.M., Insler, J., Jaffe, D.E., Ji, X., Jones, D.C., Kzylova, O., Lane, C.E., Langford, T.J., LaRosa, J., Littlejohn, B.R., Lu, X., Martinez Caicedo, D.A., Matta, J.T., McKeown, R.D., Mendenhall, M.P., Minock, J.M., Mueller, P.E., Mumm, H.P., Napolitano, J., Neilson, R., Nikkel, J.A., Norcini, D., Nour, S., Pushin, D.A., Qian, X., Romero-Romero, E., Rosero, R., Sarenac, D., Surukuchi, P.T., Telles, A.B., Tyra, M.A., Varner, R.L., Viren, B., White, C., Wilhelmi, J., Wise, T., Yeh, M., Yen, Y.-R., Zhang, A., Zhang, C., Zhang, X., "Measurement of the Antineutrino Spectrum from ^{235}U Fission at HFIR with PROSPECT," *Phys. Rev. Lett.* **122**(25), 251801 (2019).
- Ashenfelter, J., Balantekin, A.B., Band, H.R., Bass, C.D., Bergeron, D.E., Berish, D., Bowden, N.S., Brodsky, J.P., Bryan, C.D., Cherwinka, J.J., Classen, T., Conant, A.J., Davee, D., Dean, D., Deichert, G., Detweiler, A.E., Diwan, M.V., Dolinski, M.J., Erickson, A., Febbraro, M., Foust, B.T., Gaison, J.K., Galindo-Uribarri, A., Gebre, Y., Gilbert, C.E., Gilje, K.E., Gustafson, I.F., Hackett, B.T., Hans, S., Hansell, A.B., Heeger, K.M., Hermanek, K.H., Insler, J., Jaffe, D.E., Jones, D.C., Kzylova, O., Lane, C.E., Langford, T.J., LaRosa, J., Littlejohn, B.R., Lu, X., Martinez Caicedo, D.A., Matta, J.T., McKeown, R.D., Mendenhall, M.P., Minock, J.M., Mueller, P.E., Mumm, H.P., Napolitano, J., Neilson, R., Nikkel, J.A., Norcini, D., Nour, S., Pushin, D.A., Qian, X., Romero-Romero, E., Rosero, R., Sarenac, D., Surukuchi, P.T., Tyra, M.A., Varner, R.L., Viren, B., White, C., Wilhelmi, J., Wise, T., Yeh, M., Yen, Y.-R., Zhang, A., Zhang, C., Zhang, X., "A Low Mass Optical Grid for the PROSPECT Reactor Antineutrino Detector," *J. Instrum.* **14**, P04014 (2019).
- Ashenfelter, J., Balantekin, A.B., Band, H.R., Bass, C.D., Bergeron, D.E., Berish, D., Bignell, L.J., Bowden, N.S., Brodsky, J.P., Bryan, C.D., Camilo Reyes, C., Campos, S., Cherwinka, J.J., Classen, T., Conant, A.J., Davee, D., Dean, D., Deichert, G., Diaz Perez, R., Diwan, M.V., Dolinski, M.J., Erickson, A., Febbraro, M., Foust, B.T., Gaison, J.K., Galindo-Uribarri, A., Gilbert, C.E., Hackett, B.T., Hans, S., Hansell, A.B., Hayes, B., Heeger, K.M., Insler, J., Jaffe, D.E., Jones, D.C., Kzylova, O., Lane, C.E., Langford, T.J., LaRosa, J., Littlejohn, B.R., Lu, X., Martinez Caicedo, D.A., Matta, J.T., McKeown, R.D., Mendenhall, M.P., Mueller, P.E., Mumm, H.P., Napolitano, J., Neilson, R., Nikkel, J.A., Norcini, D., Nour, S., Pushin, D.A., Qian, X., Romero-Romero, E., Rosero, R., Sarenac, D., Surukuchi, P.T., Tyra, M.A., Varner, R.L., Viren, B., White, C., Wilhelmi, J., Wise, T., Yeh, M., Yen, Y.-R., Zhang, A., Zhang, C., Zhang, X., "Lithium-Loaded Liquid Scintillator Production for the PROSPECT Experiment," *J. Instrum.* **14**, P03026 (2019).
- Ashenfelter, J., Balantekin, A.B., Band, H.R., Bass, C.D., Bergeron, D.E., Berish, D., Bowden, N.S., Brodsky, J.P., Bryan, C.D., Cherwinka, J.J., Classen, T., Conant, A.J., Dean, D., Deichert, G., Diwan, M.V., Dolinski, M.J., Erickson, A., Febbraro, M., Foust, B.T., Gaison, J.K., Galindo-Uribarri, A., Gilbert, C.E., Hackett, B.T., Hans, S., Hansell, A.B., Heeger, K.M., Insler, J., Jaffe, D.E., Jones, D.C., Kzylova, O., Lane, C.E., Langford, T.J., LaRosa, J., Littlejohn, B.R., Lu, X., Martinez Caicedo, D.A., Matta, J.T., McKeown, R.D., Mendenhall, M.P., Mueller, P.E., Mumm, H.P., Napolitano, J., Neilson, R., Nikkel, J.A., Norcini, D., Nour, S., Pushin, D.A., Qian, X., Romero-Romero, E., Rosero, R., Sarenac, D., Surukuchi, P.T., Telles, A.B., Tyra, M.A., Varner, R.L., Viren, B., White, C., Wilhelmi, J., Wise, T., Yeh, M., Yen, Y.-R., Zhang, A., Zhang, C., Zhang, X., "The Radioactive Source Calibration System of the PROSPECT Reactor Antineutrino Detector," *Nucl. Instrum. Meth. A*, in press.
- Ashkar, R., Bilheux, H.Z., Bordallo, H., Briber, R., Callaway, D.J.E., Cheng, X., Chu, X.-Q., Curtis, J.E., Dadmun, M., Fenimore, P., Fushman, D., Gabel, F., Gupta, K., Herberle, F., Heinrich, F., Hong, L., Katsaras, J., Kelman, Z., Kharlampieva, E., Kneller, G.R., Kovalevsky, A., Krueger, S., Langan, P., Lieberman, R., Liu, Y., Losche, M., Lyman, E., Mao, Y., Marino, J., Mattos, C., Meilleur, F., Moody, P., Nickels, J.D., O'Dell, W.B., O'Neill, H., Perez-Salas, U., Peters, J., Petridis, L., Sokolov, A.P., Stanley, C., Wagner, N., Weinrich, M., Weiss, K., Wymore, T., Zhang, Y., Smith, J.C., "Neutron Scattering in the Biological Sciences: Progress and Prospects," *Acta Crystallogr.* **D74**(12), 1129 (2018).
- Aulakh, D., Liu, L., Varghese, J.R., Xie, H., Islamoglu, T., Duell, K., Kung, C.-W., Hsiung, C.-E., Zhang, Y., Drouot, R.J., Farha, O.K., Dunbar, K.R., Han, Y., Wriedt, M., "Direct Imaging of Isolated Single-Molecule Magnets in Metal-Organic Frameworks," *J. Am. Chem. Soc.* **141**(7), 2997 (2019).
- Badzian, A., "The X-ray Diffraction Method for Study of Growth Defects in CVD Diamond Single Crystals," *Adv. Mater.* **7**(4), 89 (2018).
- Bailey, E.J., Griffin, P.J., Tyagi, M., Winey, K.I., "Segmental Diffusion in Attractive Polymer Nanocomposites: A Quasi-Elastic Neutron Scattering Study," *Macromolecules* **52**(2), 669 (2019). [CHRS]
- Balwani, A., Faraone, A., Davis, E.M., "Impact of Nanoparticles on the Segmental and Swelling Dynamics of Ionomer Nanocomposite Membranes," *Macromolecules* **52**(5), 2120 (2019). [CHRS]
- Bao, Z., Wang, J., Zhang, Z., Xing, H., Yang, Q., Yang, Y., Wu, H., Krishna, R., Zhou, W., Chen, B., Ren, Q., "Molecular Sieving of Ethane from Ethylene through the Molecular Cross-Section Size Differentiation in Gallate-Based Metal-Organic Frameworks," *Angew. Chem. Int. Edit.* **57**(49), 16020 (2018).

- Barry, K., Zhang, B., Anand, N., Xin, Y., Vailionis, A., Neu, J., Heikes, C., Cochran, C., Zhou, H., Qiu, Y., Ratcliff, W., Siegrist, T., Beekman, C., "Modification of Spin-Ice Physics in $\text{Ho}_2\text{Ti}_2\text{O}_7$ Thin Films," *Phys. Rev. Mater.*, in press. [CHNRS]
- Benedetto, A., Ballone, P., "An Overview of Neutron Scattering and Molecular Dynamics Simulation Studies of Phospholipid Bilayers in Room-Temperature Ionic Liquid/Water Solutions," *Physica B* **551**, 227 (2018). [CHNRS]
- Bettler, S., Landolt, F., Aksoy, Ö.M., Yan, Z., Gvasaliya, S., Qiu, Y., Ressouche, E., Beauvois, K., Raymond, S., Ponomaryov, A.N., Zvyagin, S.A., Zheludev, A., "Magnetic Structure and Spin Waves in the Frustrated Ferro-Antiferromagnet $\text{Pb}_2\text{VO}(\text{PO}_4)_2$," *Phys. Rev. B* **99**(18), 184437 (2019). [CHNRS]
- Bharati, A., Hudson, S.D., Weigandt, K.M., "Poiseuille and Extensional Flow Small-Angle Scattering for Developing Structure-Rheology Relationships in Soft Matter Systems," *Curr. Opin. Colloid In.*, in press.
- Bi, Z., Naveed, H.B., Mao, Y., Yan, H., Ma, W., "Importance of Nucleation during Morphology Evolution of the Blade-Cast PffBT4T-2OD-Based Organic Solar Cells," *Macromolecules* **51**(17), 6682 (2018). [CHNRS]
- Black, D.R., Mendenhall, M.H., Whitfield, P.S., Brown, C.M., Henins, A., Filliben, J.J., Cline, J.P., "Certification of Standard Reference Material 1879b Respirable Cristobalite," *Powder Diffr.* **33**(3), 202 (2018).
- Blanco, M.A., Hatch, H.W., Curtis, J.E., Shen, V.K., "A Methodology to Calculate Small-Angle Scattering Profiles of Macromolecular Solutions from Molecular Simulations in the Grand-Canonical Ensemble," *J. Chem. Phys.* **149**(8), 084203 (2018).
- Blanco, M.A., Hatch, H.W., Curtis, J.E., Shen, V.K., "Evaluating the Effects of Hinge Flexibility on the Solution Structure of Antibodies at Concentrated Conditions," *J. Pharm. Sci.* **108**(5), 1663 (2019).
- Bleuel, M., "Phase Locked Modulated (PLM) Small Angle Neutron Scattering (SANS)," *Nucl. Instrum. Meth. A* **927**, 184 (2019).
- Bocarsly, J.D., Heikes, C., Brown, C.M., Wilson, S.D., Seshadri, R., "Deciphering Structural and Magnetic Disorder in the Chiral Skyrmion Host Materials $\text{Co}_x\text{Zn}_y\text{Mn}_z$ ($x + y + z = 20$)," *Phys. Rev. Mater.* **3**(1), 014402 (2019).
- Bordelon, M.M., Kenney, E., Liu, C., Hogan, T., Posthuma, L., Kavand, M., Lyu, Y., Sherwin, M., Butch, N.P., Brown, C., Graf, M.J., Balents, L., Wilson, S.D., "Field-Tunable Quantum Disordered Ground State in the Triangular-Lattice Antiferromagnet NaYbO_2 ," *Nat. Phys.*, in press.
- Britton, K.A., Wu, Z., "A Neutronics Feasibility Study of the Triga LEU Fuel in the 20MWt NIST Research Reactor," in "Proceedings of the 2018 International Conference on Nuclear Engineering," edited by ASME, (26th International Conference on Nuclear Engineering, July 2018, London, UK), ICONE26-82433 (2018).
- Brok, E., Krycka, K.L., Vreeland, E.C., Gomez, A., Huber, D.L., Majkrzak, C.F., "Phase-Sensitive Small-Angle Neutron Scattering Experiment," *J. Phys. Commun.* **2**, 095018 (2018). [CHNRS]
- Bucior, B.J., Bobbitt, N.S., Islamoglu, T., Goswami, S., Gopalan, A., Yildirim, T., Farha, O.K., Bagheri, N., Snurr, R.Q., "Energy-Based Descriptors to Rapidly Predict Hydrogen Storage in Metal-Organic Frameworks," *Mol. Sys. Des. Eng.* **4**(1), 162 (2019).
- Buck, Z.N., Torres, J., Miskowicz, A., Mamontov, E., Kaiser, H., Hansen, F.Y., Taub, H., Tyagi, M., Collins, L., Herwig, K.W., "Effect of Melittin on Water Diffusion and Membrane Structure in DMPC Lipid Bilayers," *Europhys. Lett.* **123**, 18002 (2018). [CHNRS]
- Buenning, E., Jestin, J., Huang, Y., Benicewicz, B.C., Durning, C.J., Kumar, S.K., "Location of Imbibed Solvent in Polymer-Grafted Nanoparticle Membranes," *ACS Macro Lett.* **7**(9), 1051 (2018). [CHNRS]
- Buttrey, D.J., Blom, D.A., Vogt, T., "Complex Molybdenum-Vanadium Oxide Bronzes and Suboxides as Catalysts for Selective Oxidation and Ammoxidation of Light Hydrocarbons," in "Complex Oxides: An Introduction," edited by Vogt, T. and Buttrey, D.J., (World Scientific Co. Pte. Ltd., Singapore) Chap. **6**, 157 (2019).
- Byrne, J., Worcester, D.L., "The Neutron Lifetime Anomaly and Charge Exchange Collisions of Trapped Protons," *J. Phys. G Nucl. Partic.*, in press.
- Cappelletti, R.L., Udovic, T.J., Li, H., Paul, R.L., "Glassy Carbon, NIST Standard Reference Material (SRM 3600): Hydrogen Content, Neutron Vibrational Density of States and Heat Capacity," *J. Appl. Crystallogr.* **51**(5), 1323 (2018).
- Carrillo, J.-M.Y., Chen, W.-R., Wang, Z., Sumpter, B.G., Wang, Y., "Chain Conformation of Polymer Melts with Associating Groups," *J. Phys. Commun.* **3**(3), 035007 (2019).
- Chakraborty, S., Abbasi, A., Bothun, G.D., Nagao, M., Kitchens, C.L., "Phospholipid Bilayer Softening due to Hydrophobic Gold Nanoparticle Inclusions," *Langmuir* **34**(44), 13416 (2018). [CHNRS]

- Chapagain, K., Brown, D.E., Kolesnik, S., Lapidus, S., Haberl, B., Molaison, J., Lin, C., Kenney-Benson, C., Park, C., Pietosa, J., Markiewicz, E., Andrzejewski, B., Lynn, J.W., Rosenkranz, S., Dabrowski, B., Chmaissem, O., "Tunable Multiferroic Order Parameters in $\text{Sr}_{1-x}\text{Ba}_x\text{Mn}_{1-y}\text{Ti}_y\text{O}_3$," *Phys. Rev. Mater.*, in press.
- Chen, C.-W., Wang, W., Loganathan, V., Carr, S.V., Harriger, L.W., Georgen, C., Nevidomskyy, A.H., Dai, P., Huang, C.-L., Morosan, E., "Possible Mott Transition in Layered $\text{Sr}_2\text{Mn}_3\text{As}_2\text{O}_2$ Single Crystals," *Phys. Rev. B* **99**(14), 144423 (2019).
- Chen, H., Chen-Mayer, H.H., Turkoglu, D.J., Riley, B.K., Draeger, E., Polf, J.P., "Spectroscopic Compton Imaging of Prompt Gamma Emission at the MeV Energy Range," *J. Radioanal. Nucl. Ch.* **318**(1), 241 (2018).
- Chen, L., Chung, J.-H., Gao, B., Chen, T., Stone, M.B., Kolesnikov, A.I., Huang, Q., Dai, P., "Topological Spin Excitations in Honeycomb Ferromagnet CrI_3 ," *Phys. Rev. X* **8**(4), 041028 (2018).
- Chen, T., Chen, Y., Kreisel, A., Lu, X., Schneidewind, A., Qiu, Y., Park, J.T., Perring, T.G., Stewart, J.R., Cao, H., Zhang, R., Li, Y., Rong, Y., Wei, Y., Andersen, B.M., Hirschfeld, P.J., Broholm, C., Dai, P., "Anisotropic Spin Fluctuations in Detwinned FeSe ," *Nat. Mater.* **18**, 709 (2019). [CHNRNS]
- Chen, W., Watson, S., Qiu, Y., Rodriguez-Rivera, J.A., Faraone, A., "Wide-Angle Polarization Analysis on the Multi-Axis Crystal Spectrometer for the Study of Collective and Single Particle Dynamics of Methanol at its Prepeak," *Physica B* **564**, 166 (2019). [CHNRNS]
- Chen, X., Hwang, S., Chisnell, R., Wang, Y., Wu, F., Kim, S., Lynn, J.W., Su, D., Li, X., "Reversible Flat to Rippling Phase Transition in Fe Containing Layered Battery Electrode Materials," *Adv. Funct. Mater.* **28**(39), 1803896 (2018).
- Chen, X., Wang, Y., Wiaderek, K., Sang, X., Borkiewicz, O., Chapman, K., LeBeau, J., Lynn, J., Li, X., "Super Charge Separation and High Voltage Phase in Na_xMnO_2 ," *Adv. Funct. Mater.* **28**(50), 1805105 (2018).
- Chen, X.C., Sacchi, R.L., Osti, N.C., Tyagi, M., Armstrong, B.L., Wang, Y., Palmer, M.J., Dudney, N.J., "Correction: Study of Segmental Dynamics and Ion Transport in Polymer-Ceramic Composite Electrolytes by Quasi-Elastic Neutron Scattering," *Mol. Sys. Des. Eng.*, in press. [CHNRNS]
- Chen, X.C., Sacchi, R.L., Osti, N.C., Tyagi, M., Wang, Y., Palmer, M.J., Dudney, N.J., "Study of Segmental Dynamics and Ion Transport in Polymer-Ceramic Composite Electrolytes by Quasi-Elastic Neutron Scattering," *Mol. Sys. Des. Eng.* **4**(2), 379 (2019). [CHNRNS]
- Chen, Z.-J., Cao, G.-X., Gan, L.-Y., Dai, H., Xu, N., Zang, M.-J., Dai, H.-B., Wu, H., Wang, P., "Highly Dispersed Platinum on Honeycomb-like NiO@Ni Film as a Synergistic Electrocatalyst for the Hydrogen Evolution Reaction," *ACS Catalysis* **8**(9), 8866 (2018).
- Chiang, W.-S., Chen, J.-H., Liu, Y., "Investigation of Porous Materials with Large Surface Heterogeneity using the Generalized Porod's Scattering Law Method," *Phys. Rev. E* **99**(4), 042801 (2019).
- Chintam, K., Wilson, M.S., Rockward, T., Stariha, S., Baker, A.M., Brosha, E.L., Hussey, D.S., LaManna, J.M., Jacobson, D.L., Rau, J.A., Borup, R.L., "Microwatt Fuel Cell for Long-Term and Wide Ambient Temperature Range Operation," *ECS Transactions* **86**(13), 233 (2018).
- Choi, J., Kim, M.-H., Han, J.Y., Chae, J.E., Lee, W.H., Lee, Y.M., Lee, S.Y., Jang, J.H., Kim, J.Y., Henkensmeier, D., Yoo, S.J., Sung, Y.-E., Kim, H.-J., "Application of Spiroindane-Based Microporous Poly(Ether Sulfone)s as Polymeric Binder on Solid Alkaline Exchange Membrane Fuel Cells," *J. Membrane Sci.* **568**, 67 (2018).
- Clifton, L.A., Hall, S.C.L., Mahmoudi, N., Knowles, T.J., Heinrich, F., Lakey, J.H., "Structural Investigations of Protein-Lipid Complexes using Neutron Scattering," in "Lipid-Protein Interactions: Methods and Protocols, Methods in Molecular Biology, vol. 2003," edited by Kleinschmidt, J.H., (Springer Science+Business Media, LLC, Berlin, Germany) Chap. **11**, 201 (2019).
- Corona, P.T., Ruocco, N., Weigandt, K.M., Leal, L.G., Helgeson, M.E., "Probing Flow-Induced Nanostructure of Complex Fluids in Arbitrary 2D Flows using a Fluidic Four-Roll Mill (FFoRM)," *Sci. Rep.* **8**(1), 15559 (2018).
- Creuziger, A., Poling, W.A., Gnaeupel-Herold, T., "Assessment of Martensitic Transformation Paths Based on Transformation Potential Calculations," *Steel Res. Int.* **90**(1), 1800370 (2019).
- Dally, R.L., Chisnell, R., Harriger, L., Liu, Y., Lynn, J.W., Wilson, S.D., "Thermal Evolution of Quasi-One-Dimensional Spin Correlations within the Anisotropic Triangular Lattice of $\alpha\text{-NaMnO}_2$," *Phys. Rev. B* **98**(14), 144444 (2018).
- Dawn, A., Mirzamani, M., Jones, C.D., Yufit, D.S., Qian, S., Steed, J.W., Kumari, H., "Investigating the Effect of Supramolecular Gel Phase Crystallization on Gel Nucleation," *Soft Matter* **14**(46), 9489 (2018). [CHNRNS]
- Dergunov, S.A., Richter, A.G., Kim, M.D., Pingali, S.V., Urban, V.S., Pinkhassik, E., "Deciphering and Controlling Structural and Functional Parameters of the Shells in Vesicle-Templated Polymer Nanocapsules," *Langmuir*, in press.

- Dilla, R.A., Motta, C.M.M., Xu, Y., Zander, Z.K., Bernard, N., Wiener, C.G., Vogt, B.D., Becker, M.L., "Mechanically Tunable, Human Mesenchymal Stem Cell Viable Poly(Ethylene Glycol)-Oxime Hydrogels with Invariant Precursor Composition, Concentration, and Stoichiometry," *Mater. Today Chem.* **11**, 244 (2019). [CHSNS]
- Dimeo, R., Coyne, K., "Researchers Combine High Magnetic Fields and Neutrons to Learn More about Superconductivity," *Fields Magazine* **23**, 1 (2018).
- Dimitrievska, M., Chotard, J.-N., Janot, R., Faraone, A., Tang, W.S., Skripov, A.V., Udovic, T.J., "Tracking the Progression of Anion Reorientational Behavior between α -Phase and β -Phase Alkali-Metal Silanides, MSiH_3 , by Quasielastic Neutron Scattering," *J. Phys. Chem. C* **122**(42), 23985 (2018). [CHSNS]
- Dimitrievska, M., Oliva, F., Guc, M., Giraldo, S., Saucedo, E., Pérez-Rodríguez, A., Izquierdo-Roca, V., "Defect Characterisation in $\text{Cu}_2\text{ZnSnSe}_4$ Kesterites via Resonance Raman Spectroscopy and the Impact on Optoelectronic Solar Cell Properties," *J. Mater. Chem. A* **7**(21), 13293 (2019).
- DiStefano, V.H., McFarlane, J., Stack, A.G., Perfect, E., Mildner, D.F.R., Bleuel, M., Chipera, S.J., Littrell, K.C., Cheshire, M.C., Manz, K.E., Anovitz, L.M., "Solvent-Pore Interactions in the Eagle Ford Shale Formation," *Fuel* **238**, 298 (2019). [CHSNS]
- Dreiling, J.M., Naing, A.S., Tan, J.N., Hanson, J.M., Hoogerheide, S.F., Brewer, S.M., "Capture of Highly Charged Ions in a Pseudo-Hyperbolic Paul Trap," *J. Appl. Phys.* **126**(2), 024501 (2019).
- Eells, R., Hoogerheide, D.P., Kienzle, P.A., Lösche, M., Majkrzak, C.F., Heinrich, F., "Structural Investigations of Membrane-Associated Proteins by Neutron Reflectometry," in "Characterization of Biological Membranes," edited by Nieh, M.-P., Heberle, F.A., and Katsaras, J., (Walter de Gruyter, Berlin, Germany) Chap. **3**, 87 (2019).
- Eklöf-Österberg, C., Nedumkandathil, R., Häussermann, U., Jaworski, A., Pell, A.J., Tyagi, M., Jalarvo, N.H., Frick, B., Faraone, A., Karlsson, M., "Dynamics of Hydride Ions in Metal Hydride-Reduced BaTiO_3 Samples Investigated with Quasielastic Neutron Scattering," *J. Phys. Chem. C* **123**(4), 2019 (2019). [CHSNS]
- Farmer, T.O., Guo, E.-J., Desautels, R.D., Debeer-Schmitt, L., Chen, A., Wang, Z., Jia, Q., Borchers, J.A., Gilbert, D.A., Holladay, B., Sinha, S.K., Fitzsimmons, M.R., "Nanoscale Magnetization Inhomogeneity within Single Phase Nanopillars," *Phys. Rev. Mater.*, in press. [CHSNS]
- Felder, J.B., Wong-Ng, W., Qabbani, R.A., Roth, R.S., Toby, B.H., Chan, J.Y., "Structural Investigation of the 'Tripled-Tetragonal-Tungsten-Bronze' Phases $\text{Sr}_2\text{M}_{10-x}\text{O}_{27-y}$ ($\text{M} = \text{Nb}, \text{Ta}$)," *Polyhedron*, in press.
- Fuglestad, B., Gupta, K., Wand, A.J., Sharp, K.A., "Water Loading Driven Size, Shape, and Composition of Cetyltrimethylammonium/Hexanol/Pentane Reverse Micelles," *J. Colloid Interf. Sci.* **540**, 207 (2019). [CHSNS]
- Gannon, W.J., Zaliznyak, I.A., Wu, L.S., Feiguin, A.E., Tselik, A.M., Demmel, F., Qiu, Y., Copley, J.R.D., Kim, M.S., Aronson, M.C., "Spinon Confinement and a Sharp Longitudinal Mode in $\text{Yb}_2\text{Pt}_2\text{Pb}$ in Magnetic Fields," *Nat. Commun.* **10**, 1123 (2019). [CHSNS]
- Gao, Q., Shi, N., Sun, Q., Sanson, A., Milazzo, R., Carnera, A., Zhu, H., Lapidus, S.H., Ren, Y., Huang, Q., Chen, J., Xing, X., "Low-Frequency Phonon Driven Negative Thermal Expansion in Cubic $\text{GaFe}(\text{CN})_6$ Prussian Blue Analogues," *Inorg. Chem.* **57**(17), 10918 (2018).
- Garg, S., Liu, Y., Perez-Salas, U., Porcar, L., Butler, P.D., "Anomalous Inter-Membrane Cholesterol Transport in Fluid Phase Phosphoserine Vesicles Driven by Headgroup Ordered to Disordered Entropic Transition," *Chem. Phys. Lipids*, in press. [CHSNS]
- Gartner, III, T.E., Haque, F.M., Gomi, A.M., Grayson, S.M., Hore, M.J.A., Jayaraman, A., "Scaling Exponent and Effective Interactions in Linear and Cyclic Polymer Solutions: Theory, Simulations, and Experiments," *Macromolecules* **52**(12), 4579 (2019). [CHSNS]
- Gaudet, J., Smith, E.M., Dudemaine, J., Beare, J., Buhariwalla, C.R.C., Butch, N.P., Stone, M.B., Kolesnikov, A.I., Xu, G., Yahne, D.R., Ross, K.A., Marjerrison, C.A., Garrett, J.D., Luke, G.M., Bianchi, A.D., Gaulin, B.D., "Quantum Spin Ice Dynamics in the Dipole-Octupole Pyrochlore Magnet $\text{Ce}_2\text{Zr}_2\text{O}_7$," *Phys. Rev. Lett.* **122**(18), 187201 (2019).
- Gehring, P.M., Xu, Z., Stock, C., Xu, G., Parshall, D., Harriger, L., Gehring, C.A., Li, X., Luo, H., "Comment on 'Giant Electromechanical Coupling of Relaxor Ferroelectrics Controlled by Polar Nanoregion Vibrations,'" *Sci. Adv.* **5**(3), eaar5066 (2019).
- Genix, A.-C., Bocharova, V., Carroll, B., Lehmann, M., Saito, T., Krueger, S., He, L., Dieudonné-George, P., Sokolov, A.P., Oberdisse, J., "Understanding the Static Interfacial Polymer Layer by Exploring the Dispersion States of Nanocomposites," *ACS Appl. Mater. Interfaces* **11**(19), 17863 (2019). [CHSNS]
- Gilbert, D.A., Grutter, A.J., "Hydrogen Finds a Home in Ionic Devices," *Nat. Mater.* **18**(1), 7 (2019).

- Gilbert, D.A., Grutter, A.J., Murray, P.D., Chopdekar, R.V., Kane, A.M., Ionin, A.L., Lee, M.S., Spurgeon, S.R., Kirby, B.J., Maranville, B.B., N'Diaye, A.T., Mehta, A., Arenholz, E., Liu, K., Takamura, Y., Borchers, J.A., "Ionic Tuning of Cobaltites at the Nanoscale," *Phys. Rev. Mater.* **2**(10), 104402 (2018).
- Gilbert, D.A., Grutter, A.J., Neves, P.M., Shu, G.-J., Zimanyi, G., Maranville, B.B., Chou, F.-C., Krycka, K., Butch, N.P., Huang, S., Borchers, J.A., "Precipitating Ordered Skyrmion Lattices from Helical Spaghetti and Granular Powders," *Phys. Rev. Mater.* **3**(1), 014408 (2019). [CHRS]
- Godfrin, P.D., Falus, P., Porcar, L., Hong, K., Hudson, S.D., Wagner, N.J., Liu, Y., "Dynamic Properties of Different Liquid States in Systems with Competing Interactions Studied with Lysozyme Solutions," *Soft Matter* **14**, 8570 (2018).
- Goel, V., Pietrasik, J., Poling-Skutvik, R., Jackson, A., Matyjaszewski, K., Krishnamoorti, R., "Structure of Block Copolymer Grafted Silica Nanoparticles," *Polymer* **159**, 138 (2018).
- Gold-Parker, A., Gehring, P.M., Skelton, J.M., Smith, I.C., Parshall, D., Frost, J.M., Karunadasa, H.I., Walsh, A., Toney, M.F., "Acoustic Phonon Lifetimes Limit Thermal Transport in Methylammonium Lead Iodide," *P. Natl. A. Sci. USA* **115**(47), 11905 (2018).
- Grinderslev, J.B., Møller, K.T., Yan, Y., Chen, X.-M., Li, Y., Li, H.-W., Zhou, W., Skibsted, J., Chen, X., Jensen, T.R., "Potassium Octahydridotriborate: Diverse Polymorphism in a Potential Hydrogen Storage Material and Potassium Ion Conductor," *Dalton T.* **48**(24), 8872 (2019).
- Grutter, A.J., Disseler, S.M., Moon, E.J., Gilbert, D.A., Arenholz, E., Suter, A., Prokscha, T., Salman, Z., Kirby, B.J., May, S.J., "Strain-Induced Competition between Ferromagnetism and Emergent Antiferromagnetism in (Eu,Sr)MnO₃," *Phys. Rev. Mater.* **2**(9), 094402 (2018).
- Guo, E.-J., Desautels, R., Keavney, D., Roldan, M.A., Kirby, B.J., Lee, D., Liao, Z., Charlton, T., Herklotz, A., Ward, T.Z., Fitzsimmons, M.R., Lee, H.N., "Nanoscale Ferroelastic Twins Formed in Strained LaCoO₃ Films," *Sci. Adv.* **5**(3), eaav5050 (2019).
- Guo, Y., Zuo, X., Xue, Y., Zhou, Y., Yang, Z., Chuang, Y.-C., Chang, C.-C., Yuan, G., Satija, S.K., Gersappe, D., Rafailovich, M.H., "Correction to Enhancing Impact Resistance of Polymer Blends via Self-Assembled Nanoscale Interfacial Structures," *Macromolecules* **52**(12), 4785 (2019).
- Gupta, S., De Mel, J.U., Schneider, G.J., "Reply to 'Comment on 'Dynamics of Phospholipid Membranes beyond Thermal Undulation'" *J. Phys. Chem. B* **123**(26), 5667 (2019). [CHRS]
- Haddock, C., Amadio, J., Anderson, E., Barrón-Palos, L., Crawford, B., Crawford, C., Esposito, D., Fox, W., Francis, I., Fry, J., Gardiner, H., Holley, A., Korsak, K., Lieffers, J., Magers, S., Maldonado-Velázquez, M., Mayorov, D., Nico, J.S., Okudaira, T., Paudel, C., Santra, S., Sarsour, M., Shimizu, H.M., Snow, W.M., Sprow, A., Steffen, K., Swanson, H.E., Tovesson, F., Vanderwerp, J., Yergeau, P.A., "A Search for Possible Long Range Spin Dependent Interactions of the Neutron from Exotic Vector Boson Exchange," *Phys. Lett. B* **783**, 227 (2018).
- Hallsteinsen, I., Grutter, A., Moreau, M., Sløetjes, S.D., Kjaernes, K., Arenholz, E., Tybell, T., "Role of Antiferromagnetic Spin Axis on Magnetic Reconstructions at the (111)-Oriented La_{0.7}Sr_{0.3}MnO₃/LaFeO₃ Interface," *Phys. Rev. Mater.* **2**(8), 084403 (2018).
- Han, B., Wang, H., Wang, C., Wu, H., Zhou, W., Chen, B., Jiang, J., "Postsynthetic Metalation of Robust Hydrogen-Bonded Organic Framework for Heterogeneous Catalysis," *J. Am. Chem. Soc.* **141**(22), 8737 (2019).
- Han, F., Westover, A.S., Yue, J., Fan, X., Wang, F., Chi, M., Leonard, D.N., Dudney, N.J., Wang, H., Wang, C., "High Electronic Conductivity as the Origin of Lithium Dendrite Formation within Solid Electrolytes," *Nat. Energy* **4**, 187 (2019).
- Hatch, H.W., Mahynski, N., Murphy, R.P., Blanco, M.A., Shen, V.K., "Monte Carlo Simulation of Cylinders with Short-Range Attractions," *AIP Adv.* **8**(9), 095210 (2018). [CHRS]
- He, Q.L., Yin, G., Yu, L., Grutter, A.J., Pan, L., Chen, C.-Z., Che, X., Yu, G., Zhang, B., Shao, Q., Stern, A.L., Casas, B., Xia, J., Han, X., Kirby, B.J., Lake, R.K., Law, K.T., Wang, K.L., "Topological Transitions Induced by Antiferromagnetism in a Thin-Film Topological Insulator," *Phys. Rev. Lett.* **121**(9), 096802 (2018).
- He, Y., Chen, F., Li, B., Qian, G., Zhou, W., Chen, B., "Porous Metal-Organic Frameworks for Fuel Storage," *Coordin. Chem. Rev.* **373**, 167 (2018).
- Healy, J., Knott, R., Edward, G., "Residual Orientation in Injection-Moulded Plaques of Atactic-Polystyrene I: The Effect of Processing Conditions," *Polym. Eng. Sci.* **58**(8), 1322 (2018). [CHRS]
- Heigel, J.C., Phan, T.Q., Fox, J.C., Gnaupel-Herold, T.H., "Experimental Investigation of Residual Stress and its Impact on Machining in Hybrid Additive/Subtractive Manufacturing," *Procedia Manuf.* **26**, 929 (2018).
- Heitmann, T., Hester, G., Mitra, S., Calloway, T., Tyagi, M.S., Miskowiec, A., Diallo, S., Osti, N., Mamontov, E., "Probing Li Ion Dynamics in Amorphous xLi₂SO₄·(1-x) LiPO₃ by Quasielastic Neutron Scattering," *Solid State Ion.* **334**, 95 (2019).

- Helton, J.S., Zhao, Y., Shulyatev, D.A., Lynn, J.W., "Damping and Softening of Transverse Acoustic Phonons in Colossal Magnetoresistive $\text{La}_{0.7}\text{Ca}_{0.3}\text{MnO}_3$ and $\text{La}_{0.7}\text{Sr}_{0.3}\text{MnO}_3$," *Phys. Rev. B* **99**(2), 024407 (2019).
- Hernandez, O.J., Geneste, G., Yajima, T., Kobayashi, Y., Okura, M., Aidzu, K., Tassel, C., Paofai, S., Swain, D., Ritter, C., Kageyama, H., "Site Selectivity of Hydride in Early-Transition-Metal Ruddlesden-Popper Oxyhydrides," *Inorg. Chem.* **57**, 11058 (2018).
- Hester, G., Nair, H.S., Reeder, T., Yahne, D.R., DeLazzer, T.N., Berges, L., Ziat, D., Neilson, J.R., Aczel, A.A., Sala, G., Quilliam, J.A., Ross, K.A., "Novel Strongly Spin-Orbit Coupled Quantum Dimer Magnet: $\text{Yb}_2\text{Si}_2\text{O}_7$," *Phys. Rev. Lett.* **123**(2), 027201 (2019).
- Heuser, B.J., Prisk, T.R., Lin, J.-L., Dax, T.J., Zhang, Y., "Direct Measurement of Hydrogen Diffusivity and Solubility Limits in Zircaloy 2 (Formula Unit of $\text{ZrH}_{0.0155}$) using Incoherent Quasi-Elastic Neutron Scattering," *J. Nucl. Mater.* **518**, 177 (2019). [CHNRS]
- Hipp, J.B., Richards, J.J., Wagner, N.J., "Structure-Property Relationships of Sheared Carbon Black Suspensions Determined by Simultaneous Rheological and Neutron Scattering Measurements," *J. Rheol.* **63**(3), 423 (2019). [CHNRS]
- Hoffmann, I., Simon, M., Bleuel, M., Falus, P., Gradzielski, M., "Structure, Dynamics, and Composition of Large Clusters in Polyelectrolyte-Surfactant Systems," *Macromolecules* **52**(6), 2607 (2019).
- Holt, A.P., Fragiadakis, D., Wollmershauser, J.A., Feigelson, B.N., Tyagi, M., Roland, C.M., "Stability Limits of Pressure Densified Polycarbonate Glass," *Macromolecules* **52**(11), 4139 (2019). [CHNRS]
- Hoogerheide, D.P., Noskov, S.Y., Kuszak, A.J., Buchanan, S.K., Rostovtseva, T.K., Nanda, H., "Structure of Voltage-Dependent Anion Channel-Tethered Bilayer Lipid Membranes Determined using Neutron Reflectivity," *Acta Crystallogr. D* **D74**(12), 1219 (2018).
- Horkay, F., "Effect of the Ionic Environment on the Supramolecular Structure and Thermodynamics of DNA Gels," *Macromol. Symp.* **385**(1), 1800199 (2019). [CHNRS]
- Horkay, F., Bassar, P.J., Hecht, A.-M., Geissler, E., "Ionic Effects in Semi-Dilute Biopolymer Solutions: A Small Angle Scattering Study," *J. Chem. Phys.* **149**(16), 163312 (2018). [CHNRS]
- Huang, A., Yao, H., Olsen, B.D., "SANS Partial Structure Factor Analysis for Determining Protein-Polymer Interactions in Semidilute Solution," *Soft Matter*, in press. [CHNRS]
- Huang, Q., "Powder Diffraction of Superconductors," in "International Tables for Crystallography Vol. H," edited by Gilmore, C.J., Kaduk, J.A., and Schenk, H., (Wiley Publishing, Hoboken, NJ) Chap. 7.13, 868 (2019).
- Huon, A., Vibhakar, A.M., Grutter, A.J., Borchers, J.A., Disseler, S., Liu, Y., Tian, W., Orlandi, F., Manuel, P., Khalyavin, D.D., Sharma, Y., Herklotz, A., Lee, H.N., Fitzsimmons, M.R., Johnson, R.D., May, S.J., "Helical Magnetism in Sr-Doped $\text{CaMn}_7\text{O}_{12}$ Films," *Phys. Rev. B* **98**(22), 224419 (2018).
- Ijiri, Y., Krycka, K.L., Hunt-Isaak, I., Pan, H., Hsieh, J., Borchers, J.A., Rhyne, J.J., Oberdick, S.D., Abdelgawad, A., Majetich, S.A., "Correlated Spin Canting in Ordered Core-Shell $\text{Fe}_3\text{O}_4/\text{Mn}_x\text{Fe}_{3-x}\text{O}_4$ Nanoparticle Assemblies," *Phys. Rev. B* **99**(9), 094421 (2019). [CHNRS]
- Ikeuchi, Y., Takatsu, H., Tassel, C., Brown, C.M., Murakami, T., Matsumoto, Y., Okamoto, Y., Kageyama, H., "Rattling Behavior in a Simple Perovskite NaWO_3 ," *Inorg. Chem.* **58**(10), 6790 (2019).
- Ishida, K., Ikeuchi, Y., Tassel, C., Takatsu, H., Brown, C.M., Kageyama, H., "High-Pressure Synthesis of Non-Stoichiometric Li_xWO_3 ($0.5 \leq x \leq 1.0$) with LiNbO_3 Structure," *Inorganics* **7**(5), 63 (2019). [CHNRS]
- Ito, K., Faraone, A., Tyagi, M., Yamaguchi, T., Chen, S.-H., "Nanoscale Dynamics of Water Confined in Ordered Mesoporous Carbon," *Phys. Chem. Chem. Phys.* **21**, 8517 (2019). [CHNRS]
- Iwamoto, T., Doi, Y., Kinoshita, K., Takano, A., Takahashi, Y., Kim, E., Kim, T.-H., Takata, S.-I., Nagao, M., Matsushita, Y., "Conformations of Ring Polystyrenes in Semidilute Solutions and in Linear Polymer Matrices Studied by SANS," *Macromolecules* **51**(17), 6836 (2018).
- Iwasa, K., Sinha, S.K., Kamitakahara, W., Fernandez-Baca, J., Tajima, K., Kakurai, K., "In Memoriam: Nobuyoshi Wakabayashi," *Neutron News* **29**(1), 32 (2018).
- Jacobs, D., Hoogerheide, D.P., Rovini, A., Jiang, Z., Lee, J.C., Rostovtseva, T.K., Bezrukov, S.M., "Probing Membrane Association of α -Synuclein Domains with VDAC Nanopore Reveals Unexpected Binding Pattern," *Sci. Rep.* **9**, 4580 (2019).
- Jadhav, V., Hoogerheide, D.P., Korlach, J., Wanunu, M., "Porous Zero-Mode Waveguides for Picogram-Level DNA Capture," *Nano Lett.* **19**(2), 921 (2019).
- Jafta, C.J., Sun, X.-G., Veith, G.M., Jensen, G.V., Mahurin, S.M., Paranthaman, M.P., Dai, S., Bridges, C.A., "Probing Microstructure and Electrolyte Concentration Dependent Cell Chemistry *Via Operando* Small Angle Neutron Scattering," *Energy Environ. Sci.* **12**(6), 1866 (2019). [CHNRS]

- Jamer, M.E., Rementer, C.R., Barra, A., Grutter, A.J., Fitzell, K., Gopman, D.B., Borchers, J.A., Carman, G.P., Kirby, B.J., Chang, J.P., "Long-Range Electric Field Control of Permalloy Layers in Strain-Coupled Composite Multiferroics," *Phys. Rev. Appl.* **10**(4), 044045 (2018).
- Jang, S., Pouse, N., Keiber, T., White, B.D., Disseler, S.M., Lynn, J.W., Collini, J.C., Janoschek, M., Bridges, F., Maple, M.B., "Tuning the Magnetic Ground State of $\text{Ce}_{1-x}\text{Yb}_x\text{RhIn}_5$ by Yb Valence Fluctuations," *Phys. Rev. B* **98**(19), 195118 (2018).
- Jensen, G.V., Barker, J.G., "Effects of Multiple Scattering Encountered for Various Small-Angle Scattering Model Functions," *J. Appl. Crystallogr.* **51**(5), 1455 (2018). [CHNRNS]
- Jeong, D.Y., Woelke, P.B., Nied, H.F., DuPont, J.N., Kizildemir, S., Fletcher, F.B., Hutchinson, J.W., "Defect Growth Characterization in Modern Rail Steels," in "Proceedings of the 2019 ASME Joint Rail Conference," edited by ASME, (2019 ASME Joint Rail Conference, April 2019, Snowbird, UT) JRC2019-1265 (2019).
- Jo, K.-I., Kim, T.-H., Choi, K.-I., Lee, H., Choi, J.-H., Bang, J., Kim, T.-H., Yuan, G., Satija, S.K., Koo, J., "Dewetting of Thin Polymer Films on Wrinkled Graphene Oxide Monolayers," *Langmuir* **35**(16), 5549 (2019).
- Jocher, G.R., Koblanski, J., Li, V.A., Negrashov, S., Dorrell, R.C., Nishimura, K., Sakai, M., Learned, J.G., Usman, S., "miniTimeCube as a Neutron Scatter Camera," *AIP Adv.* **9**(3), 035301 (2019).
- Jones, J., Phuoc, V.T., del Campo, L., Massa, N.E., Brown, C.M., Pagola, S., "Accessing New Charge-Transfer Complexes by Mechanochemistry: A Tetrathiafulvalene Chloranilic Acid Polymorph Containing Segregated Tetrathiafulvalene Stacks," *Cryst. Growth Des.*, in press.
- Jorba, P., Schulz, M., Hussey, D.S., Abir, M., Seifert, M., Tsurkan, V., Loidl, A., Pfeleiderer, C., Khaykovich, B., "High-Resolution Neutron Depolarization Microscopy of the Ferromagnetic Transitions in Ni_3Al and HgCr_2Se_4 under Pressure," *J. Magn. Magn. Mater.* **475**, 176 (2019).
- Kadowaki, H., Wakita, M., Fåk, B., Ollivier, J., Ohira-Kawamura, S., Nakajima, K., Lynn, J.W., "Spin Correlations of Quantum Spin Liquid and Quadrupole-Ordered States of $\text{Tb}_{2+x}\text{Ti}_{2-x}\text{O}_{7+y}$," *Phys. Rev. B* **99**(1), 014406 (2019).
- Kan, W.H., Deng, B., Xu, Y., Shukla, A.K., Bo, T., Zhang, S., Liu, J., Pianetta, P., Wang, B.-T., Liu, Y., Chen, G., "Understanding the Effect of Local Short-Range Ordering on Lithium Diffusion in $\text{Li}_{1.3}\text{Nb}_{0.3}\text{Mn}_{0.4}\text{O}_2$ Single-Crystal Cathode," *Chem* **4**(9), 2108 (2018).
- Kapelewski, M.T., Runčevski, T., Tarver, J.D., Jiang, H.Z.H., Hurst, K.E., Parilla, P.A., Ayala, A., Gennett, T., Fitzgerald, S.A., Brown, C.M., Long, J.R., "Record High Hydrogen Storage Capacity in the Metal-Organic Framework $\text{Ni}_2(m\text{-dobdc})$ at Near-Ambient Temperatures," *Chem. Mater.* **30**(22), 8179 (2018).
- Kelley, E.G., Butler, P.D., Nagao, M., "Collective Dynamics in Model Biological Membranes Measured by Neutron Spin Echo Spectroscopy," in "Characterization of Biological Membranes," edited by Nieh, M.-P., Heberle, F.A. and Katsaras, J., (Walter de Gruyter, Berlin, Germany) Chap. **4**, 130 (2019). [CHNRNS]
- Kelley, E.G., Butler, P.D., Nagao, M., "Scaling of Lipid Membrane Rigidity with Domain Area Fraction," *Soft Matter* **15**(13), 2762 (2019). [CHNRNS]
- Keshavarz, S., Naghibolashrafi, N., Jamer, M.E., Vinson, K., Mazumdar, D., Dennis, C.L., Ratcliff, II, W., Borchers, J.A., Gupta, A., LeClair, P., "Fe₂MnGe: A Hexagonal Heusler Analogue," *J. Alloy Compd.* **771**, 793 (2018).
- Kharel, A., Lodge, T.P., "Effect of Ionic Liquid Components on the Coil Dimensions of PEO," *Macromolecules* **52**(8), 3123 (2019). [CHNRNS]
- Kim, D., Sihn, M.R., Jeon, M.-G., Yuan, G., Satija, S.K., Kim, Y., Choi, J., "Non-Equilibrium Phase Behavior of Immiscible Polymer-Grafted Nanoparticle Blends," *Macromolecules*, in press.
- Kim, D., Song, K.S., Buyukcakir, O., Yildirim, T., Coskun, A., "Bimetallic Metal Organic Frameworks with Precisely Positioned Metal Centers for Efficient H₂ Storage," *Chem. Commun.* **54**(86), 12218 (2018).
- Kim, M.G., Winn, B., Chi, S., Savici, A.T., Rodriguez-Rivera, J.A., Chen, W.C., Xu, X., Li, Y., Kim, J.W., Cheong, S.-W., Kiryukhin, V., "Spin-Liquid-Like State in Pure and Mn-Doped TbInO_3 with a Nearly Triangular Lattice," *Phys. Rev. B* **100**(2), 024405 (2019). [CHNRNS]
- Kim, Y., Kim, J., Hussey, D.S., Kwon, O.Y., Lee, S.W., "Visualization of Magnetic Domains in Electrical Steel using High-Resolution Dark-Field Imaging," *Korean J. Met. Mater.* **57**(6), 352 (2019).
- Kim, Y., Kim, J., Kim, D., Hussey, D.S., Lee, S.W., "Characterization of the Phase Sensitivity, Visibility, and Resolution in a Symmetric Neutron Grating Interferometer," *Rev. Sci. Instrum.* **90**(7), 073704 (2019).
- Kirby, B.J., Fallarino, L., Riego, P., Maranville, B.B., Miller, C.W., Berger, A., "Nanoscale Magnetic Localization in Exchange Strength Modulated Ferromagnets," *Phys. Rev. B* **98**(6), 064404 (2018).

- Kline, S.R., "2018 NCNR Annual Report," NIST SP **1231**, (2019).
- Kofu, M., Faraone, A., Tyagi, M., Nagao, M., Yamamuro, O., "Two Inherent Crossovers of the Diffusion Process in Glass-Forming Liquids," *Phys. Rev. E* **98**(4), 042601 (2018). [CHNRNS]
- Koga, T., Barkley, D., Nagao, M., Taniguchi, T., Carillo, J.-M.Y., Sumpter, B.G., Masui, T., Kishimoto, H., Koga, M., Rudick, J.G., Endoh, M.K., "Interphase Structures and Dynamics Near Nanofiller Surfaces in Polymer Solutions," *Macromolecules* **51**(23), 9462 (2018). [CHNRNS]
- Koshari, S.H.S., Nayak, P.K., Burra, S., Zarraga, I.E., Rajagopal, K., Liu, Y., Wagner, N.J., Lenhoff, A.M., "In Situ Characterization of the Microstructural Evolution of Biopharmaceutical Solid-State Formulations with Implications for Protein Stability," *Mol. Pharmaceut.* **16**(1), 173 (2019).
- Krishnamurthy, A., Tao, R., Senses, E., Doshi, S.M., Burni, F.A., Natarajan, B., Hunston, D., Thostenson, E.T., Faraone, A., Forster, A.L., Forster, A.M., "Multiscale Polymer Dynamics in Hierarchical Carbon Nanotube Grafted Glass Fiber Reinforced Composites," *ACS Appl. Polym. Mater.* **1**(7), 1905 (2019). [CHNRNS]
- Krycka, K.L., Rhyne, J.J., Oberdick, S.D., Abdelgawad, A.M., Borchers, J.A., Ijiri, Y., Majetich, S.A., Lynn, J.W., "Spin Waves Across Three-Dimensional, Close-Packed Nanoparticles," *New J. Phys.* **20**, 123020 (2018).
- Kupwade-Patil, K., Bumajdad, A., Brown, C.M., Tyagi, M., Butch, N.P., Jamsheer, A.F., Büyüköztürk, O., "New Insights into Water Dynamics of Portland Cement Paste with Nano-Additives using Quasielastic Neutron Scattering," *J. Mater. Sci.* **54**(6), 4710 (2019).
- Kupwade-Patil, K., Bumajdad, A., Udovic, T., Littrell, K., Büyüköztürk, O., "In Situ Examination of Engineered Local Additives in Cement Paste via Neutron-Based Scattering Techniques," in "Proceedings of the 6th International Symposium of Nanotechnology in Construction," edited by NICOM, (NICOM6, December 2018, Hong Kong), 1 (2018).
- Lam, C.N., Xu, W.-S., Chen, W.-R., Wang, Z., Stanley, C.B., Carrillo, J.-M.Y., Uhrig, D., Wang, W., Hong, K., Liu, Y., Porcar, L., Do, C., Smith, G.S., Sumpter, B.G., Wang, Y., "Scaling Behavior of Anisotropy Relaxation in Deformed Polymers," *Phys. Rev. Lett.* **121**(11), 117801 (2018). [CHNRNS]
- Lee, B., Bleuel, M., Zhao, A., Ott, D., Hakem, I.F., Bockstaller, M.R., "Kinetics and Energetics of Solute Segregation in Granular Block Copolymer Microstructures," *Macromolecules* **51**(24), 10285 (2018).
- Lee, C.H., Dura, J.A., LeBar, A., DeCaluwe, S.C., "Direct, Operando Observation of the Bilayer Solid Electrolyte Interphase Structure: Electrolyte Reduction on a Non-Intercalating Electrode," *J. Power Sources* **412**, 725 (2019).
- Lee, H., Choi, K.-I., Choi, J.-H., Yoo, J., Seo, Y.-S., Satija, S., Koo, J., "Free-Standing Janus Graphene Oxide with Anisotropic Properties for 2D Materials as Surfactant," *ACS Appl. Nano Mater.* **2**(7), 4203 (2019).
- Lee, J.C.-W., Weigandt, K.M., Kelley, E.G., Rogers, S.A., "Structure-Property Relationships via Recovery Rheology in Viscoelastic Materials," *Phys. Rev. Lett.* **122**(24), 248003 (2019). [CHNRNS]
- Li, B., Wen, H.-M., Yu, Y., Cui, Y., Zhou, W., Chen, B., Qian, G., "Nanospace within Metal-Organic Frameworks for Gas Storage and Separation," *Mater. Today Nano* **2**, 21 (2018).
- Li, C., Xu, H., Gao, J., Du, W., Shangguan, L., Zhang, X., Lin, R.-B., Wu, H., Zhou, W., Liu, X., Yao, J., Chen, B., "Tunable Titanium Metal-Organic Frameworks with Infinite 1D Ti-O Rods for Efficient Visible-Light-Driven Photocatalytic H₂ Evolution," *J. Mater. Chem. A* **7**(19), 11928 (2019).
- Li, H., Li, L., Lin, R.-B., Ramirez, G., Zhou, W., Krishna, R., Zhang, Z., Xiang, S., Chen, B., "Microporous Metal-Organic Framework with Dual Functionalities for Efficient Separation of Acetylene from Light Hydrocarbon Mixtures," *ACS Sustain. Chem. Eng.* **7**(5), 4897 (2019).
- Li, H., Li, L., Lin, R.-B., Zhou, W., Zhang, Z., Xiang, S., Chen, B., "Porous Metal-Organic Frameworks for Gas Storage and Separation: Status and Challenges," *EnergyChem* **1**(1), 100006 (2019).
- Li, J., Subramanian, M.A., "Inorganic Pigments with Transition Metal Chromophores at Trigonal Bipyramidal Coordination: Y(In,Mn)O₃ Blues and Beyond," *J. Solid State Chem.* **272**, 9 (2019).
- Li, L., Lin, R.-B., Krishna, R., Li, H., Xiang, S., Wu, H., Li, J., Zhou, W., Chen, B., "Ethane/Ethylene Separation in a Metal-Organic Framework with Iron-Peroxo Sites," *Science* **362**, 443 (2018).
- Li, L., Lin, R.-B., Wang, X., Zhou, W., Jia, L., Li, J., Chen, B., "Kinetic Separation of Propylene over Propane in a Microporous Metal-Organic Framework," *Chem. Eng. J.* **354**, 977 (2018).
- Li, L., Wen, H.-M., He, C., Lin, R.-B., Krishna, R., Wu, H., Zhou, W., Li, J., Li, B., Chen, B., "A Metal-Organic Framework with Suitable Pore Size and Specific Functional Sites for the Removal of Trace Propyne from Propylene," *Angew. Chem. Int. Edit.* **57**(46), 15183 (2018).

- Li, Q., Yi, T., Wang, X., Pan, H., Quan, B., Liang, T., Guo, X., Yu, X., Wang, H., Huang, X., Chen, L., Li, H., "In-Situ Visualization of Lithium Plating in All-Solid-State Lithium-Metal Battery," *Nano Energy*, in press.
- Li, T., Zhang, X., Lacey, S.D., Mi, R., Zhao, X., Jiang, F., Song, J., Liu, Z., Chen, G., Dai, J., Yao, Y., Das, S., Yang, R., Briber, R.M., Hu, L., "Cellulose Ionic Conductors with High Differential Thermal Voltage for Low-Grade Heat Harvesting," *Nat. Mater.* **18**, 608 (2019). [CHRS]
- Li, W.M., Zhao, J.F., Cao, L.P., Hu, Z., Huang, Q.Z., Wang, X.C., Liu, Y., Zhao, G.Q., Zhang, J., Liu, Q.Q., Yu, R.Z., Long, Y.W., Wu, H., Lin, H.J., Chen, C.T., Li, Z., Gong, Z.Z., Guguchia, Z., Kim, J.S., Stewart, G.R., Uemura, Y.J., Uchida, S., Jin, C.Q., "Superconductivity in a Unique Type of Copper Oxide," *P. Natl. A. Sci. USA* **116**(25), 12156 (2019).
- Li, X., Zhang, S., Li, H., Venero, D.A., White, J.S., Cubitt, R., Huang, Q., Chen, J., He, L., van der Laan, G., Wang, W., Hesjedal, T., Wang, F., "Oriented 3D Magnetic Biskymions in MnNiGa Bulk Crystals," *Adv. Mater.* **31**(17), 1900264 (2019).
- Lima, T.A., Li, Z., Tyagi, M., Ribeiro, M.C.C., Z, Y., "Spatial and Thermal Signatures of α and β Relaxations in Glassy and Glacial Aliphatic Ionic Liquids," *J. Chem. Phys.* **150**(14), 144506 (2019). [CHRS]
- Lin, R.-B., He, Y., Li, P., Wang, H., Zhou, W., Chen, B., "Multifunctional Porous Hydrogen-Bonded Organic Framework Materials," *Chem. Soc. Rev.* **48**(5), 1362 (2019).
- Lin, R.-B., Li, L., Zhou, H.-L., Wu, H., He, C., Li, S., Krishna, R., Li, J., Zhou, W., Chen, B., "Molecular Sieving of Ethylene from Ethane using a Rigid Metal-Organic Framework," *Nat. Mater.* **17**, 1128 (2018).
- Lin, R.-B., Wu, H., Li, L., Tang, X.-L., Li, Z., Gao, J., Cui, H., Zhou, W., Chen, B., "Boosting Ethane/Ethylene Separation within Isorecticular Ultramicroporous Metal-Organic Frameworks," *J. Am. Chem. Soc.* **140**(40), 12940 (2018).
- Lin, R.-B., Xiang, S., Li, B., Cui, Y., Qian, G., Zhou, W., Chen, B., "Our Journey of Developing Multifunctional Metal-Organic Frameworks," *Coordin. Chem. Rev.* **384**, 21 (2019).
- Lin, R.-B., Xiang, S., Li, B., Cui, Y., Zhou, W., Qian, G., Chen, B., "Reticular Chemistry of Multifunctional Metal-Organic Framework Materials," *Israel J. Chem.* **58**, 949 (2018).
- Lin, R.-B., Xiang, S., Xing, H., Zhou, W., Chen, B., "Exploration of Porous Metal-Organic Frameworks for Gas Separation and Purification," *Coordin. Chem. Rev.* **378**, 87 (2019).
- Lindstrom, R.M., "Nuclear Analysis at NBS and NIST," *J. Radioanal. Nucl. Ch.* **318**(3), 1465 (2018).
- Lindstrom, R.M., Downing, R.G., Chatt, A., "Laudation for Dr. Rolf L. Zeisler: Hevesy Medal Award 2018 Recipient," *J. Radioanal. Nucl. Ch.* **318**(1), 3 (2018).
- Liu, C., Wang, T., Ji, J., Wang, C., Wang, H., Jin, P., Zhou, W., Jiang, J., "The Effect of Pore Size and Layer Number of Metal-Porphyrin Coordination Nanosheets on Sensing DNA," *J. Mater. Chem. C*, in press.
- Liu, J., Savici, A.T., Granroth, G.E., Habicht, K., Qiu, Y., Hu, J., Mao, Z.Q., Bao, W., "A Triplet Resonance in Superconducting $\text{Fe}_{1.03}\text{Se}_{0.4}\text{Te}_{0.6}$," *Chinese Phys. Lett.* **35**(12), 127401 (2018).
- Liu, Q., Febbraro, M., deBoer, R.J., Boeltzig, A., Chen, Y., Cerjan, C., Couder, M., Frentz, B., Görres, J., Henry, E.A., Lamere, E., Macon, K.T., Manukyan, K.V., Morales, L., O'Malley, P.D., Pain, S.D., Peters, W.A., Schneider, D., Seymour, C., Seymour, G., Temanson, E., Toomey, R., Vande Kolk, B., Weaver, J., Wiescher, M., "Measurement of the $^{10}\text{B}(\alpha, n_0)^{13}\text{N}$ Cross Section for $2.2 < E\alpha < 4.9$ MeV and its Applications as a Diagnostic at the National Ignition Facility," *Phys. Rev. C*, in press.
- Liu, T., Gautam, S., Wang, H.-W., Anovitz, L.M., Mamontov, E., Allard, L.F., Cole, D.R., "Structure and Dynamics of Water on the Forsterite Surface," *Phys. Chem. Chem. Phys.* **20**(44), 27822 (2018). [CHRS]
- Liu, Y., "Short-Time Dynamics of Proteins in Solutions Studied by Neutron Spin Echo," *Curr. Opin. Colloid In.*, in press. [CHRS]
- Liu, Y., Xi, Y., "Colloidal Systems with a Short-Range Attraction and Long-Range Repulsion: Phase Diagrams, Structures, and Dynamics," *Curr. Opin. Colloid In.* **39**, 123 (2019). [CHRS]
- Liu, Z., Lemmonds, S., Huang, J., Tyagi, M., Hong, L., Jain, N., "Entropic Contribution to Enhanced Thermal Stability in the Thermostable P450 CYP119," *P. Natl. A. Sci. USA* **115**(43), E10049 (2018). [CHRS]
- Liu, Z., Yang, C., Huang, J., Ciampalini, G., Li, J., García Sakai, V., Tyagi, M., O'Neill, H., Zhang, Q., Capaccioli, S., Ngai, K.L., Hong, L., "Direct Experimental Characterization of Contributions from Self-Motion of Hydrogen and from Interatomic Motion of Heavy Atoms to Protein Anharmonicity," *J. Phys. Chem. B* **122**(43), 9956 (2018). [CHRS]
- Livingston, R., O'Connor, A., LaManna, J., Chen-Mayer, H., Turkoglu, D., "Investigation of a Simulated Chinese Jade and Bronze Dagger-Axe by Neutron Radiography and Prompt Gamma Activation Analysis," *J. Archaeol. Sci. Rep.* **21**, 99 (2018).

- Livingston, R., O'Connor, A., LaManna, J.M., Chen-Mayer, H., King, L., "Investigation of a Simulated Chinese Jade Dagger by Multiple Imaging Techniques," *Microsc. Microanal.* **24**(Suppl 1), 2146 (2018).
- Lorzing, G.R., Gosselin, E.J., Trump, B.A., York, A.H.P., Sturluson, A., Rowland, C.A., Yap, G.P.A., Brown, C.M., Simon, C.M., Bloch, E.D., "Understanding Gas Storage in Cuboctahedral Porous Coordination Cages," *J. Am. Chem. Soc.* **141**(30), 12128 (2019).
- Lu, F., Chen, Q., Geng, S., Allix, M., Wu, H., Huang, Q., Kuang, X., "Innovative Lithium Storage Enhancement in Cation-Deficient Anatase via Layered Oxide Hydrothermal Transformation," *J. Mater. Chem. A* **6**(47), 24232 (2018).
- Lu, X., Scherer, D.D., Tam, D.W., Zhang, W., Zhang, R., Luo, H., Harriger, L.W., Walker, H.C., Adroja, D.T., Andersen, B.M., Dai, P., "Spin Waves in Detwinned BaFe_2As_2 ," *Phys. Rev. Lett.* **121**(6), 067002 (2018).
- Luckyanova, M.N., Mendoza, J., Lu, H., Song, B., Huang, S., Zhou, J., Li, M., Dong, Y., Zhou, H., Garlow, J., Wu, L., Kirby, B.J., Grutter, A.J., Poretzky, A.A., Zhu, Y., Dresselhaus, M.S., Gossard, A., Chen, G., "Phonon Localization in Heat Conduction," *Sci. Adv.* **4**, eaat9460 (2018).
- Ma, C.T., Kirby, B.J., Li, X., Poon, S.J., "Thickness Dependence of Ferrimagnetic Compensation in Amorphous Rare-Earth Transition-Metal Thin Films," *Appl. Phys. Lett.* **113**(17), 172404 (2018).
- Maliszewskyj, N.C., Osovizky, A., Pritchard, K., Yehuda-Zada, Y., Binkley, E., Ziegler, J., Tsai, P., Hadad, N., Baltic, G.M., Jackson, M., Hurlbut, C., Majkrzak, C.F., "An Energy Analyzing Detector for Cold Neutrons," *Nucl. Instrum. Meth. A* **907**, 90 (2018).
- Mallamace, F., Corsaro, C., Mallamace, D., Chen, S.-H., Fratini, E., Baglioni, P., "The Boson Peak Interpretation and Evolution in Confined Amorphous Water," *Sci. China Phys. Mech.*, in press.
- Manley, M.E., Abernathy, D.L., Christianson, A.D., Lynn, J.W., "Response to Comment on 'Giant Electromechanical Coupling of Relaxor Ferroelectrics Controlled by Polar Nanoregion Vibrations,'" *Sci. Adv.* **5**, eaaw4367 (2019).
- Manley, M.E., Hellman, O., Shulumba, N., May, A.F., Stonaha, P.J., Lynn, J.W., Garlea, V.O., Alatas, A., Hermann, R.P., Budai, J.D., Wang, H., Sales, B.C., Minnich, A.J., "Intrinsic Anharmonic Localization in Thermoelectric PbSe ," *Nat. Commun.* **10**, 1928 (2019).
- Mao, Y., Hsiao, B.S., Chu, B., "Static and Dynamic Light Scattering," in "World Scientific Series in Nanoscience and Nanotechnology Handbook of Synthetic Methodologies and Protocols of Nanomaterials," edited by Zhu, Y. and Han, Y., (World Scientific Publishing Co. PTE. Ltd, Singapore), in press.
- Mao, Y., Zavalij, P.Y., "Two- and Three-Dimensional Coordination Polymers Based on Zinc(II) and Furan-2,5-Dicarboxylic Acid: Structure Variation due to Metal-to-linker Ratio," *Acta Crystallogr. C* **C74**(12), 1719 (2018).
- Mao, Y., Zavalij, P.Y., "Two Furan-2,5-Dicarboxylic Acid Solvates Crystallized from Dimethylformamide and Dimethyl Sulfoxide," *Acta Crystallogr. C* **C74**(7), 986 (2018).
- Maranville, B., Ratcliff, II, W., Kienzle, P., "*Reductus*: A Stateless Python Data Reduction Service with a Browser Front End," *J. Appl. Crystallogr.* **51**(5), 1500 (2018).
- Martin, H.J., White, B.T., Yuan, G., Saito, T., Dadmun, M.D., "Relative Size of the Polymer and Nanoparticle Controls Polymer Diffusion in All-Polymer Nanocomposites," *Macromolecules* **52**(7), 2843 (2019).
- Martínez, M.I.V., Zeisler, R., De Nadai Fernandes, E.A., Bacchi, M.A., Turkoglu, D.J., "Characterization of an Innovative Sugarcane Leaves Reference Material by INAA and PGAA," *J. Radioanal. Nucl. Ch.* **318**(1), 739 (2018).
- Martínez, M.I.V., Zeisler, R., De Nadai Fernandes, E.A., Bacchi, M.A., "Innovative Reference Material for Improving the Quality Control in the Sucroenergetic Sector," *Accredit. Qual. Assur.* **23**, 329 (2018).
- Matsumoto, Y., Yamamoto, T., Nakano, K., Takatsu, H., Murakami, T., Hongo, K., Maezono, R., Ogino, H., Song, D., Brown, C.M., Tassel, C., Kageyama, H., "High-Pressure Synthesis of $\text{A}_2\text{NiO}_2\text{Ag}_2\text{Se}_2$ (A = Sr, Ba) with a High-Spin Ni^{2+} in Square-Planar Coordination," *Angew. Chem. Int. Edit.* **58**(3), 756 (2019).
- Mattes, D.A., Şahin, D., "Design and Implementation of a Reactor Safety System Digital Upgrade, Normal Air Radiation Monitor," *T. Am. Nucl. Soc.*, in press.
- McDonald, I.J., Jamer, M.E., Krycka, K.L., Anber, E., Foley, D., Lang, A.C., Ratcliff, W.D., Heiman, D., Taheri, M.L., Borchers, J.A., Lewis, L.H., "Exchange Bias in Bulk $\alpha\text{-Fe}/\gamma\text{-Fe}_{70}\text{Mn}_{30}$ Nanocomposites for Permanent Magnet Applications," *ACS Appl. Nano Mater.* **2**(4), 1940 (2019). [CHRS]

- Miao, L., Basak, R., Ran, S., Xu, Y., Kotta, E., He, H., Denlinger, J.D., Chuang, Y.-D., Zhao, Y., Xu, Z., Lynn, J.W., Jeffries, J.R., Saha, S.R., Giannakis, I., Aynajian, P., Kang, C.-J., Wang, Y., Kotliar, G., Butch, N.P., Wray, L.A., "High Temperature Singlet-Based Magnetism from Hund's Rule Correlations," *Nat. Commun.* **10**, 644 (2019).
- Mihailescu, M., Sorci, M., Seckute, J., Silin, V.I., Hammer, J., Perrin, Jr., B.S., Hernandez, J.I., Smajic, N., Shrestha, A., Bogardus, K.A., Greenwood, A.I., Fu, R., Blazys, J., Pastor, R.W., Nicholson, L.K., Belfort, G., Cotten, M.L., "Structure and Function in Antimicrobial Piscidins: Histidine Position, Directionality of Membrane Insertion, and pH-Dependent Permeabilization," *J. Am. Chem. Soc.* **141**(25), 9837 (2019).
- Milner, J.L., Gnäupel-Herold, T., "Design of an Octo-Strain Specimen for Biaxial Tension Testing," in "Proceedings of the ASME 2018 13th International Manufacturing Science and Engineering Conference," edited by ASME, (13th International Manufacturing Science and Engineering Conference, June 2018, College Station, TX), MSEC2018-6612 (2018).
- Mirri, F., Ashkar, R., Jamali, V., Liberman, L., Pinnick, R.A., van der Schoot, P., Talmon, Y., Butler, P.D., Pasquali, M., "Quantification of Carbon Nanotube Liquid Crystal Morphology via Neutron Scattering," *Macromolecules* **51**, 6892 (2018).
- Mongcopa, K.I.S., Poling-Skutvik, R., Ashkar, R., Butler, P., Krishnamoorti, R., "Conformational Change and Suppression of the Θ -Temperature for Solutions of Polymer-Grafted Nanoparticles," *Soft Matter* **14**, 6102 (2018). [CHNRNS]
- Montfrooij, W., Heitmann, T., Qiu, Y., Watson, S., Erwin, R., Chen, W., Zhao, Y., Aronson, M., Huang, Y., de Visser, A., "Quantum Critical Behavior in $\text{Ce}(\text{Fe}_{0.76}\text{Ru}_{0.24})_2\text{Ge}_2$," *Phys. Rev. B* **99**(19), 195113 (2019).
- Morey, J.R., Scheie, A., Sheckelton, J.P., Brown, C.M., McQueen, T.M., " $\text{Ni}_2\text{Mo}_3\text{O}_8$: Complex Antiferromagnetic Order on a Honeycomb Lattice," *Phys. Rev. Mater.* **3**(1), 014410 (2019).
- Motokawa, R., Kobayashi, T., Endo, H., Mu, J., Williams, C.D., Masters, A.J., Antonio, M.R., Heller, W.T., Nagao, M., "A Telescoping View of Solute Architectures in a Complex Fluid System," *ACS Central Sci.* **5**(1), 85 (2019). [CHNRNS]
- Mozur, E.M., Trowbridge, J.C., Maughan, A.E., Gorman, M.J., Brown, C.M., Prisk, T.R., Neilson, J.R., "Dynamical Phase Transitions and Cation Orientation-Dependent Photoconductivity in $\text{CH}(\text{NH}_2)_2\text{PbBr}_3$," *ACS Mater. Lett.*, in press. [CHNRNS]
- Mussel, M., Basser, P.J., Horkay, F., "Effects of Mono- and Divalent Cations on the Structure and Thermodynamic Properties of Polyelectrolyte Gels," *Soft Matter* **15**(20), 4153 (2019). [CHNRNS]
- Nanda, H., García Sakai, V., Khodadadi, S., Tyagi, M.S., Schwalbach, E.J., Curtis, J.E., "Relaxation Dynamics of Saturated and Unsaturated Oriented Lipid Bilayers," *Soft Matter* **14**(29), 6119 (2018). [CHNRNS]
- Need, R.F., Marshall, P.B., Weschke, E., Grutter, A.J., Gilbert, D.A., Arenholz, E., Shafer, P., Stemmer, S., Wilson, S.D., "Resolving Interfacial Charge Transfer in Titanate Superlattices using Resonant X-ray Reflectometry," *Phys. Rev. Mater.* **2**(9), 093801 (2018).
- Nemoto, F., Kofu, M., Nagao, M., Ohishi, K., Takata, S.-I., Suzuki, J.-I., Yamada, T., Shibata, K., Ueki, T., Kitazawa, Y., Watanabe, M., Yamamuro, O., "Neutron Scattering Studies on Short- and Long-Range Layer Structures and Related Dynamics in Imidazolium-Based Ionic Liquids," *J. Chem. Phys.* **149**(5), 054502 (2018). [CHNRNS]
- Nguyen, M.H.L., DiPasquale, M., Rikeard, B.W., Stanley, C.B., Kelley, E.G., Marquardt, D., "Methanol Accelerates DMPC Flip-Flop and Transfer: A SANS Study on Lipid Dynamics," *Biophys. J.* **116**, 755 (2019). [CHNRNS]
- Noferini, D., Faraone, A., Rossi, M., Mamontov, E., Fratini, E., Baglioni, P., "Disentangling Polymer Network and Hydration Water Dynamics in Polyhydroxyethyl Methacrylate Physical and Chemical Hydrogels," *J. Phys. Chem. C*, in press.
- Nsofini, J., Sarenac, D., Cory, D.G., Pushin, D.A., "Coherence Optimization in Neutron Interferometry through Defocusing," *Phys. Rev. A* **99**(4), 043614 (2019).
- Okuyama, D., Bleuel, M., White, J.S., Ye, Q., Krzywon, J., Nagy, G., Im, Z.Q., Živković, I., Bartkowiak, M., Rønnow, H.M., Hoshino, S., Iwasaki, J., Nagaosa, N., Kikkawa, A., Taguchi, Y., Tokura, Y., Higashi, D., Reim, J.D., Nambu, Y., Sato, T.J., "Deformation of the Moving Magnetic Skyrmion Lattice in MnSi under Electric Current Flow," *Comm. Phys.* **2**, 79 (2019).
- Orvis, T., Surendran, M., Liu, Y., Niu, S., Muramoto, S., Grutter, A.J., Ravichandran, J., "Electron Doping BaZrO_3 via Topochemical Reduction," *ACS Appl. Mater. Interfaces* **11**(24), 21720 (2019).
- Osti, N.C., Matsumoto, R.A., Thompson, M.W., Cummings, P.T., Tyagi, M., Mamontov, E., "Microscopic Dynamics in an Ionic Liquid Augmented with Organic Solvents," *J. Phys. Chem. C*, in press.

- Osti, N.C., Thompson, M.W., Van Aken, K.L., Alhabeib, M., Tyagi, M., Keum, J.-K., Cummings, P.T., Gogotsi, Y., Mamontov, E., "Humidity Exposure Enhances Microscopic Mobility in a Room-Temperature Ionic Liquid in MXene," *J. Phys. Chem. C* **122**(48), 27561 (2018). [CHRNS]
- Pajerowski, D.M., Krayner, L.A., Jeon, H., Borchers, J.A., Biswas, A., Ravel, B., "Correlation of Cation Deficiency and Nanostructure to Decreased Magnetism in a Ferroelectric BiMnO₃ Film," *J. Appl. Phys.*, in press. [CHRNS]
- Pajerowski, D.M., Krayner, L.J., Kirby, B.J., Maranville, B.B., Borchers, J.A., Kim, K.-W., Norton, D.P., "Pulsed Laser Deposition Films from a Ba₂FeMoO₆ Target onto SrTiO₃[001]: Chemical and Magnetic Inhomogeneity," *J. Appl. Phys.* **124**(16), 163903 (2018). [CHRNS]
- Pan, Z., Chen, J., Yu, R., Patra, L., Ravindran, P., Sanson, A., Milazzo, R., Carnera, A., Hu, L., Wang, L., Yamamoto, H., Ren, Y., Huang, Q., Sakai, Y., Nishikubo, T., Ogata, T., Fan, X., Li, Y., Li, G., Hojo, H., Azuma, M., Xing, X., "Large Negative Thermal Expansion Induced by Synergistic Effects of Ferroelectrostriction and Spin Crossover in PbTiO₃-Based Perovskites," *Chem. Mater.* **31**(4), 1296 (2019).
- Pásztorová, J., Howell, A., Songvilay, M., Sarte, P.M., Rodriguez-Rivera, J.A., Arévalo-López, A.M., Schmalzl, K., Schneidewind, A., Dunsiger, S.R., Singh, D.K., Petrovic, C., Hu, R., Stock, C., "Relaxing Kondo-Screened Kramers Doublets in CeRhSi₃," *Phys. Rev. B* **99**(12), 125144 (2019). [CHRNS]
- Paul, R.L., "Improving Accuracy, Precision, Detection Limits, and Sample Throughput in Prompt Gamma-Ray Activation Analysis using Cold and Thermal Neutrons and Element Ratios," *J. Radioanal. Nucl. Ch.* **318**(3), 2273 (2018).
- Phan, T.Q., Strantz, M., Hill, M.R., Gnaupel-Herold, T.H., Heigel, J., D'Elia, C.R., DeWald, A.T., Clausen, B., Pagan, D.C., Ko, J.Y.P., Brown, D.W., Levine, L.E., "Elastic Residual Strain and Stress Measurements and Corresponding Part Deflections of 3D Additive Manufacturing Builds of IN625 AM-Bench Artifacts using Neutron Diffraction, Synchrotron X-ray Diffraction, and Contour Method," *Integr. Mater. Manuf. Innovat.*, in press.
- Plumb, K.W., Changlani, H.J., Scheie, A., Zhang, S., Krizan, J.W., Rodriguez-Rivera, J.A., Qiu, Y., Winn, B., Cava, R.J., Broholm, C.L., "Continuum of Quantum Fluctuations in a Three-Dimensional $S = 1$ Heisenberg Magnet," *Nat. Phys.* **15**, 54 (2019). [CHRNS]
- Polf, J.C., Mille, M.M., Mossahebi, S., Chen, H., Maggi, P., Chen-Mayer, H., "Determination of Proton Stopping Power Ratio with Dual-Energy CT in 3D-Printed Tissue/Air Cavity Surrogates," *Med. Phys.* **46**(7), 3245 (2019).
- Poling-Skutvik, R., Slim, A.H., Narayanan, S., Conrad, J.C., Krishnamoorti, R., "Soft Interactions Modify the Diffusive Dynamics of Polymer-Grafted Nanoparticles in Solutions of Free Polymer," *ACS Macro Lett.*, in press.
- Prasai, N., Akopyan, A., Trump, B.A., Marcus, G.G., Huang, S.X., McQueen, T.M., Cohn, J.L., "Spin Phases of the Helimagnetic Insulator Cu₂OSeO₃ Probed by Magnon Heat Condition," *Phys. Rev. B* **99**(2), 020403 (2019).
- Prawoto, Y., Manville, S., Sakai, T., Lee, L., Tanaka, M., Gnaupel-Herold, T., "Fracture Mechanics Approach to Splitting in Low Spring Index Cold Coiling Process," *J. Fail. Anal. Prevent.* **19**(3), 738 (2019).
- Qavi, S., Foudazi, R., "Rheological Characteristics of Mesophases of Block Copolymer Solutions," *Rheol. Acta*, in press.
- Quarterman, P., Hallsteinsen, I., Dunz, M., Meinert, M., Arenholz, E., Borchers, J.A., Grutter, A.J., "Effects of Field Annealing on MnN/CoFeB Exchange Bias Systems," *Phys. Rev. Mater.* **3**(6), 064413 (2019).
- Quintana, A., Menéndez, E., Liedke, M.O., Butterling, M., Wagner, A., Sireus, V., Torruella, P., Estradé, S., Peiró, F., Dendooven, J., Detavernier, C., Murray, P.D., Gilbert, D.A., Liu, K., Pellicer, E., Nogues, J., Sort, J., "Voltage-Controlled ON-OFF Ferromagnetism at Room Temperature in a Single Metal Oxide Film," *ACS Nano* **12**(10), 10291 (2018).
- Rahalkar, A., Wei, G., Nieuwendaal, R., Prabhu, V.M., Srivastava, S., Levi, A.E., de Pablo, J.J., Tirrell, M.V., "Effect of Temperature on the Structure and Dynamics of Triblock Polyelectrolyte Gels," *J. Chem. Phys.* **149**(16), 163310 (2018).
- Rai, B.K., Chikara, S., Ding, X., Oswald, I.W.H., Schönemann, R., Loganathan, V., Hallas, A.M., Cao, H.B., Stavinocha, M., Chen, T., Man, H., Carr, S., Singleton, J., Zapf, V., Benavides, K.A., Chan, J.Y., Zhang, Q.R., Rhodes, D., Chiu, Y.C., Balicas, L., Aczel, A.A., Huang, Q., Lynn, J.W., Gaudet, J., Sokolov, D.A., Walker, H.C., Adroja, D.T., Dai, P., Nevidomskyy, A.H., Huang, C.-L., Morosan, E., "Anomalous Metamagnetism in the Low Carrier Density Kondo Lattice YbRh₃Si₇," *Phys. Rev. X* **8**(4), 041047 (2018).
- Rai, B.K., Oswald, I.W.H., Ban, W., Huang, C.-L., Loganathan, V., Hallas, A.M., Wilson, M.N., Luke, G.M., Harriger, L., Huang, Q., Li, Y., Dzsaber, S., Chan, J.Y., Wang, N.L., Paschen, S., Lynn, J.W., Nevidomskyy, A.H., Dai, P., Si, Q., Morosan, E., "Low-Carrier Density and Fragile Magnetism in a Kondo Lattice System," *Phys. Rev. B* **99**(8), 085120 (2019).

- Ramazanoglu, M., Ueland, B.G., Pratt, D.K., Harriger, L.W., Lynn, J.W., Ehlers, G., Granroth, G.E., Bud'ko, S.L., Canfield, P.C., Schlager, D.L., Goldman, A.I., Lograsso, T.A., McQueeney, R.J., "Suppression of Antiferromagnetic Spin Fluctuations in Superconducting $\text{Cr}_{0.8}\text{Ru}_{0.2}$," *Phys. Rev. B* **98**(13), 134512 (2018).
- Ran, S., Eckberg, C., Ding, Q.-P., Furukawa, Y., Metz, T., Saha, S.R., Liu, I.-L., Zic, M., Kim, H., Paglione, J., Butch, N.P., "Nearly Ferromagnetic Spin-Triplet Superconductivity," *Science*, in press.
- Ran, S., Schmiedeshoff, G.M., Pouse, N., Jeon, I., Butch, N.P., Adhikari, R.B., Almasan, C.C., Maple, M.B., "Rapid Suppression of the Energy Gap and the Possibility of a Gapless Hidden Order State in $\text{URu}_{2-x}\text{Re}_x\text{Si}_2$," *Philos. Mag.* **99**(14), 1751 (2019).
- Rau, J.G., Wu, L.S., May, A.F., Taylor, A.E., Liu, I.-L., Higgins, J., Butch, N.P., Ross, K.A., Nair, H.S., Lumsden, M.D., Gingras, M.J.P., Christianson, A.D., "Behavior of the Breathing Pyrochlore Lattice $\text{Ba}_3\text{Yb}_2\text{Zn}_5\text{O}_{11}$ in Applied Magnetic Field," *J. Phys.: Condens. Mat.* **30**, 455801 (2018).
- Reid, D.R., Jackson, N.E., Bourque, A.J., Snyder, C.R., Jones, R.L., de Pablo, J.J., "Aggregation and Solubility of a Model Conjugated Donor-Acceptor Polymer," *J. Phys. Chem. Lett.* **9**(16), 4802 (2018).
- Richards, J.J., Riley, J.K., "Dielectric RheoSANS: A Mutual Electrical and Rheological Characterization Technique using Small-Angle Neutron Scattering," *Curr. Opin. Colloid In.*, in press.
- Rinehart, S.J., Yuan, G., Dadmun, M.D., "Elucidating the Kinetic and Thermodynamic Driving Forces in Polymer Blend Film Self-Stratification," *Macromolecules* **51**(19), 7836 (2018).
- Robertson, L.A., Li, Z., Cao, Y., Shkrob, I.A., Tyagi, M., Smith, K.C., Zhang, L., Moore, J.S., Z, Y., "Observation of Microheterogeneity in Highly Concentrated Nonaqueous Electrolyte Solutions," *J. Am. Chem. Soc.* **141**(20), 8041 (2019). [CHRS]
- Rowland, C.A., Lorz, G.R., Gosselin, E.J., Trump, B.A., Yap, G.P.A., Brown, C.M., Bloch, E.D., "Methane Storage in Paddlewheel-Based Porous Coordination Cages," *J. Am. Chem. Soc.* **140**(36), 11153 (2018).
- Rubinson, K.A., "Why Proteins are Big: Length Scale Effects on Equilibria and Kinetics," *Protein J.* **38**(2), 95 (2019).
- Şahin, D., Stakhovsky, K., Cavazos, O., "NBSR Virtual Reality Training Simulator," *T. Am. Nucl. Soc.*, in press.
- Saini, A., Wolff, M., "Macroscopic Alignment of Micellar Crystals with Magnetic Microshearing," *Langmuir* **35**(11), 3980 (2019).
- Sarenac, D., Clark, C.W., Cory, D.G., Kapahi, C., Heacock, B., Huber, M.G., Nsofini, J., Shahi, C.B., Pushin, D.A., "Structured Neutron Waves," in "Proceedings of SPIE," edited by Shahriar, S.M. and Scheuer, J., (Optical, Opto-Atomic, and Entanglement-Enhanced Precision Metrology, February 2019, San Francisco, CA) **10934**, 1093425 (2019).
- Sarenac, D., Cory, D.G., Nsofini, J., Hincks, I., Miguel, P., Arif, M., Clark, C.W., Huber, M.G., Pushin, D.A., "Generation of a Lattice of Spin-Orbit Beams via Coherent Averaging," *Phys. Rev. Lett.* **121**(18), 183602 (2018).
- Sarenac, D., Nsofini, J., Hincks, I., Arif, M., Clark, C.W., Cory, D.G., Huber, M.G., Pushin, D.A., "Methods for Preparation and Detection of Neutron Spin-Orbit States," *New J. Phys.* **20**, 103012 (2018).
- Sarte, P.M., Arévalo-López, A.M., Songvilay, M., Le, D., Guidi, T., García-Sakai, V., Mukhopadhyay, S., Capelli, S.C., Ratcliff, W.D., Hong, K.H., McNally, G.M., Pachoud, E., Attfield, J.P., Stock, C., "Ordered Magnetism in the Intrinsically Decorated $j_{\text{eff}} = 1/2$ $\alpha\text{-CoV}_3\text{O}_8$," *Phys. Rev. B* **98**(22), 224410 (2018).
- Scheie, A., Dasgupta, S., Sanders, M., Sakai, A., Matsumoto, Y., Prisk, T.R., Nakatsuji, S., Cava, R.J., Broholm, C., "Homogeneous Reduced Moment in a Gapful Scalar Chiral Kagome Antiferromagnet," *Phys. Rev. B* **100**(2), 024414 (2019). [CHRS]
- Scheie, A., Sanders, M., Krizan, J., Christianson, A.D., Garlea, V.O., Cava, R.J., Broholm, C., "Crystal Field Levels and Magnetic Anisotropy in the Kagome Compounds $\text{Nd}_3\text{Sb}_3\text{Mg}_2\text{O}_{14}$, $\text{Nd}_3\text{Sb}_3\text{Zn}_2\text{O}_{14}$, and $\text{Pr}_3\text{Sb}_3\text{Mg}_2\text{O}_{14}$," *Phys. Rev. B* **98**(13), 134401 (2018).
- Senses, E., Narayanan, S., Faraone, A., "Nanoscale Particle Motion Reveals Polymer Mobility Gradient in Nanocomposites," *ACS Macro Lett.* **8**(5), 558 (2019). [CHRS]
- Senses, E., Tyagi, M., Pasco, M., Faraone, A., "Dynamics of Architecturally Engineered All-Polymer Nanocomposites," *ACS Nano* **12**(11), 10807 (2018). [CHRS]
- Shan, L., Xie, R., Wagner, N.J., He, H., Liu, Y., "Microstructure of Neat and SBS Modified Asphalt Binder by Small-Angle Neutron Scattering," *Fuel*, in press. [CHRS]
- Shao, Q., Grutter, A., Liu, Y., Yu, G., Yang, C.-Y., Gilbert, D.A., Arenholz, E., Shafer, P., Chi, X., Tang, C., Aldosary, M., Navabi, A., He, Q.L., Kirby, B.J., Shi, J., Wang, K.L., "Exploring Interfacial Exchange Coupling and Sublattice Effect in Heavy Metal/Ferrimagnetic Insulator Heterostructures using Hall Measurements, X-ray Magnetic Circular Dichroism, and Neutron Reflectometry," *Phys. Rev. B* **99**(10), 104401 (2019).

- Shih, K.-C., Shen, Z., Li, Y., Kröger, M., Chang, S.-Y., Liu, Y., Nieh, M.-P., Lai, H.-M., "What Causes the Anomalous Aggregation in Pluronic Aqueous Solutions?" *Soft Matter* **14**(37), 7653 (2018). [CHRS]
- Shmueli, Y., Jiang, J., Zhou, Y., Xue, Y., Chang, C.-C., Yuan, G., Satija, S.K., Lee, S., Nam, C.-Y., Kim, T., Marom, G., Gersappe, D., Rafailovich, M.H., "Simultaneous in Situ X-ray Scattering and Infrared Imaging of Polymer Extrusion in Additive Manufacturing," *ACS Appl. Polym. Mater.* **1**(6), 1559 (2019).
- Shteinberg, E., Şahin, D., "NBSR Refueling Canon Control System Upgrade," *T. Am. Nucl. Soc.*, in press.
- Shu, S., Almirall, N., Wells, P.B., Yamamoto, T., Odette, G.R., Morgan, D.D., "Precipitation in Fe-Cu and Fe-Cu-Mn Model Alloys under Irradiation: Dose Rate Effects," *Acta Mater.* **157**, 72 (2018).
- Skoryunov, R.V., Babanova, O.A., Soloninin, A.V., Skripov, A.V., Chotard, J.-N., Janot, R., Tang, W.S., Dimitrievska, M., Udovic, T.J., "Nuclear Magnetic Resonance Study of Anion and Cation Dynamics in CsSiH₃," *J. Alloy Compd.* **781**, 913 (2019).
- Smolyaninova, V.N., Lynn, J.W., Butch, N.P., Chen-Mayer, H., Prestigiacomo, J.C., Osofsky, M.S., Smolyaninov, I.I., "Observation of Plasmon-Phonons in a Metamaterial Superconductor using Inelastic Neutron Scattering," *Phys. Rev. B* **100**(2), 024515 (2019).
- Snow, W.M., Dickerson, K.A., Devaney, J.S., Haddock, C., "Calculations of Neutron Reflectivity in the eV Energy Range from Mirrors made of Heavy Nuclei with Neutron-Nucleus Resonances," *Phys. Rev. A*, in press.
- Sokolov, D.A., Kikugawa, N., Helm, T., Borrmann, H., Burkhardt, U., Cubitt, R., White, J.S., Ressouche, E., Bleuel, M., Kummer, K., Mackenzie, A.P., Röbber, U.K., "Metamagnetic Texture in a Polar Antiferromagnet," *Nat. Phys.* **15**, 671 (2019).
- Soloninin, A.V., Skoryunov, R.V., Babanova, O.A., Skripov, A.V., Dimitrievska, M., Udovic, T.J., "Comparison of Anion and Cation Dynamics in a Carbon-Substituted *clos*-Hydroborate Salt: ¹H and ²³Na NMR Studies of Solid-Solution Na₂(CB₉H₁₀)(CB₁₁H₁₂)," *J. Alloy Compd.*, in press.
- Song, Y., Cao, H., Chakoumakos, B.C., Zhao, Y., Wang, A., Lei, H., Petrovic, C., Birgeneau, R.J., "Intertwined Magnetic and Nematic Orders in Semiconducting KFe_{0.8}Ag_{1.2}Te₂," *Phys. Rev. Lett.* **122**(8), 087201 (2019).
- Song, Y., Qiao, Y., Huang, Q., Wang, C., Liu, X., Li, Q., Chen, J., Xing, X., "Opposite Thermal Expansion in Isostructural Noncollinear Antiferromagnetic Compounds of Mn₃A (A = Ge and Sn)," *Chem. Mater.* **30**(18), 6236 (2018).
- Songvilay, M., Bari, M., Ye, Z.-G., Xu, G., Gehring, P.M., Ratcliff, W.D., Schmalzl, K., Bourdarot, F., Roessli, B., Stock, C., "Lifetime-Shortened Acoustic Phonons and Static Order at the Brillouin Zone Boundary in the Organic-Inorganic Perovskite CH₃NH₃PbCl₃," *Phys. Rev. Mater.* **2**(12), 123601 (2018).
- Songvilay, M., Rodriguez, E.E., Lindsay, R., Green, M.A., Walker, H.C., Rodriguez-Rivera, J.A., Stock, C., "Anharmonic Magnon Excitations in Noncollinear and Charge-Ordered RbFe²⁺Fe³⁺F₆," *Phys. Rev. Lett.* **121**(8), 087201 (2018). [CHRS]
- Spernjak, D., Mukundan, R., Borup, R.L., Connolly, L.G., Zackin, B.I., De Andrade, V., Wojcik, M., Parkinson, D.Y., Jacobson, D.L., Hussey, D.S., More, K.L., Chan, T., Weber, A.Z., Zenyuk, I.V., "Enhanced Water Management of Polymer Electrolyte Fuel Cells with Additive-Containing Microporous Layers," *ACS Appl. Energy Mater.* **1**, 6006 (2018).
- Stavretis, S.E., Cheng, Y., Daemen, L.L., Brown, C.M., Moseley, D.H., Bill, E., Atanasov, M., Ramirez-Cuesta, A.J., Neese, F., Xue, Z.-L., "Probing Magnetic Excitations in Co^{II} Single-Molecule Magnets by Inelastic Neutron Scattering," *Eur. J. Inorg. Chem.* **2019**(8), 1119 (2019).
- Stephen, G.M., Buda, G., Jamer, M.E., Lane, C., Kaprzyk, S., Barbiellini, B., Graf, D., Lewis, L.H., Bansil, A., Heiman, D., "Structural and Electronic Properties of the Spin-Filter Material CrVTiAl with Disorder," *J. Appl. Phys.* **125**, 123903 (2019).
- Sun, R., Jin, S., Gu, L., Zhang, Q., Huang, Q., Ying, T., Peng, Y., Deng, J., Yin, Z., Chen, X., "Intercalating Anions between Terminated Anion Layers: Unusual Ionic S-Se Bonds and Hole-Doping Induced Superconductivity in S_{0.24}(NH₃)_{3/0.26}Fe₂Se₂," *J. Am. Chem. Soc.*, in press.
- Sun, R.J., Quan, Y., Jin, S.F., Huang, Q.Z., Wu, H., Zhao, L., Gu, L., Yin, Z.P., Chen, X.L., "Realization of Continuous Electron Doping in Bulk Iron Selenides and Identification of a New Superconducting Zone," *Phys. Rev. B* **98**(21), 214508 (2018).
- Sun, Y., Hu, P., Shi, K., Wu, H., Deng, S., Huang, Q., Mao, Z., Song, P., Wang, L., Hao, W., Deng, S., Wang, C., "Giant Zero-Field Cooling Exchange-Bias-Like Behavior in Antiperovskite Mn₃Co_{0.61}Mn_{0.39}N Compound," *Phys. Rev. Mater.* **3**(2), 024409 (2019).
- Suzuki, T., Savary, L., Liu, J.-P., Lynn, J.W., Balents, L., Checkelsky, J.G., "Singular Angular Magnetoresistance in a Magnetic Nodal Semimetal," *Science* **365**, 377 (2019).

- Swanson, H.E., Heckel, B.R., Bass, C.D., Bass, T.D., Dawkins, J.M., Horton, J.C., Luo, D., Snow, W.M., Walbridge, S.B., Crawford, B.E., Gan, K., Micherdzinska, A.M., Huffer, C., Markoff, D.M., Mumm, H.P., Nico, J.S., Sarsour, M., Sharapov, E.I., Zhumabekova, V., "Experimental Upper Bound and Theoretical Expectations for Parity-Violating Neutron Spin Rotation in ^4He ," *Phys. Rev. C* **100**(1), 015204 (2019).
- Tavera-Vázquez, A., Arenas-Gómez, B., Garza, C., Liu, Y., Castillo, R., "Structure, Rheology, and Microrheology of Wormlike Micelles made of PB-PEO Diblock Copolymers," *Soft Matter* **14**(35), 7264 (2018).
- Taylor, M.K., Runčevski, T., Oktawiec, J., Bachman, J.E., Siegelman, R.L., Jiang, H., Mason, J.A., Tarver, J.D., Long, J.R., "Near-Perfect CO_2/CH_4 Selectivity Achieved through Reversible Guest Templating in the Flexible Metal-Organic Framework Co(bdp)," *J. Am. Chem. Soc.* **140**(32), 10324 (2018).
- Teixeira, S.C.M., "High-Pressure Small-Angle Neutron Scattering for Food Studies," *Curr. Opin. Colloid In.*, in press.
- Tian, Q., Yan, G., Bai, L., Chen, J., Liu, D., Chen, L., Sun, L., Huang, C., Chen, B., Nagy, G., Wacha, A., Almásy, L., "Calibration of the Suanni Small-Angle Neutron Scattering Instrument at the China Mianyang Research Reactor," *J. Appl. Crystallogr.* **51**(6), 1662 (2018).
- Tomko, J.A., Pena-Francesch, A., Jung, H., Tyagi, M., Allen, B.D., Demirel, M.C., Hopkins, P.E., "Tunable Thermal Transport and Reversible Thermal Conductivity Switching in Topologically Networked Bio-Inspired Materials," *Nat. Nanotechnol.* **13**, 959 (2018). [CHRS]
- Torres, J., Buck, Z.N., Kaiser, H., He, X., White, T., Tyagi, M., Winholtz, R.A., Hansen, F.Y., Herwig, K.W., Taub, H., "A Neutron Scattering and Electron Microscopy Study of the Structure, Wetting, and Freezing Behavior of Water Near Hydrophilic CuO -Nanostructured Surfaces," *J. Appl. Phys.* **125**(2), 025302 (2019). [CHRS]
- Tosado, J., Chen, W.C., Gnewuch, S., Hasaan, T., Dax, T., Rodriguez, E.E., "Small-Angle Neutron Polarimetry Apparatus (SANPA): Development at the NIST Center for Neutron Research," *Rev. Sci. Instrum.* **90**(6), 063303 (2019).
- Treece, B.W., Kienzle, P.A., Hoogerheide, D.P., Majkrzak, C.F., Lösche, M., Heinrich, F., "Optimization of Reflectometry Experiments using Information Theory," *J. Appl. Crystallogr.* **52**(1), 47 (2019).
- Turkoglu, D.J., Wu, Z., Williams, R.E., Newton, T.H., "Comparison of Neutronics Performance Characteristics of the Proposed NIST Reactor with Different LEU Fuels," in "Proceedings of the PHYSOR 2018 Conference," edited by PHYSOR, (PHYSOR 2018: Reactor Physics Paving the Way Towards more Efficient Systems, April 2018, Cancun, Mexico), 50009238 (2018).
- Turkoglu, D.J., Wu, Z., Williams, R.E., Newton, T.H., "Neutronic Performance Characteristics of Different LEU Fuels in a Proposed NIST Research Reactor," *Ann. Nucl. Energy* **128**, 209 (2019).
- Tyagi, P., Goulet, T., "Nanoscale Tantalum Layer Impacting Magnetic Properties of Tunnel Junction-Based Molecular Devices," *MRS Commun.* **8**(3), 1024 (2018).
- Ueland, B.G., Kreyssig, A., Mun, E.D., Lynn, J.W., Harriger, L.W., Pratt, D.K., Prokeš, K., Hüsches, Z., Toft-Petersen, R., Sauerbrei, S., Saunders, S.M., Furukawa, Y., Bud'ko, S.L., McQueeney, R.J., Canfield, P.C., Goldman, A.I., "Magnetic-Field Effects on the Fragile Antiferromagnetism in YbBiPt ," *Phys. Rev. B* **99**(18), 184431 (2019).
- Uppuluri, R., Akamatsu, H., Gupta, A.S., Wang, H., Brown, C.M., Agueda Lopez, K.E., Alem, N., Gopalan, V., Mallouk, T.E., "Competing Polar and Antipolar Structures in the Ruddlesden-Popper Layered Perovskite $\text{Li}_2\text{SrNb}_2\text{O}_7$," *Chem. Mater.* **31**(12), 4418 (2019).
- Urosov, I., Dorrington, H., Muzzin, N., Alsop, R., Bakaic, E., Gilbert, T., Rheinstädter, M., Hoare, T., "Injectable Poly(Oligoethylene Glycol Methacrylate)-Based Hydrogels Fabricated from Highly Branched Precursor Polymers: Controlling Gel Properties by Precursor Polymer Morphology," *ACS Appl. Polym. Mater.* **1**(3), 369 (2019). [CHRS]
- Vicenzi, E.P., Pearce, C.I., Weaver, J.L., McCloy, J.S., Wight, S., Lam, T., Whittaker, S., Sjöblom, R., Peeler, D.K., Schweiger, M.J., Kruger, A.A., "Compositional Imaging and Analysis of Late Iron Age Glass from the Broborg Vitrified Hillfort, Sweden," *Microsc. Microanal.* **24**(Suppl 1), 2134 (2018).
- Virtue, A., Zhou, X., Wilfong, B., Lynn, J.W., Taddei, K., Zavalij, P., Wang, L., Rodriguez, E.E., "Magnetic Order Effects on the Electronic Structure of KMMnS_2 ($M = \text{Cu}, \text{Li}$) with the ThCr_2Si_2 -Type Structure," *Phys. Rev. Mater.* **3**(4), 044411 (2019).
- Wang, C., Deitrick, K., Seo, J., Cheng, Z., Zacharia, N.S., Weiss, R.A., Vogt, B.D., "Manipulating the Mechanical Response of Hydrophobically Cross-Linked Hydrogels with Ionic Associations," *Macromolecules*, in press. [CHRS]

- Wang, C., Wiener, C.G., Sepulveda-Medina, P.I., Ye, C., Simmons, D.S., Li, R., Fukuto, M., Weiss, R.A., Vogt, B.D., "Antifreeze Hydrogels from Amphiphilic Statistical Copolymers," *Chem. Mater.* **31**(1), 135 (2019). [CHRNS]
- Wang, C., Xie, H., Ping, W., Dai, J., Feng, G., Yao, Y., He, S., Weaver, J., Wang, H., Gaskell, K., Hu, L., "A General, Highly Efficient, High Temperature Thermal Pulse Toward High Performance Solid State Electrolyte," *Energy Storage Mater.* **17**, 234 (2019).
- Wang, J., Fishman, R.S., Qiu, Y., Fernandez-Baca, J.A., Ehlers, G., Liang, K.-C., Wang, Y., Lorenz, B., Chu, C.W., Ye, F., "Comprehensive Inelastic Neutron Scattering Study of the Multiferroic $\text{Mn}_{1-x}\text{Co}_x\text{WO}_4$," *Phys. Rev. B* **98**(21), 214425 (2018).
- Wang, J., Zhou, L., Wang, Y., Xu, J., Yang, X., Kuang, X., "Molecular Dynamic Simulation of Interstitial Oxide Ion Migration in $\text{Pb}_{1-x}\text{La}_x\text{WO}_{4+x/2}$ Scheelite," *J. Solid State Chem.* **268**, 16 (2018).
- Wang, J.-Y., Chen, W., Nagao, M., Shelat, P., Hammer, B.A.G., Tietjen, G.T., Cao, K.D., Henderson, J.M., He, L., Lin, B., Akgun, B., Meron, M., Qian, S., Ward, S., Marks, J.D., Emrick, T., Lee, K.Y.C., "Tailoring Biomimetic Phosphorylcholine-Containing Block Copolymers as Membrane-Targeting Cellular Rescue Agents," *Biomacromolecules*, in press. [CHRNS]
- Wang, W., Song, Y., Cao, C., Tseng, K.-F., Keller, T., Li, Y., Harriger, L.W., Tian, W., Chi, S., Yu, R., Nevidomskyy, A.H., Dai, P., "Local Orthorhombic Lattice Distortions in the Paramagnetic Tetragonal Phase of Superconducting $\text{NaFe}_{1-x}\text{Ni}_x\text{As}$," *Nat. Commun.* **9**, 3128 (2018).
- Wang, X., Mathis, T.S., Li, K., Lin, Z., Vlcek, L., Torita, T., Osti, N.C., Hatter, C., Urbankowski, P., Sarycheva, A., Tyagi, M., Mamontov, E., Simon, P., Gogotsi, Y., "Influences from Solvents on Charge Storage in Titanium Carbide MXenes," *Nat. Energy* **4**, 241 (2019). [CHRNS]
- Wang, Y., Qin, Y., Zhang, R., Anovitz, L.M., Bleuel, M., "Investigation of Nanopore Structure and its Effect on Methane Storage in Chinese Marine Shales using Combined Methods: Small-Angle Neutron Scattering, Low-Pressure N_2/CO_2 Adsorption and High-Pressure Mercury Intrusion," in "Proceedings of TSOP Annual Meeting," edited by TSOP, (35th TSOP Annual Meeting, August 2018, Beijing, China) Abstract **67**, 271 (2018). [CHRNS]
- Wang, Y., Qin, Y., Zhang, R., He, L., Anovitz, L.M., Bleuel, M., Mildner, D.F.R., Liu, S., Zhu, Y., "Evaluation of Nanoscale Accessible Pore Structures for Improved Prediction of Gas Production Potential in Chinese Marine Shales," *Energy Fuel.* **32**(12), 12447 (2018).
- Wang, Z., Guo, H., Liu, Y., Wang, X., "Investigating the Effective Interaction between Silica Colloidal Particles Near the Critical Point of a Binary Solvent by Small Angle Neutron Scattering," *J. Chem. Phys.* **149**(8), 084905 (2018). [CHRNS]
- Wang, Z., Iwashita, T., Porcar, L., Wang, Y., Liu, Y., Sánchez-Díaz, L.E., Wu, B., Huang, G.-R., Egami, T., Chen, W.-R., "Local Elasticity in Nonlinear Rheology of Interacting Colloidal Glasses Revealed by Neutron Scattering and Rheometry," *Phys. Chem. Chem. Phys.* **21**(1), 38 (2019).
- Wang, Z.-Y., Kong, D., Yang, L., Ma, H., Su, F., Ito, K., Liu, Y., Wang, X., Wang, Z., "Analysis of Small-Angle Neutron Scattering Spectra from Deformed Polymers with the Spherical Harmonic Expansion Method and a Network Model," *Macromolecules* **51**(21), 9011 (2018). [CHRNS]
- Weaver, J.L., Downing, R.G., "Near-Surface Elemental Analysis of Solids by Neutron Depth Profiling," in "Contributed Papers from Materials Science and Technology 2018," edited by AIME, (MS&T18, October 2018, Columbus, OH) 1334 (2019).
- Weaver, J.L., Pearce, C.I., Arey, B., Conroy, M., Vicenzi, E.P., Sjöblom, R., Koestler, R.J., DePriest, P.T., Lam, T.F., Peeler, D.K., McCloy, J.S., Kruger, A.A., "Microscopic Identification of Micro-Organisms on Pre-Viking Swedish Hillfort Glass," *Microsc. Microanal.* **24**(Suppl. 1), 2136 (2018).
- Weaver, J.L., Turkoglu, D., "Natural Alteration of ^6Li Aluminosilicate Glass," *J. Nucl. Mater.* **512**, 56 (2018).
- Weaver, J.L., Pearce, C.I., Sjöblom, R., McCloy, J.S., Miller, M., Varga, T., Arey, B.W., Conroy, M.A., Peeler, D.K., Koestler, R.J., DePriest, P.T., Vicenzi, E.P., Hjärthner-Holdar, E., Ogenhall, E., Kruger, A.A., "Pre-Viking Swedish Hillfort Glass: A Prospective Long-Term Alteration Analogue for Vitrified Nuclear Waste," *Int. J. Appl. Glass Sci.* **9**(4), 540 (2018).
- Weber, J., Cheshire, M.C., Distefano, V.H., Littrell, K.C., Ilavsky, J., Bleuel, M., Bozell-Messerschmidt, J.K., Levlev, A.V., Stack, A.G., Anovitz, L.M., "Controls of Microstructure and Chemical Reactivity on the Replacement of Limestone by Fluorite Studied using Spatially Resolved Small Angle X-ray and Neutron Scattering," *ACS Earth Space Chem.*, in press. [CHRNS]
- Wegner, A., Louca, D., Yang, J., "Local Trigonal Modes and the Suppression of the Charge Density Wave in $\text{TiSe}_{2-x}\text{Te}_x$," *Phys. Rev. B* **99**(20), 205110 (2019).

- Wei, P.-C., Bhattacharya, S., Liu, Y.-F., Liu, F., He, J., Tung, Y.-H., Yang, C.-C., Hsing, C.-R., Nguyen, D.-L., Wei, C.-M., Chou, M.-Y., Lai, Y.-C., Hung, T.-L., Guan, S.-Y., Chang, C.-S., Wu, H.-J., Lee, C.-H., Li, W.-H., Hermann, R.P., Chen, Y.-Y., Rao, A.M., "Thermoelectric Figure-of-Merit of Fully Dense Single-Crystalline SnSe," *ACS Omega* **4**(3), 5442 (2019).
- Weinrich, M., Worcester, D.L., "The Actions of Volatile Anesthetics: A New Perspective," *Acta Crystallogr. D* **D74**(12), 1169 (2018).
- Wen, H., Gan, L.-Y., Dai, H.-B., Wen, X.-P., Wu, L.-S., Wu, H., Wang, P., "In Situ Grown Ni Phosphide Nanowire Array on Ni Foam as a High-Performance Catalyst for Hydrazine Electrooxidation," *Appl. Catal. B-Environ.* **241**, 292 (2019).
- Wen, H.-M., Liao, C., Li, L., Alsalmeh, A., Allothman, Z., Krishna, R., Wu, H., Zhou, W., Hu, J., Chen, B., "A Metal-Organic Framework with Suitable Pore Size and Dual Functionalities for Highly Efficient Post-Combustion CO₂ Capture," *J. Mater. Chem. A* **7**, 3128 (2019).
- Wiechert, A.I., Liao, W.-P., Hong, E., Halbert, C.E., Yiacoumi, S., Saito, T., Tsouris, C., "Influence of Hydrophilic Groups and Metal-Ion Adsorption on Polymer-Chain Conformation of Amidoxime-Based Uranium Adsorbents," *J. Colloid Interf. Sci.* **524**, 399 (2018).
- Wiener, C.G., Qiang, Z., Xia, Y., Tyagi, M., Vogt, B.D., "Impact of Surface Wettability on Dynamics of Supercooled Water Confined in Nitrogen-Doped Ordered Mesoporous Carbon," *Phys. Chem. Chem. Phys.* **20**(44), 28019 (2018). [CHNRS]
- Winslow, S.W., Liu, Y., Swan, J.W., Tisdale, W.A., "Quantification of a PbCl_x Shell on the Surface of PbS Nanocrystals," *ACS Mater. Lett.*, in press.
- Winslow, S.W., Shcherbakov-Wu, W., Liu, Y., Tisdale, W.A., Swan, J.W., "Characterization of Colloidal Nanocrystal Surface Structure using Small Angle Neutron Scattering and Efficient Bayesian Parameter Estimation," *J. Chem. Phys.* **150**(24), 244702 (2019).
- Wo, H., Wang, Q., Shen, Y., Zhang, X., Hao, Y., Feng, Y., Shen, S., He, Z., Pan, B., Wang, W., Nakajima, K., Ohira-Kawamura, S., Steffens, P., Boehm, M., Schmalzl, K., Forrest, T.R., Matsuda, M., Zhao, Y., Lynn, J.W., Yin, Z., Zhao, J., "Coexistence of Ferromagnetic and Stripe-Type Antiferromagnetic Spin Fluctuations in YFe₂Ge₂," *Phys. Rev. Lett.* **122**(21), 217003 (2019).
- Wolf, C.M., Kanekal, K.H., Yimer, Y.Y., Tyagi, M., Omar-Diallo, S., Pakhnyuk, V., Luscombe, C.K., Pfaendner, J., Pozzo, L.D., "Assessment of Molecular Dynamics Simulations for Amorphous Poly(3-Hexylthiophene) using Neutron and X-ray Scattering Experiments," *Soft Matter* **15**(25), 5067 (2019). [CHNRS]
- Wolff, M., Devishvili, A., Dura, J.A., Adlmann, F.A., Kitchen, B., Pálsson, G.K., Palonen, H., Maranville, B.B., Majkrzak, C.F., Toperverg, B.P., "Nuclear Spin Incoherent Neutron Scattering from Quantum Well Resonators," *Phys. Rev. Lett.* **123**(1), 016101 (2019).
- Woo, W., Kim, J., Kim, E.-Y., Choi, S.-H., Em, V., Hussey, D.S., "Multi-Scale Analyses of Constituent Phases in a Trip-Assisted Duplex Stainless Steel by Electron Backscatter Diffraction, In Situ Neutron Diffraction, and Energy Selective Neutron Imaging," *Scripta Mater.* **158**, 105 (2019).
- Woodard, L.E., Dennis, C.L., Borchers, J.A., Attaluri, A., Velarde, E., Dawidczyk, C., Searson, P.C., Pomper, M.G., Ivkov, R., "Nanoparticle Architecture Preserves Magnetic Properties during Coating to Enable Robust Multi-Modal Functionality," *Sci. Rep.* **8**, 12706 (2018). [CHNRS]
- Worthington, P., Drake, K.M., Li, Z., Napper, A.D., Pochan, D.J., Langhans, S.A., "Implementation of a High-Throughput Pilot Screen in Peptide Hydrogel-Based Three-Dimensional Cell Cultures," *SLAS Discov.*, in press.
- Wu, H., Yang, Y., Hussey, D.S., Wang, Z., Song, K., Zhang, Z., Wang, Z., Wang, Z., Wang, X., "Study of a Nested Neutron-Focusing Supermirror System for Small-Angle Neutron Scattering," *Nucl. Instrum. Meth. A*, in press.
- Wu, S., Phelan, W.A., Liu, L., Morey, J.R., Tutmaher, J.A., Neuefeind, J.C., Huq, A., Stone, M.B., Feynson, M., Tam, D.W., Frandsen, B.A., Trump, B., Wan, C., Dunsiger, S.R., McQueen, T.M., Uemura, Y.J., Broholm, C.L., "Incommensurate Magnetism Near Quantum Criticality in CeNiAsO," *Phys. Rev. Lett.* **122**(19), 197203 (2019).
- Xi, Y., Wolf, C.M., Pozzo, L.D., "Self-Assembly of Donor-Acceptor Conjugated Polymers induced by Miscible 'Poor' Solvents," *Soft Matter* **15**(8), 1799 (2019). [CHNRS]
- Xu, J., McLaurin, J., Beckett, C., "Nucleate Boiling Heat Transfer and Bubble Dynamics of Water-in-Polyalphaolefin Nanoemulsion," in "Proceedings of the American Society of Mechanical Engineers 2018," edited by ASME, (5th Joint US-European Fluids Engineering Division Summer Meeting, July 2018, Montreal, Canada) FEDSM2018-83397 (2018). [CHNRS]
- Xu, N., Cao, G., Gan, L., Chen, Z., Zang, M., Wu, H., Wang, P., "Carbon-Coated Cobalt Molybdenum Oxide as a High-Performance Electrocatalyst for Hydrogen Evolution Reaction," *Int. J. Hydrogen Energ.* **43**(52), 23101 (2018).
- Xu, Z., Li, F., Zhang, S., Stock, C., Luo, J., Gehring, P.M., Xu, G., "Electric Field Effect on Short-Range Polar Order in a Relaxor Ferroelectric System," *Phys. Rev. B* **100**(2), 024113 (2019).

- Xue, Z.-L., Ramirez-Cuesta, A.J., Brown, C.M., Calder, S., Cao, H., Chakoumakos, B.C., Daemen, L.L., Huq, A., Kolesnikov, A.I., Mamontov, E., Podlesnyak, A.A., Wang, X., "Neutron Instruments for Research in Coordination Chemistry," *Eur. J. Inorg. Chem.* **2019**(8), 1065 (2019).
- Yablon, L.M., Sanders, S.N., Li, H., Parenti, K.R., Kumarasamy, E., Fallon, K.J., Hore, M.J.A., Cacciuto, A., Sfeir, M.Y., Campos, L.M., "Persistent Multiexcitons from Polymers with Pendent Pentacenes," *J. Am. Chem. Soc.* **141**(24), 9564 (2019).
- Yamaguchi, T., Faraone, A., Nagao, M., "Collective Mesoscale Dynamics of Liquid 1-Dodecanol Studied by Neutron Spin-Echo Spectroscopy with Isotopic Substitution and Molecular Dynamics Simulation," *J. Phys. Chem. B* **123**(1), 239 (2019). [CHNRNS]
- Yang, H., Guo, F., Lama, P., Gao, W.-Y., Wu, H., Barbour, L.J., Zhou, W., Zhang, J., Aguila, B., Ma, S., "Visualizing Structural Transformation and Guest Binding in a Flexible Metal-Organic Framework under High Pressure and Room Temperature," *ACS Central Sci.* **4**(9), 1194 (2018).
- Yang, J., Du, B., Liu, J., Krishna, R., Zhang, F., Zhou, W., Wang, Y., Li, J., Chen, B., "MIL-100Cr with Open Cr Sites for a Record N₂O Capture," *Chem. Commun.* **54**(100), 14061 (2018).
- Yang, J., Wegner, A., Brown, C.M., Louca, D., "Defect-Driven Extreme Magnetoresistance in an I-Mn-V Semiconductor," *Appl. Phys. Lett.* **113**(12), 122105 (2018).
- Yang, J., Yang, W., Zhao, H., Shao, Z., "Hard Magnetic Properties of MnBi Low-Temperature Phase," in "Materials Science and Technology," edited by Cahn, R.W., Haasen, P., and Kramer, E.J., (Wiley Publishing, Weinham, Germany) 2 (2019).
- Yang, M., Zhao, W., Singh, S., Simmons, B., Chang, G., "On the Solution Structure of Kraft Lignin in Ethylene Glycol and its Implication for Nanoparticle Preparation," *Nanoscale Adv.* **1**, 299 (2019). [CHNRNS]
- Yang, M., Zhao, W., Wang, S., Yu, C., Singh, S., Simmons, B., Cheng, G., "Dimethyl Sulfoxide Assisted Dissolution of Cellulose in 1-Ethyl-3-Methylimidazoium Acetate: Small Angle Neutron Scattering and Rheological Studies," *Cellulose* **26**(4), 2243 (2019).
- Yang, M.-D., Ho, C.-H., Ruta, S., Chantrell, R., Krycka, K., Hovorka, O., Chen, F.-R., Lai, P.-S., Lai, C.-H., "Magnetic Interaction of Multifunctional Core-Shell Nanoparticles for Highly Effective Theranostics," *Adv. Mater.* **30**(50), 1802444 (2018).
- Ye, Y., Ma, Z., Lin, R.-B., Krishna, R., Zhou, W., Lin, Q., Zhang, Z., Xiang, S., Chen, B., "Pore Space Partition within a Metal-Organic Framework for Highly Efficient C₂H₂/CO₂ Separation," *J. Am. Chem. Soc.* **141**(9), 4130 (2019).
- Yoshimune, W., Harada, M., "Effect of Pt Loading on the Adsorption of Perfluoro-Sulfonic Acid Ionomer in Catalyst Ink for Polymer Electrolyte Fuel Cells," *Chem. Lett.* **48**, 487 (2019).
- Yuan, G., Hammouda, B., "Solvent and Polymer H/D Isotope Effects on Miscibility in Poly(Ethylene Oxide)/Ethanol System," *Polymer* **166**, 178 (2019). [CHNRNS]
- Yue, A.T., Anderson, E.S., Dewey, M.S., Gilliam, D.M., Greene, G.L., Laptev, A.B., Nico, J.S., Snow, W.M., "Precision Determination of Absolute Neutron Flux," *Metrologia* **55**(4), 460 (2018).
- Yumnam, G., Chen, Y., Zhao, Y., Thamizhavel, A., Dhar, S.K., Singh, D.K., "Microscopic Nature of Magnetic Ground State in CeAuSb₂," *Phys. Status Solidi RRL*, in press.
- Zhan, P., Zhang, W., Jacobs, I.E., Nisson, D.M., Xie, R., Weissen, A.R., Colby, R.H., Moulé, A.J., Milner, S.T., Maranas, J.K., Gomez, E.D., "Side Chain Length Affects Backbone Dynamics in Poly(3-Alkylthiophene)s," *J. Polym. Sci. Pol. Phys.* **56**(17), 1193 (2018). [CHNRNS]
- Zhang, J., Pajeroski, D.M., Botana, A.S., Zheng, H., Harriger, L., Rodriguez-Rivera, J., Ruff, J.P.C., Schreiber, N.J., Wang, B., Chen, Y.-S., Chen, W.C., Norman, M.R., Rosenkranz, S., Mitchell, J.F., Phelan, D., "Spin Stripe Order in a Square Planar Trilayer Nickelate," *Phys. Rev. Lett.* **122**(24), 247201 (2019). [CHNRNS]
- Zhang, Q., Kale, T.S., Plunkett, E., Shi, W., Kirby, B.J., Reich, D.H., Katz, H.E., "Highly Contrasting Static Charging and Bias Stress Effects in Pentacene Transistors with Polystyrene Heterostructures Incorporating Oxidizable N,N'-Bis(4-Methoxyphenyl)aniline Side Chains as Gate Dielectrics," *Macromolecules* **51**(15), 6011 (2018).
- Zhang, X., Huestis, P.L., Pearce, C.I., Hu, J.Z., Page, K., Anovitz, L.M., Aleksandrov, A.B., Prange, M.P., Kerisit, S., Bowden, M.E., Cui, W., Wang, Z., Jaegers, N.R., Graham, T.R., Dembowski, M., Wang, H.-W., Liu, J., N'Diaye, A.T., Bleuel, M., Mildner, D.F.R., Orlando, T.M., Kimmel, G.A., La Verne, J.A., Clark, S.B., Rosso, K.M., "Boehmite and Gibbsite Nanoplates for the Synthesis of Advanced Alumina Products," *ACS Appl. Nano Mater.* **1**(12), 7115 (2018). [CHNRNS]
- Zhang, X., Mao, Y., Tyagi, M., Jiang, F., Henderson, D., Jiang, B., Lin, Z., Jones, R.L., Hu, L., Briber, R.M., Wang, H., "Molecular Partitioning in Ternary Solutions of Cellulose," *Carbohydr. Polym.*, in press. [CHNRNS]

- Zhang, X., Yuan, Q., Gao, T., Ren, Y., Wu, H., Huang, Q., Zhao, J., Wang, X., Yuan, Y., Xu, C., Hu, Y., Dynes, J.J., Zhou, J., Zhou, S., Liu, Y., Song, B., "Transition from Antiferromagnetic Ground State to Robust Ferrimagnetic order with Curie Temperatures above 420 K in Manganese-Based Antiperovskite-Type Structures," *J. Mater. Chem. C* **6**(48), 13336 (2018).
- Zhang, Y., Barber, T.J., Hu, Q., Bleuel, M., El-Sobky, H.F., "Complementary Neutron Scattering, Mercury Intrusion and SEM Imaging Approaches to Micro- and Nano-Pore Structure Characterization of Tight Rocks: A Case Study of the Bakken Shale," *Int. J. Coal Geol.*, in press. [CHRS]
- Zhang, Y., Hu, Q., Long, S., Zhao, J., Peng, N., Wang, H., Lin, X., Sun, M., "Mineral-Controlled nm- μ m-Scale Pore Structure of Saline Lacustrine Shale in Qianjiang Depression, Jiangnan Basin, China," *Mar. Petrol. Geol.* **99**, 347 (2019). [CHRS]
- Zhang, Z., Orski, S., Woys, A.M., Yuan, G., Zarraga, I.E., Wagner, N.J., Liu, Y., "Adsorption of Polysorbate 20 and Proteins on Hydrophobic Polystyrene Surfaces Studied by Neutron Reflectometry," *Colloid Surface. B* **168**, 94 (2018).
- Zhao, D., Ma, Y., Wang, E., Lodge, T.P., "Micellization of Binary Diblock Co-Polymer Mixtures in an Ionic Liquid," *Macromolecules* **52**(12), 4729 (2019).
- Zhao, L., Wang, D., Huang, Q., Wu, H., Sun, R., Fan, X., Song, Y., Jin, S., Chen, X., "Structural Evolution and Phase Diagram of the Superconducting Iron Selenides $\text{Li}_x(\text{C}_2\text{H}_8\text{N}_2)_y\text{Fe}_2\text{Se}_2$ ($x = 0 \sim 0.8$)," *Phys. Rev. B* **99**(9), 094503 (2019).
- Zheng, L., Frandsen, B.A., Wu, C., Yi, M., Wu, S., Huang, Q., Bourret-Courchesne, E., Simutis, G., Khasanov, R., Yao, D.-X., Wang, M., Birgeneau, R.J., "Gradual Enhancement of Stripe-Type Antiferromagnetism in the Spin-Ladder Material BaFe_2S_3 under Pressure," *Phys. Rev. B* **98**(18), 180402 (2018).
- Zhong, R., Guo, S., Xu, G., Xu, Z., Cava, R.J., "Strong Quantum Fluctuations in a Quantum Spin Liquid Candidate with a Co-Based Triangular Lattice," *P. Natl. A. Sci. USA* **116**(29), 14505 (2019).
- Zhou, Y., Josey, B., Anim-Danso, E., Maranville, B., Karapetrova, J., Jiang, Z., Zhou, Q., Dhinojwala, A., Foster, M.D., "In Situ Nanoscale Characterization of Water Penetration through Plasma Polymerized Coatings," *Langmuir* **34**(33), 9634 (2018).

Instruments and Contacts

(name, tel. 301-975-xxxx, email)

High resolution powder diffractometer (BT-1):

- J. K. Stalick, 6223, judith.stalick@nist.gov
- H. Wu, 2387, hui.wu@nist.gov
- Q. Z. Huang, 6164, qing.huang@nist.gov
- C. M. Brown, 5134, craig.brown@nist.gov

Engineering diffractometer (BT-8):

- T. Gnaeupel-Herold, 5380, thomas.gnaeupel-herold@nist.gov

vSANS instrument (NG-3) (CHRS):

- E. Kelley, 8584, elizabeth.kelley@nist.gov
- Y. Liu, 6235, yun.liu@nist.gov
- K. Krycka, 8685, kathryn.krycka@nist.gov
- J. G. Barker, 6732, john.barker@nist.gov
- C. Gagnon, 2020, cedric.gagnon@nist.gov

30-m SANS instrument (NG-B) (CHRS):

- P. D. Butler, 2028, paul.butler@nist.gov
- S. Krueger, 6734, susan.krueger@nist.gov
- M. Zhang, 5513, zhenhuan.zhang@nist.gov

10-m SANS instrument (NG-B) (nSoft):

- R. Jones, 4624, ronald.jones@nist.gov
- K. Weigandt, 8396, kathleen.weigandt@nist.gov
- T. Martin, 8866, tyler.martin@nist.gov
- M. Zhang, 5513, zhenhuan.zhang@nist.gov

uSANS, Perfect Crystal SANS (BT-5) (CHRS):

- M. Bleuel, 5165, markus.bleuel@nist.gov
- P. D. Butler, 2028, paul.butler@nist.gov

30-m SANS instrument (NG-7):

- S. Teixeira, 4404, susana.marujoteixeira@nist.gov
- Y. Mao, 5250, yimin.mao@nist.gov
- J. G. Barker, 6732, john.barker@nist.gov
- K. Krycka, 8685, kathryn.krycka@nist.gov
- J. R. Krzywon, 6650, jkrzywon@nist.gov

Polarized Beam Reflectometer/Diffractometer (NG-D):

- B. J. Kirby, 8395, brian.kirby@nist.gov
- J. A. Borchers, 6597, julie.borchers@nist.gov
- C. F. Majkrzak, 5251, cmajkrzak@nist.gov

MAGIK, Off-Specular Reflectometer (NG-D):

- J. A. Dura, 6251, joseph.dura@nist.gov
- F. Heinrich, 4507, frank.heinrich@nist.gov
- C. F. Majkrzak, 5251, cmajkrzak@nist.gov

Neutron reflectometer-horizontal sample (NG-7):

- S. K. Satija, 5250, satija@nist.gov
- G. Yuan, 5098, guangcui.yuan@nist.gov

CANDOR, White-beam reflectometer/diffractometer (CHRS):

- A. Grutter, 4198, alexander.grutter@nist.gov
- D. Hoogerheide, 8839, david.hoogerheide@nist.gov
- B. Maranville, 6034, brian.maranville@nist.gov
- C. F. Majkrzak, 5251, charles.majkrzak@nist.gov

HFBS, High-flux backscattering spectrometer (NG-2) (CHRS):

- M. Tyagi, 2046, madhusudan.tyagi@nist.gov
- T. Prisk, 5010, timothy.prisk@nist.gov

NSE, Neutron spin echo spectrometer (NG-A) (CHRS):

- A. Faraone, 5254, antonio.faraone@nist.gov
- M. Nagao, 5505, michihiro.nagao@nist.gov

MACS, Multi-angle crystal spectrometer (BT-9) (CHRS):

- J. A. Rodriguez-Rivera, 6019, jose.rodriguez@nist.gov
- Y. Qiu, 3274, yiming.qiu@nist.gov

Double-focusing triple-axis Spectrometer (BT-7):

- Y. Zhao, 2164, yang.zhao@nist.gov
- Z. Xu, 8097, zhijun.xu@nist.gov
- J. W. Lynn, 6246, jeff.lynn@nist.gov

SPINS, Spin-polarized triple-axis spectrometer (NG-5):

- G. Xu, 4144, guangyong.xu@nist.gov

Triple-axis spectrometer (BT-4):

- W. Ratcliff, 4316, william.ratcliff@nist.gov

FANS, Filter-analyzer neutron spectrometer (BT-4):

- T. J. Udovic, 6241, udovic@nist.gov

DCS, Disk-chopper time-of-flight spectrometer (NG-4):

- N. Butch, 4863, nicholas.butch@nist.gov
- W. Zhou, 8169, wei.zhou@nist.gov
- C. M. Brown, 5134, craig.brown@nist.gov

Cold neutron depth profiling (CNDP):

- J. Weaver, 6311, jamie.weaver@nist.gov

Cold-neutron prompt-gamma neutron activation analysis (PGAA):

- R. L. Paul, 6287, rpaul@nist.gov
- H. H. Chen-Mayer, 5595, heather.chen-mayer@nist.gov

Thermal-neutron prompt-gamma activation analysis (VT-5):

- R. L. Paul, 6287, rpaul@nist.gov

Other activation analysis facilities:

- N. Sharp, 3926, nicholas.sharp@nist.gov
- R. L. Paul, 6287, rpaul@nist.gov

Thermal Neutron Imaging Station (BT-2):

- J. LaManna, 6809, jacob.lamanna@nist.gov
- D. Jacobson, 6207, david.jacobson@nist.gov
- E. Baltic, 4842, eli.baltic@nist.gov
- D. Hussey, 6465, daniel.hussey@nist.gov

Cold Neutron Imaging Station (NG-6):

- D. Hussey, 6465, daniel.hussey@nist.gov
- E. Baltic, 4842, eli.baltic@nist.gov
- D. Jacobson, 6207, david.jacobson@nist.gov
- J. LaManna, 6809, jacob.lamanna@nist.gov

Neutron interferometer (NG-7):

- M. Huber, 5641, michael.huber@nist.gov
- D. Pushin, 4792, dmitry.pushin@nist.gov
- S. Hoogerheide, 8582, shannon.hoogerheide@nist.gov

Quantum-based neutron interferometer facility (NG-7):

- M. Huber, 5641, michael.huber@nist.gov
- S. Hoogerheide, 8582, shannon.hoogerheide@nist.gov
- D. Pushin, 4792, dmitry.pushin@nist.gov

Fundamental neutron physics station (NG-C):

- S. Hoogerheide, 8582, shannon.hoogerheide@nist.gov
- M. S. Dewey, 4843, maynard.dewey@nist.gov

Fundamental neutron physics station (NG-6):

- NG-6M: M. S. Dewey, 4843, mdewey@nist.gov
- NG-6M: H. P. Mumm, 8355, hans.mumm@nist.gov
- MDM (NG-6A): M. Huber, 5641, michael.huber@nist.gov
- MDM (NG-6A): T. Gentile, 5431, thomas.gentile@nist.gov
- a- γ : H. P. Mumm, 8355, hans.mumm@nist.gov
- a- γ : M. S. Dewey, 4843, mdewey@nist.gov

Theory and modeling:

- J. E. Curtis, 3959, joseph.curtis@nist.gov
- T. Yildirim, 6228, taner@nist.gov

Neutron test station (PHADES):

- R. Erwin, 6245, ross.erwin@nist.gov
- S. Watson, 6232, shannon.watson@nist.gov
- K. Krycka, 8685, kathryn.krycka@nist.gov

Instruments under development:**SPINS-II:**

- L. Harriger, 8360, leland.harriger@nist.gov

NIST Center for Neutron Research Contacts

Copies of annual reports, facility information, user information, and research proposal guidelines are available electronically.

Please visit [the homepage of the NIST Center for Neutron Research](#).

For a paper copy of this report:

Steve Kline
301-975-6243
steven.kline@nist.gov

For general information on the facility:

Rob Dimeo
301-975-6210
robert.dimeo@nist.gov

Dan Neumann
301-975-5252
dan.neumann@nist.gov

For information on visiting the facility and/or user access questions:

Julie Keyser
301-975-8200
julie.keyser@nist.gov

Mary Ann FitzGerald
301-975-8200
maryann.fitzgerald@nist.gov

Becky Ogg
301-975-8200
rebecca.ogg@nist.gov

For information on performing research at the facility:

Yamali Hernandez
301-975-5295
yamali.hernandez@nist.gov

Facility address:

NIST Center for Neutron Research
National Institute of Standards and Technology
100 Bureau Drive, Mail Stop 6100
Gaithersburg, MD 20899-6100 USA

NIST CENTER FOR NEUTRON RESEARCH

National Institute of Standards and Technology
100 Bureau Drive, MS 6100
Gaithersburg, MD 20899-6100

www.ncnr.nist.gov

